Precision Calibration of Large Area Micro Pattern Gaseous Detectors

Philipp Lösel

München 2017

Precision Calibration of Large Area Micro Pattern Gaseous Detectors

Philipp Lösel

Dissertation der Fakultät für Physik
der Ludwig–Maximilians–Universität München

vorgelegt von
Philipp Lösel
aus München

München, den 30. Juni 2017

Erstgutachter: Prof. Dr. Otmar Biebel
Zweitgutachter: Priv. Doz. Dr. Peter Thirolf
Tag der mündlichen Prüfung: 24. Juli 2017

Zusammenfassung

Um die erhöhte Luminosität des Large Hadron Colliders am CERN verarbeiten zu können, müssen die inneren Endkappen des ATLAS Muon Spectrometers, die sogenannten Small Wheels, verbessert werden. Jedes dieser neuen Small Wheels wird in acht kleine und acht große Sektoren unterteilt sein, die jeweils aus zwei trapezförmigen Modulen bestehen werden. Zu diesem Zwecke wurde die MICRO-MEsh GAseous Structure (Micromegas) Detektortechnologie ausgewählt. Jedes Micromegas-Modul wird aus vier aktiven Detektorebenen mit jeweils 2-3 m^2 Größe bestehen. Micromegas-Detektoren in dieser Größe wurden noch nie zuvor gebaut. Um die sehr gute Impulsauflösung der derzeitig verwendeten Detektortechnologien von 15 % bei 1 TeV Myonen zu erhalten, müssen die Micromegas eine Genauigkeit der Ortsrekonstruktion von ungefähr 100 µm haben, sogar bei erhöhter Untergrundstrahlung von ungefähr 15 $\mathrm{kHz\,cm^{-2}}$. Um dies zu erreichen, sind eine sehr genaue Konstuktion und Kalibration nötig. Der Schwerpunkt dieser Arbeit liegt bei den Modulen, die in Deutschland gebaut werden. Diese sogenannten SM2-Module gehören zu den kleineren Modulen mit einer Größe von ungefähr 2 m^2.

Jedes Modul besteht aus fünf Paneelen, drei Drift- und zwei Auslese-Paneelen, die einen Kern aus einer Aluminium-Wabenstruktur haben, auf dessen Oberflächen zwei 0,5 mm dicke Leiterplatten (PCB) geklebt werden. Auf diesen PCBs sind entweder Kathoden- oder resistive Auslesestrukturen geätzt. Wegen Einschränkungen bei der industriellen Produktion dieser PCBs muss jede Oberfläche der Paneele aus drei PCBs gebaut werden, die eine Streifenpositionsgenauigkeit von unter 30 µm haben müssen. Die Planarität jedes Paneels muss sehr gut sein, mit einem quadratischen Mittel besser als 37 µm. Nachdem diese Paneele fertiggestellt sind werden Alignierungsstifte und Präzisionsabstandshalter für den Zusammenbau des Moduls verwendet. Damit wird sicher gestellt, dass die Streifenposition der vier Oberflächen der Auslesepaneele zueinander die selbe Genauigkeit haben wie die Streifenpositionen innerhalb einer einzigen Auslesefläche. Zusätzlich werden an sechs Positionen im Modul Stabilisierungen gegen die Deformation eingebaut, die durch einen geringen Überdruck in den Detektoren auftreten würde.

Nach dem Zusammenbau der Module, werden sie in dem Höhenstrahlungs-Messstand der LMU in Garching kalibiert. Dieser Messstand besteht aus zwei Referenzdetektoren, Monitored Drift Tube Kammern (MDTs), und zwei Szintillatorebenen, die bei koinzidenten Signalen die Auslese starten und zusätzlich eine grobe Information über die Position des Teilchendurchgangs senkrecht zu den Drähten der MDTs geben. Anhand eines 1 m^2 großen Prototyp-Micromegas mit einer Ausleseebene wurden Kalibrationsmethoden entwi-

ckelt, um den Versatz und die Rotation zwischen zwei Auslese-PCBs zu bestimmen. Diese Messung ist zusätzlich sehr sensitiv auf Abweichungen von der erwarteten Streifenperiodizität, die in der Größenordnung von 10 nm bestimmt werden kann. Auch die Deformation des Driftvolumens kann auf diese Weise bestimmt werden, die auf Grund eines leichten Überdrucks auftritt. Da der $1\,\mathrm{m}^2$ große Prototyp-Micromegas keine Stabilisierung gegen Überdruck im Detektorvolumen hat, zeigte er eine Deformation von ungefähr 3 mm.

Bei einer Woche Messzeit hat der $1\,\mathrm{m}^2$ große Prototyp Micromegas unter Berücksichtigung von Vielfachstreuung und der Genauigkeit der Spurvorhersage eine Ortauflösung von ungefähr 150 µm für Myonspuren senkrecht zur Detektorebene gezeigt. Im Vergleich zeigte eine eintägige Messung eine Ortauflösung von ungefähr 80 µm. Dies liegt vermutlich an dem Beitrag von etwa 100 µm durch die thermische Bewegung des gesamten experimentellen Aufbaus. Zudem zeigte die Messung, dass größere Spursteigungen die Ortauflösung verschlechtern. Dies stimmt mit den Ergebnissen einer Teststrahlmessung mit 120 GeV Pionen am CERN überein. Während dieser Messungen zeigte der $1\,\mathrm{m}^2$ große Prototyp-Micromegas, der unmittelbar vor der Messung zusammen gebaut wurde, wegen erhöhten elektronischen Rauschens eine schlechtere Ortauflösung als ein kleinerer Test-Micromegas, mit einer aktiven Fläche von ungefähr $(10 \times 10)\,\mathrm{cm}^2$.

Zusätzlich wurden anhand des $1\,\mathrm{m}^2$ großen Prototyp-Micromegas im Höhenstrahlungs-Messstand unterschiedliche Gasmischungen untersucht, die auf Argon und Neon basieren. Mit diesen Messungen konnten Einflüsse von Driftgeschwindigkeit, transversaler und longitudinaler Diffusion und der Elektronentransparenz des Mikro-Gitters auf die Pulshöhe, die Effizienz und die Ortauflösung bestimmt werden.

Eine aktuelle Anwendung kosmischer Myonen ist die Myon-Tomographie. Als Testbeispiel wurde bei der Messung im Höhentrahlungs-Messstands der Punkt der Coulomb-Streuung des kosmischen Myons bestimmt, womit dann Bereiche mit dichterem Material identifiziert werden können. Dies zeigt die exzellente Auflösung des Höhenstrahlungs-Messstands für kosmische Myonen.

Abstract

To cope with the increased luminosity of the Large Hadron Collider at CERN the innermost end-cap regions of the ATLAS Muon Spectrometer, the so-called Small Wheels, have to be upgraded. Each New Small Wheel will be subdivided in eight large and eight small sectors each consisting of two trapezoidal modules. The MICRO-MEsh GAseous Structure (Micromegas) detector technology has been chosen for this upgrade. Every Micromegas module will consist of four active detection layers with a size of 2-3 m^2 each. Micromegas detectors in this size were never built before. To maintain the excellent momentum resolution of 15 % at 1 TeV muons of the current Muon Spectrometer the Micromegas have to reconstruct the hit position with a spatial resolution of about 100 µm at high background hit rate of 15 kHz cm^{-2}. Herefore a very accurate construction and a calibration of the modules is demanded. This thesis focuses on the modules built in Germany, the so-called SM2-modules, which belong to the small modules with a size of about 2 m^2.

Each module consists of five panels, three drift and two readout panels, with an aluminum honeycomb core sandwiched by two 0.5 mm thick printed circuit boards (PCB). The PCB surfaces are etched either as cathodes or as resistive anode readout structures. Due to production limitations in industrial PCB production the panel surface has to be constructed out of three PCBs which have to have a strip alignment better than 30 µm. This is ensured by a very accurate alignment frame during gluing of the panels. The planarity of each panel has to be better than 37 µm. After completion the panels are assembled to a module with dedicated alignment pins and precise spacers to assure the same accuracy between the strips of the four surfaces of the two readout panels relative to each other as within one surface. Six so-called interconnections are used to stabilize the module against a slight overpressure of about 2-3 mbar.

Each assembled module will be calibrated in the LMU Cosmic Ray Facility in Garching consisting of two reference tracking detectors, i.e. Monitored Drift Tube chambers, and two trigger hodoscopes, which provide also a coarse position information on the coordinate perpendicular to the precision measurement direction. Techniques have been developed while calibrating the shift and rotation between two readout PCBs of a 1 m^2 prototype Micromegas with one detection plane. This measurement is very sensitive to strip pitch variations down to a few ten nm. The deformation of the drift region due to a slight overpressure can be determined as well. This 1 m^2 prototype Micromegas lacks an overpressure stabilization and thus shows a deformation of about 3 mm.

The 1 m^2 large prototype Micromegas yields a spatial resolution of about 150 µm for

cosmic muon tracks perpendicular to the detection plane considering multiple scattering and the track prediction accuracy of the reference detectors in a measurement of about one week. A shorter measurement of about one day with the same parameters yielded a spatial resolution of about 80 µm for perpendicular tracks. It seems there is a contribution of about 100 µm as a function of time due to thermal movement, which is reasonable considering the size of the experimental setup. The experiment shows additionally, that larger reference angles degrade the achievable spatial resolution, which is in good agreement with the results of a testbeam campaign with 120 GeV pions at CERN. A degraded spatial resolution is found for the $1\,m^2$ prototype when compared to small test Mircomegas with an active area of about $(10 \times 10)\,cm^2$ during this testbeam campaign. This is due to the high noise level of the large prototype Micromegas, which had been assembled just before the measurement.

Additionally Argon and Neon based drift gases are investigated in the Cosmic Ray Facility using the large prototype Micromegas. In these measurements effects of the drift velocity, lateral and longitudinal diffusion, and the electron transparency of the mesh on pulse height, tracking efficiency and spatial resolution, are determined with the centroid and the TPC-like method, have been determined.

One application of cosmic muons is muon tomography. In the Cosmic Ray Facility the point of Coulomb scattering of a traversing muon is determined and thus any area with more dense material can be identified. This demonstrates the excellent resolution of the Cosmic Ray Facility.

Contents

Chapter 1

Introduction

In this chapter the upgrade of the Large Hadron Collider to High Luminosity LHC will be described. This defines the motivation for the upgrade of the inner end-cap region of the ATLAS Muon Spectrometer.

1.1 LHC High Luminosity Upgrade

During the last years the Large Hadron Collider (LHC) at CERN has increased the center of mass energy from 7 TeV to 13 TeV and will soon reach its design center of mass energy of 14 TeV. The instantaneous luminosity was also increased over the years and in 2015 the nominal luminosity of $1 \times 10^{34}\,\mathrm{s}^{-1}\mathrm{cm}^{-2}$ was reached. For example an integrated luminosity of $38.5\,\mathrm{fb}^{-1}$ at 13 TeV was delivered to ATLAS until end of 2016. To allow the experiments to fully explore their sensitivity to new phenomena the luminosity of the LHC will be further increased. This is called the High Luminosity LHC (HL-LHC). After the Long Shutdown 2 (LS2) in 2019/2020 the instantaneous luminosity will reach two times the nominal luminosity. And after Long Shutdown 3 (LS3) the HL-LHC will deliver up to seven times and maybe even ten times the nominal luminosity (see fig. 1.1).

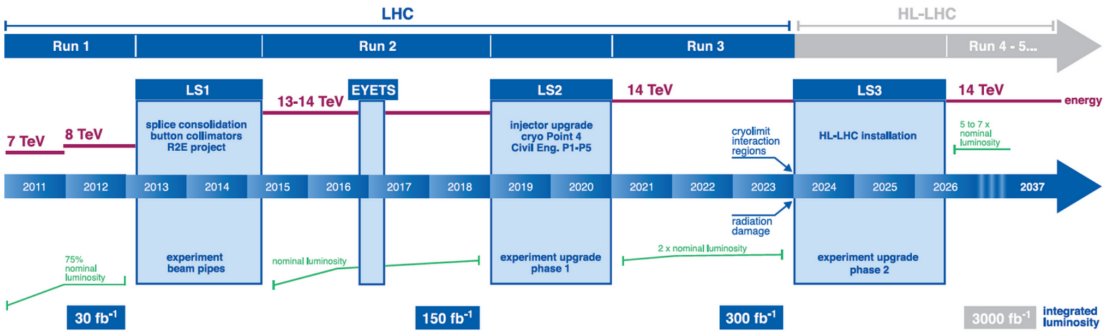

Figure 1.1: Time line for the upgrade of the Large Hadron Collider (LHC) to High Luminosity LHC. The Long Shutdowns (LS) are marked and values for the instantaneous luminosity and center of mass energy are given. Figure taken from [CERN website, 2016].

The experiments at LHC (see fig. 1.2) have to cope with this increased luminosity. Therefore they need upgrades as well. Each experiment has its specific upgrades. This thesis focuses on the upgrade of the inner end-cap region of the ATLAS Muon Spectrometer [ATLAS Collaboration, 2013]. In figure 1.2 also the Super Proton Synchrotron (SPS) is shown with the North Area, where the testbeam campaign for this thesis was performed.

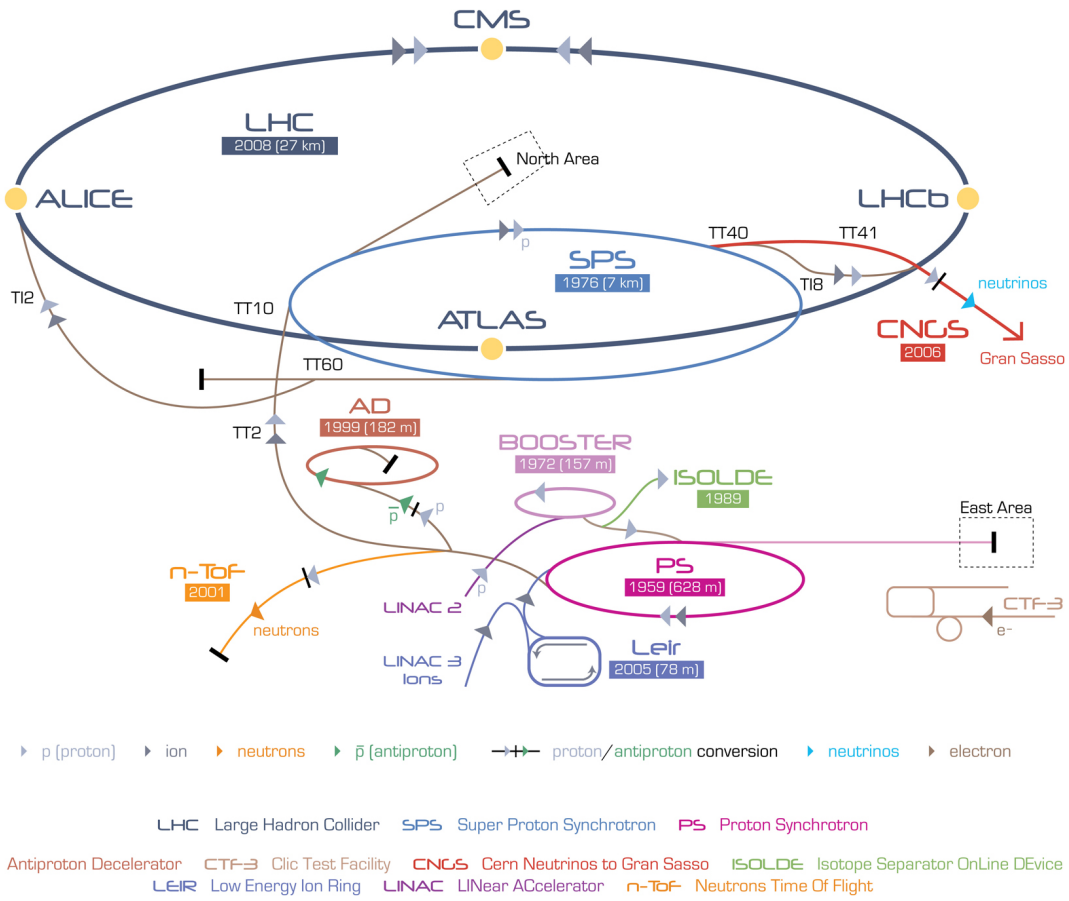

Figure 1.2: Schematic of the Large Hadron Collider (LHC) with the pre-accelerators and booster. Also shown are the four large LHC experiments. Figure taken from [CERN website, 2008].

1.2 Motivation for the ATLAS NSW Upgrade Project

Figure 1.3 shows the ATLAS experiment (A Toroidal LHC ApparatuS) [ATLAS Collaboration, 2008]. This thesis focuses on the upgrade of the ATLAS Muon Spectrometer. The Muon Spectrometer has a cylindrical shape with three detection layers and can be divided in the barrel and end-cap regions. The end-cap regions are defined as forward direction

with a pseudorapidity of $|\eta| > 1$ (see eq. 1.1).

$$\eta \equiv -\ln\left[\tan\left(\frac{\Theta}{2}\right)\right] \tag{1.1}$$

The Muon Spectrometer is located in the magnetic field B of the toroid, hence the momentum p of the muons can be calculated with

$$p = BqR\ , \tag{1.2}$$

where q is the charge of the muons and R is the curvature radius of the muon track.

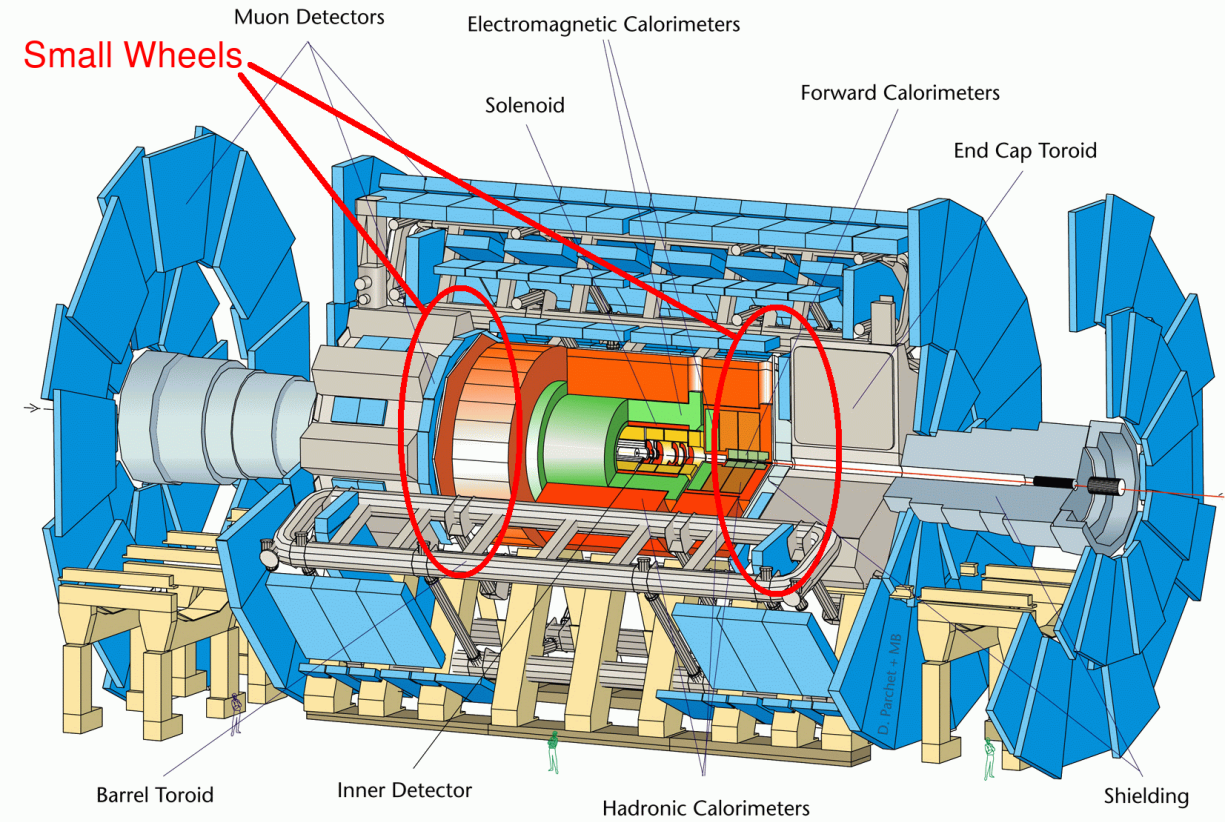

Figure 1.3: Schematic of the ATLAS experiment. The Muon Spectrometer is indicated in blue and the inner-most end-cap regions (Smalls Wheels) in red. Figure adopted from [ATLAS website, 1997].

The inner-most part of the end-cap regions are called Small Wheels (indicated in red in fig. 1.3) with $1.3 < |\eta| < 2.7$. Hence the angular acceptance is $30° > |\Theta| > 8°$. The upgrade of the inner end-cap regions during LS2 is called the New Small Wheel (NSW) Upgrade Project and is necessary for multiple reasons.

The trigger of the ATLAS experiment is a multistage trigger. In the first stage (Level 1) the Muon Spectrometer is included. For the end-cap regions only one of the three wheels

provides trigger information, the middle big wheel. One reason for the NSW upgrade is the full inclusion of the NSW in the Level 1 trigger. Figure 1.4 shows the trigger rate as function of η. It can be seen that with the current trigger (L1_MU11) the online rate for $|\eta| > 1$ is strongly increased. When the triggers are matched to reconstructed muons with transverse momenta $p_T > 10\,\text{GeV}$, the rate is almost homogeneous in η. This effect occurs due to a large fraction of tracks in the middle end-cap wheel, which are pointing to the interaction point (IP), but do not start in the IP. With the inclusion of the Small Wheels in the trigger this can be prevented.

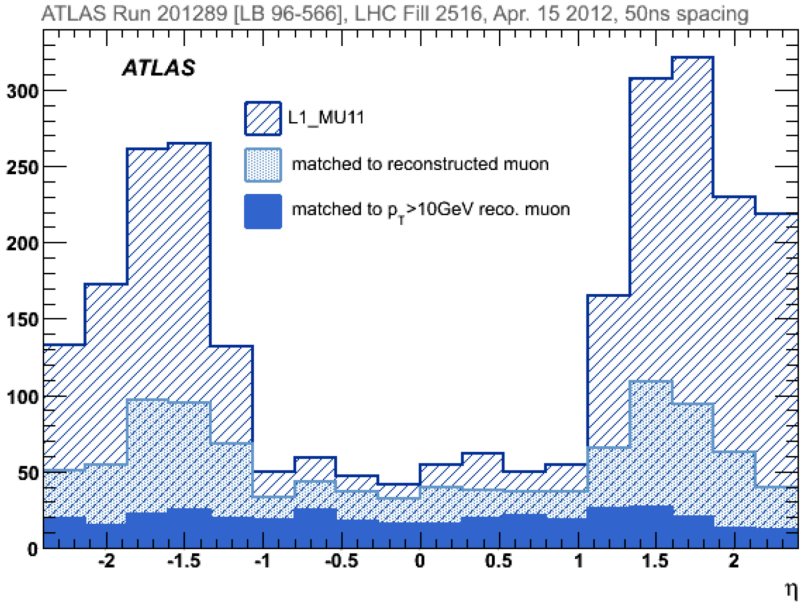

Figure 1.4: Trigger rate as a function of the pseudorapidity η of the ATLAS Muon Spectrometer for different reconstruction methods. The trigger without matching to reconstructed muons shows a much higher rate for $|\eta| > 1$. With matching to reconstructed muons with $p_T > 10\,\text{GeV}$ it is almost homogeneous in η. Figure taken from [ATLAS Collaboration, 2013].

Figure 1.5 shows three example tracks in the Muon Spectrometer. The reconstruction in the middle wheel suggests that all three tracks originate from the IP. Two lead to fake triggers and one is a good muon track without inclusion of the NSW in the Level 1 trigger. Track A is the good muon track, which can be reconstructed to the IP. Track B is a proton scattered in the beam-pipe and track C comes from background induced in the calorimeters. Those two lead to fake triggers in the end-cap regions. With the full inclusion of the Small Wheels in the trigger, those fake triggers can be prevented.

The other important reason for the NSW upgrade is the efficiency loss of the currently used Monitored Drift Tube (MDT) chambers due to increased background hit rates. MDTs are used as trackers in the ATLAS Muon Spectrometer. Figure 1.6 shows the efficiency of

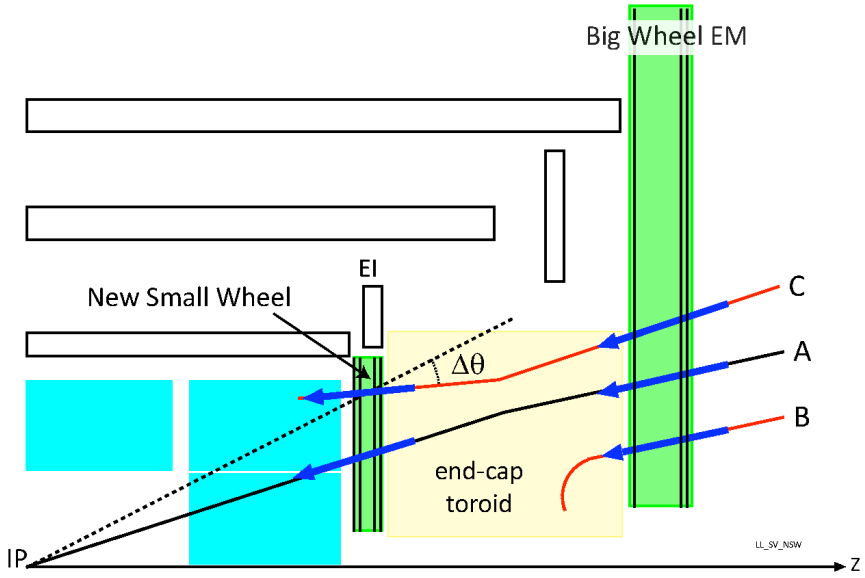

Figure 1.5: Schematic of one quarter of the ATLAS detector. Three example tracks are shown. Track A is a good muon track, which can be reconstructed to the interaction point (IP). Track B is a proton scattered in the beam-pipe and track C is a track starting in the calorimeters. Figure taken from [ATLAS Collaboration, 2013].

the MDTs. The dashed line is for a whole chamber with two times four tube layers and the solid line is for one single tube. The hit rate for the design luminosity of 300 kHz/tube is equivalent with about 15 kHz/cm^2. The efficiency for one whole chamber is still above 90 %, but at the luminosity for HL-LHC the efficiency will decrease below 60 %. Hence high-rate capable detector technologies with an excellent spatial resolution have to be used as replacement.

To do so it was decided to use small-strip Thin Gas Chambers (sTGC), which are multi-wire proportional chambers, and MICRO-MEsh GAseous Stucture (Micromegas), which are micro-pattern gaseous detectors. The design and layout of the New Small Wheel will be discussed in chapter 5. This thesis focuses on Micromegas. Information on sTGCs can be found in [Smakhtin et al., 2009].

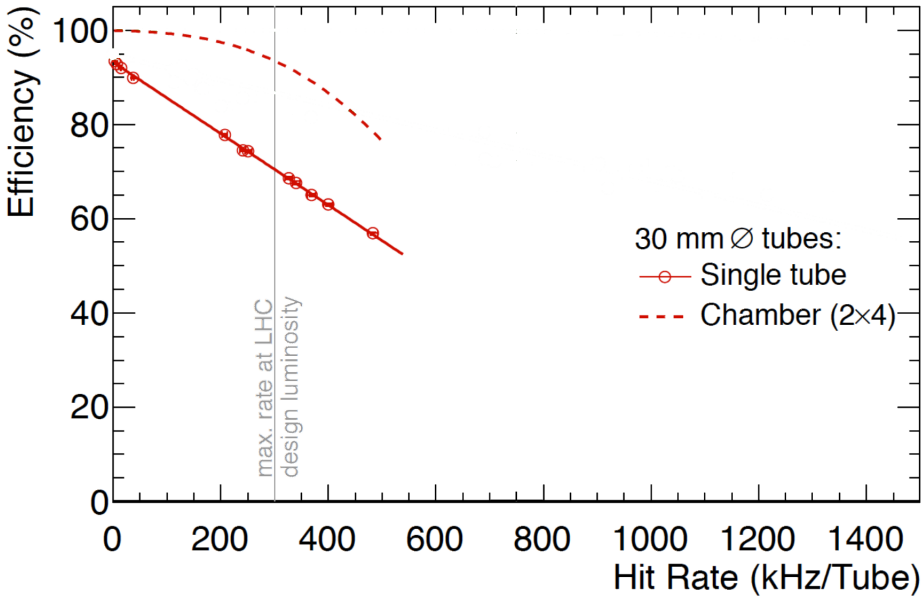

Figure 1.6: Efficiency of Monitored Drift Tube chambers as a function of the hit rate. The red dots are measurements for a single tube and the dotted line shows the extrapolated efficiency for a whole chamber with two times four tube layers. The indicated design luminosity is equivalent to the nominal luminosity mentioned before. Figure taken from [ATLAS Collaboration, 2013].

Chapter 2

Micromegas

This chapter describes the interaction of charged particles with matter, the working principle of Micromegas and discharge protection. The reconstruction methods used with Micromegas are explained as well.

2.1 Energy Loss in Matter

The averaged energy loss in matter of a charged particle follows the Bethe-Bloch equation [Leo, 1994].

$$-\left\langle \frac{dE}{dx} \right\rangle = 2\pi N_{\mathrm{A}} r_{\mathrm{e}}^2 m_{\mathrm{e}} c^2 \rho \frac{Z}{A} \frac{z^2}{\beta^2} \left[ln\left(\frac{2m_{\mathrm{e}}\gamma^2 v^2 W_{\max}}{I^2} \right) - 2\beta^2 - \delta^2 - 2\frac{C}{Z} \right] , \tag{2.1}$$

where c is the speed of light, r_{e} is the classical electron radius, m_{e} is the electron mass, N_{A} is the Avogadro's number, I is the mean excitation potential, Z, A and ρ are the atomic number, atomic weight and density of the absorbing material, z and v are the charge in units of e and the velocity of the incident particle with $\beta = v \cdot c^{-1}$ and $\gamma = \left(\sqrt{1-\beta^2}\right)^{-1}$, and $W_{\max} \approx 2m_{\mathrm{e}}c^2\beta^2\gamma^2$ is the maximum energy transfer to an electron in a single collision.

Figure 2.1 shows the stopping power of copper for a muon as a function of the muon momentum. Particles with $\beta\gamma \approx 4$ are called minimum ionizing particles (MIP). MIPs deposit the lowest amount of energy in matter. With a higher momentum the particles are in the relativistic rise, where the energy deposit gets larger. The more homogeneous the energy deposit is, the better the position can be reconstructed (see sec. 2.4). For gaseous Argon the stopping power is smaller due to the dependence on the density and atomic number. In table 2.1 the differential energy loss is given for some material relevant for this thesis. Particles used in the measurement for this thesis are 120 GeV pions, which have more momentum than MIPs, and cosmic muons. Cosmic muons have a very broad energy range with a Landau-function like distribution. The most probable value is about 2 GeV and the average energy at about 4 GeV.

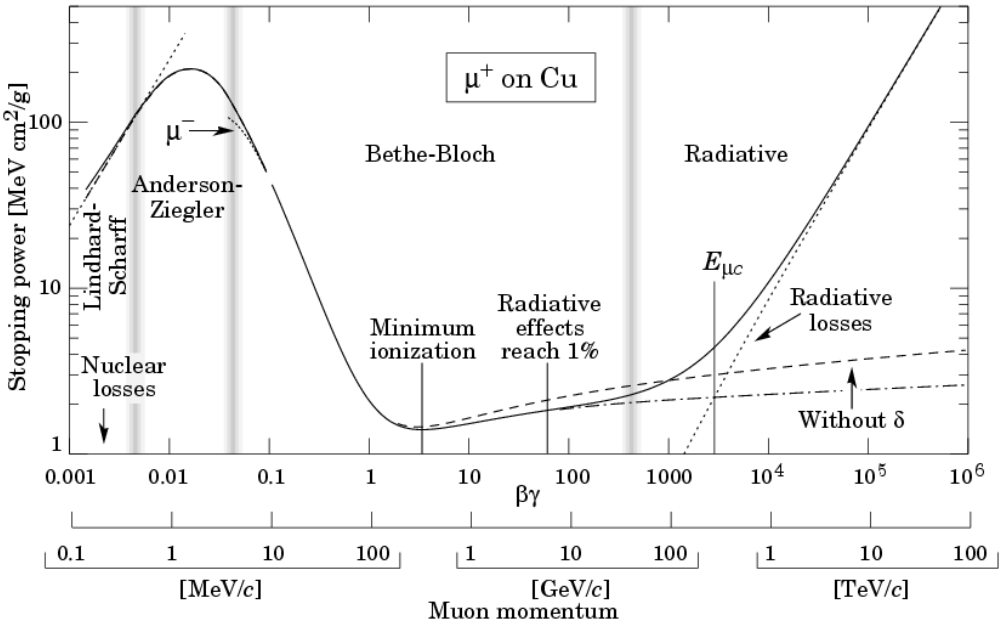

Figure 2.1: The stopping power of copper for a positively charged muon as a function of the muon momentum. The muon has a large energy deposit for small momenta, which decreases to minimum ionization and rises again in the relativistic rise. Figure taken from [Groom et al., 2001].

Table 2.1: Differential energy loss for various materials. Values taken from [Beringer, J. et. al. (Particle Data Group), 2012].

material	$^{dE}/_{dx}\|_{min}$ [keV cm^{-1}]
Ar	2.53
CO_2	3.35
Ar:CO_2 93:7 vol%	2.59
Al	4.36×10^3

Cosmic muons with rather low energy are likely scattered in matter by substantial angle. The multiple scattering through small angles follows equation 2.2 and hence is energy dependent. Table 2.2 gives examples for four typical energies of cosmic muons with the width σ_Θ of the Gauss distributed scattering angle and the averaged position deviation after 0.5 m.

$$\sigma_\Theta = \frac{13.6\,\mathrm{MeV}}{\beta c p} z \sqrt{\frac{x}{X_0}} \left[1 + 0.038 \ln\left(\frac{x}{X_0}\right)\right] , \tag{2.2}$$

where z is the charge of the incident particle, x is the thickness of the scattering medium and X_0 is the radiation length ($X_0(\mathrm{Al}) = 8.9\,\mathrm{cm}$, $X_0(\mathrm{FR4}) = 15.9\,\mathrm{cm}$ [Adler, 2006]. The radiation length of FR4 can vary with 10 % depending on the composition of glass fiber and epoxy resin.).

Table 2.2: Muon energy E_μ, the width of the distribution of scattered angles and the sigma of the position deviation in 0.5 m distance ($z = 0.5\,\mathrm{m}$).

E_μ [MeV]	σ_Θ [°]	$\sigma_{x,\ \mathrm{mult.\ scatt.}}(z = 0.5\,\mathrm{m})$ [mm]
700	0.22	1.92
2000	0.077	0.67
4000	0.038	0.33
120×10^3	0.0013	0.01

2.2 Working Principle

Figure 2.2 shows a schematic drawing of a MICRO-MEsh GAseous Structure (Micromegas) [Giomataris et al., 1996] consisting of three planar elements, the cathode, the anode-structure and the woven micro-mesh, which divides the active volume in drift and amplification region. A charged particle traversing the detector ionizes gas atoms along its path. Due to the electric field in the drift region the positive ion-electron pairs get separated and the positively charged ions drift towards the cathode, whereas the electrons drift towards the stainless-steel micro-mesh.

The amount of charges produced during the ionization is not sufficient for detection and thus additional amplification is needed. Therefore the electrons are guided by the electric field through the micro-mesh into the amplification region. In the very high electric field ($\mathcal{O}(40\,\mathrm{kV\,cm^{-1}})$) the electrons are accelerated to high energies and create new electrons in collisions with gas atoms, so-called avalanches. The multiplication factor or gas gain G can be calculated with the first Townsend coefficient $\alpha = \lambda^{-1}$, where λ is the mean free path of the electron:

$$G = \frac{n}{n_0} = \exp(\alpha x) , \tag{2.3}$$

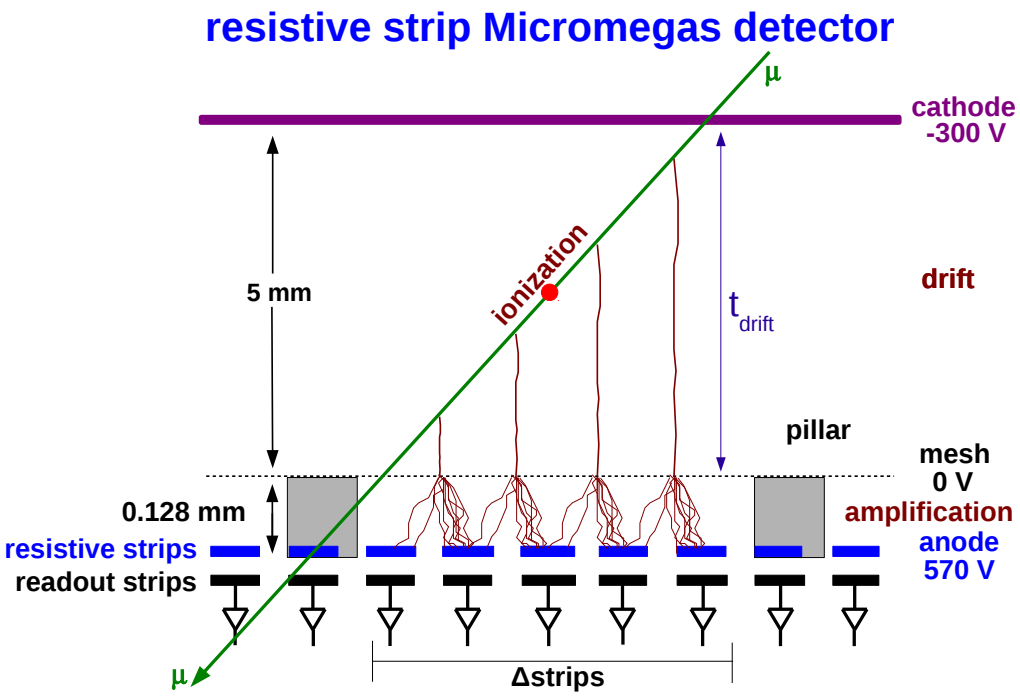

Figure 2.2: Scheme of a resistive strip Micromegas detector. A muon is traversing the detector and ionizes the gas atoms along its path. The electrons drift through the mesh into the amplification region, where avalanches are created. The multiplicated charge is collected on the resistive strips and read out on the copper readout strips with charge sensitive preamplifiers. High values of $E_{\mathrm{amp}}/E_{\mathrm{drift}}$ enable high transmission transparencies for electrons through the mesh.

where n is the total number of electrons, n_0 the number of primary electrons and x the amplification distance.

Physically the gas gain is limited at $\alpha x \approx 20$, the so-called Raether limit [Raether, 1964]. Then the electron density in the amplification region is so high, that local streamer occur and equalize the potential between mesh and anode. This happens for instance in Micromegas set up for minimum ionizing particle detection that are also bombarded with strongly ionizing background particles like in the ATLAS experiment. To prevent this effect or localize it to a small area in the detector a discharge protection has to be used. In standard Micromegas the high voltage is connected to mesh and cathode keeping the anode at ground potential. Micromegas with discharge protection can have their high voltage connection at anode and cathode thus keeping the mesh on ground potential. For simplicity reasons in measurements for this thesis the high voltage was connected to the anode. This allows additionally for triggering on the signal capacitively coupled to the mesh.

One possibility to protect against discharges is to use resistive strips. These strips are sputtered on a Kapton foil which is glued on top of the copper readout strips. Resistive and readout strips are precisely aligned. A slightly distinct pattern with connections between the resistive strips can be used to minimize effects due to defects. The resistive material is so high ohmic ($\mathcal{O}(\mathrm{M\Omega cm^{-1}})$), that the equalization of the electric potential between mesh and anode can be limited to a very small area of the Micromegas or even to one resistive strip [Alexopoulos et al., 2011].

Another possibility is to use floating strips. Here a second layer of copper strips on top but insulated to the readout strips is connected to the power supply with a high ohmic resistor. Therefore only on few strips, located close to the discharge, the electric potential drops [Bortfeldt, 2014].

2.3 Electron Drift

The drift of the electrons in the electric field is a key feature of the Micromegas. After the ionization of the gas atoms the electrons drift to the mesh. This is defined by their drift velocity v_{drift} (see eq. 2.4). Figure 2.3 shows the electron drift velocity computed with *MAGBOLTZ* [Biagi, 1999] as a function of the electric field for Ar:CO_2 93:7 vol% and Ne:CF_4 80:20 vol%. These two gas mixtures were used in measurements for this thesis. It can be seen that the electron drift velocity in Ne:CF_4 80:20 vol% is much higher. This can be relevant for high rate applications. Whereas the electron drift velocity in Ar:CO_2 93:7 vol% is rather constant for an electric field above $500\,\mathrm{V\,cm^{-1}}$. With a time sensitive readout the drift time can be measured and used for track reconstruction (see 2.4.3). See appendix A for electron drift velocities of other gas mixtures.

$$v_{\mathrm{drift}} = \mu E_{\mathrm{drift}} \ , \tag{2.4}$$

where μ is the electron mobility and E_{drift} is the electric drift field [Leo, 1994].

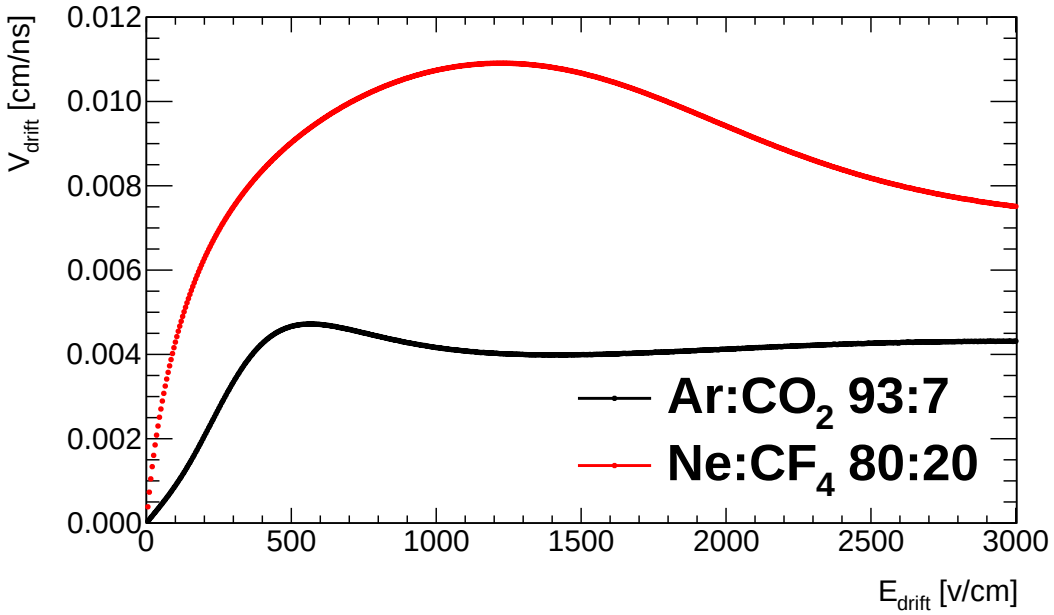

Figure 2.3: Electron drift velocity as a function of the drift field for Ar:CO_2 93:7 vol% and Ne:CF_4 80:20 vol%. A typical drift field for Micromegas is $600\,\mathrm{V\,cm^{-1}}$. Computed with *MAGBOLTZ* [Biagi, 1999].

Another part of the electron drift which is important for the position reconstruction are transverse and longitudinal diffusion computed with *MAGBOLTZ* of the electrons in the drift field. Figures 2.4 and 2.5 show the transverse and longitudinal diffusion as a function of the drift field for Ar:CO_2 93:7 vol% and Ne:CF_4 80:20 vol%. This means the RMS of the transverse position deviation for a 1 cm long drift. For some reconstruction methods the spreading of the charge helps to reconstruct the position of the traversing particle better. Whereas the longitudinal diffusion leads to an uncertainty on the drift time of the electrons. Figure 2.6 shows the drift time of electrons for 5 mm in Ar:CO_2 93:7 vol% at an electric field of $600\,\mathrm{V\,cm^{-1}}$. This distribution is fitted with a Gaussian function leading to a drift time $t_{\mathrm{drift}} = (105.8 \pm 2.9)\,\mathrm{ns}$. The uncertainty depends on the length of the drift path for a constant electric field.

2.4 Position Reconstruction Methods

To reconstruct tracks of traversing particles two major reconstruction methods for Micromegas detectors can be used, the charge weighted strip position (centroid) and a TPC-like method using the measured drift time (μTPC). The name TPC-like method is inspired by the Time Projection Chambers [Nygren and Marx, 1978].

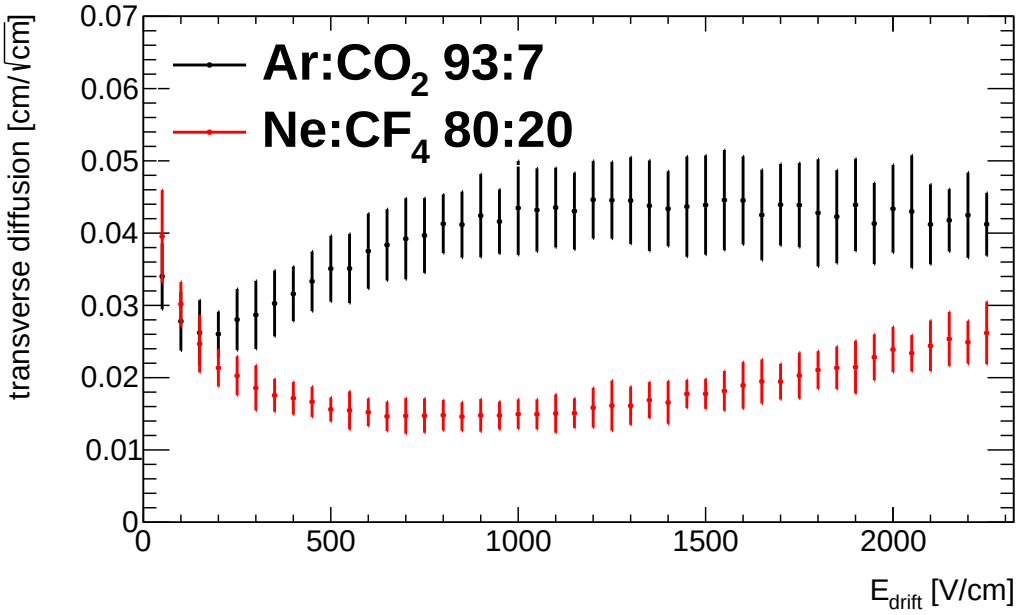

Figure 2.4: Transverse diffusion as a function of the drift field for Ar:CO_2 93:7 vol% and Ne:CF_4 80:20 vol%. A typical drift field for Micromegas is 600 V cm^{-1}. Computed with *MAGBOLTZ* [Biagi, 1999].

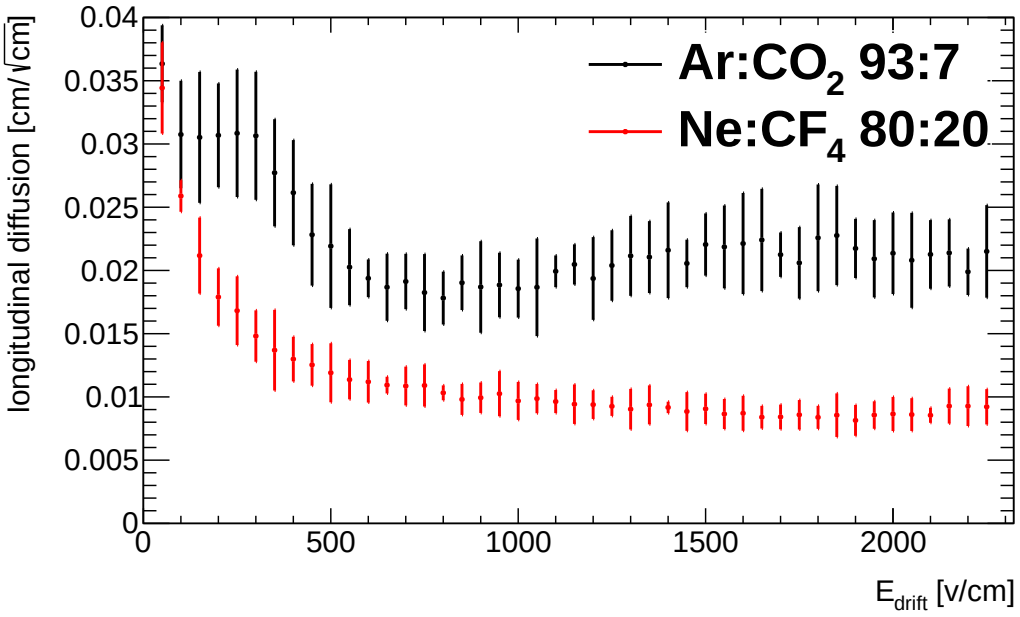

Figure 2.5: Longitudinal diffusion as a function of the drift field for Ar:CO_2 93:7 vol% and Ne:CF_4 80:20 vol%. A typical drift field for Micromegas is 600 V cm^{-1}. Computed with *MAGBOLTZ* [Biagi, 1999].

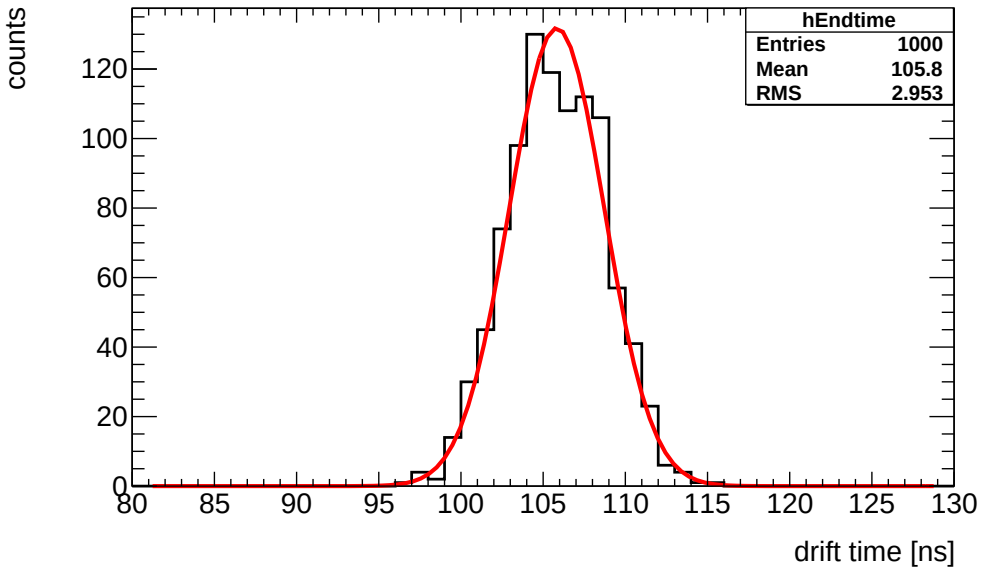

Figure 2.6: Simulated drift time of electrons for 5 mm in Ar:CO_2 93:7 vol% at an electric field of 600 V cm^{-1} fitted with a Gaussian function. The uncertainty on the drift time is about 2.9 ns due to the longitudinal diffusion. Computed with *Garfield* [Garfield website, 2010].

2.4.1 Signal Identification

Before the tracks can be reconstructed the signals have to be identified determining signal time and pulse height. Figure 2.7 shows the time evolution of the integrated charge $q(t)$ of a single Micromegas strip. The front-end electronics boards used for the measurement in this thesis integrates the charge over 25 ns and samples the signal at up to 27 time steps (see chap. 3). A group of responding strips matched to a traversing particle are called cluster (see fig. 2.8).

In the following the difference between maximum charge q_{max} and baseline q_0 is used as pulse height $q = q_{max} - q_0$ on one strip given in ADC counts. To determine the signal timing with an accuracy better than 25 ns the signal rise is fitted using an inverse Fermi function (see eq. 2.5).

$$q(t) = \frac{q_{max}}{1 + \exp\left(\frac{t_0 - t}{\Delta t}\right)} + q_0 \ , \tag{2.5}$$

where Δt is the rise time and t_0 is the point of inflection. This function has three well defined points at $0.1\,q_0$, $0.5\,q_0$ and $0.9\,q_0$. With a linear extrapolation through these points to the baseline the start of the signal t_s is calculated with equation 2.6. This timing should be independent of the pulse height and is used in the following for drift time measurements.

$$t_s = t(q_0) = t_0 - \frac{\ln(81)}{1.6}\Delta t \tag{2.6}$$

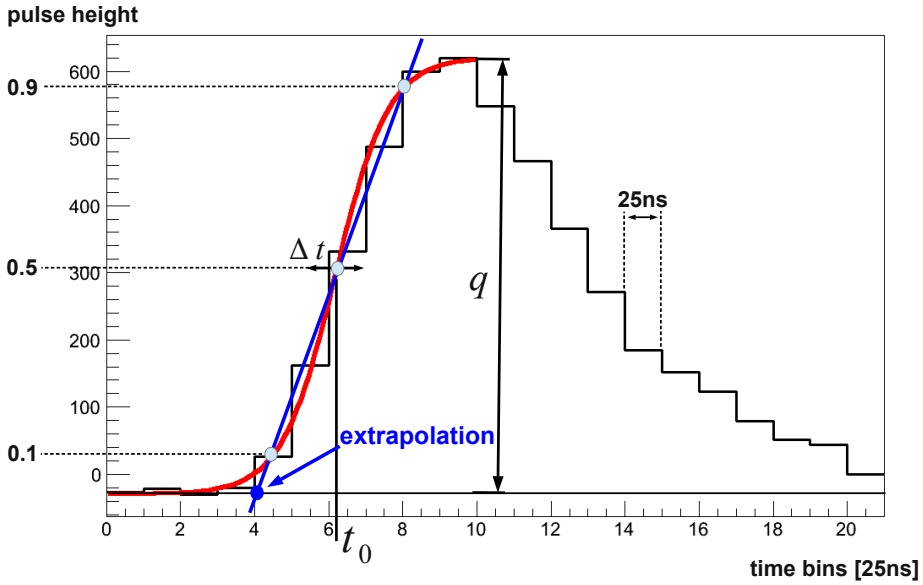

Figure 2.7: Typical signal of a Micromegas read out with an APV25 front-end board (see chap. 3). The rise of the charge distribution is fitted with an inverse Fermi function, which is used to extrapolate to the signal start. Figure taken from [Lösel, 2013]

.

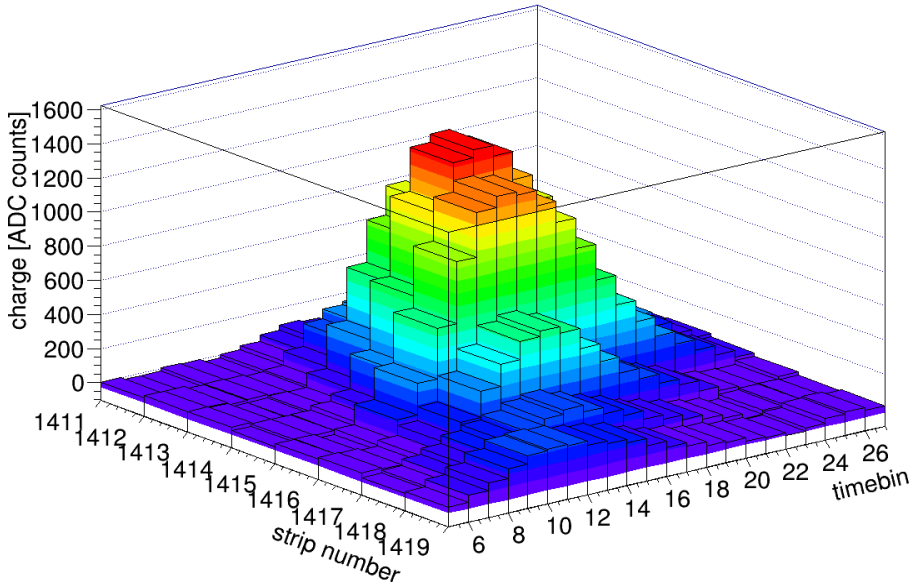

Figure 2.8: A group of responding strips in a Micromegas detector, so-called cluster. The start of the signals varies as a function of the strip number, thus the inclination of the track can be reconstructed (see sec. 2.4.3). Figure taken from [Lösel, 2013]

.

To distinguish between signal and noise the following cuts are applied:

- $\Delta t < 0.1\,\text{timebins} = 2.5\,\text{ns}$
- $\chi^2/_{NdF} < 50$,

where χ^2 is the quadratic distance between data point and fit and NdF is the number of degrees of freedom of the fit.

Figure 2.9 shows the signal rise time distribution. The peak below 0.1 timebins appears due to noise. If only one timebin shows a certain level of charge the fit using the inverse Fermi function shows a very small rise time. Therefore a cut at 0.1 timebins is applied.

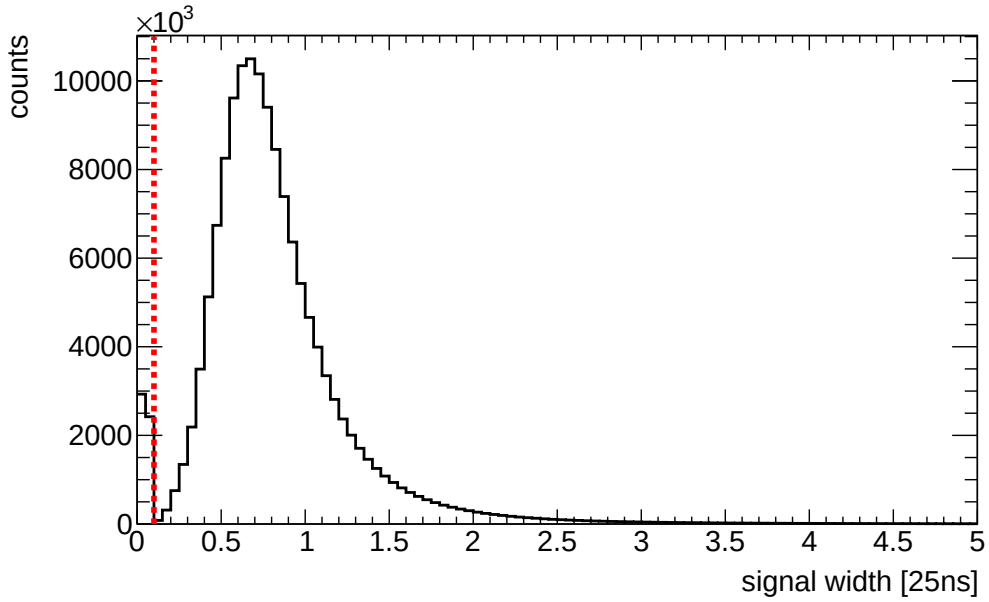

Figure 2.9: Distribution of the rise time of the signal. Only signals with a rise time above 0.1 timebins are meaningful signals. The cut is indicated by the dotted red line.

2.4.2 Centroid Method

The most intuitive position reconstruction method is to weigh the position of the strips responding to a signal by the pulse height, the so-called centroid method (see eq. 2.7). This method reconstructs the hit position corresponding to the middle of the drift region. A group of responding strips is called cluster and therefore the hit position will also be called cluster position. The centroid method works better with higher transverse diffusion due to the larger size of the cluster.

$$x_{\text{cen}} = \frac{\sum\limits_{\text{strips}} x_{\text{strip}} \cdot q_{\text{strip}}}{\sum\limits_{\text{strips}} q_{\text{strip}}} \tag{2.7}$$

2.4.3 TPC-like Method

For the reconstruction of the incident angle in a single plane the drift time measurement is used similar to Time Projection Chambers (TPC) and hence is called TPC-like or μTPC method. Figure 2.10 shows the linear fit of the signal timing as a function of the strip number. The slope m_{fit} corresponds to the incident angle using the electron drift velocity v_{drift} and the strip pitch p of the Micromegas (see eq. 2.8). The μTPC method works better with smaller transverse diffusion due to a better defined signal timing. As well as the uncertainty of the signal times increases with the longitudinal diffusion (see sec. 2.3).

$$\Theta = \arctan\left(\frac{1}{m_{fit}} \times \frac{p}{v_{drift}}\right) \tag{2.8}$$

To determine the hit position corresponding to the middle of the drift region the time in the middle of the drift region t_{mid} has to be determined (see eq. 2.9). In theory it can be calculated with the mean of the timing for the first and last strip hit $t_{mid} = 0.5\,(t_{first}+t_{last})$. How this is done experimentally will be described in chapter 7.

$$x_{\mu TPC} = \frac{t_{mid} - t_{fit}}{m_{fit}}\ , \tag{2.9}$$

where t_{fit} is the intercept of the linear fit.

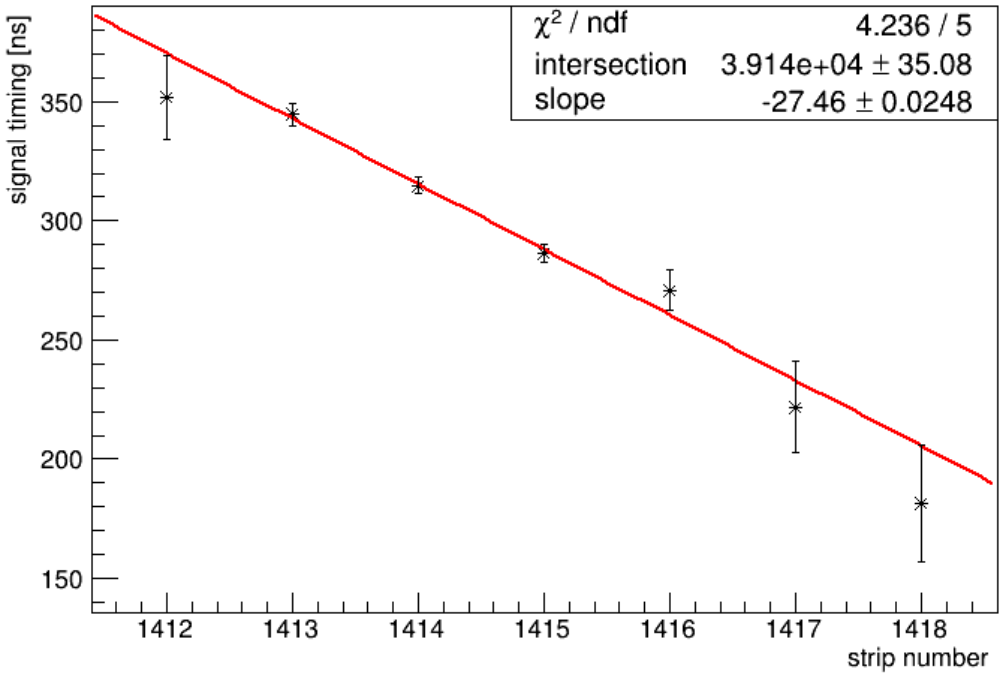

Figure 2.10: Signal timing as function of the strip number fitted linearly. The slope of the straight line is used for the reconstruction of the track angle. For the determination of the μTPC position intercept and slope are used. Figure taken from [Lösel, 2013]

2.4.4 Combination of TPC-like and Centroid Method

After reconstruction of the measured position typically the difference to a reference position is determined, the residual. Figure 2.11 shows the residual determined using the centroid method as a function of the residual determined using the TPC-like method for a track inclination of 40°. A correlation is clearly visible. To improve the position reconstruction, those two methods can be combined by weighting the µTPC and centroid position with the cluster size, i.e the number of strips in the cluster. The weight has to be related to the number of strips for perpendicular incidence, where the cluster size is approximately 4 strips. K. Ntekas has shown in his thesis [Ntekas, 2016] that for $10 \times 10\,\mathrm{cm}^2$ Micromegas detectors indeed $n_{cut} = 4$ is a reasonable parameter.

$$x_{comb} = \frac{(n_{strips}/n_{cut})^2 x_{\mu TPC} + (n_{cut}/n_{strips})^2 x_{cen}}{(n_{strips}/n_{cut})^2 + (n_{cut}/n_{strips})^2} \,, \tag{2.10}$$

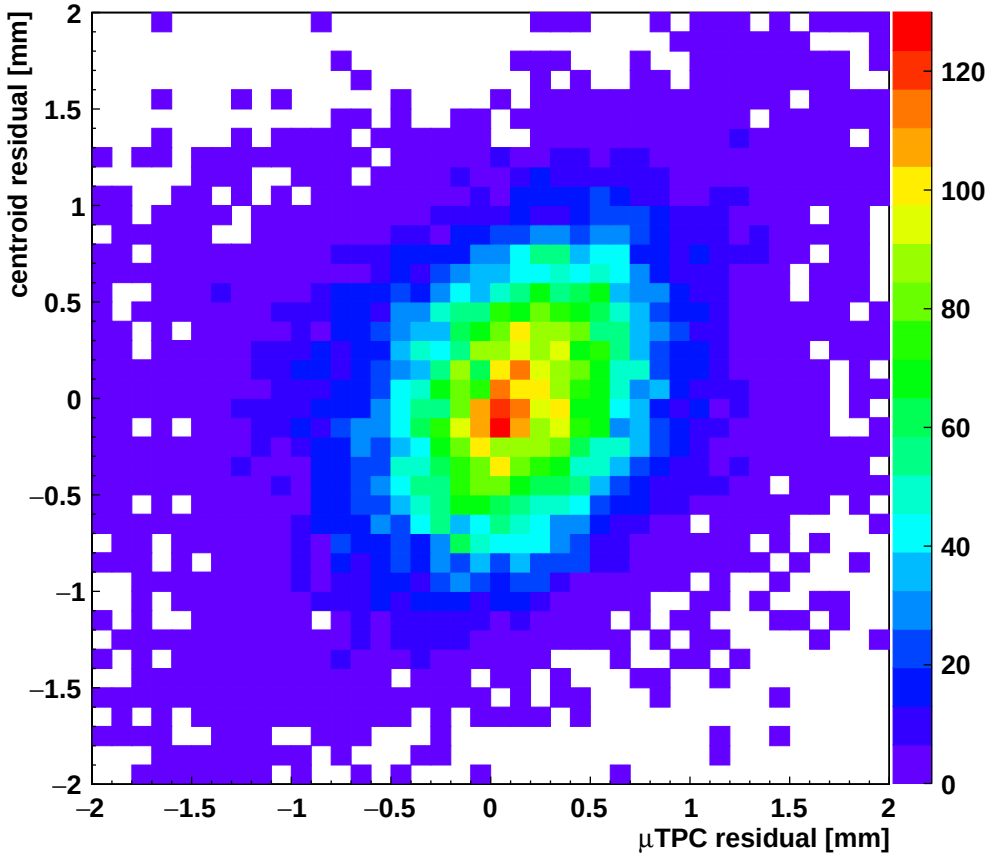

Figure 2.11: Centroid residual as a function of the µTPC residual measured with a $(10 \times 10)\,\mathrm{cm}^2$ Micromegas rotated by 40° with 120 GeV pions at H8 SPS/CERN (see chap. 7.2). Due to the correlation the position reconstruction can be improved by combining the two methods with dedicated weights.

Chapter 3

Readout Electronics

This Chapter gives an introduction to the readout of Micromegas. First the charge sensitive APV25 front-end boards will be described, then the Scalable Readout System consisting of one Scalable Readout Unit (SRU) and up to six Front-End Concentrator (FEC) cards will be described.

3.1 The Charge Sensitive APV25 ASIC

Figure 3.1 shows a picture of the APV25 front-end board developed by the RD51 collaboration [Jones, 2001]. It is connected via a 130 pin Panasonic plug to the Micromegas detector. Each channel is individually protected against discharges. The charge on the strips is integrated over 25 ns by each of the 128 charge sensitive amplifier channels and stored in an analog pipeline buffer of 192 cells depth for each input channel. The buffer is filled consecutively with each clock cycle. Blocks of up to 27 pipeline columns, sampling the signal in 27 steps of 25 ns width, can be read out for each trigger.

There are two kinds of APV25 front-end boards, master and slave. Each slave board is connected via a ribbon cable to a master board. Only the master board has the HDMI connector and the PLL25 chip. The analog signals for both boards are sent via a HDMI cable from the master board to the Scalable Readout System (see. sec. 3.2). With the PLL25 chip the readout phase can be varied to compensate for the HDMI cable length.

Due to the 25 ns integration time of the APV25 asic it is not guaranteed that the start of the signals in cosmic muon measurements or testbeam campaigns is synchronous to the trigger time. Hence the trigger time with respect to the signals varies within a 25 ns broad distribution. Figure 3.2 shows this distribution measured with a TDC[1] by comparing the external trigger signal with the 25 ns starting clock of the APV25. This shift with respect to the 25 ns clock timing, the so-called time-jitter, needs to be corrected for the analysis.

[1] TDC: Time-to-Digital Converter

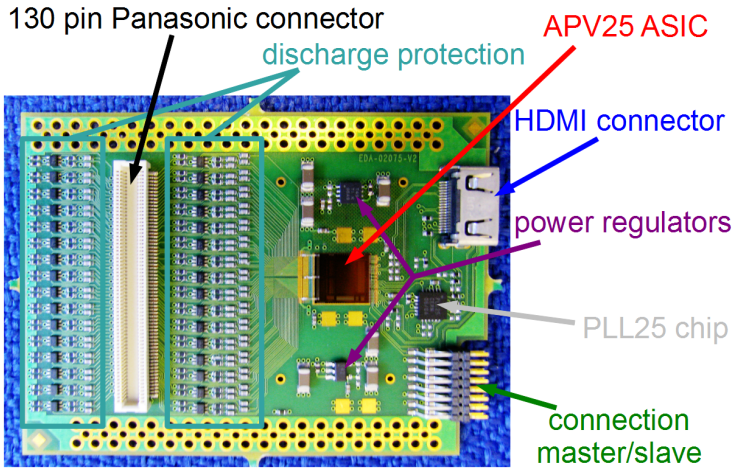

Figure 3.1: Picture of the APV25 front-end board (master). Indicated are the APV25 asic, the PLL25 chip, the Panasonic connector, the discharge protection circuit, the power regulators, the HDMI connector and the connection between master and slave board. Figure taken from [Lösel, 2013]

.

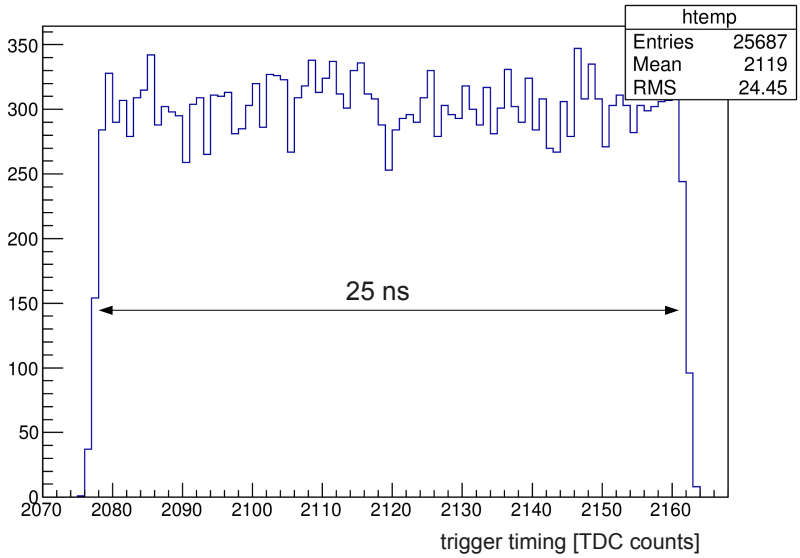

Figure 3.2: 25 ns broad distribution of the trigger time (1 TDC count = 296 ps), the so-called time-jitter. Figure taken from [Lösel, 2013]

.

3.2 The Scalable Readout System

Due to the separation of master and slave APV25 front-end boards twice as many physical strips can be read out using one HDMI cable. Eight HDMI cables can be connected to the Analog-to-Digital Converter (ADC) card, which processes the analog data from the APV25 ASIC. Therefore one ADC card can process 2048 readout channels. The ADC card is directly connected to the Front-End Concentrator (FEC) card, which sorts the channels and can with a special firmware perform a Zero-Suppression (ZS). With the ZS a strong data reduction is possible. The FEC calculates pedestals and sigmas of the pedestals for each readout channel. The sigmas of the pedestals correspond to the noise level of the individual strips. For each channel the pulse height is integrated over all 25 ns timebins after subtracting the pedestal. If this integrated signal exceeds a certain threshold the channel is read out. The threshold is calculated multiplying the number of timebins with the sigma and an adjustable factor, which is typically 1. The combination of ADC and FEC card will in the following only be referred to as FEC card. Up to six FEC cards can be connected to the Scalable Readout Unit (SRU) via ethernet cables. The cable has to be at least a standardized twisted pair cable for ethernet (Cat 6) to assure the minimal bandwidth of 250 MHz. The SRU adds some more information to the data like the FEC number, etc. (see fig. 3.4) and sends the data to the readout computer via optical fiber. A Scalable Readout System (SRS) consisting of the SRU and the connected FEC cards is shown in figure 3.3 [Martoiu et al., 2011]. In total one SRS can handle six FEC cards and thus readout 12288 physical strips.

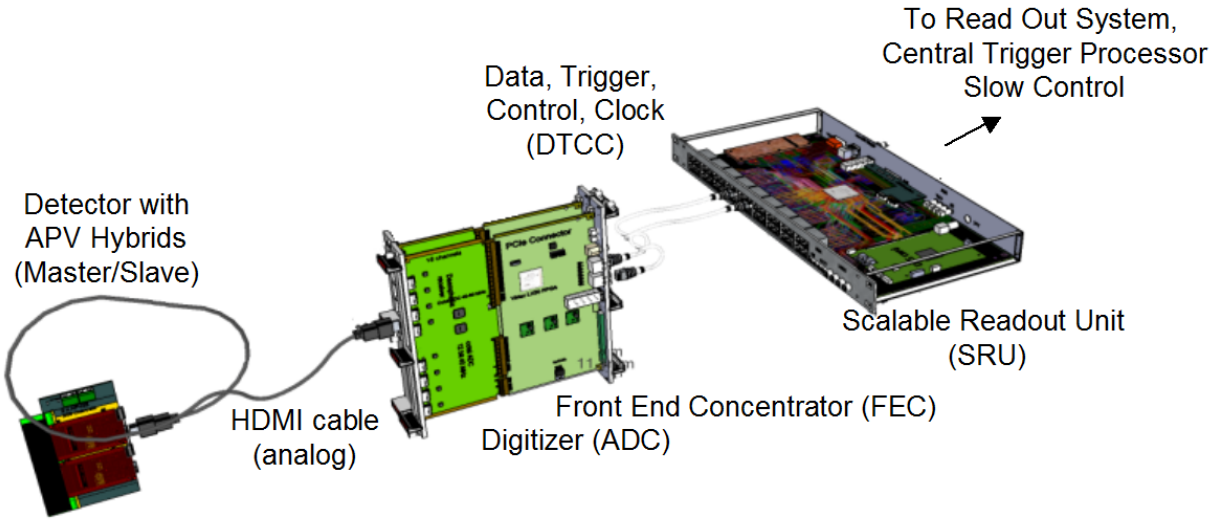

Figure 3.3: Schematic drawing of a Scalable Readout System consisting of Scalable Readout Unit and Front-End Concentrator card. The APV25 front-end boards are connected via HDMI cables to the Front-End Concentrator card. Figure taken from [Zibell, 2014].

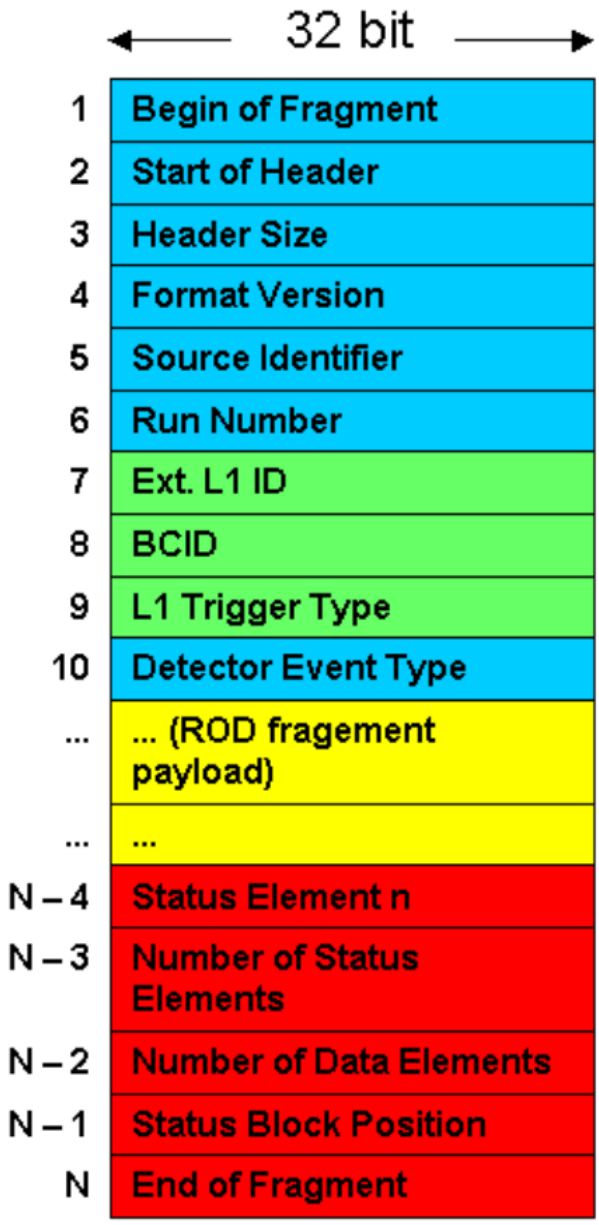

Figure 3.4: Data structure sent by the SRU. The SRU header with information about the fragment (blue) and trigger information (green). Then the event payload with the actual data from the detector (yellow) concluded by several trailer words containing information of the status, errors or loss of data, of the event (red). Figure taken from [Zibell, 2014].

Chapter 4

Electron Transparency of the Mesh

One very essential part of the Micromegas is the micro-mesh. For large area applications a stainless steel mesh woven of wires with a diameter of 30 µm and a pitch of 100 µm is used. For smaller detectors finer but less stable meshes are available with 18 µm wire-diameter and 63 µm pitch. This leads to an optical transparency in the order of 50 %, but the electron transparency is much higher. Depending on the electric field in the amplification and drift region the electron transparency can reach almost 100%. A high electron transparency is important for good spatial and angular resolution of the Micromegas. Position and angle of the traversing particle can be better reconstructed if more initial electrons reach the amplification region.

In this chapter the simulation of the electron transparency under various conditions will be presented starting with the explanation of the procedure. These results will be compared to measurements taken with 23 MeV protons at the tandem accelerator Garching and with results using a ^{55}Fe-source.

4.1 Simulation

Crucial for the simulation is the high resolution of the field lines between amplification and drift region. Figure 4.1 (left) shows the field lines on which the electrons are guided into the amplification region. A picture of a woven mesh is shown in figure 4.1 (right). Due to the weaving of the mesh the field lines around the connection points seem kind of chaotic. This is simulated by the precise construction of the geometry.

4.1.1 Procedure

First the geometry of the detector has to be constructed using the program *Gmsh* [Gmsh website, 2009]. *Gmsh* is a finite element method (FEM) program, where the geometry is approximated by rebuilding it with small tetrahedrons. The result is called mesh, but in the following it will be referred to as FEM-mesh. The size of tetrahedrons can be arbitrarily chosen and defines the granularity of the FEM-mesh. The finer the FEM-mesh the preciser

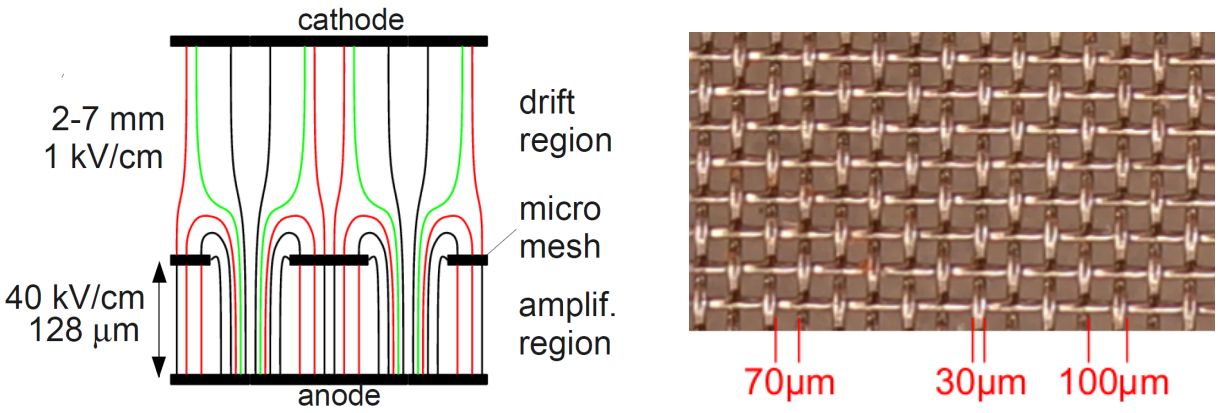

Figure 4.1: Left: Schematics of electric field lines in a Micromegas in amplification and drift region. Right: Photo of a woven stainless steel mesh used for the Micromegas of the upgrade of the inner-most end-cap region of the ATLAS Muon Spectrometer with wire diameter 30 µm and pitch 100 µm.

the simulation. Figure 4.2 shows the geometry of an unit cell of the detector with its woven mesh, a readout strip and the gas volume. The FEM-mesh around the woven mesh and the readout strip is very fine. This is not needed for the gas volume, which is not shown in the figure for simplification.

The FEM-mesh, generated by *Gmsh* with the potentials on cathode, mesh and readout strip is given to *Elmer* [Elmer website, 2005]. *Elmer* is a finite element electric field solver, which calculates the electric field in the unit cell. The result for a potential of 460 V on the mesh is shown in figure 4.3. On the right side the potential for the whole unit cell is shown. It is mostly homogeneous for the gas volume except for the areas around readout strip and woven mesh. A zoom-in to the area around the mesh is shown on the left side. It can be seen that the electric field from the amplification region reaches into the drift area and guides the electrons through the mesh. Thus a higher electron transparency than the optical transparency is achieved. An electron transparency above 90 % can be reached, if the amplification field is 40 to 100 times higher than the drift field. But this depends on the mesh type and gas mixture.

The electric fields are transferred to *Garfield++* [Garfield website, 2010] for the microscopic simulation of electron tracks in the gas detector. This program is used because various parameters can be easily adjusted, e.g. mixture of gases, temperature, pressure, etc.

A single initial electron is started randomly in the upper part of the drift region. It drifts through the mesh and creates a gas avalanche. All generated electrons are collected on the readout strip (see fig. 4.4).

The total number of electrons collected on the readout strip for one starting electron is the gas amplification factor. It has to be averaged over several simulated electron tracks due to statistical variations. Electrons which were stopped before the amplification region due to recombination, attachment or absorption on the mesh are not used for the calculation

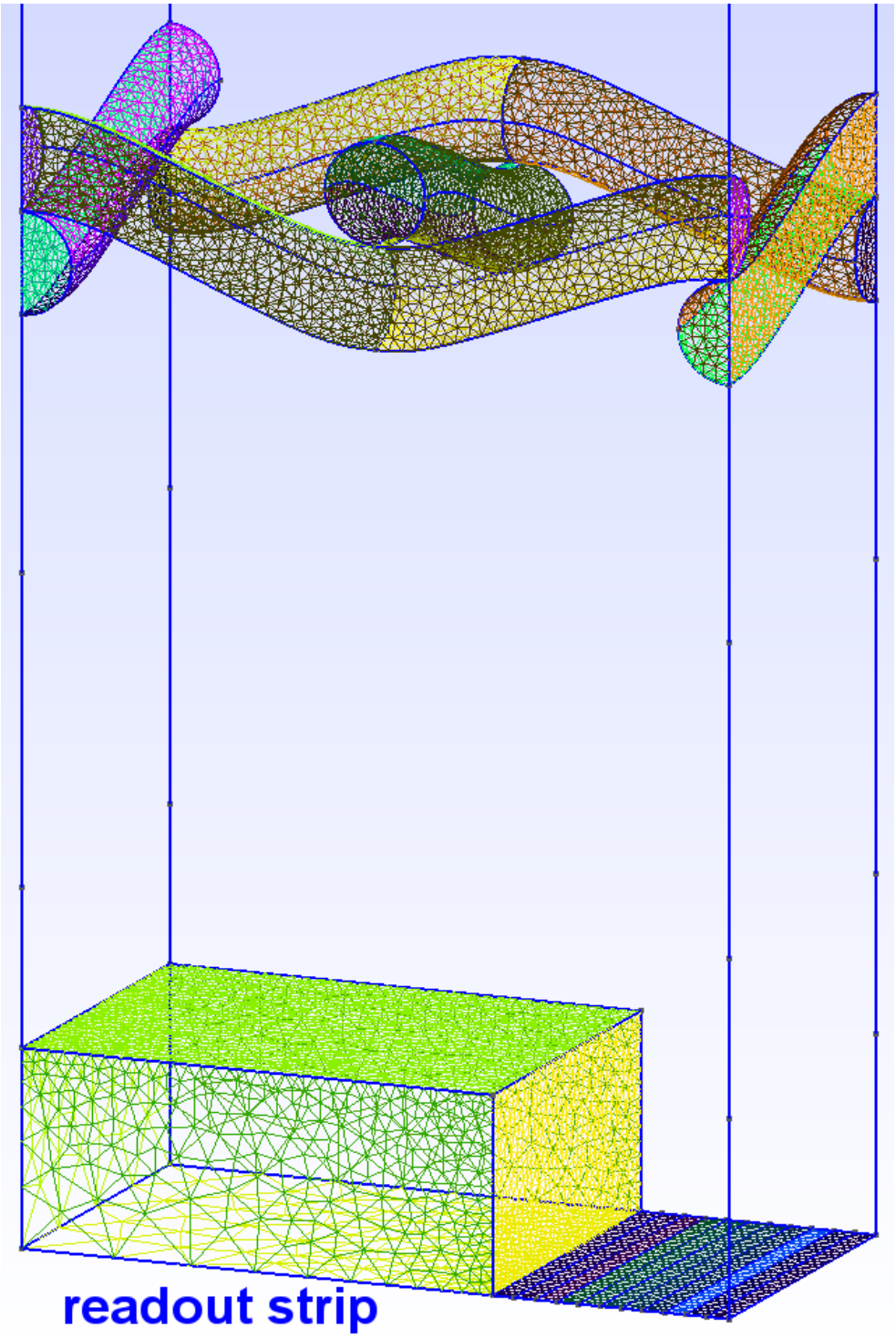

Figure 4.2: Geometry of a unit cell of the Micromegas generated with *Gmsh* consisting of woven micro-mesh, readout strip and gas volume. The FEM-mesh for the gas volume is not shown in this figure to clarify the geometry.

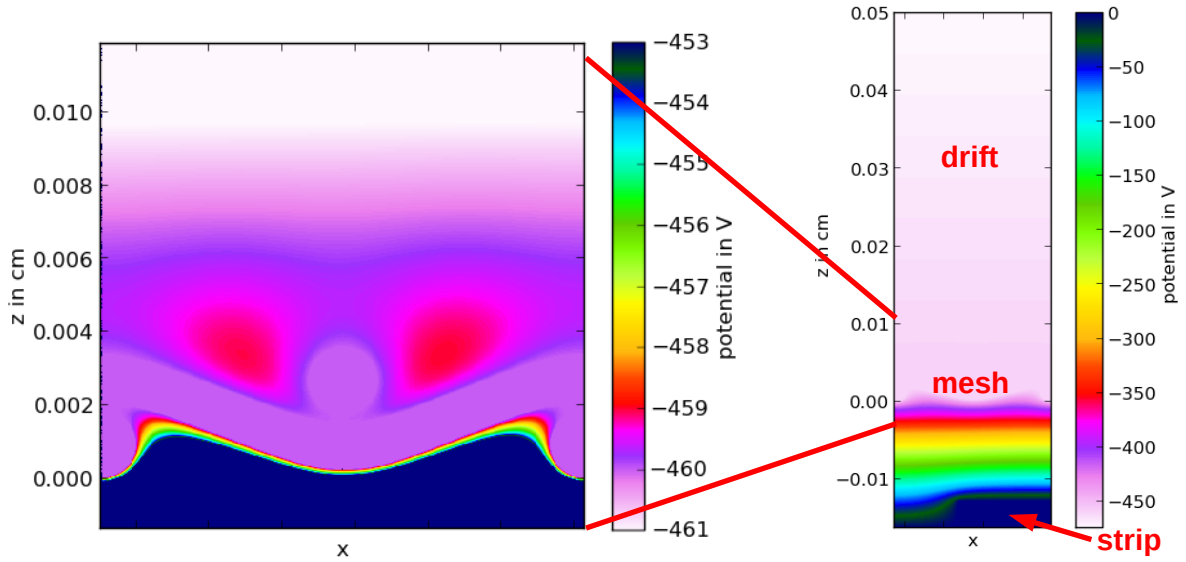

Figure 4.3: Electric potential around the mesh, so-called demon-mask (left) and for the whole unit cell (right). The potentials of readout strip, mesh and cathode are 0 V, 460 V and 480 V, respectively. It can be seen that the electric field from the amplification region reaches into the drift region (potential in red) to lead the electrons through the mesh shown as purple wires. The red potential can be seen below and above the mesh, in between the view is blocked by the mesh.

of the gas amplification factor. The number of simulated electron tracks N is typically 500 for the results of this thesis.

All simulated tracks have to be used to calculate the electron transparency t of the mesh.

$$t = \frac{N_s}{N}\,, \tag{4.1}$$

where N_s is the number of tracks with at least one electron reaching the strip. The statistical uncertainty is given by:

$$\Delta t = \sqrt{\frac{t(1-t)}{N}} \tag{4.2}$$

4.1.2 Electron Transparency

Four different woven micro-meshes currently are commercially available and in the usable range for Micromegas. Companies, which sell woven micro-meshes, are for example *Bopp* and *Weisse & Eschrich*. As specification the nomenclature

wire diameter/opening width

is used (see fig. 4.5). The sum of wire diameter and opening width gives the pitch. For these four meshes the electron transparency was simulated as a function of the drift field.

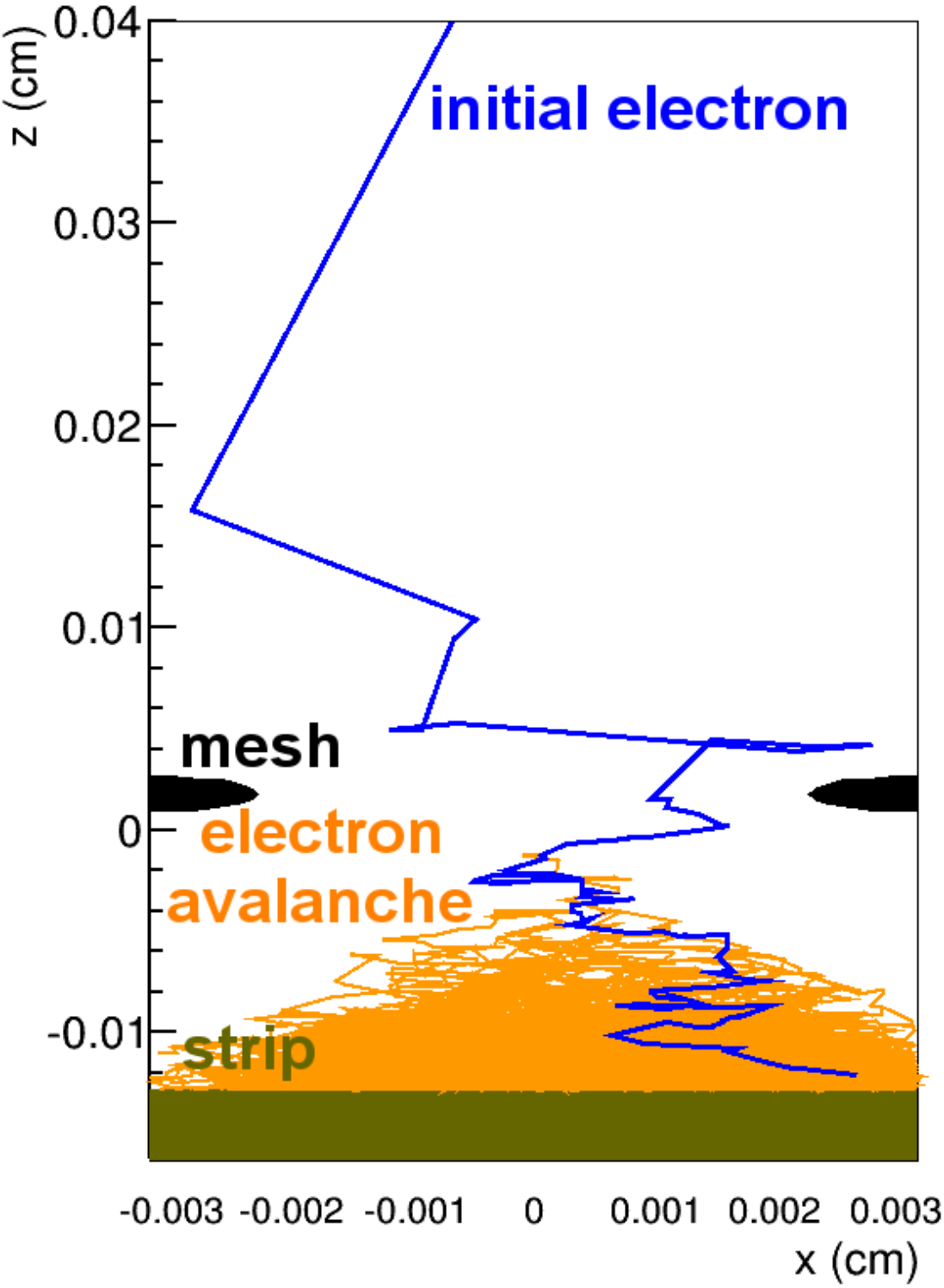

Figure 4.4: Simulation of a single initial electron randomly placed in the gas volume. It drifts into the amplification region and creates an electron avalanche.

All other parameters were constant, e.g. the gas mixture of Ar:CO_2 93:7 vol% and the amplification field of $E_{\text{amp}} = 39\,\text{kV}\,\text{cm}^{-1}$.

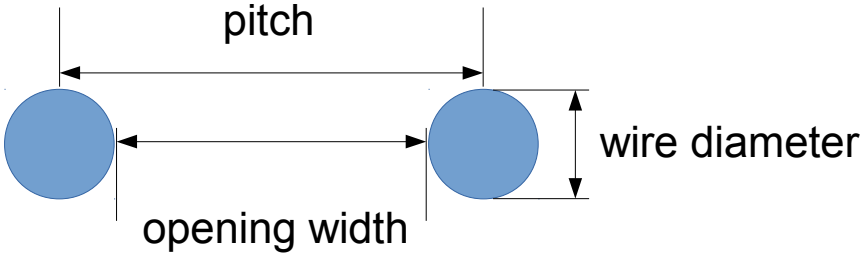

Figure 4.5: Schematics as nomenclature explaining the wire diameter and opening width. The sum of wire diameter and opening width gives the pitch.

The results of these simulations are shown in figure 4.6. Clearly the meshes 18/45 and 30/70 with higher optical transparency t_{opt} show better results for the working point around $E_{\text{drift}} = 600\,\text{V}\,\text{cm}^{-1}$. They have a higher electron transparency at high drift fields and the reconstruction of the traversing particle is probably satisfying up to a drift field of $E_{\text{drift}} = 600\,\text{V}\,\text{cm}^{-1}$. The meshes 25/38 and 30/50 show a fast drop in the electron transparency already at much lower drift fields. Therefore the reconstruction of position and angle will not be as good as for the other two at the same electric fields. This corresponds to the differences in the optical transparency.

4.2 Variation of the Gas Mixture

A very interesting question is, if the electron transparency depends only on the micromesh or on the gas mixture as well. So the simulation for the 18/45 mesh was repeated for different gas components, Ar:CO_2, Ne:CF_4 and Ne:CO_2, and various gas mixtures (see fig. 4.7 to 4.9). For a higher drift field the electron drift velocity rises for many gas mixtures (see app. A) and thus the detector increases in high rate capability. With respect to this effect a high drift field strength is favored. But the electron transparency of the mesh decreases. For a sufficient position reconstruction a high transparency is necessary. Table 4.1 states the highest drift field strength where the electron transparency is still above 90 %.

4.3 Measurement at the Tandem Accelerator in Garching

To confirm these simulations with data a measurement at the tandem accelerator in Garching was performed. The tandem accelerator provides 23 MeV protons. Figure 4.10 shows the setup. After leaving the beampipe through a 50 µm Kapton window the protons cross a small path in air, before entering the Micromegas. The proton beam is 7 cm wide and

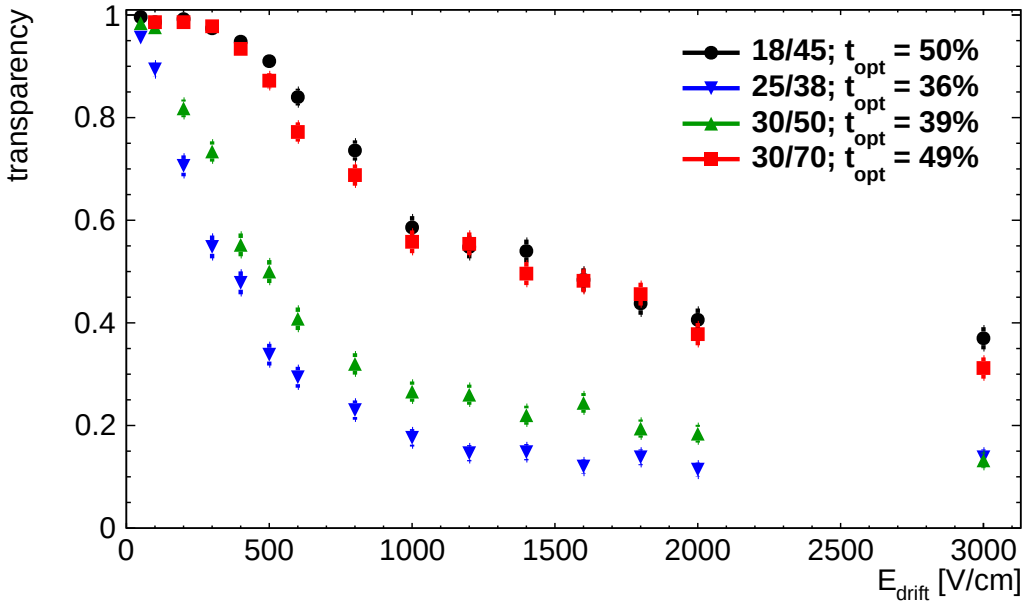

Figure 4.6: Simulated electron transparency as a function of the drift field for four commercially available woven micro-meshes and for a gas mixture of Ar:CO_2 93:7 vol%. The meshes 18/45 and 30/70 show a much slower drop of transparency than the meshes 25/38 and 30/50. Additionally the optical transparency t_{opt} is stated in the legend.

Table 4.1: Gas Mixture, |vol%|, maximum drift field strength and ratio of amplification and drift field strength, where the transparency is still above 90 %.

gas mixture	vol%	$E_{\mathrm{drift}}(t > 90\,\%)$ [V/cm]	$E_{\mathrm{amp}}/E_{\mathrm{drift}}(t > 90\,\%)$
Ar:CO_2	93:7	500	78
	85:15	800	49
	80:20	1000	39
Ne:CF_4	90:10	800	49
	85:15	1000	39
	80:20	1000	39
Ne:CO_2	90:10	700	56
	85:15	950	41
	80:20	1050	37

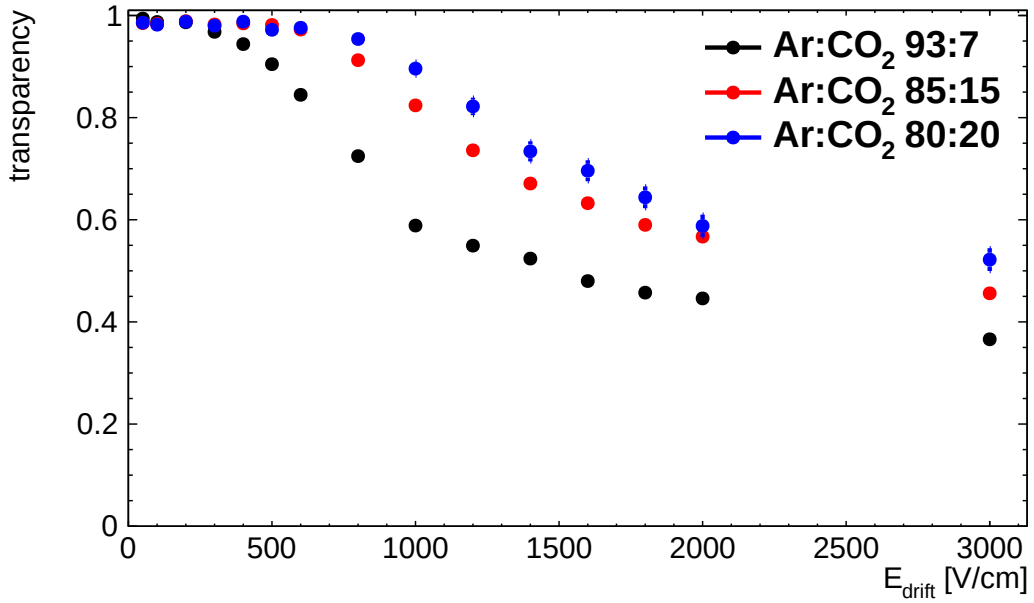

Figure 4.7: Simulated electron transparency of a 18/45 mesh as a function of the drift field for various gas mixtures of Ar:CO_2. The mixture with the smallest amount of CO_2 shows the fastest drop of transparency.

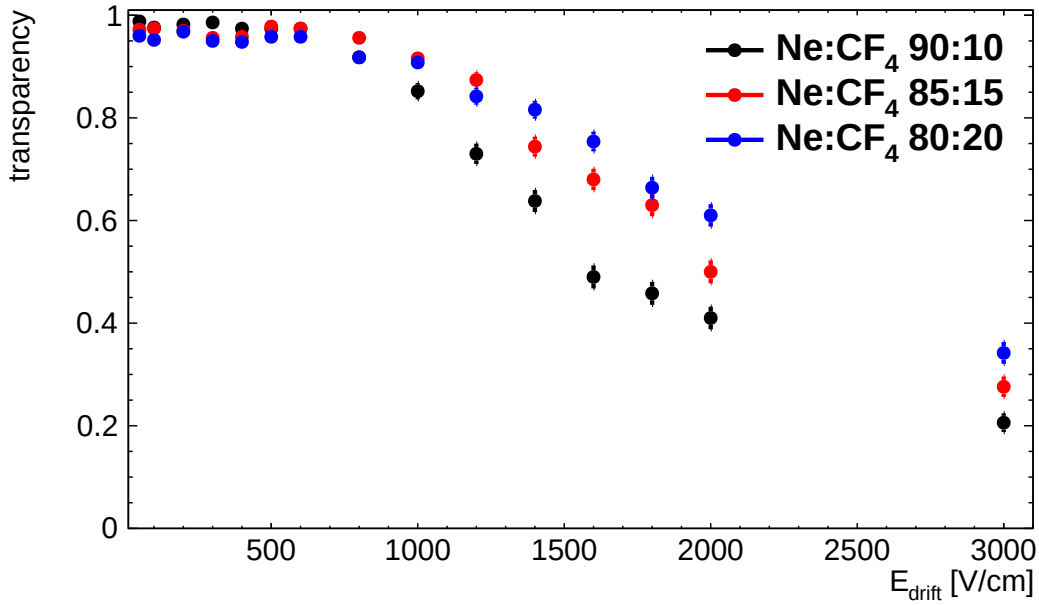

Figure 4.8: Simulated electron transparency of a 18/45 mesh as a function of the drift field for various gas mixtures of Ne:CF_4. The mixture with the smallest amount of CF_4 shows the fastest drop of transparency.

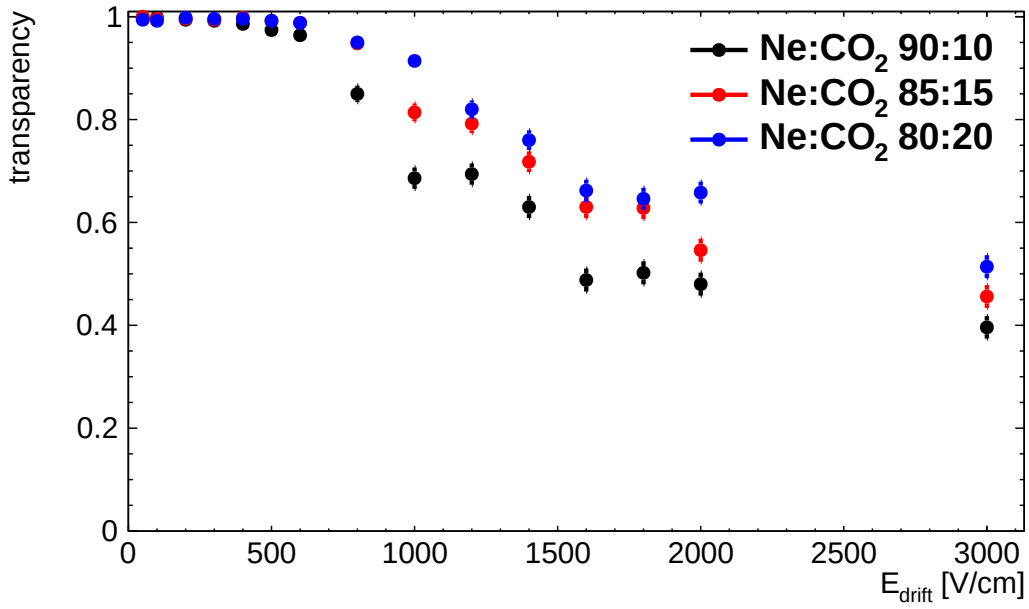

Figure 4.9: Simulated electron transparency of a 18/45 mesh as a function of the drift field for various gas mixtures of Ne:CO_2. The mixture with the smallest amount of CO_2 shows the fastest drop of transparency.

5 mm in height. The protons traverse the Micromegas parallel to the readout plane and perpendicular to the strips just beneath the cathode. Behind the Micromegas a scintillator as proton counter is mounted to measure the proton rate r (see fig. 4.11). The Micromegas under test is equipped with an 18/45 mesh.

If the amount of charge between anode and mesh of the Micromegas is macroscopic a current can be measured. In theory this current should be a linear function of the proton rate if all other parameters are kept constant. Figure 4.12 shows the current as a function of the proton rate for the range of proton rates between a few Hz and 50 kHz. It can be clearly seen, that this is not a linear function. If the proton rate is very high the ion density in the amplification region is very high as well. The ions drift to the mesh and act like a shield. Therefore the gas gain drops. For proton rates below 4 kHz it can be approximated as linear.

4.3.1 Determination of the Electron Transparency from Data

To determine the electron transparency from data, apart from using the pulse height, which is difficult for small drift fields due to the long drift time, the current I between strips and mesh can be used:

$$I(r, E_{\text{drift}}, E_{\text{amp}}) = q_0\, r\, t(E_{\text{drift}})\, G(E_{\text{amp}}) \tag{4.3}$$

q_0 can be derived from the well defined energy deposition in matter of the protons ($E_0 = W_i \cdot q_0$). W_i for Ar:CO_2 93:7 vol% is about 26.6 eV. Their 10 cm long path in the active

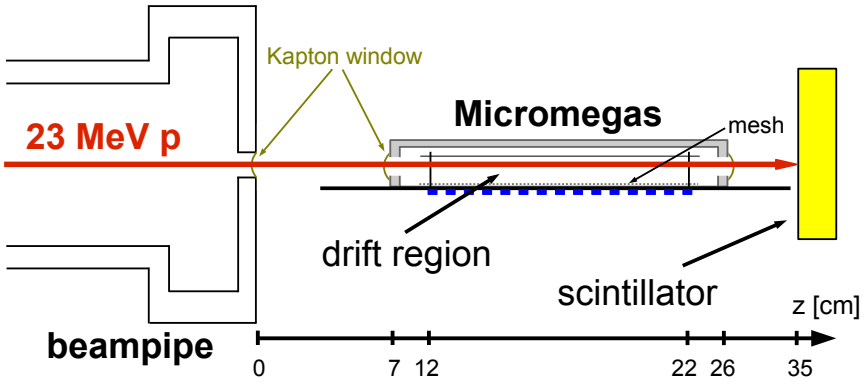

Figure 4.10: Schematics of the experimental setup at the tandem accelerator. 23 MeV protons traversing the drift region of a $(10 \times 10)\,\mathrm{cm}^2$ Micromegas perpendicular to the readout strips with a scintillator behind the setup as proton counter. The proton beam is 7 cm wide and 5 mm in height.

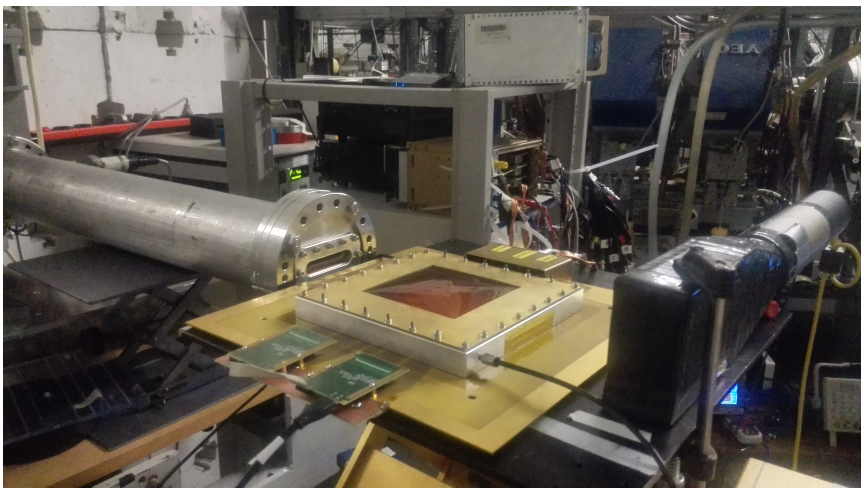

Figure 4.11: Picture of the experimental setup at the tandem accelerator. Here the detector, the beampipe and the scintillator can be seen.

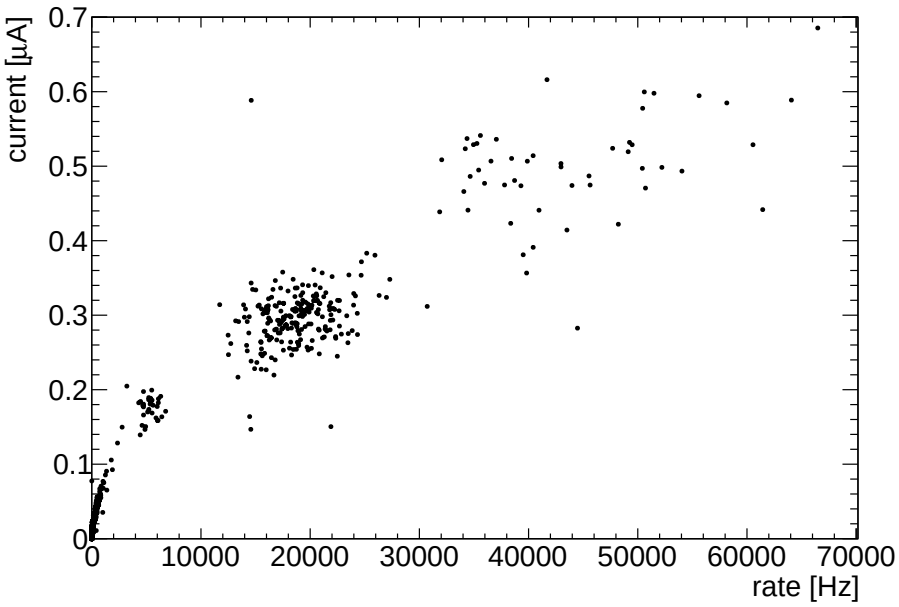

Figure 4.12: Current between anode and mesh of the Micromegas as a function of the proton rate. The rate was sampled by the scaler every 0.1 s and the current every 0.5 s. For proton rates below 4 kHz it is approximated as linear.

volume leads to in average about 10260 ionizations in the gas corresponding to an energy loss on 273 keV. As many primary electrons drift in the amplification region to create electron avalanches and are multiplied by the gas gain G. G is constant due to the constant amplification field of about 35 kV cm^{-1}. When the drift field was varied, the change in the result leads to the electron transparency t. The proton rate r is gained from the trigger scintillator counting the protons. Additionally the current I between strips and mesh is measured.

The current as a function of the proton rate is given by equation 4.4. With the linear approximation the slope of the curve is determined by a fit. The slope of the fit m_{fit} corresponds to $t\, q_0\, G$. Data point examples for two drift field configurations are shown in figure 4.13 for clarity reasons without the fit curves.

$$I(r) = t\, q_0\, G \cdot r \tag{4.4}$$

Now the transparency times gas gain for all data points is calculated with equation 4.5. The exact value of the gas gain is not known. Therefore the measured transparency is scaled with a constant factor of 1950 to the simulated values to compare the progression of the curves (see fig. 4.14). Measurement and simulation are in poor agreement for small electric fields due to a contaminations of the gas mixture. With additional air in the detector the electrons are captured by oxygen.

$$tG = \frac{m_{fit}}{q_0} \tag{4.5}$$

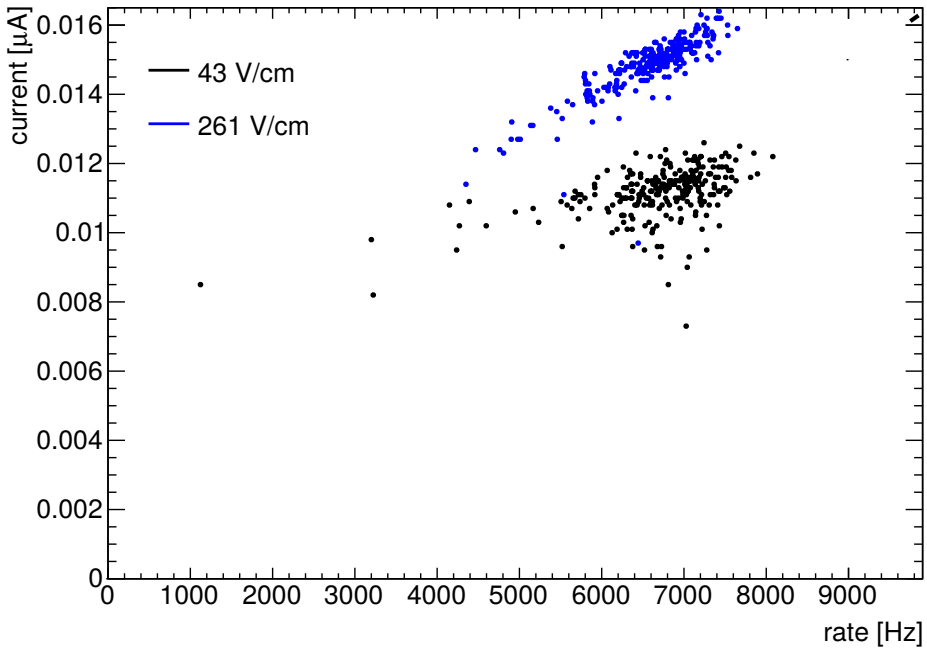

Figure 4.13: Current between anode and mesh as a function of the proton rate for two drift field configurations.

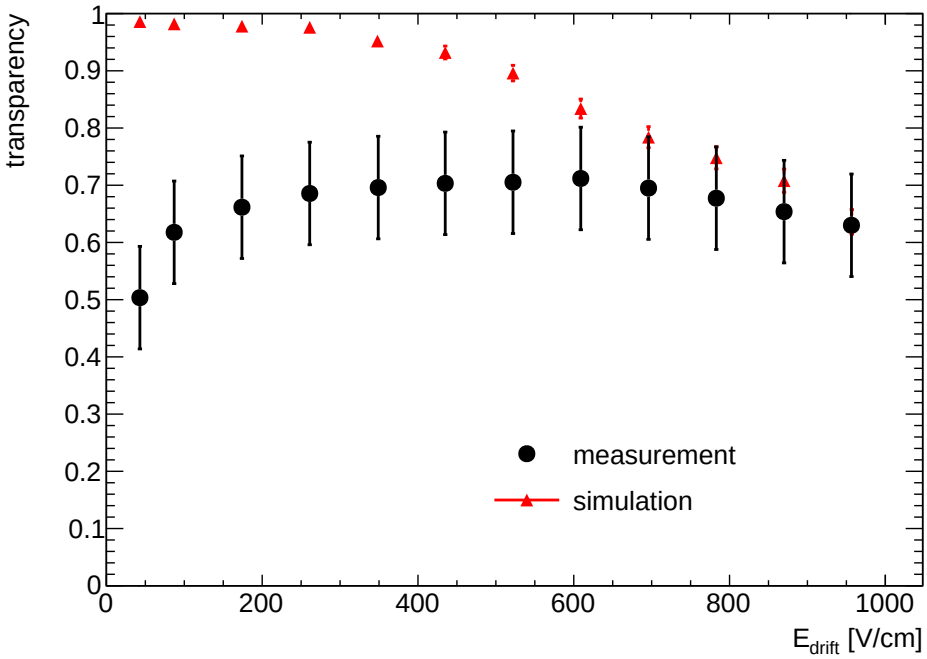

Figure 4.14: Electron transparency of the mesh as a function of the drift field for Ar:CO_2 93:7 vol%. The black circles are data points from the measurement scaled with constant factor to the simulation (red triangles). Measurement and simulation are in poor agreement.

4.3.2 Contamination of the Gas Mixture

Due to a suspected contamination in the gas mixture the simulation of the transparency was repeated with different contents of air. It was assumed to have a small part of air in the gas mixture. So values between 0.1 % and 1.0 % were chosen. Figure 4.15 shows the electron transparency for air contamination of 0.1 %, 0.3 % and 0.5 % additional to the former simulation and the measurement. The measured transparency is again scaled with a constant factor, the assumed gas gain, to the simulation with an air contamination of 0.3 %. This seems to fit quite well. But there could also be a temporal evolution in the contamination. Hence the simulation has some variations compared to the measurement.

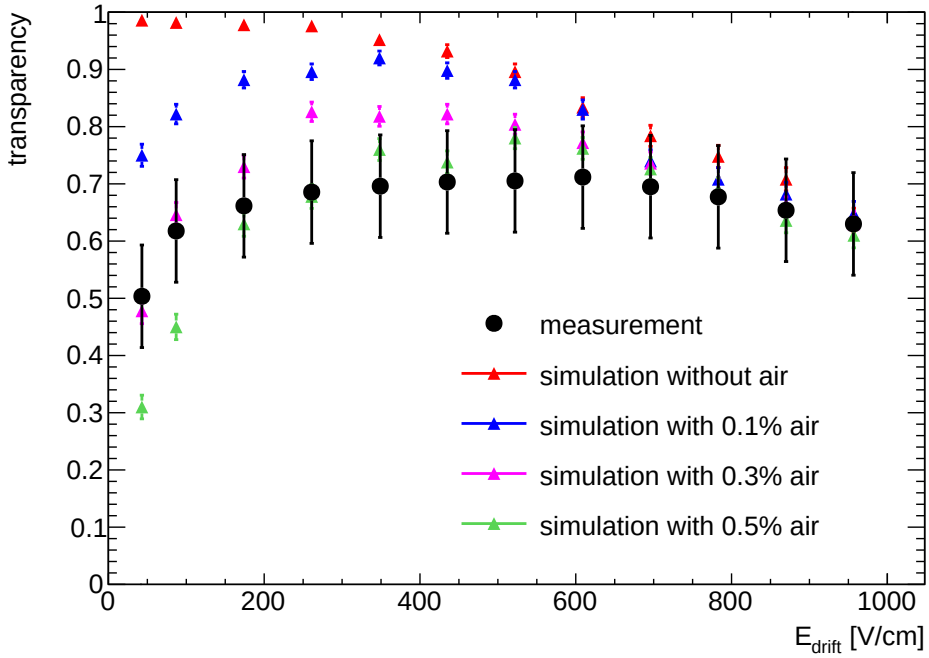

Figure 4.15: Electron transparency of the mesh as a function of the drift field for Ar:CO_2 93:7 vol%. The black circles are data points from the measurement scaled with constant factor to the simulation with 0.3 % air contamination of the gas mixture, which shows the best agreement with the measurement. Various other parts of contamination are shown as well.

4.4 Measurement of the Electron Transparency using a ^{55}Fe-Source

With a floating Strip Micromegas (see sec. 2.2) equipped with a 25/38 mesh the transparency was measured using Ne:CF_4 gas mixtures. A ^{55}Fe-source was placed on top of the detector emitting 5.9 keV X-rays, which approximately lead to 220 primary electrons in the active volume of the Micromegas. The opening window of the ^{55}Fe-source was strongly collimated, therefore the ionization area in the Micromegas is very focused, so to say point-like. Hence all charges arrive very localized on the Micromegas readout plane. The pulse height of all strips short-circuited was measured under variation of the drift field strength. For more details see [König, 2015]. The measured pulse heights are scaled with a constant factor to simulation (see fig. 4.16). Measurement and simulation are in good agreement.

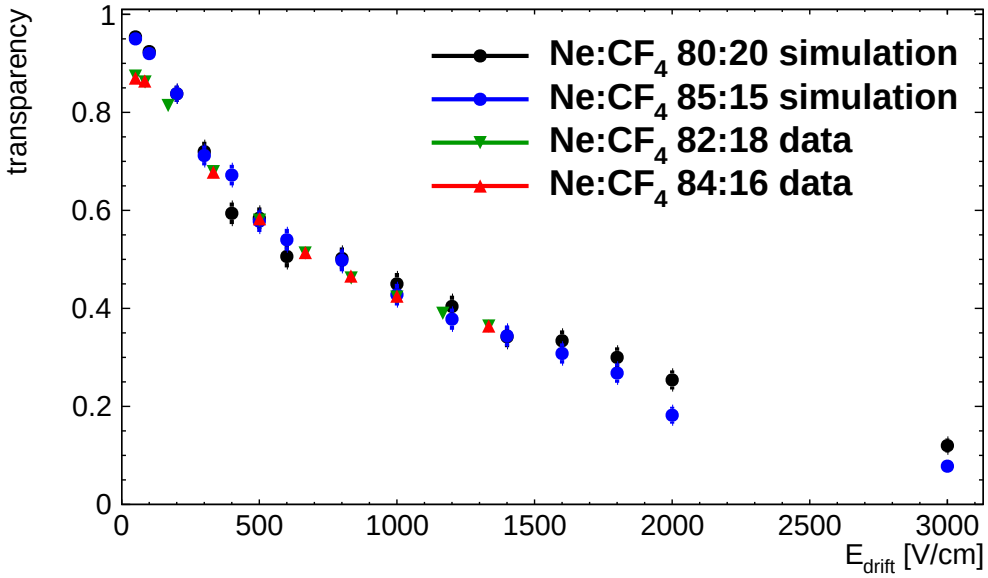

Figure 4.16: Electron transparency of the mesh as a function of the drift field for Ne:CF_4 gas mixtures. The data points are scaled with a constant factor to the simulation.

Chapter 5

Construction of SM2 Quadruplets

In this chapter the design of the New Small Wheel will be described including how to fulfill the mechanical requirement during the construction of the Mircomegas detectors. It concludes with the quadruplet assembly and the installation of the readout using Zebra connectors.

5.1 Layout of the New Small Wheel

The inner end-cap regions of the ATLAS experiment (Small Wheels) have a disk-like design with a diameter of about 10 m. This design will be preserved for the detectors of the New Small Wheel (NSW) upgrade consisting of eight small and eight large sectors (see fig. 5.1). Each sector consists of two Micromegas wedges mounted on the holding structure and sandwiched by two sTGC wedges (see fig. 5.2). The main purpose of the sTGCs is triggering, the Micromegas act predominantly as precision trackers. Great care has been taken to develop the system totally redundant, which means the Micromegas are trigger capable and the sTGCs can also act as tracker. The sTGCs as well as the Micromegas wedges have four active layers each. Therefore the NSWs have in total eight active layers of sTGCs and Micromegas. This thesis will focus on Micromegas.

Each Micromegas wedge is subdivided into two modules, also called quadruplets, due to the four active detector layers. All modules have an active area between 2 and 3 m^2. The strip-anode structure is photo-lithographically etched onto printed circuit boards (PCB), which are industrially produced. Due to size limitation for the width of the PCBs the layers of the module have to be constructed out of three or five PCBs depending on the module. The inner modules of small and large sector are called SM1 and LM1, the outer ones SM2 and LM2 (see fig. 5.3). Each module is built at its specific construction site with slightly different methods. This thesis focuses on SM2 being built by the German construction sites.

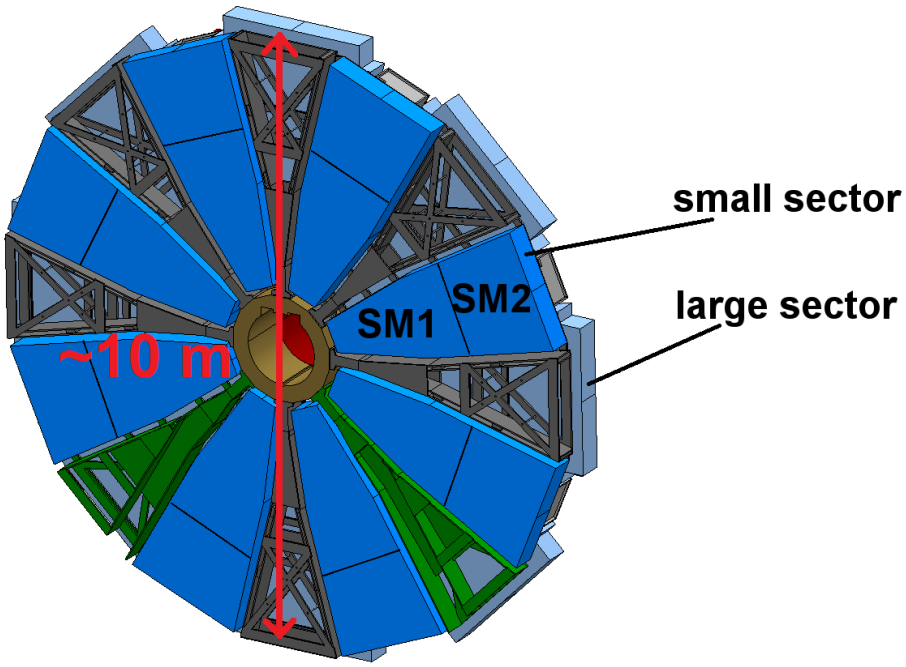

Figure 5.1: Disk-like design of the New Small Wheels with a diameter of about 10 m and consisting each of eight small and eight large sectors. The internal names for the two modules of the small sector, SM1 and SM2[1], are indicated as well. Figure adopted from [ATLAS Collaboration, 2013].

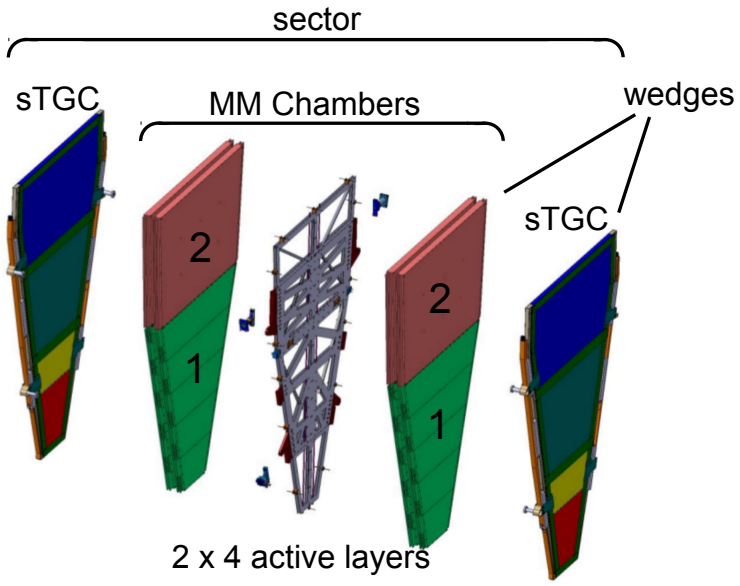

Figure 5.2: One sector of the New Small Wheel consisting of two Micromegas wedges mounted on a holding structure, the spacer frame, and sandwiched by two sTGC wedges. In total one New Small Wheel has eight active layers of sTGCs and eight active layers of Micromegas. Figure adopted from [ATLAS Collaboration, 2013].

[1]SMX: Small sector Micromegas 1 or 2. SM1 is sitting at smaller radii, SM2 at larger radii.

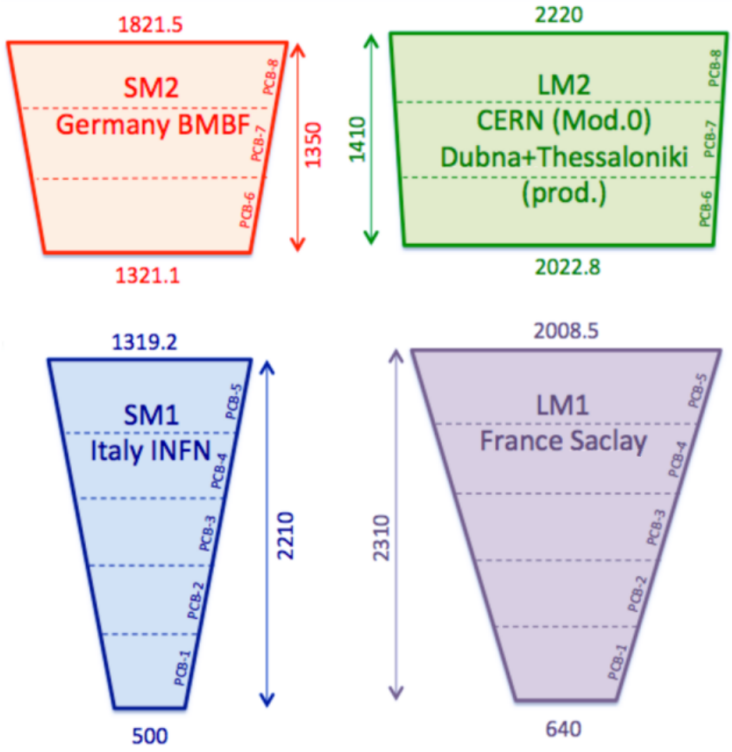

Figure 5.3: Dimensions of the Micromegas modules for the New Small Wheel upgrade. The internal names and construction sites are indicated as well.

5.2 Design of an SM2 Quadruplet

Each Micromegas quadruplet consists of three drift panels and two readout panels (see fig. 5.4). A panel is a rigid structure consisting of a 10 mm high aluminum honeycomb core framed by aluminum bars and sandwiched by 0.5 mm thick PCBs. There are two kinds of drift panels, outer drift panels and a central drift panel. The central drift panel has on both sides copper cathodes etched on the PCBs, whereas the outer drift panels have a cathode on one side and are bare FR4 on the other side. There are also two kinds of readout panels, eta and stereo, with anode-strip structures on both sides of the panel. The strip orientation of the eta panel defines the precision direction perpendicular to the strips. Due to the radially symmetric magnetic field of the toroid in the ATLAS experiment only the position perpendicular to the strips is needed to reconstruct the muon momentum. The strips of the stereo panel are slightly rotated with respect to the eta strips, one side with $+1.5°$ the other with $-1.5°$ (see fig. 5.5). This allows for a coarse position information perpendicular to the precision direction. [Ntekas, 2016] shows a measurement with a prototype detector, where a spatial resolution perpendicular to the precision direction in the order of 2 mm has been achieved.

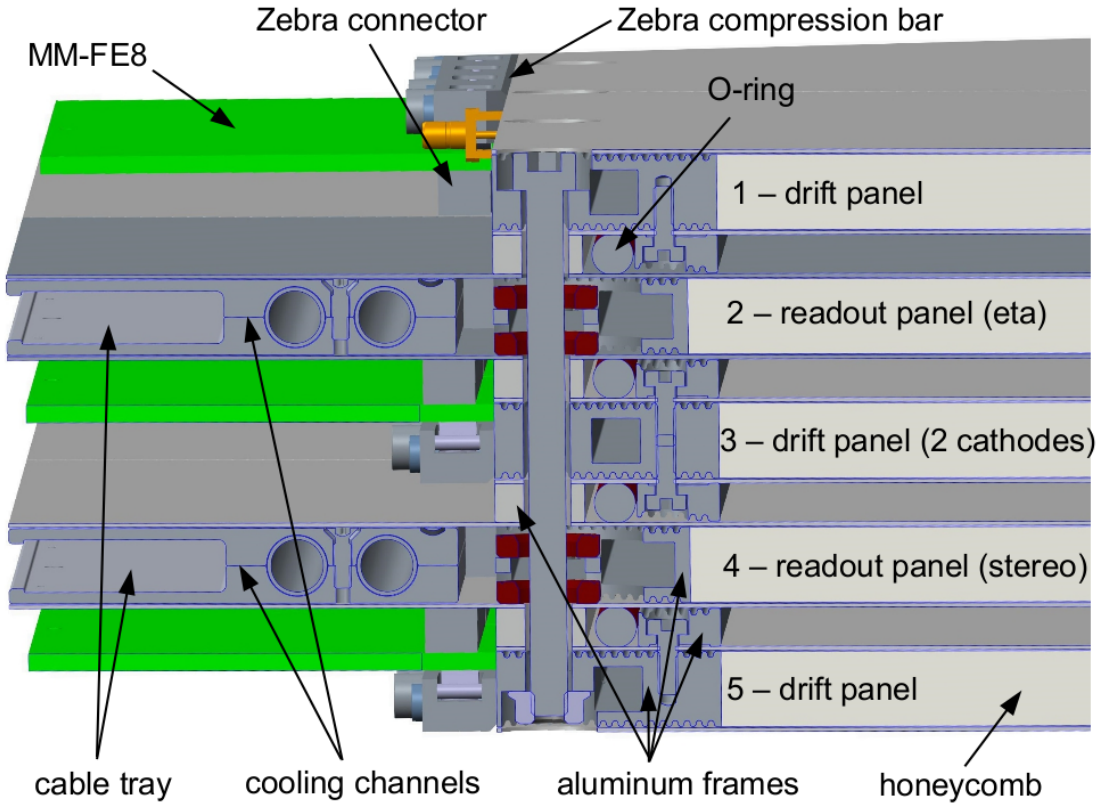

Figure 5.4: Schematic of a Micromegas quadruplet consisting of three drift and two readout panels. The active detector layers are the volumes between the panels.

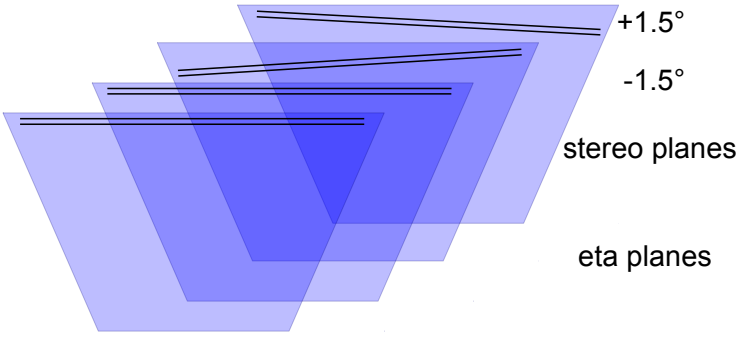

Figure 5.5: Strip layout of a Micromegas quadruplet with two so-called eta planes and two stereo planes, which are slightly rotated with respect to the eta strips.

The woven micro-mesh is mounted onto the drift panel in a distance of exactly 5 mm defining the drift region. During the assembly, when the panels are screwed together, the mesh is pressed onto the insulation pillars of 128 µm height etched on top of the anode-strip structure. The distance of 128 µm defines the amplification region. Therefore the active detector layer is the gas volume between two panels sealed by an O-ring.

5.3 Production of the Resistive Strip Readout Boards

The PCBs with the copper readout strips are commercially produced with a pitch of 425 µm and a strip width of 300 µm. Simultaneously to the etching of the readout strips multiple markers for various alignments are etched as well. One kind of these markers are for the alignment of the Kapton foils with the resistive pattern to the readout PCBs. The resistive pattern is screen printed onto 50 µm thick Kapton foils simultaneously with matching markers for the alignment to the PCBs. Therefore the alignment between readout strips and resistive pattern can be controlled. The Kapton foils are glued onto the PCBs with a 25 µm thick layer of Krempel Akaflex CDF 25 [Krempel, 2017]. The high voltage (HV) connection to the power supply sits on the PCB and has to be connected to the resistive pattern (see fig. 5.6). This is done via a screen printed silver polymer conduct ESL 1901 SD [ESL ElectroScience, 2017], which connects the high voltage to the whole resistive pattern of a high voltage sector. Each PCB has two high voltage sectors. To insulate the HV from the grounded mesh a coverlay line is placed on top of the silver polymer conduct. This line encloses the active area of a layer and assures the height of the amplification region at the border. In the same step the 128 µm mesh supporting pillars are etched on top of the resistive pattern. The pillars consist of two layers of 64 µm thick coverlay Pyralux PC1025 [DuPont Electronic Materials, 2017].

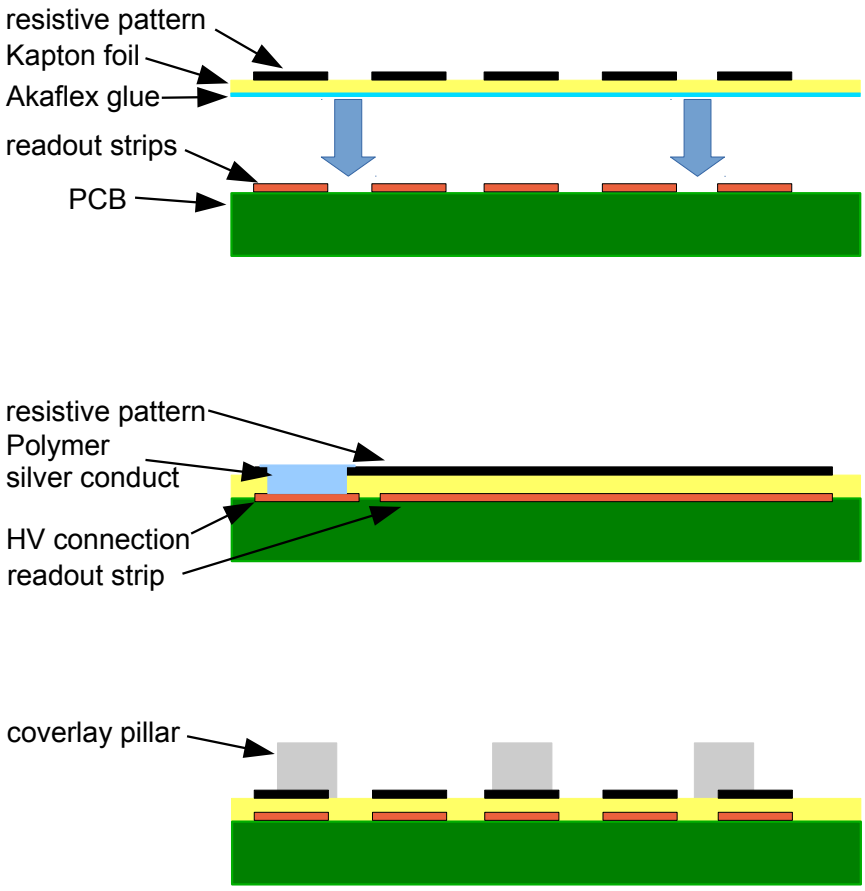

Figure 5.6: Three important steps of the readout board production. The upper scheme shows the gluing of the Kapton foil with the resistive pattern onto the PCB with the copper readout strips. On the Kapton foil as well as on the PCB are dedicated markers for the alignment between readout strips and resistive pattern. The scheme in the middle shows the connection between high voltage connector on the PCB and the resistive pattern via silver polymer conduct. The lower scheme shows the 128 µm coverlay pillars on top of the resistive pattern.

5.4 Panel Construction

To maintain the excellent momentum resolution $\Delta p_T = 15\,\%$ at a transverse momentum $p_T = 1\,\text{TeV}$ of the currently used detectors the Micromegas have to have a spatial resolution better than 100 µm in a single layer independent of the track angle. This is very challenging over an area of 2 to $3\,\text{m}^2$. To achieve this excellent spatial resolution the alignment accuracy of the readout strips on the individual PCBs and especially the alignment within the whole quadruplet has to be below 30 µm. And the accuracy perpendicular to the detector plane has to be below 80 µm including the planarity of the panels and a possible deformation of the drift region. First the construction of the panel with a method to assure the planarity will be described. Then the alignment of the readout boards will be explained.

5.4.1 Gluing of Sandwich Structures in Two Steps

The basic idea of the sandwich gluing process is to transfer the planarity of a planar precision granite table to the sandwich panel. The granite table has a planarity of better than 6 µm. Using a slight underpressure of about 100 mbar the PCBs are sucked to the granite table after alignment of the PCBs (see sec. 5.4.3). The outer PCB edges and the joint edges between the PCBs are sealed with tape. At the edges of the PCBs the material is 15 mm larger than the actual panel size, therefore the sealing tape is always outside of the panel. Then the glue is distributed on top of the PCBs with a height of about 300 µm. The aluminum frame consisting of four bars for the edges and two as inner reinforcement at the joints of the PCBs is placed on top and three pre-cut aluminum honeycomb sheets are placed between the bars (see fig. 5.7). After curing over night under a vacuum hood this so-called halfpanel is removed from the granite table and the overlapping PCBs material is cut off at the edges of the aluminum frame. Then the halfpanel is vacuum sucked to a so-called stiffback. A stiffback is a rigid aluminum structure similarly built as the panels. It consists of a 10 cm thick aluminum honeycomb perforated to allow for vacuum suction framed by a 20 mm thick Bosch profile frame and sandwiched by two 1 mm thick aluminum plates instead of the PCBs. The planarity of this stiffback is very good with an RMS of about 14 µm. It serves as counter part for the surface of the halfpanel. Therefore the two PCB surfaces of the panel will be parallel in the second gluing step. The second step starts like the first with a second set of PCBs and the procedure is repeated to the point when the aluminum frame and honeycomb is placed on the PCBs. Instead of this now the stiffback with the halfpanel sucked on the bottom side is lowered into the glue distributed on the second set of PCBs. Precision distance pieces are used to define the thickness of the panel, which is homogeneous due to the parallel surfaces of the panel (see fig. 5.7).

The construction of drift and readout panels is very similar except for one point. Whereas for the drift panel a precise alignment between the PCBs is not very important, within 1 mm is sufficient, the readout panel PCB alignment has to be very precise. Not only the three PCBs on one side of the panel, but also the two sides of the panel have to be exactly aligned (see sec. 5.4.3).

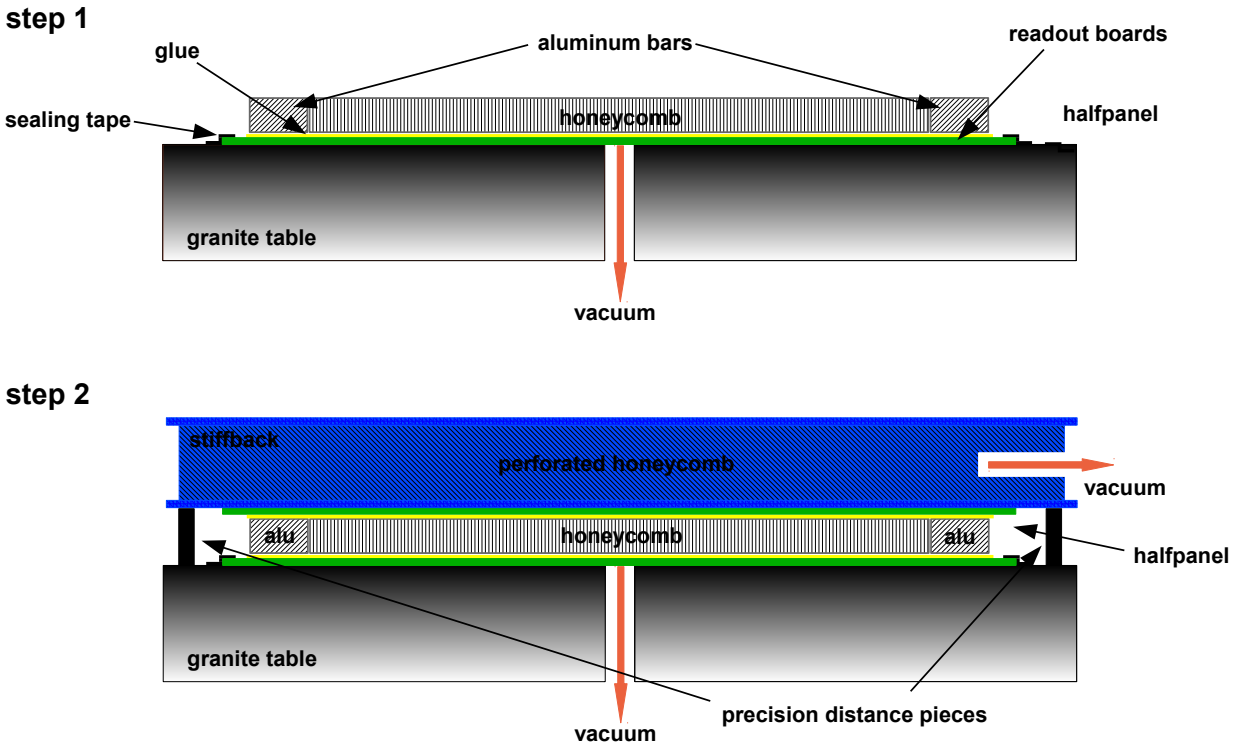

Figure 5.7: This figure shows the two gluing steps of the sandwich panel production. Step 1: After the alignment of the PCBs, they are vacuum sucked to the granite table and sealed with tape. The glue is distributed on the PCBs and the aluminum bars and honeycomb is placed on top. This so-called halfpanel cures over night in a vacuum bag. Step 2: This procedure is repeated with a second set of PCBs to the point before placing the bars and honeycomb. Then the halfpanel from step 1 is vacuum sucked to a so-called stiffback, a rigid aluminum structure with a very good planarity. The stiffback with the halfpanel on the bottom side is lowered into the glue on the second set of PCBs and placed on precision distance pieces to define the thickness of the panel. After curing a second night the sandwich panel is completed.

5.4.2 Planarity Measurement of the Panels

All panels undergo a planarity measurement to assure the given requirements of an RMS better than 37 µm. This is done with a laser triangulation head mounted on a coordinate measurement machine (CMM). Figure 5.8 shows the results of the planarity measurement for the first stereo readout panel built at LMU Munich. The difference between measurement and reference measurement, the residual, is plotted as a function of the CMM coordinates x and y. In green the active area of the Micromegas with an RMS of about 15 µm can be seen. This is well within the requirements. An interplay between measurement and the coverlay pillars can be seen in red, as well as the coverlay line at the edges of the active area. The coverlay should be 128 µm higher than the active area. In figure 5.9, in which the residual to a reference measurement of the granite table is shown, the difference between active area and pillar height is about 105 µm. This could result from the semitransparent coverlay material. Left and right of the active area the about 100 µm lower electronics region is shown in blue. For more details see [Müller, 2017].

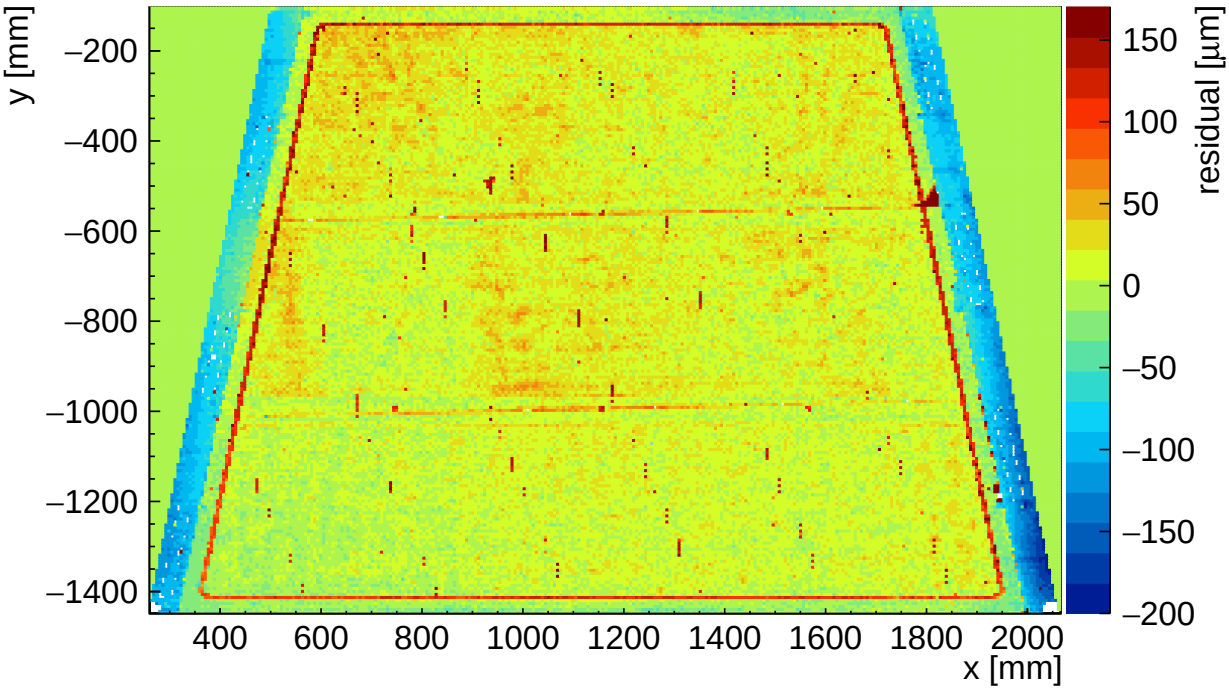

Figure 5.8: Planarity measurement of a stereo readout panel measured with a laser triangulation head mounted on a CMM. The difference between measurement and reference measurement of the granite table is plotted as a function of the CMM coordinates. In this plot the active area (green), the interplay between measurement and pillar and coverlay line (red) and the electronics region (blue) can be seen.

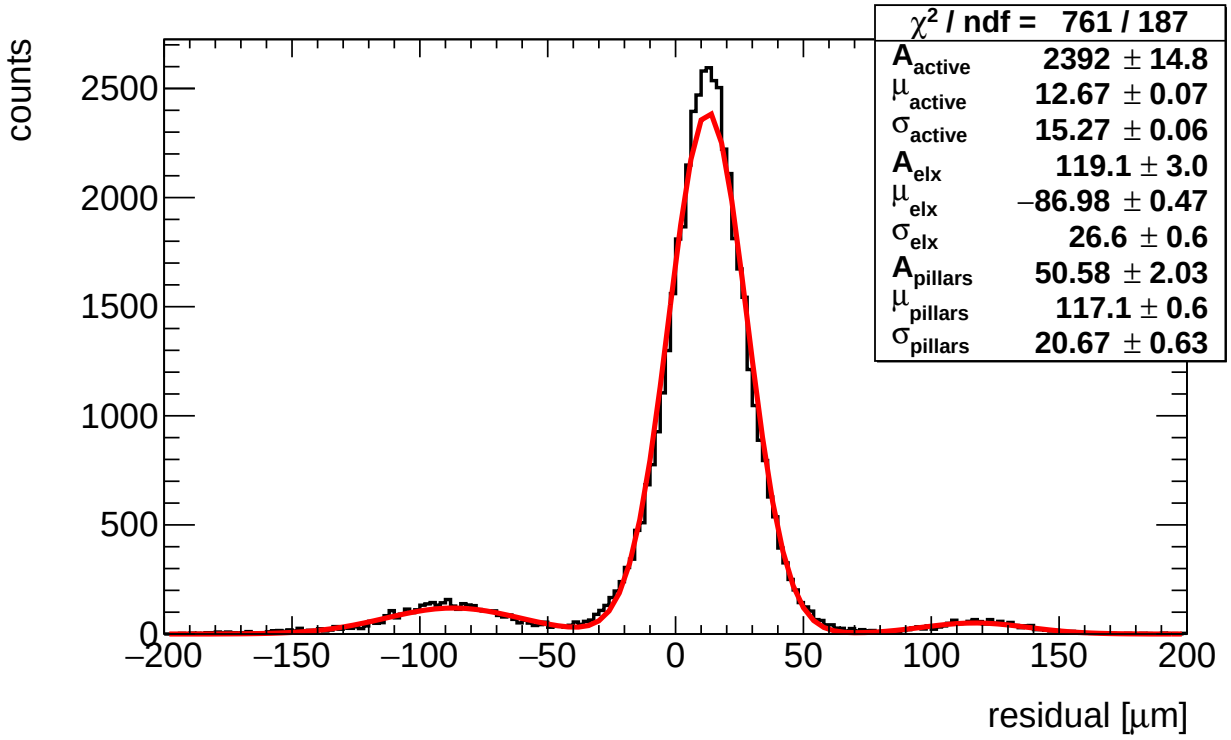

Figure 5.9: Residual distribution of the planarity measurement fitted with three Gaussian functions. The three regions can be clearly separated. The electronics region is about 100 µm lower than the active area and the coverlay line and pillars are about 105 µm higher. The pillars should be 128 µm higher than the active area. This effect occurs probably due to the semitransparent coverlay material.

5.4.3 Alignment of the Readout Boards

Figure 5.10 shows a set of three eta PCBs for the SM2 module. The former mentioned markers for the alignment are two circular markers on each PCB for the alignment of the PCBs during panel construction and eight coded masks on each PCB for the verification of the strip alignment. For the alignment of the SM2 PCBs, before gluing the panel, precision washers are glued on the backside of the PCBs at the position of the circular washers (see figure 5.11 (right)). This is done using a telecentric camera and an online optical pattern recognition software. The software recognizes the circular marker with the cross and the inner edge of the precision washer. The precision washer is then aligned concentric to the marker using an x-y-manipulator. When the washer is perfectly aligned to the marker it is glued on the PCB using the UV-light cure adhesive LOCTITE 4305 LC [LOCTIDE, 2013]. Each PCB has two precision washers, one circular and one oval.

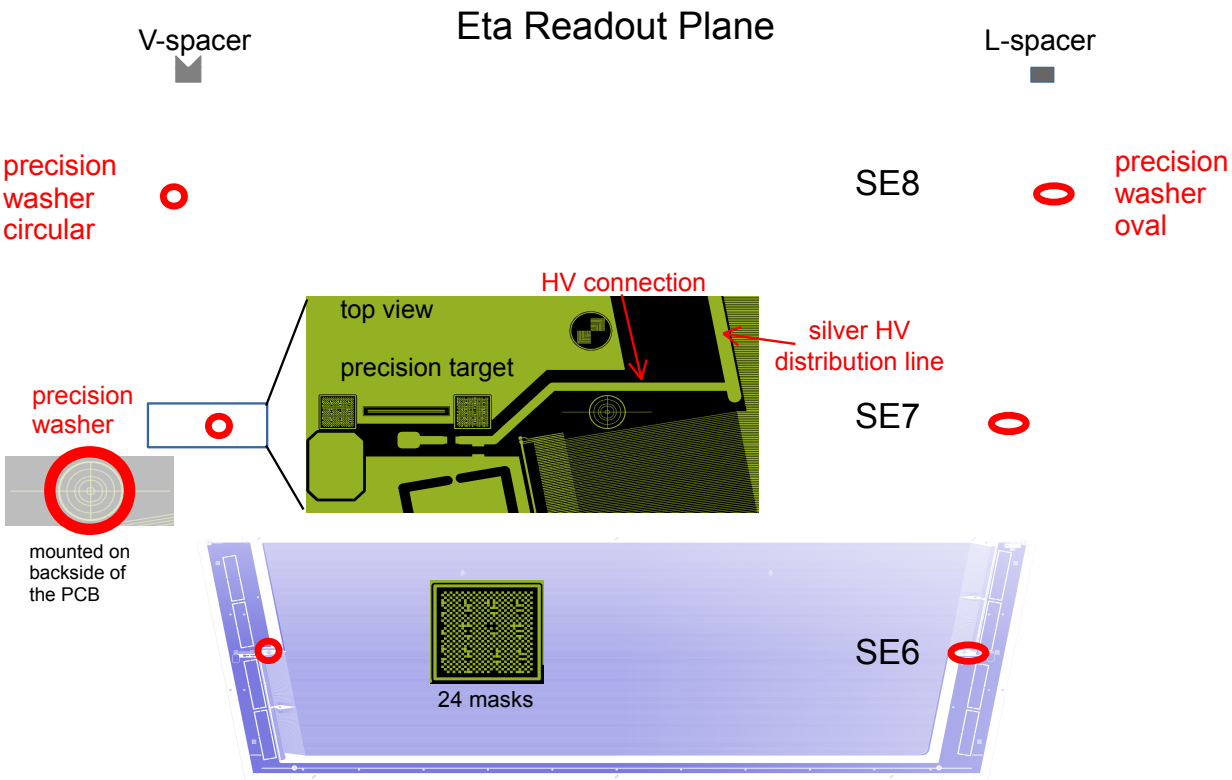

Figure 5.10: A set of three eta PCBs for the SM2 module with the etched readout strips. Simultaneously to the readout strips precision targets are photo-lithographically etched onto the PCBs. The circular markers with the cross are used for the alignment of the PCBs during the panel construction. The coded masks are used for verification of the strip alignment. Also seen can be a schematic precision washer glued on a circular marker.

The set of readout PCBs is placed on the granite table with the resistive strip pattern facing towards the granite table. The precision washers are on the upper surface for the

Figure 5.11: Left: Telecentric camera with x-y-manipulator for the positioning of the precision washer. Right: Picture of the precision washer aligned to the circular marker on the PCB taken by the telecentric camera.

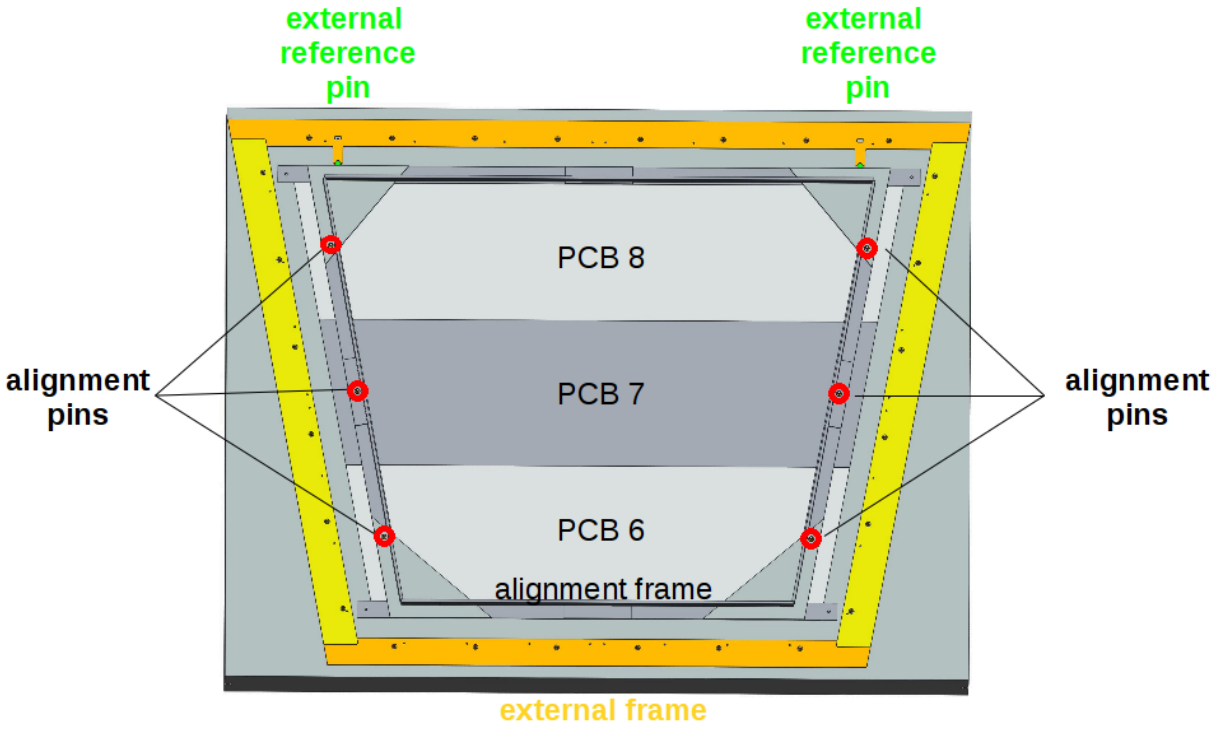

Figure 5.12: Scheme of the granite table with a set of three PCBs and the accurate alignment frame for the PCB alignment. In yellow and orange a global reference frame mounted on the granite table is shown. The alignment frame is globally aligned with external reference pins (green) on the granite table. Now alignment pins are guided through bushes in the frame and the precision washers (red) for the relative alignment between the PCBs.

alignment of the PCBs. Figure 5.12 shows a scheme of the alignment. An external reference frame is mounted on the granite table with two reference pins for the global alignment. After placing the PCBs on the granite table with a coarse alignment, the accurate alignment frame is aligned to the external reference frame. It has six bushes, which are used to guide the alignment pins. With these alignment pins the readout PCBs are perfectly aligned to each other and their position is fixed by applying vacuum. Then the alignment frame is removed and, if this is the first set of PCBs for the readout panel, two spacers are glued on one of the PCBs matching the V- and L-spacer on the alignment frame (see fig. 5.10). Therefore the halfpanel of the first gluing step can be realigned to the external reference frame in the second gluing step and has thus the same position as in the first gluing step. The PCBs of both sides of the panel have the same global alignment and therefore are aligned to each other as well.

5.5 Mesh Stretching and Mounting

Before the mesh can be mounted on the drift panels, the mesh has to be stretched with a tension of about $11\,\mathrm{N\,cm^{-1}}$. These $(2120 \times 1620)\,\mathrm{mm^2}$ large meshes are stretched using 28 pneumatic clamps (see fig. 5.13). A so-called transfer frame consisting of four aluminum Bosch profiles is placed within the pneumatic clamps. A photo of an aluminum Bosch profile with a cross section of $(60 \times 30)\,\mathrm{mm^2}$ is shown in figure 5.14. The mesh is glued on the side without slots, the upper side in the picture. The transfer frame is necessary as counter part for the clamps. It deforms slightly, but this can be adjusted with the pressure in the pistons of the clamps. The clamps are closed on the edge of the mesh and with a pressure of about 3 bar the mesh is stretched with the desired tension and glued to the transfer frame. Figure 5.15 shows the homogeneous tension distribution with a mean value of $(11.66 \pm 0.38)\,\mathrm{N\,cm^{-1}}$. After stretching the mesh it has to be cleaned and holes

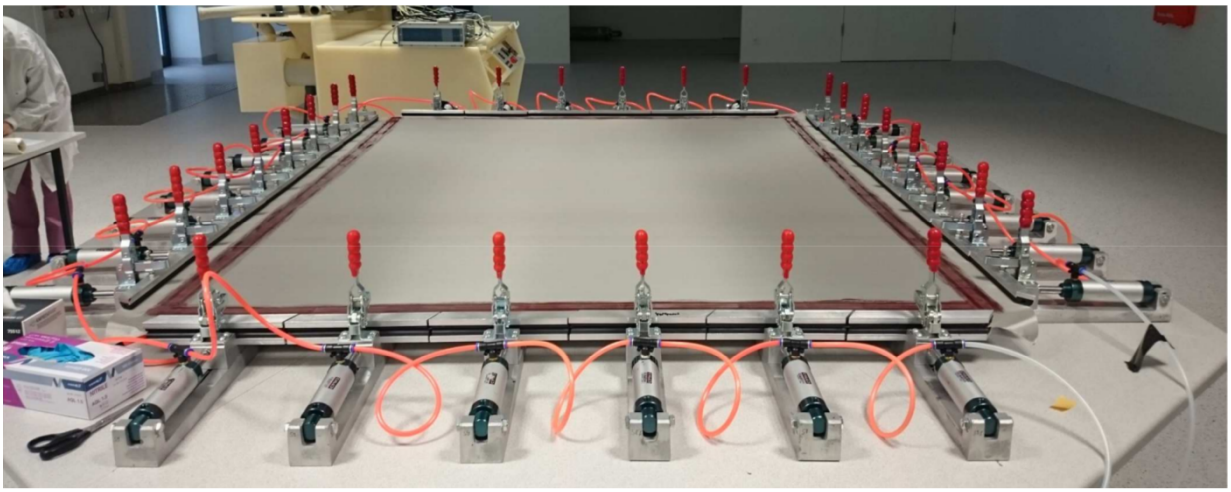

Figure 5.13: Photo of a stretched mesh within the stretching setup consisting of 28 pneumatic clamps. The mesh is already glued onto the transfer frame.

for the interconnections (see sec. 5.7) have to be punched into the mesh at six positions. Afterwards it can be transferred to the drift panel.

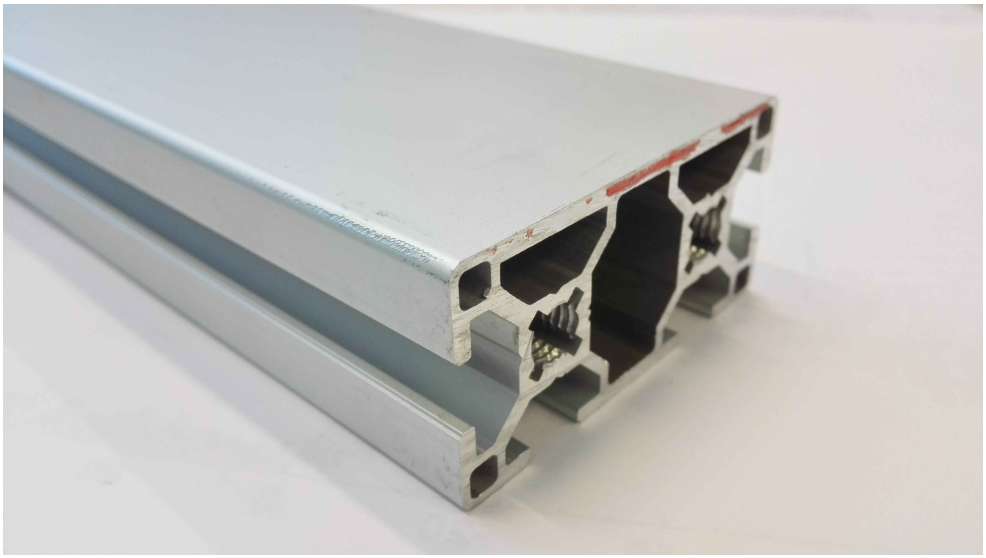

Figure 5.14: Photo of an aluminum Bosch profiles with a cross section of $(60 \times 30)\,\mathrm{mm}^2$. The mesh is glued on the upper side without slots.

For the transfer of the mesh glue is distributed on the mesh frame mounted on the drift panel (see figure 5.16). The mesh on the transfer frame is placed on top. The glue has to cure over night. Then the overlapping mesh is cut away at the edges of the mesh frame. After this process the drift panel is ready for the assembly.

5.6 Quadruplet Assembly

With two readout and three drift panels the assembly can begin. Figure 5.17 shows the setup of the assembly. An assembly frame consisting of aluminum Bosch profiles is mounted perpendicular on a very flat table. It has two rails in the front to guide the panels. Alternating the drift and readout panels are placed on the assembly frame and the gas volume of the detectors are sealed with an O-ring between mesh and gas frame. The position of the drift panel is sufficient within half a millimeter. But the positions of the readout panels to each other have to be perfect at a level of 20 µm. For this alignment V- and L-spacers are used, which are perfectly aligned to the readout PCBs (see sec. 5.4.3). These two spacers slide on two rails on the assembly frame (see fig. 5.17) until the readout panels are in their position. Two dedicated pins and bushes (see fig. 5.18) are used to conserve the alignment after assembly. The pins have to be perfectly perpendicular to the readout plane. To assure this the pins are glued with a precision template into the stereo readout panel (see fig. 5.19). The two bushes are glued into the eta panel. During the assembly the pins perpendicular to the stereo panel slide into the bushes in the eta panel. Afterwards the panels are screwed together at the edges of the quadruplet.

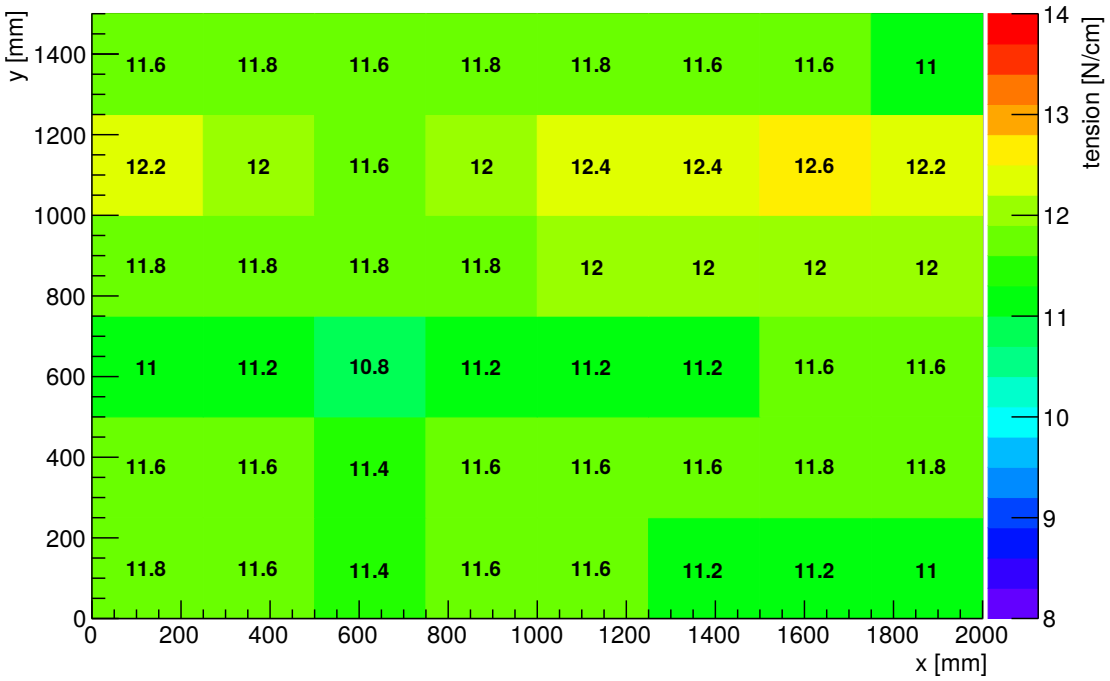

Figure 5.15: Tension distribution over the whole area of the mesh glued to the transfer frame after stretching. The mean tension is $(11.66 \pm 0.38)\,\mathrm{N\,cm^{-1}}$.

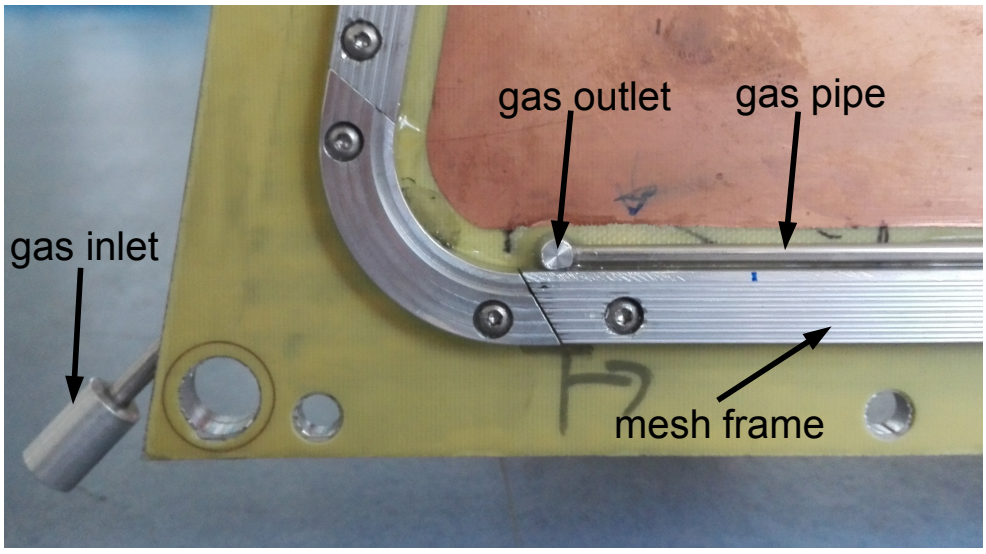

Figure 5.16: Photo of a drift panel with the mounted mesh frame on top before the mesh transfer. Additionally, the gas inlet and outlet and the gas distribution pipe can be seen. A gas frame will be mounted around the mesh frame. Between mesh and gas frame the O-ring is positioned to seal the gas volume of the detector.

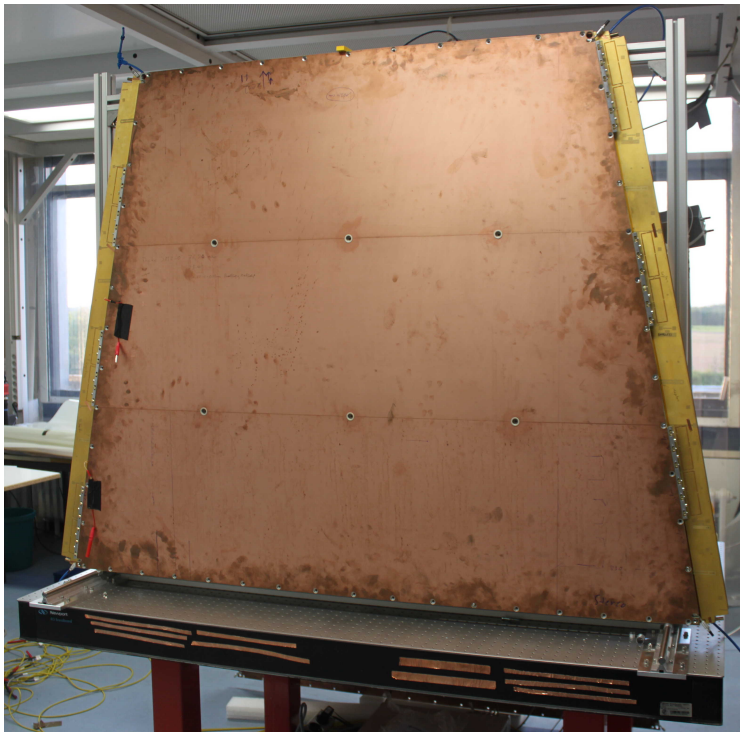

Figure 5.17: Photo of the SM2 quadruplet assembly. An assembly frame is mounted on a table. The formerly mentioned spacers on the lower side of the readout panels are guided by two rails.

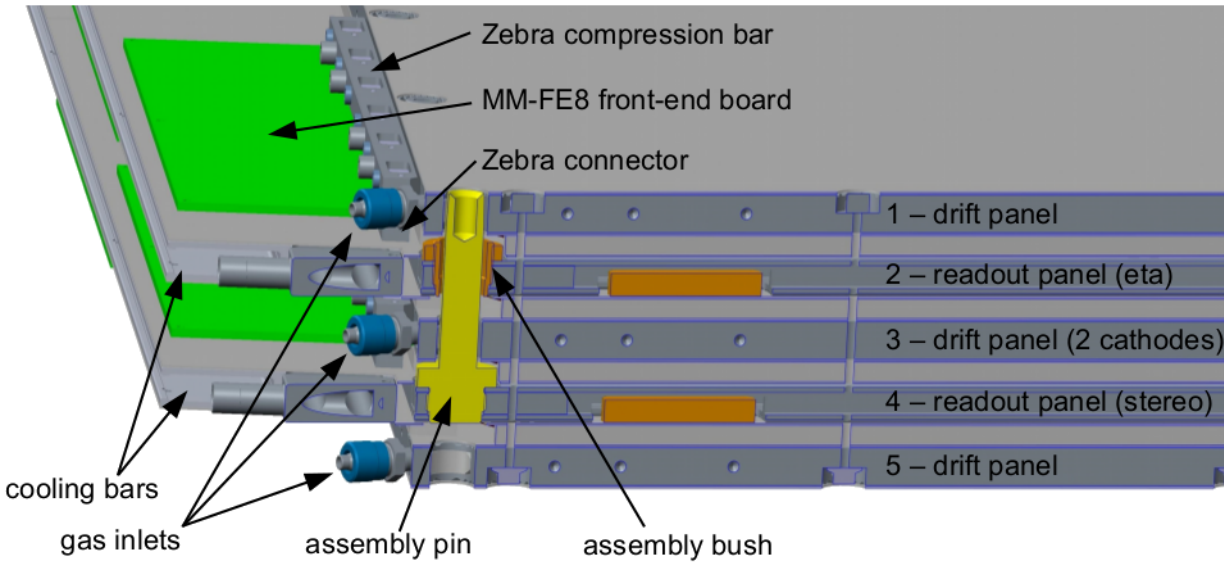

Figure 5.18: Cross section of an assembled quadruplet. Two dedicated assembly pins and assembly bushes are used to conserve the perfect alignment of the two readout panels after assembly. Figure taken from [Lösel, 2017].

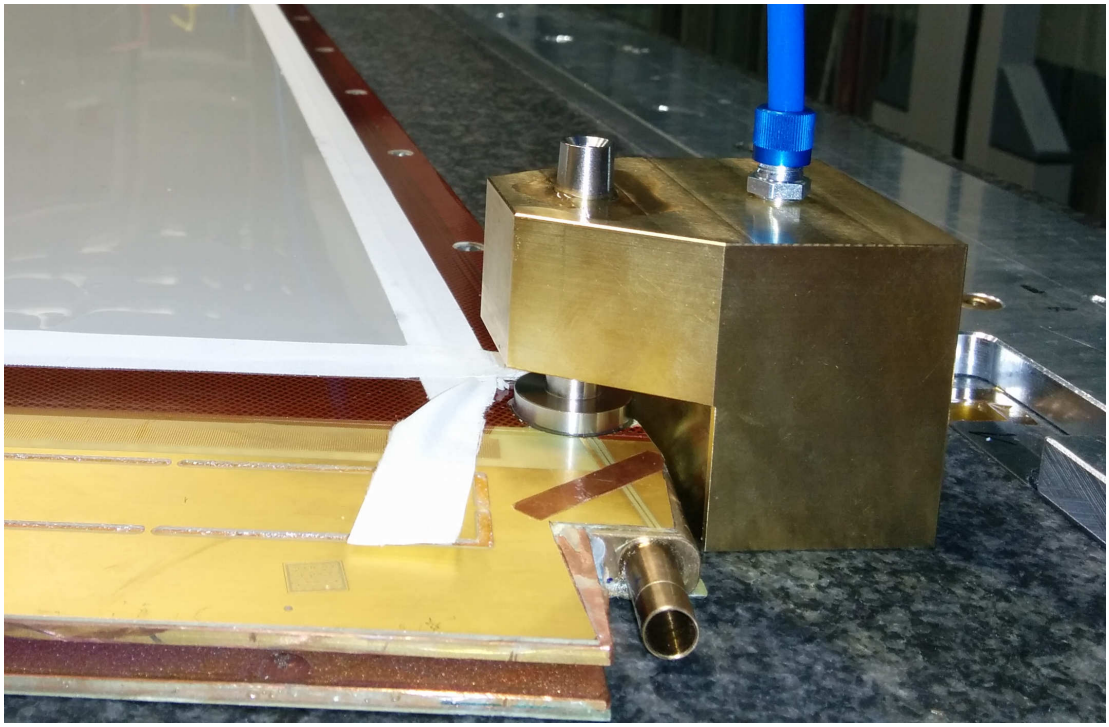

Figure 5.19: Photo of the precision template to glue the pins to conserve the alignment of the two readout panels into the stereo panel.

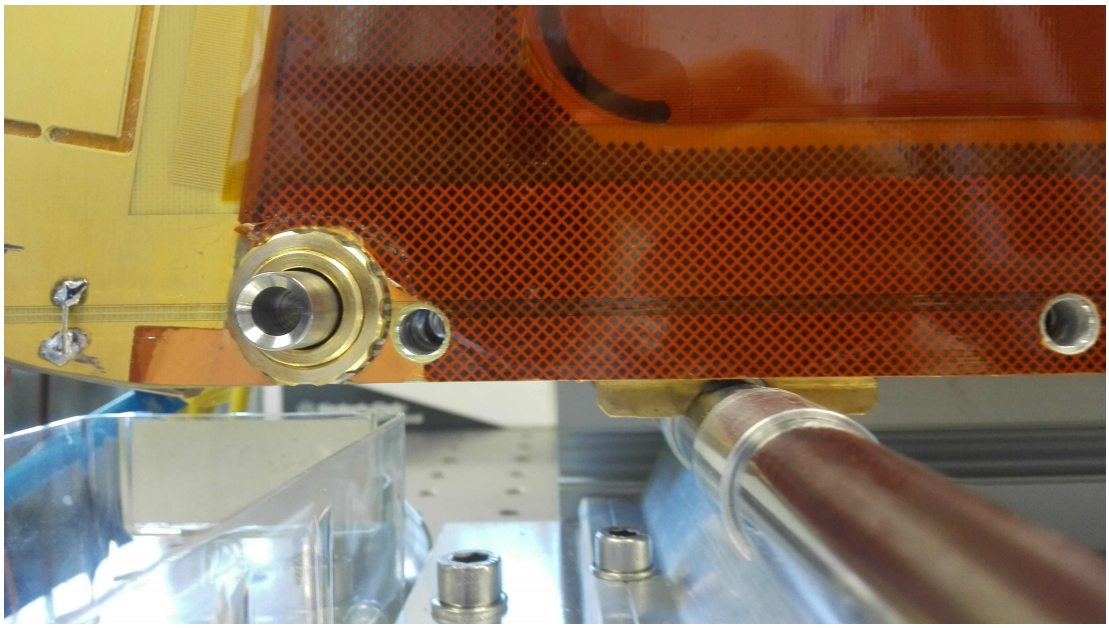

Figure 5.20: Photo of a pin for alignment conservation. The pin is glued into the stereo panel and guided by a bush in the eta panel. On the right also the V-spacer on the rail is shown.

5.7 Stabilization Against Overpressure

ANSYS [ANSYS, Inc., 2017] finite element simulations have shown [Herrmann, 2017], that with an overpressure of 2 mbar in the gas volumes of the Micromegas the outer drift volume would deform in the order of millimeters. But if the quadruplet is screwed together at dedicated positions within the active area this deformation is reduced to a few ten micrometers. Figure 5.21 shows the result of an ANSYS simulation with six so-called interconnections. The maximum deformation is then only 69 µm with the positions chosen for the series modules of SM2. The positions of the interconnections can be seen in figure 5.21 as area with no deformation in the active area of the Micromegas. One of the interconnections is shown in figure 5.22. The blue distance pieces are screwed into the drift panels to assure the height of the drift region. At the outer drift panels the interconnections are sealed with O-rings in the end-cap to assure the gas tightness of the quadruplet.

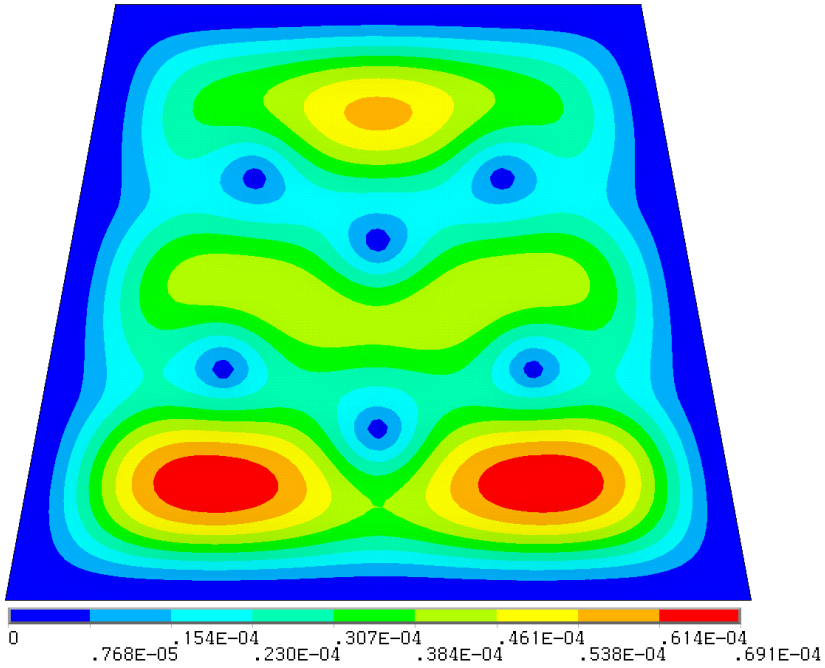

Figure 5.21: ANSYS [ANSYS, Inc., 2017] finite element simulation of the deformation of the drift region for an outer drift panel with an overpressure of 2 mbar given in meters. Due to the interconnections the maximum deformation is only 69 µm. Figure taken from [Herrmann, 2017].

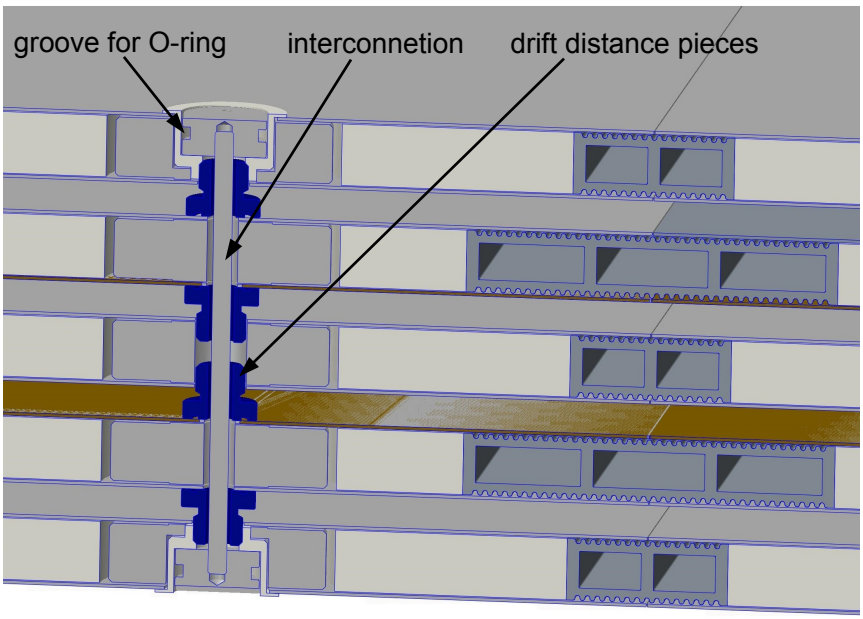

Figure 5.22: Schematic drawing of an interconnection integrated in a quadruplet. The blue distance pieces assure the 5 mm large drift region. They are screwed to precise height into the drift panels using precision templates. This position is fixed using the two component adhesive Araldite 2011 [Huntsman, 2015]. The holes are sealed by caps with integrated O-rings at the outer drift panels.

5.8 Readout using Zebra Connectors

For the readout of the NSW Micromegas MM-FE8 front-end boards are developed. Eight VMM asics will be mounted on the front-end boards. The MM-FE8 are connected to the readout strips using Zebra elastomeric connectors of the type FG-S [COMPELMA, 2015]. The Zebra connectors chosen for the NSW project with the dimensions 105.5(L) × 6.4(H) × 3.0(W) have six rows of gold plated wires with a diameter of 30 µm and a pitch of 50 µm (see fig. 5.23 (right)). The Zebra connectors are mounted on the front-end boards in holders (see app. B) to prevent deformations (see fig. 5.23 (left)). They have to be compressed by 0.4 mm to have optimal electric conductivity. Therefore a compression bar is mounted at the edge of the drift panels to compress the Zebra connectors with a force of about 30 kg equivalent. If compression of the Zebra connectors and therefore the electric conductivity is not sufficient the readout strip can not be read out and appears to be dead.

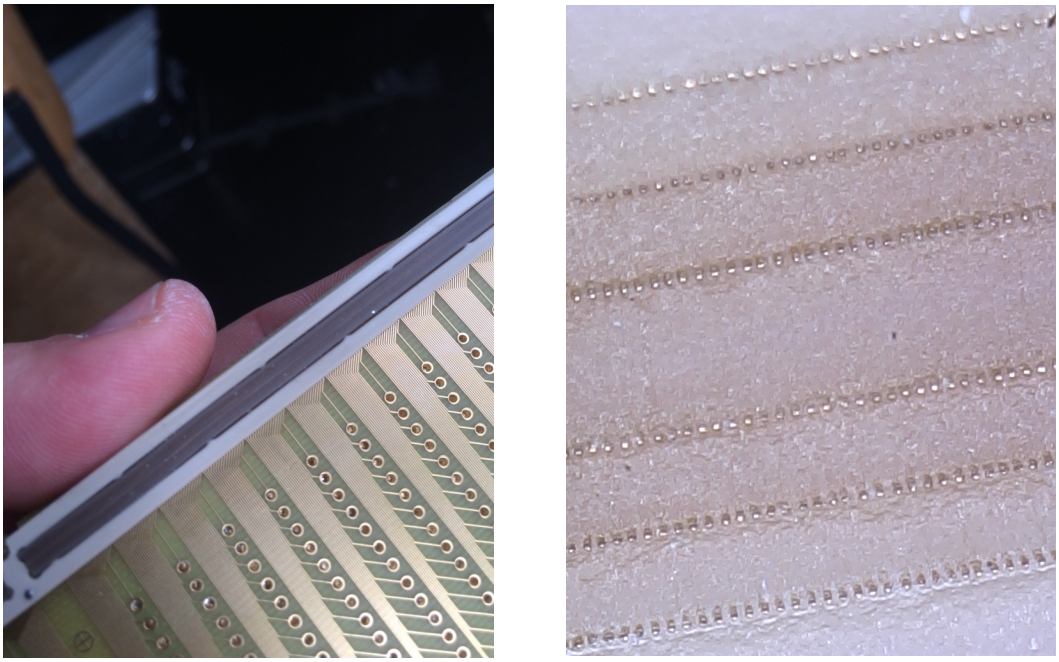

Figure 5.23: Left: Zebra connector in its FR4 holder mounted on a front-end board. Right: The six rows of gold wires in the Zebra connector with a pitch of 50 µm.

A $(10 \times 10)\,\mathrm{cm}^2$ Micromegas detector with footprints suited for the Zebra connector was used to test the connectors on compression and defects. The detector was equipped with a compression bar and an APV adapter board was used to read out the Micromegas using APV25 front-end boards (see fig. 5.24). First the sigmas of the electronic pedestals were calculated with various stages of compression. Figure 5.25 shows the sigma of the pedestals as a function of the strip number for both a good compression and an insufficient compression. It can be seen that around strip 125 a few readout strips are not connected to the readout electronics due to insufficient compression. If the compression is high enough this effect does not occur.

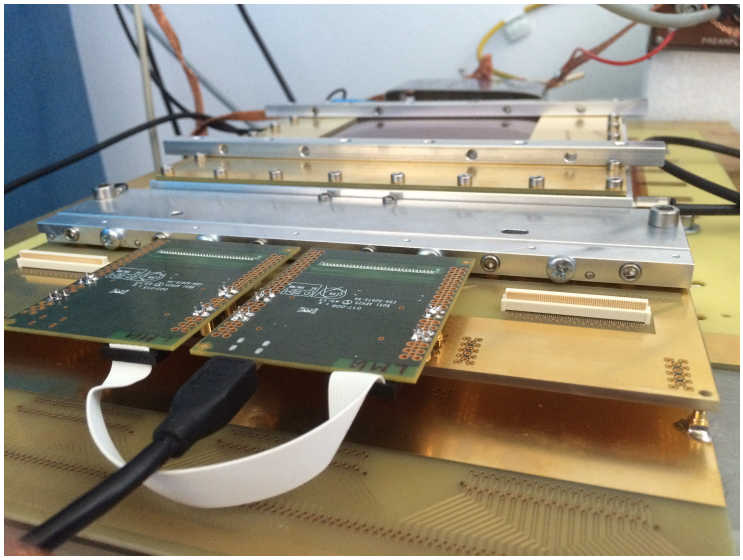

Figure 5.24: Photo of a the setup to test Zebra connectors with cosmic muons or the pulser test. An APV adapter board is used to connect the $(10 \times 10)\,\mathrm{cm}^2$ Micromegas to the front-end boards.

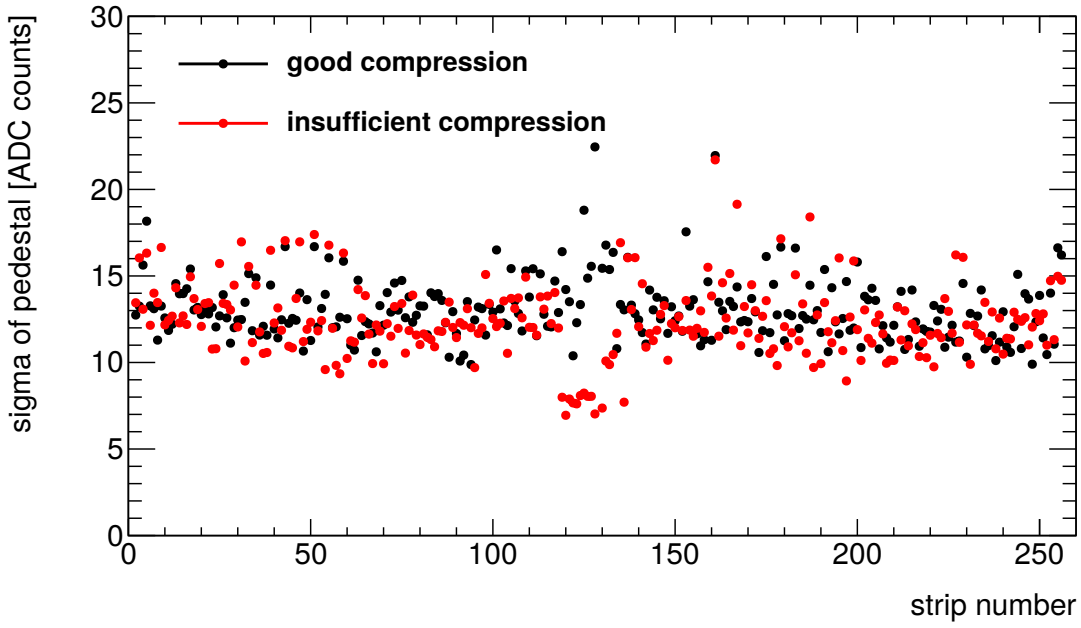

Figure 5.25: Sigma of the pedestals as a function of the strip number. If the compression of the Zebra connector is sufficient, the distribution is homogeneous (black). When the compression is insufficient, the strips in the middle, around strip number 125, are not connected to the front-end boards (red). Therefore the sigmas of the pedestals are smaller.

With the two compression configurations shown in figure 5.25 a measurement with cosmic muons was performed. The position of the muon is reconstructed using the centroid method. Figure 5.26 shows the hit distribution of the muon position. For a good compression the hit distribution is very homogeneous except at the edges of the active area due to mis-reconstructions of the muon position, if not the whole path of the muon was in the active detector volume. If the compression is not sufficient, the reconstructed position is shifted towards readout channels, where the compression is good enough.

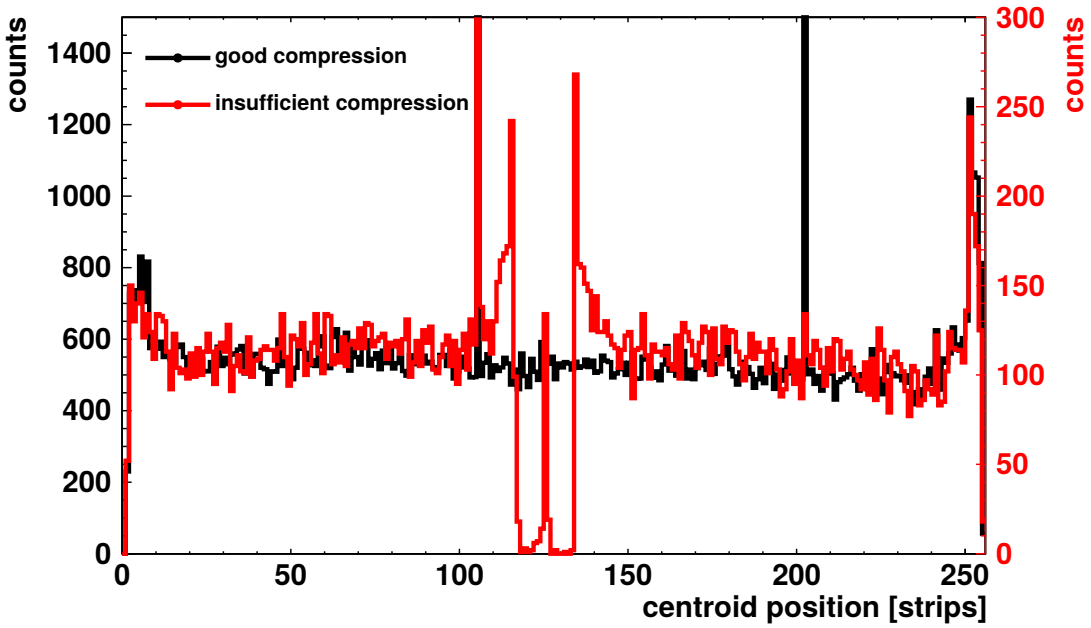

Figure 5.26: Hit distribution of the position of the cluster measured with cosmic muons. With a good compression of the Zebra connector the position distribution is very homogeneous except for the edges, there the centroid method works not that well (black). Whereas the distribution for an insufficient compression of the Zebra connector leads to mis-reconstructions for example in the middle (red).

The Zebra connectors are delivered by a company, for example *Fujipoly* or *Compelma*, and have to be tested for defects. A procedure was developed to test the connectors for defects and to test the conductivity while equipping the Micromegas with readout electronics for the operation within the ATLAS detector. With this so-called pulser test a short voltage pulse generated by a function generator is propagated through the pulse adapter. The pulser is basically a voltage divider to terminate the circuit against 50 Ω and a 20 nF capacitor to transform the voltage pulse into a current pulse (see fig. 5.27). The pulser is connected to the high voltage connection of the Micromegas. There the signal is distributed using the silver conduct line to the whole resistive anode structure and capacitively coupled to the readout strips. The signal should be the same on all strips, therefore the conductivity of the Zebra connector can be measured. Figure 5.28 shows the pulse height as a function of the strip number for a good and a bad Zebra connector. The

data points of the good Zebra connector show small fluctuations. Whereas the data points of the bad zebra show large variations in the pulse height. It is therefore rejected. The reject rate of the Zebra connectors is about 5 %.

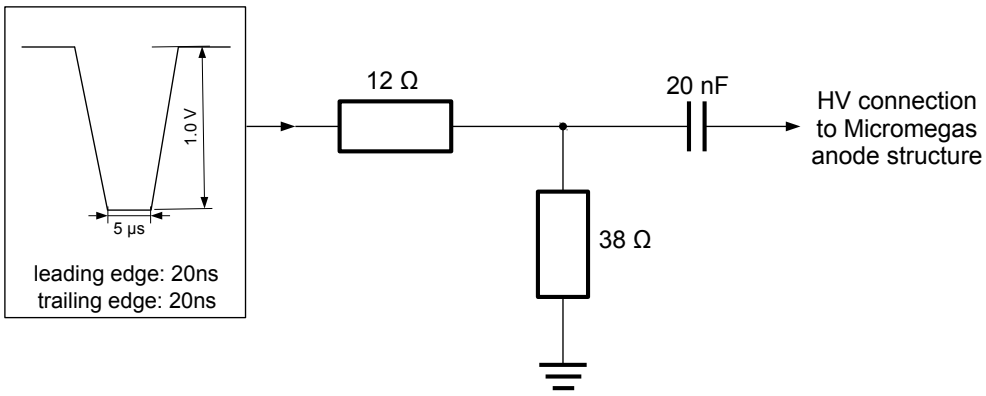

Figure 5.27: Circuit diagram of the pulse-adapter. A pulse from a function generator is propagated via the pulse-adapter to the high voltage distribution line, which connects the high voltage to the resistive strip anode structure. With this setup the connection between the readout strips and the front-end boards can be verified.

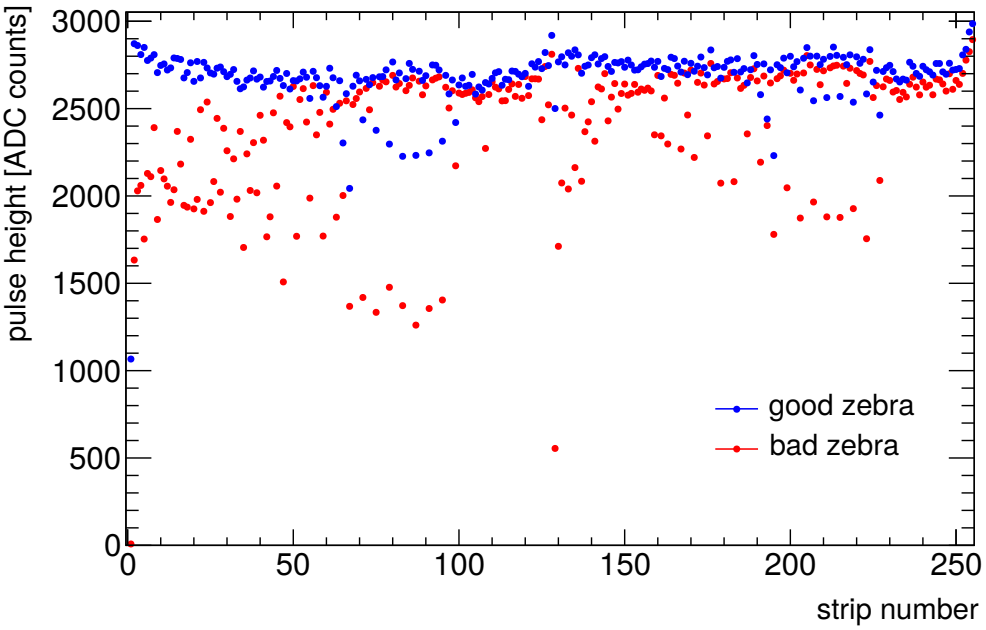

Figure 5.28: Results of the pulser test with a well working Zebra connector (blue) and a defective Zebra connector (red). The pulse height is plotted as a function of the strip number. The well working Zebra connector shows a smooth pulse height distribution with small variations. Whereas for the defective Zebra connector larger variations are observed.

Chapter 6

Precision Calibration using Cosmic Muons

In this chapter the experimental setup for the calibration of large area Micromegas will be explained, then the calibration procedure developed with a $1\,m^2$ prototype Micromegas will be presented followed by the results obtained with this detector.

6.1 Cosmic Ray Facility (CRF)

The LMU Cosmic Ray Facility (CRF) in Garching was originally built to calibrate the wire positions in Monitored Drift Tube chambers (MDT) for the ATLAS Muon Spectrometer. Now it will be adapted for the calibration and quality assurance of the SM2 Micromegas quadruplets.

The CRF consists of two ATLAS MDT BOS chambers for reference tracking, which have an active area of $2.2 \times 4\,m^2$. Their centers of gravity are 1121 mm apart. The chambers have a height of about 500 mm, which leaves about 600 mm for test detectors in between. Each drift chamber consists of two multi-layers with three tube layers. The position of the traversing muon is determined using a well defined drift time - drift range relation. With six layers of drift tubes the track of the muon is reconstructed unambiguously. The two reference chambers are sandwiched by two trigger hodoscopes which give a coarse position information of about 100 mm along the wires of the MDTs and a trigger time information with sub-nanosecond resolution. The trigger hodoscopes have a distance of 2766 mm to each other which leads to an angular acceptance between -30° and +30° for the whole test-stand. It is triggered on coincident signals of upper and lower scintillator hodoscope. Between the lower MDT and lower trigger hodoscope a 34 cm thick iron absorber is installed (see fig. 6.2) discarding muons with energies below 600 MeV to harden the energy spectrum.

Figure 6.1: Photo of the LMU Cosmic Ray Facility in Garching. The CRF consists of two Monitored Drift Tube (MDT) chambers, two spare chambers for the ATLAS Muon Spectrometer, sandwiched by two trigger hodoscopes. In between the MDTs a 1 m^2 large Micromegas detector is installed for the calibration.

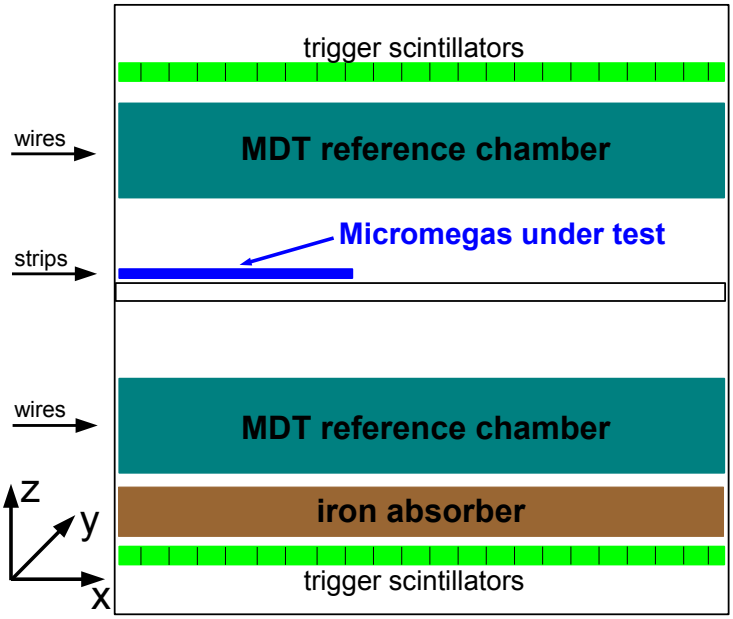

Figure 6.2: Schematic drawing of the LMU CRF consisting of two MDT reference chambers sandwiched by two trigger hodoscopes. Between the lower MDT and the lower trigger hodoscope a 34 cm thick iron absorber is installed to perform a hardware cut on muon energies below 600 MeV. In between the two MDTs the Micromegas under test is installed. Wires and strips are oriented along the x direction.

6.2 The 1 m^2 Prototype Micromegas Detector

The Micromegas prototype detector (L1) has a very similar construction as the SM2 quadruplets, but with only one active layer. It has an active area of $(92.16 \times 102)\,\mathrm{cm}^2$. Due to industrial limitations it had to be constructed out of two readout PCBs similar to the SM2 quadruplets (see fig. 6.3). During the gluing of the two readout PCBs no alignment tooling was used, therefore this detector is well suited for the test calibration in the CRF. The gas volume of the detector is directly enclosed by the readout structure and the cathode, which are the surfaces of the stiffening panels. The readout panel in this case is more rigid than the drift panel due to an additional 2 mm aluminum plate (see fig. 6.4). Hence a deformation of the drift region due to a small overpressure of a few millibars in the detector mainly inflicts the drift panel. No interconnections are integrated in this detector to prevent the deformation as they are used for the SM2 quadruplets (see chap. 5).

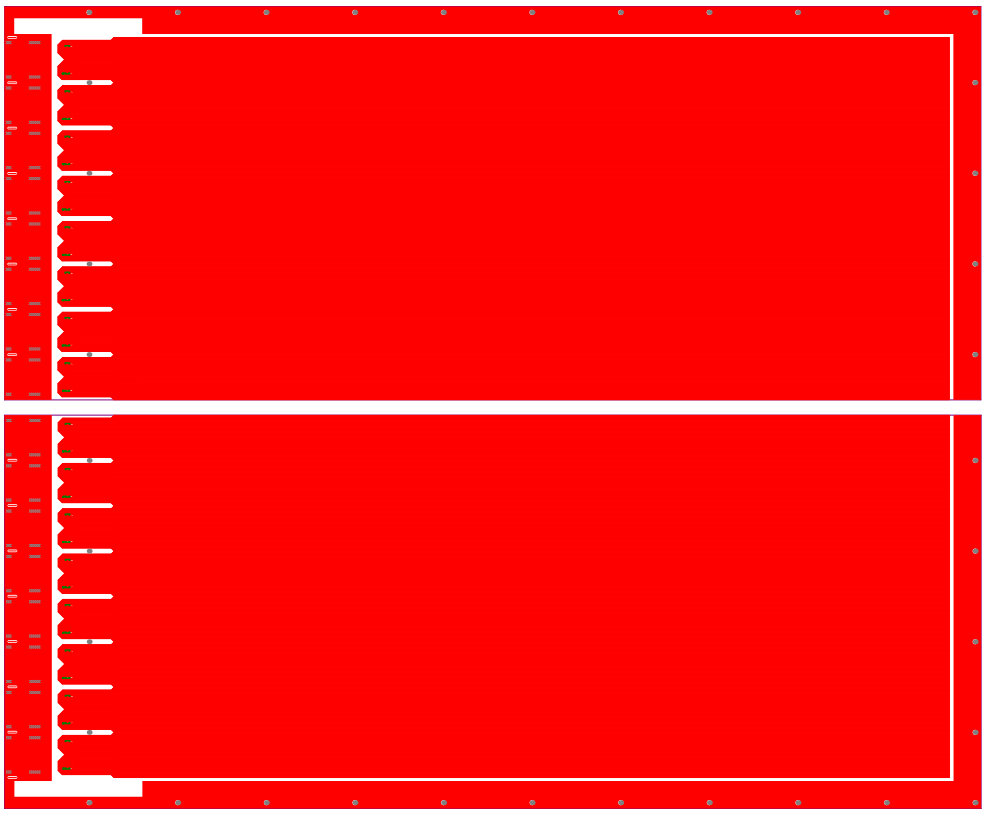

Figure 6.3: Drawing of the two PCBs of the prototype Micromegas (L1). Each PCB is read out by 8 APV25. The gap between the two readout PCBs is not to scale.

The prototype Micromegas was placed in the middle between the two reference MDTs with the readout strips orientated in the same direction as the MDT wires and thus perpendicular to the precision direction of the CRF. The L1 chamber is operated with the same gas mixture (Ar:CO_2 93:7 vol%) as the MDTs, but at atmospheric pressure. Additional

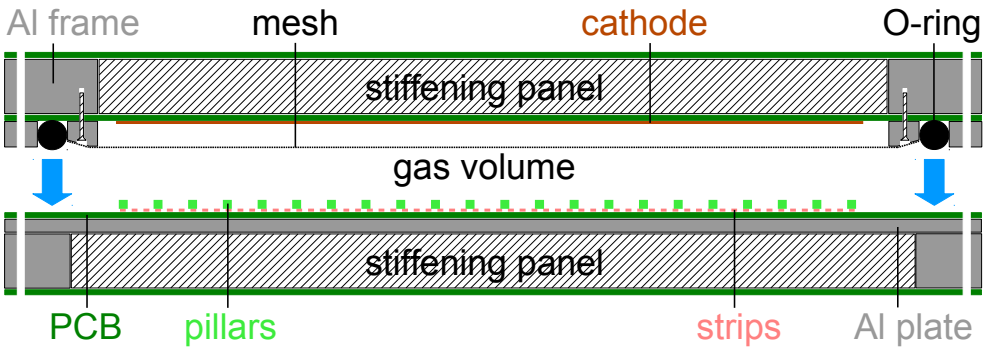

Figure 6.4: Schematic drawing of the assembly of the prototype Micromegas (L1) consisting of a resistive anode structure and cathode mounted on two stiffening panels. The readout panel is reinforced by a 2 mm thick aluminum plate. As for the NSW Micromegas the mesh is mounted on the drift panel and the gas volume is sealed by an O-ring.

power supplies were installed for the high voltages of the test Micromegas. For the readout of the Micromegas a SRS[1] was installed. The data stream of the SRS has to be merged with the data stream of the CRF. This is done using the integrated counter in the SRU and the trigger counter of the TTCvi[2] included in the VMEbus[3] readout of the CRF. One FEC[4] card is sufficient for the readout of the 2048 electronic channels of the prototype Micromegas. But the SRS was expanded to six FEC cards for the readout of a whole SM2 quadruplet with in total 12288 readout channels.

6.3 Subdivision of the Active Area and Alignment using Reference Tracks

For the alignment and calibration of the prototype Micromegas the active area is subdivided into 160 partitions. Along the readout strips it is segmented using the information of the trigger hodoscopes in 10 scintillator segments. Perpendicular to the strips it is subdivided using the granularity of the 16 APV25 front-end boards.

For each of the 160 partitions of the Micromegas the alignment procedure is individually performed. The alignment in x direction has to be with an accuracy of a few millimeters only due to the one dimensional readout of the Micromegas. In y and z direction the muon reference track can be used for the alignment. Therefore the reference tracks are distinguished in two types: tracks perpendicular to the Micromegas detection plane and inclined tracks.

Perpendicular tracks are used for the alignment in y direction, because for perpendicular tracks the residual is independent of the z position. The residual Δy is the difference

[1]SRS: Scalable Readout System, development of RD51 collaboration (see chap. 3)
[2]TTCvi: TTC-VMEbus interface
[3]VMEbus: Versa Module Eurocard-bus
[4]FEC: Front-End Concentrator card

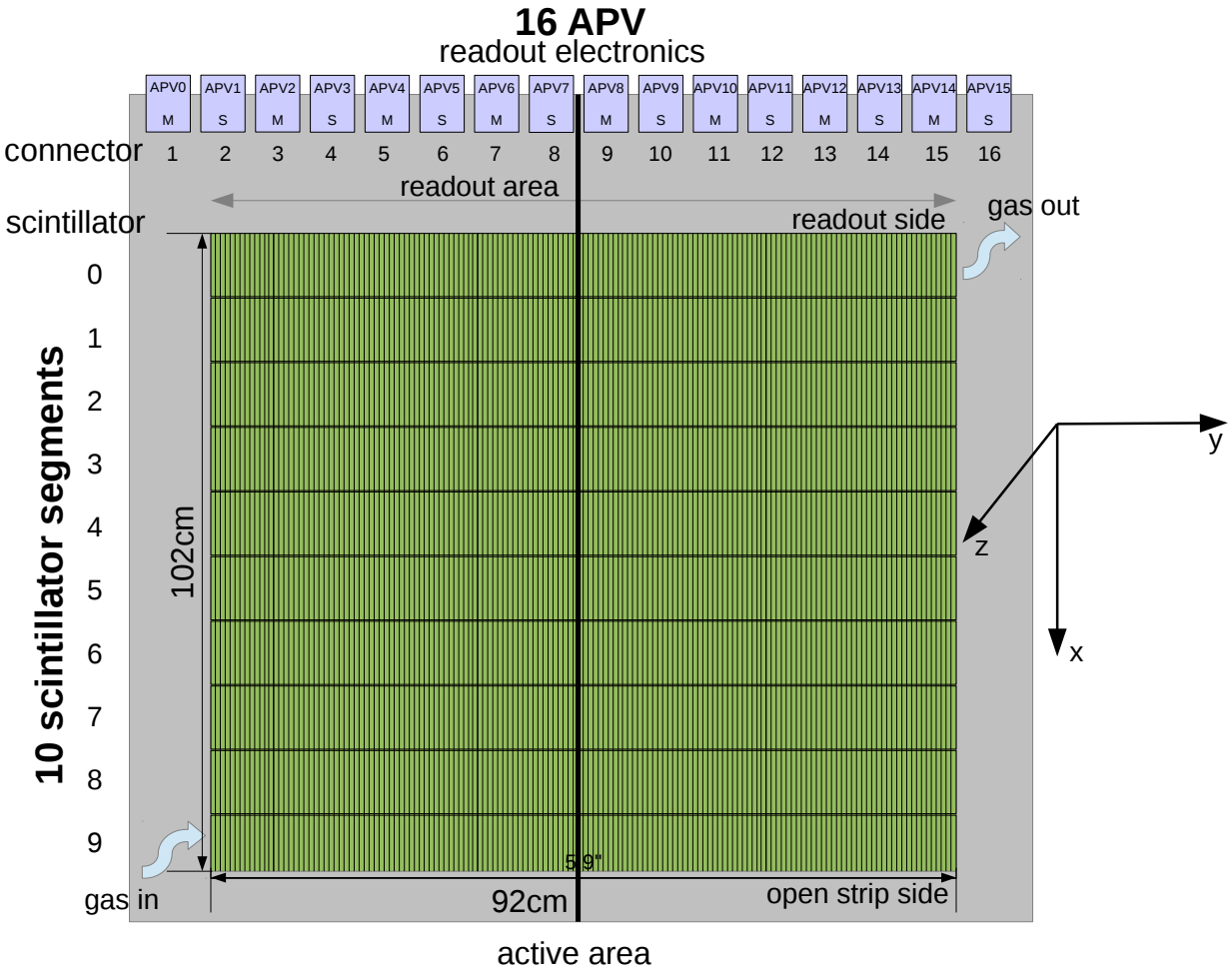

Figure 6.5: Schematic drawing of the Micromegas prototype detector consisting of two readout PCBs and read out by 16 APV25 front-end boards. The active area is subdivided by the APVs and the 10 scintillator segments along the strips into 160 partitions.

between the measured hit position in the Micromegas and the position predicted by the reference chambers. The measured hit position is determined by the centroid method (see sec. 2.4.2). If a muon traverses the Micromegas perpendicular to the detection plane as shown in figure 6.6, the mean of the residual distribution gives directly the shift in y.

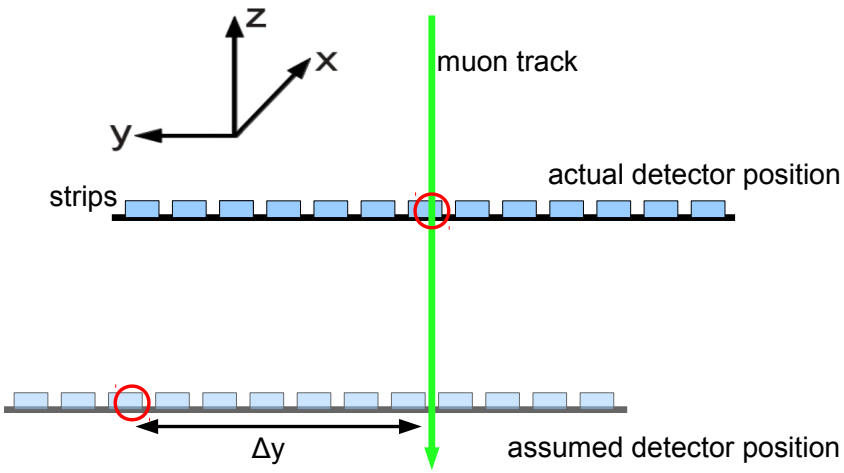

Figure 6.6: Sketch of a detector segment not aligned in y and z. With the perpendicular muon track the detector can be aligned in y direction using the residual Δy. x is the coordinate along the strips.

After the detector is aligned in y direction inclined tracks can be used to align the Micromegas in z. Figure 6.7 shows a sketch of a detector segment, which is aligned in y, but not in z. The residual Δy as function of the track inclination α can be used for the alignment in z, where $\alpha = \arctan m_y$ and m_y is the slope of the reference track in y. The detector shift Δz in z can be calculated with equation 6.1.

$$\Delta z = \frac{\Delta y}{\tan \alpha} = \frac{\Delta y}{m_y} \tag{6.1}$$

Figure 6.8 shows the mean of the residual distribution as a function of the track slope for one detector partition. With this plot the correction of the position of each detector partition in y as well as in z can be determined. A linear fit is used to calculate intercept and slope, where the sign inverted intercept is the shift in y and the slope the shift in z.

After applying this procedure on all detector partitions the translations are corrected. With z and y as a function of the partitions in x and y all three possible rotations can be calculated and corrected. Therefore the detector is now perfectly aligned using the reference tracks.

With this calibration the rotation of the stereo strips for the SM2 modules can be verified as well. The result must be a rotation around z by +1.5° and -1.5°

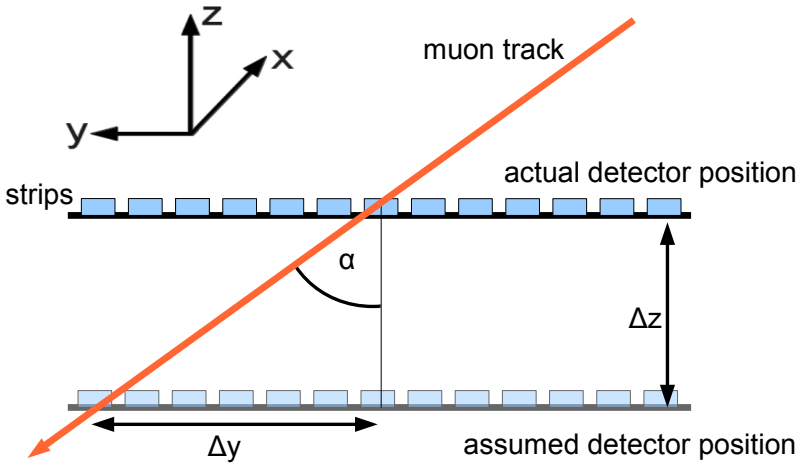

Figure 6.7: Sketch of a detector segment not aligned in z, but well aligned in y. With the inclined muon track the detector can be aligned in z direction using the residual Δy as a function of the angle of incidence.

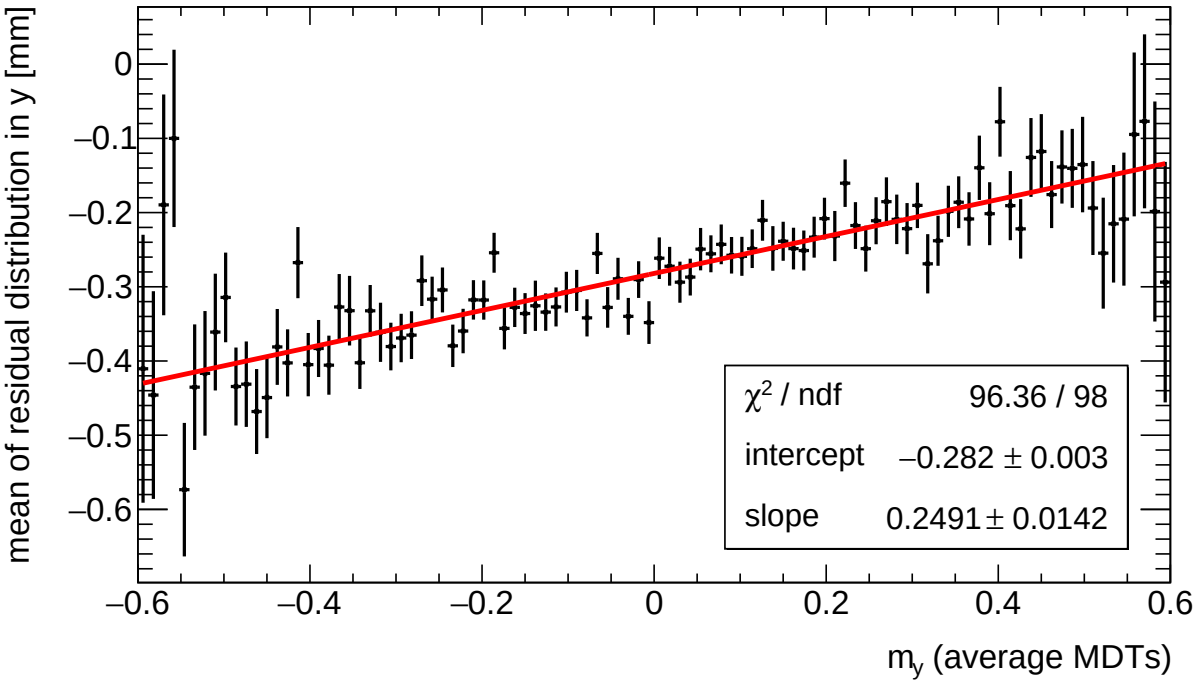

Figure 6.8: Mean of the residual distribution as a function of the track slope for one detector partition fitted linearly. The sign inverted intercept gives the shift in y and the slope the shift in z. In this case the position of the detector partition has to be corrected in y by 0.282 mm and in z by 0.2491 mm.

6.4 Calibration of the Prototype Micromegas

All deviation from zero still visible in y and z after alignment (see fig. 6.9) are mechanical properties of the prototype Micromegas. Two effects can clearly be seen, the shift between the two readout PCBs and the deformation of the drift region. But this can be calibrated and corrected for. The measurement for the following results of the calibration of the prototype Micromegas took about one week and was performed with a drift voltage of 300 V and an amplification voltage of 570 V.

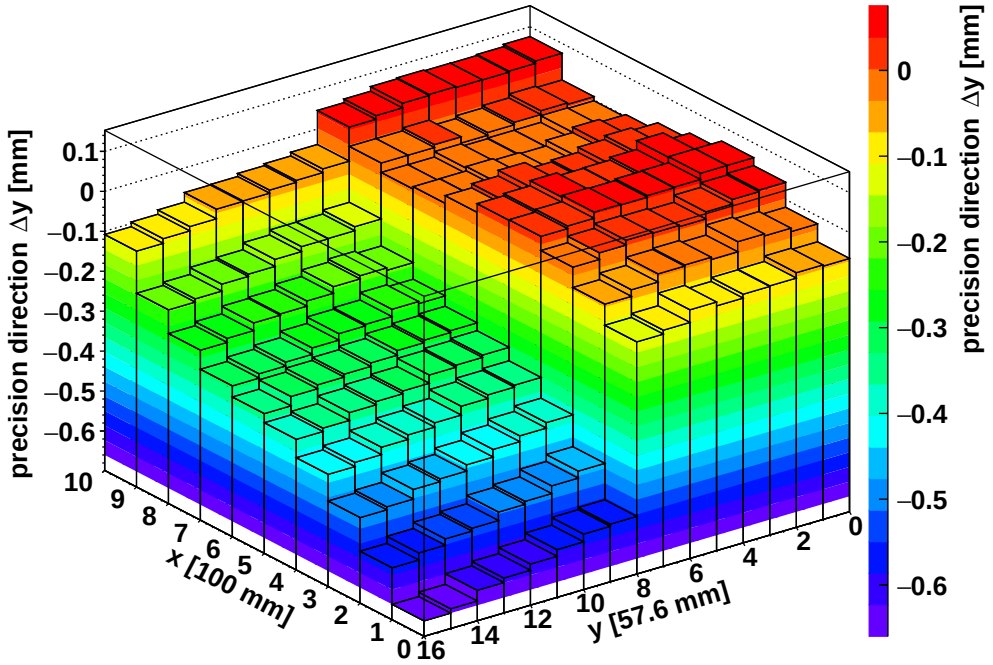

Figure 6.9: Measured strip position for each partition of the prototype Micromegas with one readout PCB aligned. The alignment parameters of the first PCB are applied on the second PCB as well. Therefore the mis-alignment between the two PCBs can be seen. The mis-alignment occurs, because no alignment tool was used during the gluing of the two readout PCBs. The shift between the readout PCBs is about 100 µm and the rotation about 350 µm m^{-1}.

6.4.1 Shift and Rotation between Readout Boards

As well as for the calibration of the deformation of the drift region (see sec. 6.4.2) the alignment parameters for all 160 partitions are used to calibrate the readout plane. Figure 6.9 shows the strip position as a function of x and y. For this plot the same calibration parameters were applied on the alignment of both readout PCBs. The first one between $y = 0$ and $y = 8$ is well aligned. For the second the deviation from the expected position can be determined. This calibration procedure shows a shift of the PCBs of about 100 µm

at $x = 10$ and of 450 µm at $x = 0$. Figure 6.10 shows a schematic drawing of the two readout PCBs to illustrate this calibration result.

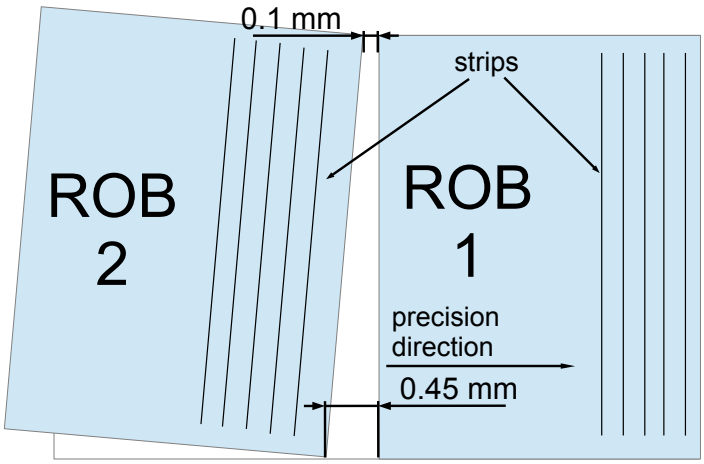

Figure 6.10: Schematic drawing of the mis-alignment between the two readout PCBs. A shift of 100 µm at the top side and of 450 µm at the bottom side illustrates the mis-alignment.

After the alignment of both readout PCBs the detector plane is calibrated. Figure 6.11 (left) shows the measured detector plane after calibration. Deviations from a plane within ±60 µm can still be seen. The deviation in y along the y direction occurs due to a slightly different strip pitch. For the first readout PCB the difference to the assumed strip pitch of 450 µm is 0.02 µm and for the second readout PCB it is 0.06 µm. After this correction the deviation in y along the x direction still remains (see fig. 6.11 (right)). This could be due to not entirely straight readout strips, but it was not possible to calibrate this using linear functions. It could be, that the deviation from the strip straightness is not homogeneous for one readout partition, i.e. one APV25 front-end board to which the strips are connected. Figure 6.12 shows the deviation from the readout plane for each partition of the alignment and calibration procedure. The mean is 0 with an RMS of about 34 µm. This effect can lead to a worsened spatial resolution for the whole detector.

The spatial resolution for the whole active area of the prototype Micromegas should improve after calibration. The sigma of a Gaussian function fitted to the residual distribution is used as measure of the spatial resolution. In this case a double Gaussian function is fitted to the residual distribution. Figure 6.13 shows the fit on the example for tracks perpendicular to the detector plane. This fit is performed for all reference angles. The sigmas of the narrow Gaussian function σ_{narrow} as a function of the reference angle are shown in figure 6.14. In black the result before calibration is shown and in red the result for the calibrated readout plane. The calibration improves the result by about 100 µm for perpendicular tracks. This measure for the spatial resolution is limited by remaining deviations from an ideal readout plane and by multiple scattering of the cosmic muons. The track prediction accuracy is not yet considered.

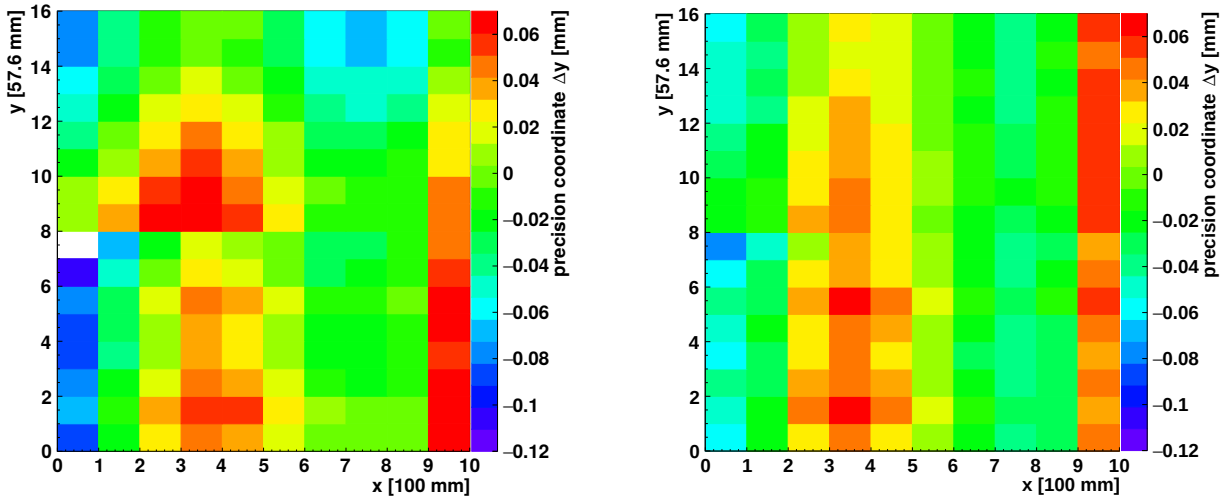

Figure 6.11: Measured deviation from the expected strip position in y after calibration of the two readout boards. Left: Before correction of the pitch deviation. A linear deviation along y is observed due to a small deviation of the strip pitch. Right: After correction of the pitch deviation from the assumed strip pitch of 0.02 µm for the first readout board and of 0.06 µm for the second readout board.

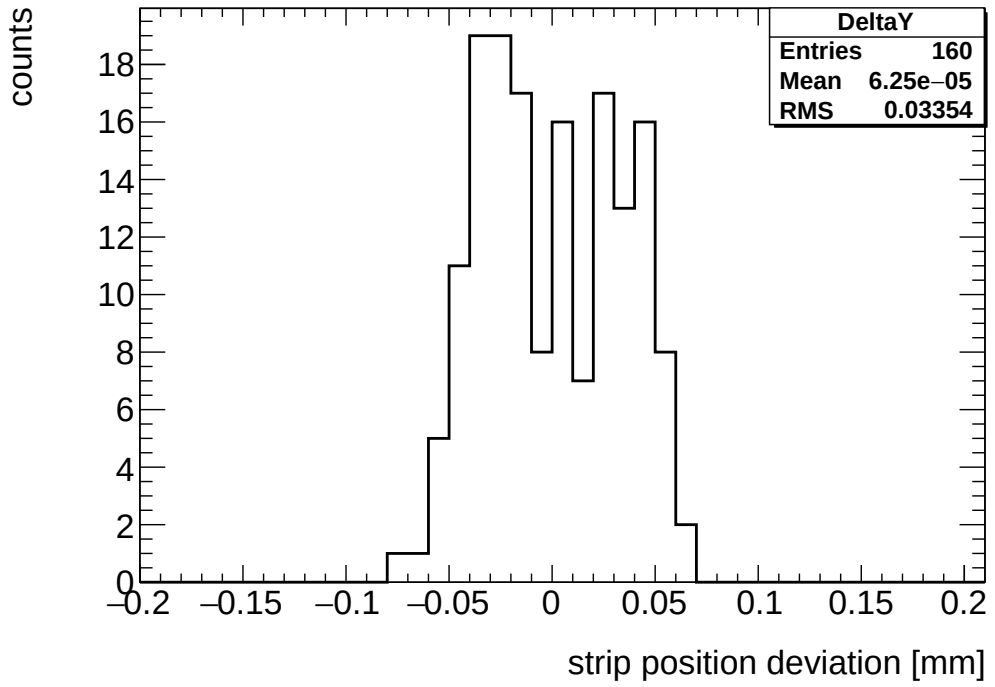

Figure 6.12: Measured deviation from the expected strip position in y after calibration of the two readout boards and the correction of the pitch variation. The distribution has an almost negligible RMS of about 34 µm.

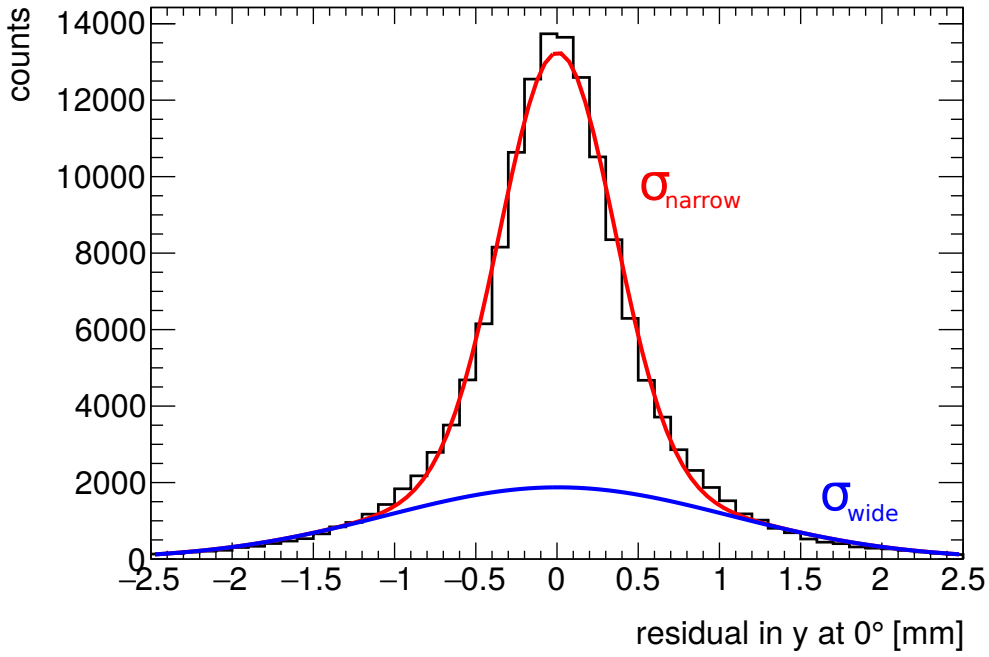

Figure 6.13: Example of a residual distribution fitted with a double Gaussian function. The function fits well the data points.

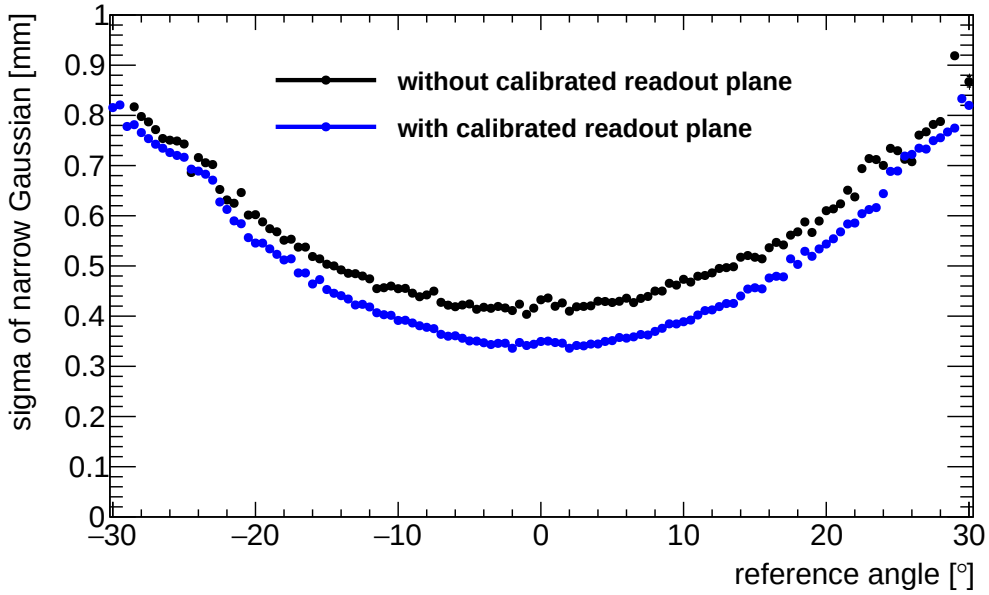

Figure 6.14: Sigma of the narrow Gaussian function (σ_{narrow}) as a function of the reference angle. In black the sigmas before calibration of the readout plane are shown. The sigmas after calibrating the readout plane are shown in blue. These distributions are still limited by multiple scattering and marginally by the strip position deviation shown in figure 6.11.

6.4.2 Deformation of the Drift Region Due to Overpressure

Due to the gas flux through the Micromegas a ram pressure occurs in the detector. This slight overpressure of about 5 mbar in the prototype Micromegas leads to a deformation of the drift region. Figure 6.15 shows the measured deformation of the detector plane for the 160 partitions of the alignment. This is the result after the alignment of the detector and is only visible due to the much stiffer base plate of the Micromegas. If both stiffening panels, anode and cathode, would have the same rigidness, the deformation could not be seen. The centroid method (see sec. 2.4.2) determines the hit position in the virtual plane in the middle of the drift region of the Micromegas. A deformation of the detection plane of about 0.7 mm is observed. The z measurement has an accuracy of about 15 µm.

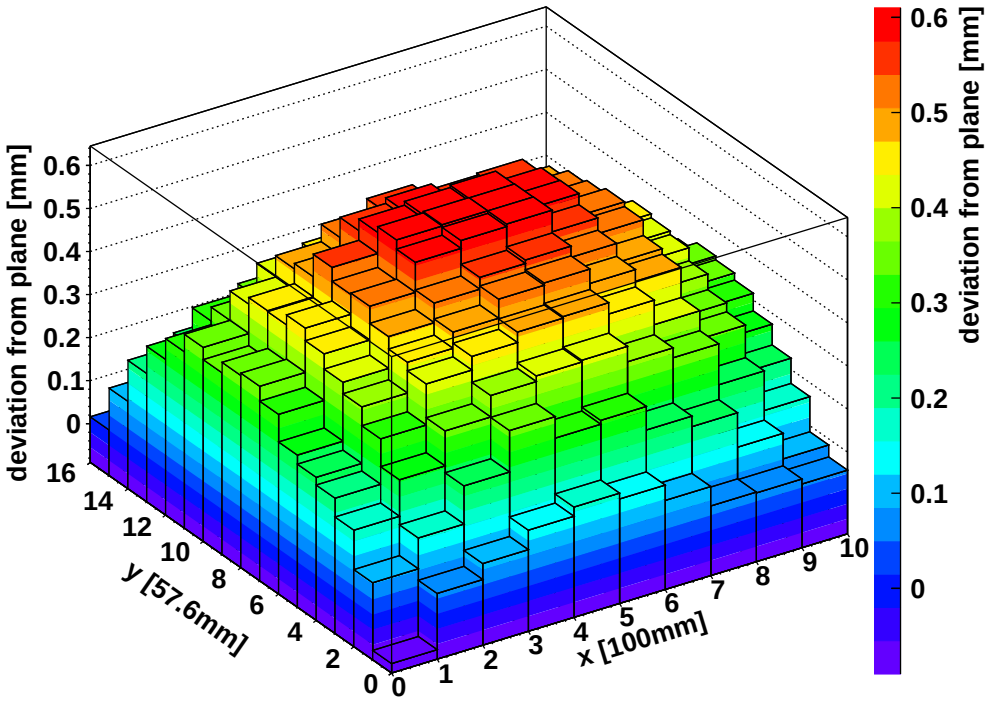

Figure 6.15: Measured deformation of the drift region of the prototype Micromegas of about 0.7 mm. Due to the centroid method (see sec. 2.4.2) this effect is measured in the middle of the drift region.

To confirm the measurement the deformation of the drift region was simulated with the finite element method software ANSYS [ANSYS, Inc., 2017]. The result is shown in figure 6.16 (left). It shows a maximum deformation of the upper panel of about 2.17 mm. Whereas the deformation of the reinforced readout panel due to the overpressure is only 0.82 mm (see fig. 6.16 (right)). Therefore the expected total deformation of the drift region in the center of the detector is about 2.99 mm. Due to the reconstruction of the virtual plane in the middle of the drift region the difference of upper and lower deformation divided by 2 can be measured, which is $(2.17\,\text{mm} - 0.82\,\text{mm})/2 = 0.675\,\text{mm}$. This is in good agreement with the measured value of about 0.7 mm. Interconnections in the NSW Micromegas will

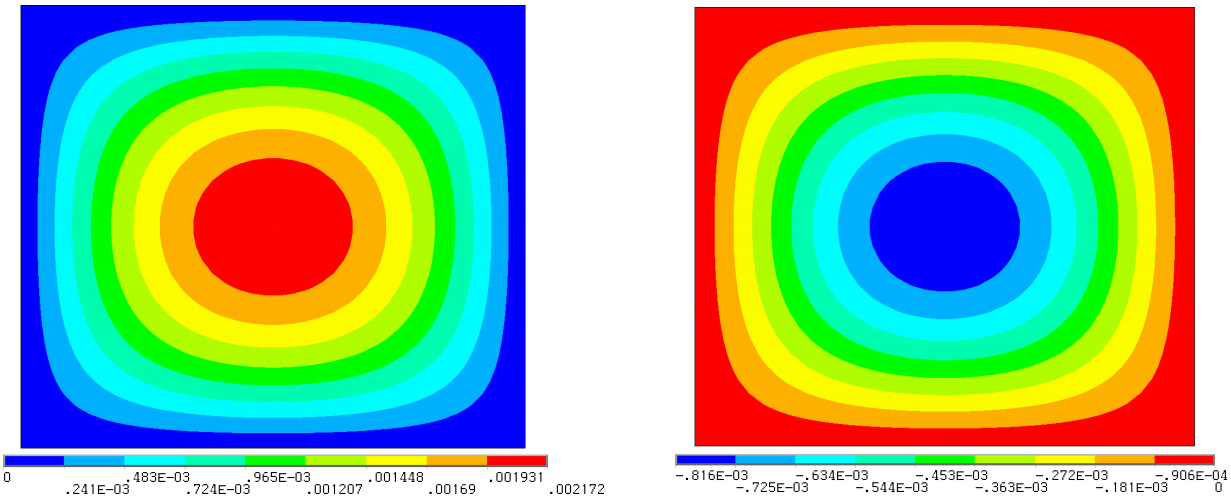

Figure 6.16: Simulation of the deformation of the drift region with ANSYS [ANSYS, Inc., 2017]. Left: For the upper panel the maximum simulated deformation is about 2.17 mm. Right: For the reinforced readout panel the maximum simulated deformation is about 0.82 mm. Figures taken from [Herrmann, 2016].

prevent this effect. Moreover, the overpressure in the NSW Micromegas during operation in the ATLAS detector is about a factor of 2 lower, between 2 and 3 mbar.

Figure 6.17 shows a simulation of the drift time t_{drift} as a function of the drift path d_{drift}, which is equivalent to the deformation of the drift region. For all simulated drift times the same drift voltage $U_{\text{drift}} = 300\,\text{V}$ was used varying the size of drift region. The red line corresponds to a fit with a second degree polynomial function, according to expectation (see eq. 2.4 and 6.2 and fig. 2.3). This shows a drift time of about 195 ns for a drift path of 8 mm.

$$t_{\text{drift}} = \frac{d_{\text{drift}}}{v_{\text{drift}}} = \frac{d_{\text{drift}}}{\mu E_{\text{drift}}} = \frac{d_{\text{drift}}^2}{\mu U_{\text{drift}}} \ , \tag{6.2}$$

where v_{drift} is the electron drift velocity, μ the electron mobility and E_{drift} the electric drift field.

In Figure 6.18 the fastest and the slowest signal timing for a central part of the detector, where the largest deformation is located, is shown as a function of the track inclination. The red lines correspond to the estimated borders of the drift region, when the number of entries are below 20 % of the maximum of the distribution. The minimum is around 20 ns. This is constant over the whole detector area due to ionizations near the mesh. The upper border in this central part of the detector is around 220 ns. Therefore the drift time for the electrons created near the cathode is about 200 ns. This is in good agreement with the simulation for a 8 mm drift region and confirms the ram pressure induced deformation in the detector center of about 3 mm. Additionally figure 6.18 shows that the maximal drift time is depending on the track inclination. For example at a track inclination of 0.4 the fastest and slowest signal can be separated. Whereas for small track inclinations around

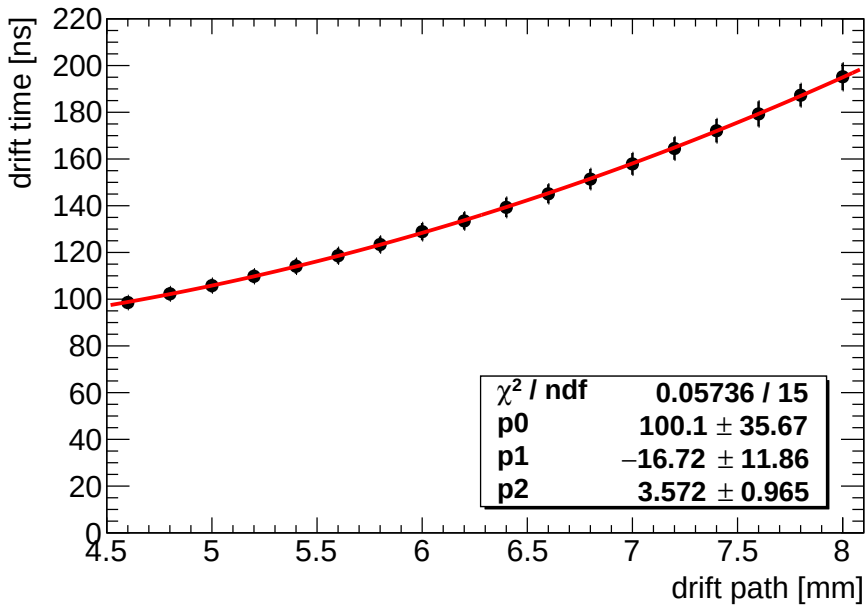

Figure 6.17: Simulation of the drift time as a function of the deformation of the drift region fitted with a second degree polynomial function. The drift voltage is for all drift times set to 300 V. Therefore the electric field varies, if the distance between mesh and cathode is varying. For 8 mm drift path the drift time is about 195 ns. Calculated with *Garfield* [Garfield website, 2010].

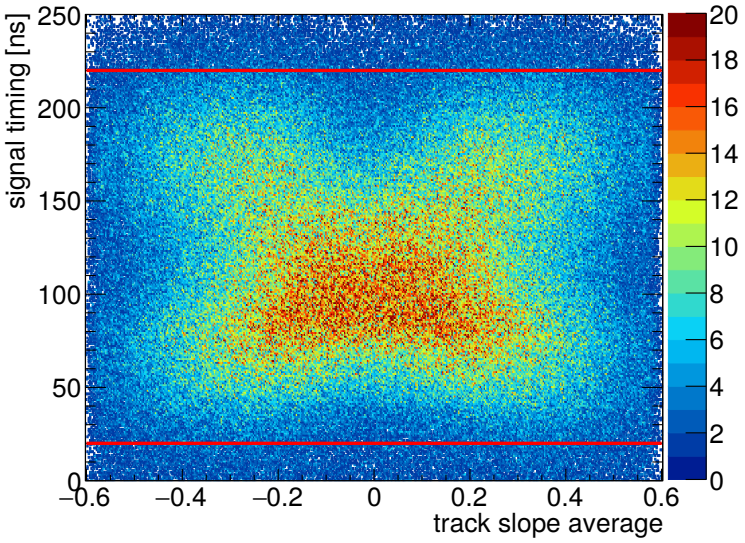

Figure 6.18: Measured signal timing for the fastest and slowest responding strip as a function of the track inclination for hit positions in the central part of the detector at maximum deformation. The red lines are the estimated borders of the drift region. Therefore the signal timing difference between fastest and slowest strips is about 200 ns.

0 the fastest signal is shifted towards the center of the drift region due to superposition of many ionizations, which cannot be distinguished within a responding strip. The same effect occurs for the slowest signal. Hence all signal timing are shifted towards the center of the drift region. But this is dominated by the faster signals due to the determination method of the timing as start of the signal. But due to a not homogeneous energy loss of the cosmic muons in the detector the fastest signals originate not directly above the mesh and are thus shifted to larger a signal timing. Every signal timing shown in this chapter is corrected for capacitive coupling between the strips (see sec. 7.1.2).

To correct for the non uniformity of the drift region the deformation is fitted with a two dimensional hyperbolic cosine function (see eq. 6.3). This function is used due to an assumed deformation similar to beam bending[5]. The intersection of this two dimensional hyperbolic cosine function and the muon track is then calculated using Newton's method to determine roots.

$$z = \cosh(x, y) = p_0 + p_1 \cdot \cosh(p_2 \cdot x + p_3) + p_4 \cdot \cosh(p_5 \cdot y + p_6) \tag{6.3}$$

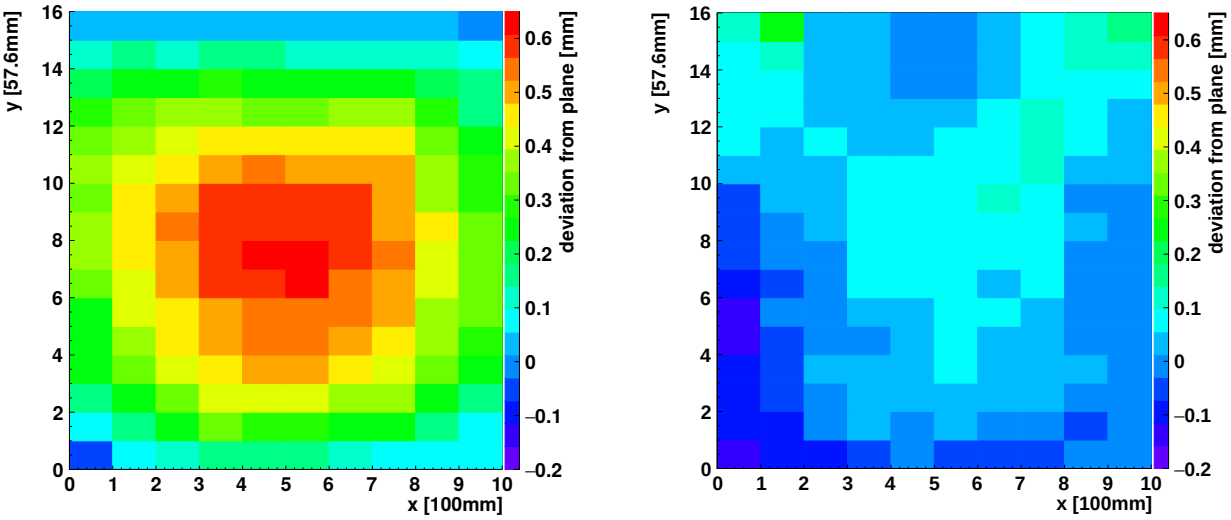

Figure 6.19: Measured deviation from the plane in z. Left: Without calibration the deviation from the plane is about 0.7 mm. Right: After calibration with the two-dimensional hyperbolic cosine function the deviation improves by a factor of 3, but the function for the correction does not fit perfectly.

Figure 6.19 (right) shows the deviation in z from the plane after correction with the two-dimensional hyperbolic cosine function. The deviation from the plane with this correction improves by a factor of 3 compared to the deformation before the calibration (see fig. 6.19

[5] Beam bending: $\frac{d^2}{dx^2}(EI\frac{d^2w}{dx^2}) = q$, where $w(x)$ describes the deflection of the beam in z direction at position x, q is the distributed load, E is the elastic modulus and I is the second moment of the area of the beam cross section [Gere, 2004].

(left)). A direct comparison is shown in figure 6.20. The corrected distribution is now centered around zero, but it is not yet perfect.

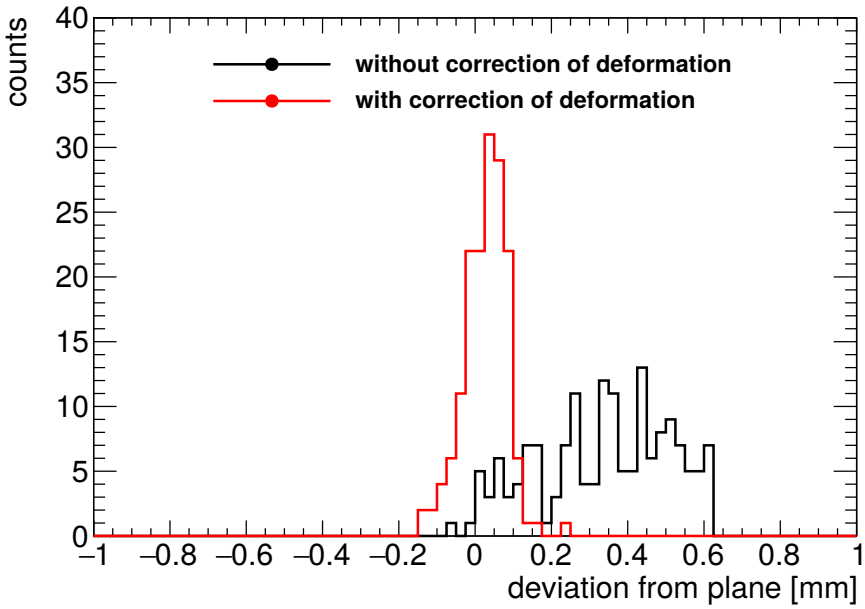

Figure 6.20: Measured deviation from the plane with and without correction of the deformation of the drift region. The deviation improves by a factor of 3 with the two dimensional hyperbolic cosine correction.

Using the results of the calibration the signal timing is plotted as a function of the deformation of the drift region given by the two dimensional hyperbolic cosine function. Figure 6.21 shows the mean timing of the slowest signal and the mean timing of the fastest responding strip. For the slowest signal the quadratic dependency can be seen. Whereas the timing of the fastest signal is almost constant. Both values are shifted towards the center of the drift region due to the track inclination dependency shown in figure 6.22. Additionally these two curves are shown, when only responding strips are considered, if the track inclination is larger than 28°. Therefore the timing of the fastest responding strip is shifted by about 15 ns towards the mesh. The slowest signal shows as well a steeper rise as a function of the deformation of the drift region. The values for all track inclinations are shown is black lines in figure 6.22. This fits well to the average of fastest signals as well as to the average of the slowest signals. Furthermore the red lines represent the averaged signal timing, if only signal timing are considered, when the track inclination is above 28°. Here it can be seen, that the average timing moves towards the borders of the drift region as shown is figure 6.21.

The deformation of the drift region has two effects on the TPC-like method. At first the drift velocity is not uniform in the Micromegas and has to be corrected for. And furthermore due to the non uniformity of the drift velocity the signal timing t_{mid} equivalent to the middle of the drift region is also not uniform. This will be discussed in section 7.3.

With the known z position for each track, the drift velocity can be calculated event-wise

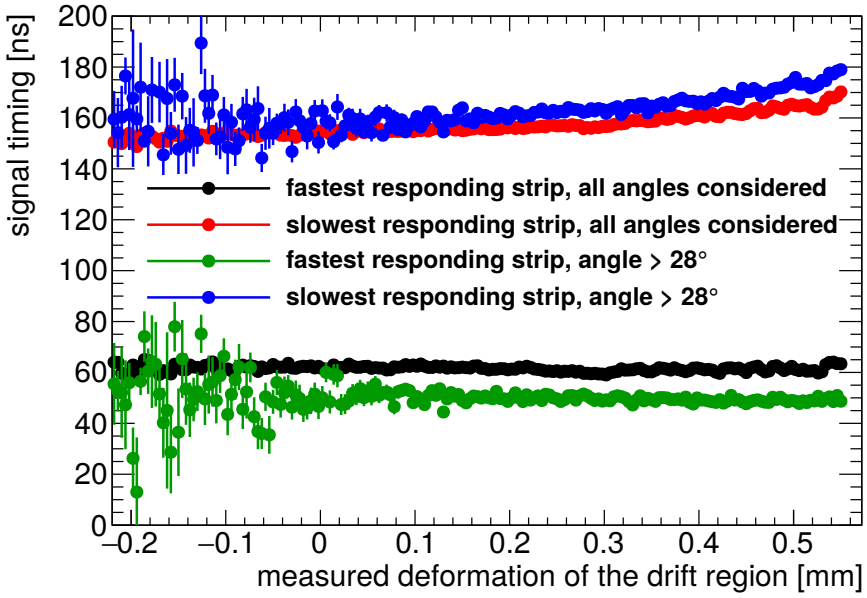

Figure 6.21: Measured signal timing as a function of the deformation of the drift region given by the two dimensional hyperbolic cosine function for the slowest and the fastest responding strip. For the fastest signals the signal timing is almost constant The slowest signal shows a quadratic dependency on the deformation. To show the shift towards each other the same plots are shown when only tracks with a reference angle above 28° are considered. The larger the reference angle the closer the signal timing moves towards the borders of the drift region.

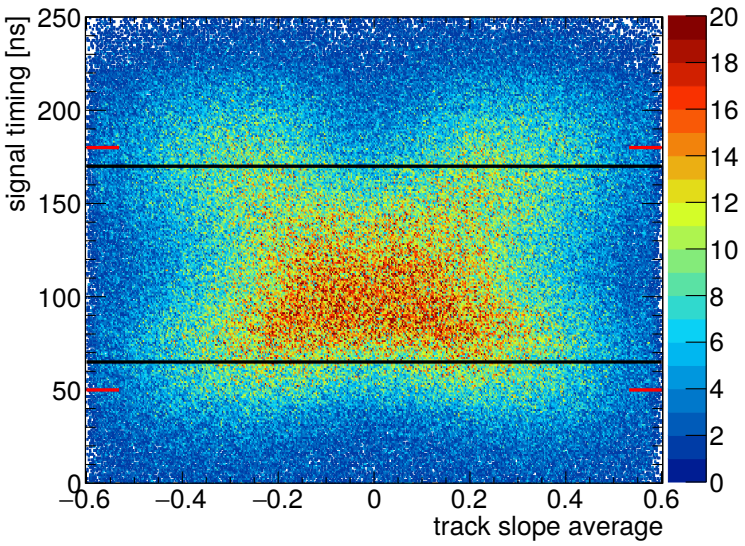

Figure 6.22: Measured signal timing for the fastest and slowest responding strip as a function of the track inclination for hit positions in the central part of the detector at maximum deformation. The red lines are the estimated borders of the drift region. Therefore the signal timing difference between fastest and slowest strips is about 200 ns.

and used for the reconstruction of the track angle. Figure 6.23 shows the reconstructed angle as a function of the reference track angle for a constant drift velocity without calibration and for the event-wise calculated drift velocity using the calibration. Without the calibration the mean reconstructed angle is shifted considerably below the angle bisector. With the calibration the reconstructed angle is for small reference angles larger than the reference angle. This is a systematic and expected behavior for the TPC-like method. For larger angles it converges almost to the angle bisector. The reconstruction of the track angle below 10° is known to not work at all, but above 15° it works quite well.

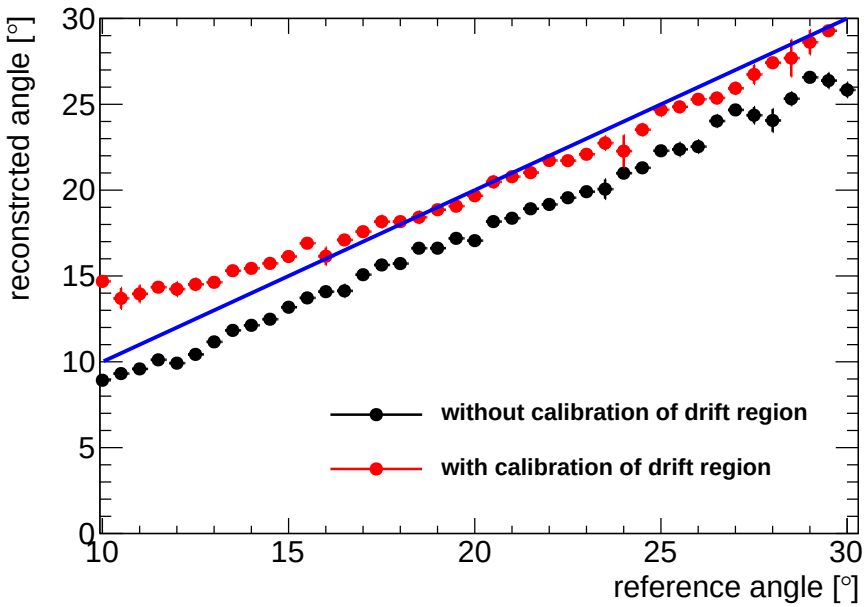

Figure 6.23: Reconstructed angle as a function of the reference track angle with (red) and without (black) calibration of the deformation of the drift region. With the calibration the reconstructed angle runs closely parallel to the angle bisector (blue).

6.5 Influence of Multiple Scattering on the Spatial Resolution

Using two reference trackers has two advantages. It is possible to perform a cut on the difference of the track slope of the two reference tracks. A smaller difference between the two track slopes means a smaller scattering angle of the cosmic muons. Various cuts on the difference of the track slopes were performed with the hardest at $\Delta m_y < 0.001$. Furthermore it is possible to determine the track prediction accuracy σ_{track} using the difference of the two track positions in the Micromegas plane. This distribution is fitted with a double Gaussian function. The sigma of the Gaussian function has to be divided by a factor of $\sqrt{2}$ due to the superposition of the two Gaussian functions of the track prediction of the two reference chambers, which have an identical spatial resolution. Figure 6.24 shows the

track prediction accuracy calculated with the two sigmas of the double Gaussian function weighted by the integral of the two function as a function of the track inclination. The peak around 0° due to increased multiple scattering vanishes with the harder cut on multiple scattering of $\Delta m_y < 0.001$.

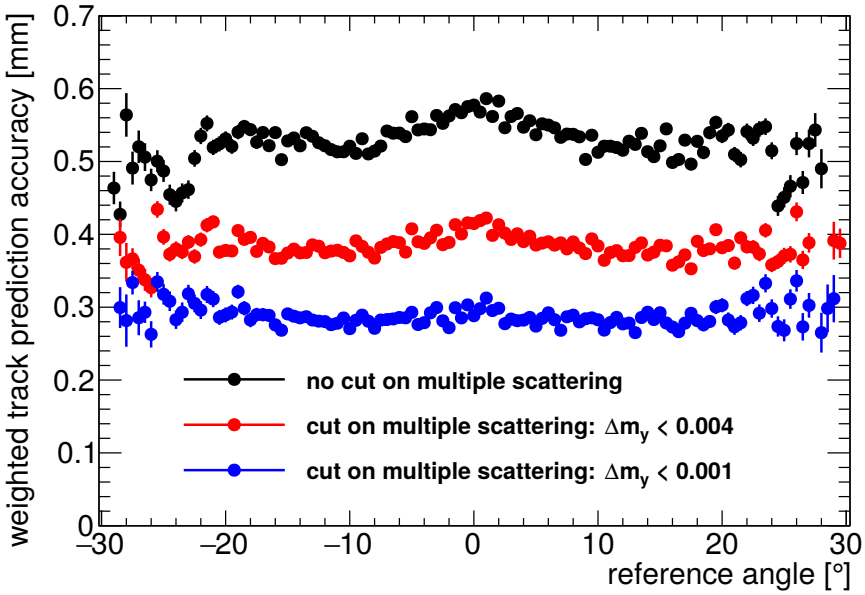

Figure 6.24: Track prediction accuracy as a function of the reference angle for various cuts on multiple scattering calculated with both sigmas of the double Gaussian function weighted by the integral of each Gaussian function. With a cut on the multiple scattering of $\Delta m_y < 0.001$ the track prediction accuracy improves to a value of about 290 µm.

Figure 6.25 shows the track prediction accuracy determined using the narrow Gaussian function only as a function of the reference angle for various cuts on multiple scattering. It can be seen, that the track prediction accuracy is almost constant between −15° and 15° at about 300 µm and rises to a value of about 400 µm for 30° without cut on multiple scattering. This is due to reconstruction ambiguities for angles around 30°. If a muon traverses the MDTs under an angle of around 30°, the MDTs cannot distinguish between the muons passing on the left or right side of the wire (see fig 6.26). Therefore the track prediction accuracy gets worse for larger angles. There is not a global shift of the track prediction accuracy with the cuts on multiple scattering, but the track prediction accuracy improves more for larger angles. This is due to the finite thickness of the tube walls of 0.4 mm. The spatial resolution of the MDT chambers is better, the nearer to the tube wall the particle traverses the tube (see. app. C). There is a lot more material in the path, if the muon traverses the tube near to the tube wall than near to the wire. But the spatial resolution of the MDT chambers is near to the walls better than near to the wires, where the multiple scattering is considerably lower. Hence with a tighter cut on the multiple scattering the spatial resolution degrades for large angles. Table 6.1 shows the track prediction accuracy at $\Theta = \pm 30°$ and on the plateau between −15° and 15° for

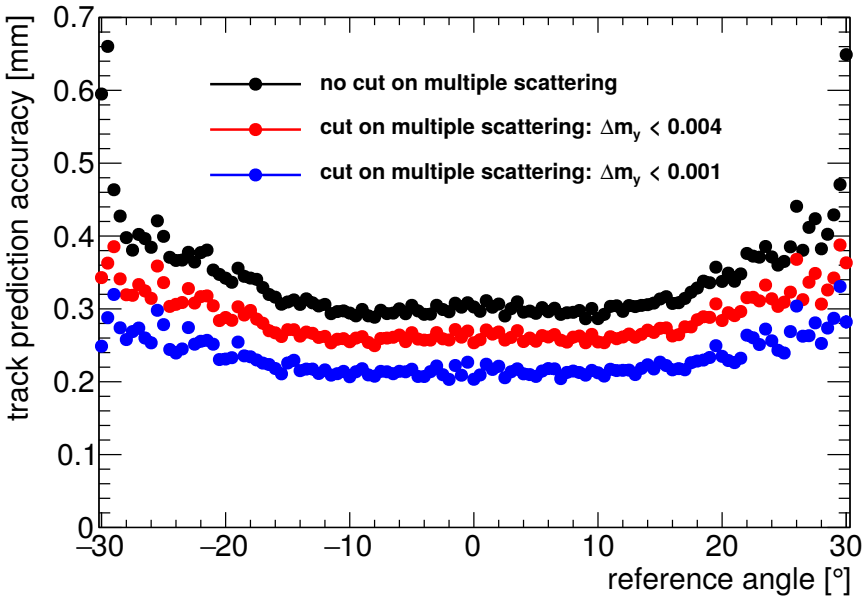

Figure 6.25: Track prediction accuracy as a function of the reference angle for various cuts on multiple scattering. Calculated with the narrow sigma only. With a cut on the multiple scattering of $\Delta m_y < 0.001$ the track prediction accuracy improves to a rather constant value of about 210 µm between $-15°$ and $15°$. For larger angles it reaches a value of about 290 µm.

various cuts on multiple scattering.

Table 6.1: Track prediction accuracy calculated using only the sigma of the narrow Gaussian function for the plateau between $-15°$ and $15°$ $\sigma_{track}(|\Theta| < 15°)$ and for $\pm 30°$ $\sigma_{track}(\Theta = \pm 30°)$ for various cuts on multiple scattering Δm_y.

Δm_y	$\sigma_{track}(\lvert\Theta\rvert < 15°)$ [mm]	$\sigma_{track}(\Theta = \pm 30°)$ [mm]
none	0.3	0.45
< 0.004	0.26	0.36
< 0.001	0.21	0.29

The result for the position reconstruction using the centroid method improves with the cut on multiple scattering as well. Figure 6.27 shows the sigma of the narrow Gaussian function determined using the centroid method as function of the track inclination. The blue dots represent the result of the calibration (see fig. 6.14). This improves by about 100 µm over the whole angular acceptance with the hardest cut on multiple scattering, shown as red dots.

To determine the spatial resolution of the prototype Mircomegas with cosmic muons not only the multiple scattering has to be considered but also the track prediction accuracy

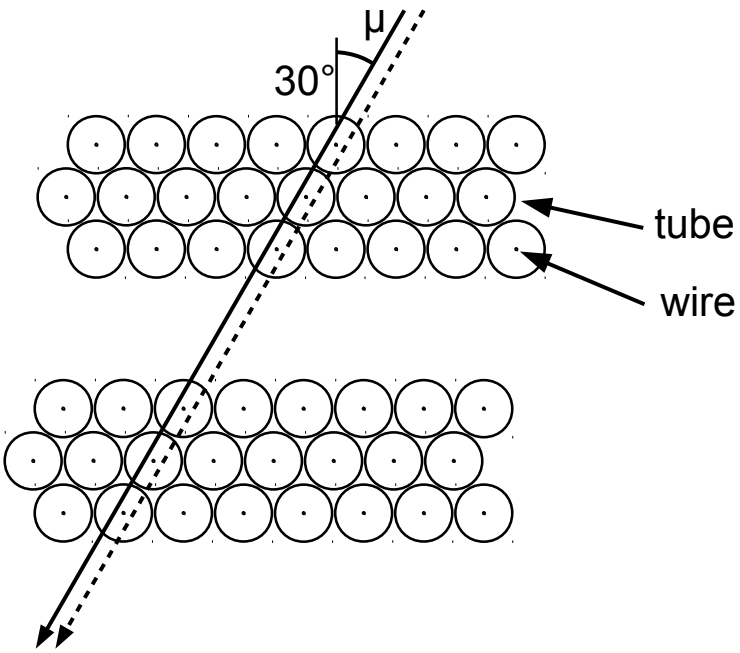

Figure 6.26: Sketch of a MDT chamber with two multilayers of three layers each. With a muon traversing under 30° the MDT can not distinguish between the solid and dashed line due to the hexagonal close packing of the drift tubes. Therefore reconstruction ambiguities occur.

σ_{track}. Therefore the spatial resolution σ_{sr} is defined as:

$$\sigma_{\text{sr}} = \sqrt{\sigma_{\text{L1}}^2 - \sigma_{\text{track}}^2}\,, \tag{6.4}$$

where σ_{L1} is the sigma of the residual distribution of the detector under test. Figure 6.28 shows again the track prediction accuracy for a cut on multiple scattering of $\Delta m_y < 0.001$ as well as the red centroid method curve with cut on multiple scattering from figure 6.27 and the resulting spatial resolution of the prototype Micromegas. The spatial resolution reaches a value of about 150 µm for perpendicular tracks and rises then almost linearly up to reference angles of 25°. For 30° track inclination the spatial resolution is about 600 µm.

Figure 6.29 shows the spatial resolution as function of the track inclination for various cuts on multiple scattering. For the two curves with cuts on multiple scattering the spatial resolutions show only a slight shift, but are almost equal. Without cut on multiple scattering the spatial resolution for perpendicular tracks is as well almost the same as with cuts. But for larger track inclinations the difference to the curves with cuts gets larger. A spatial resolution of 700 µm at 30° is achieved, which is 100µm worse than for the curves with cuts on multiple scattering. Additionally the spatial resolution determined in a testbeam campaign with 120 GeV pions (see sec. 7.2) is shown for the large prototype Micromegas (L1) and a small test Micromegas (T4) for comparison. The result of the testbeam for the

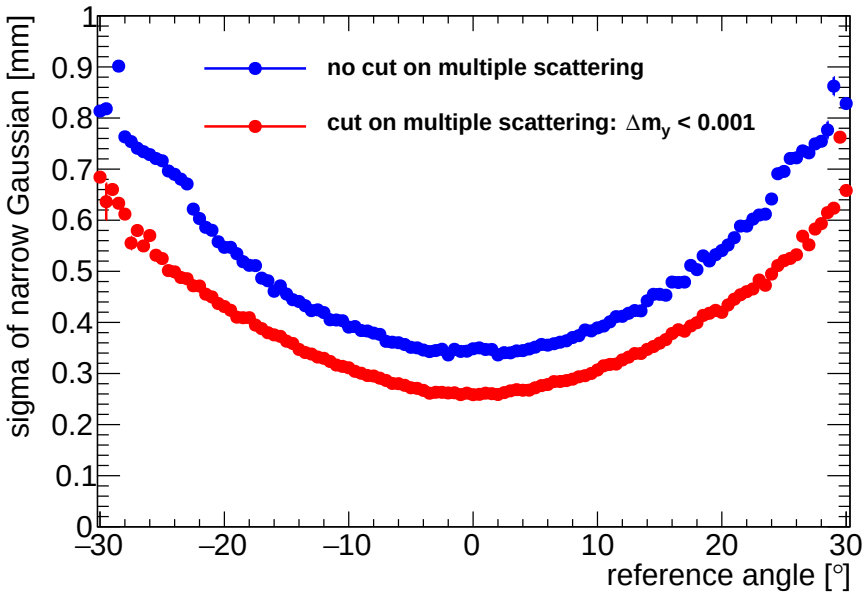

Figure 6.27: Sigma of the residual distribution as a function of the reference angle. The result with the calibration, but without a cut on multiple scattering from figure 6.14 is shown in blue. In red the result with a cut on the multiple scattering of $\Delta m_y < 0.001$ is shown. The cut on the multiple scattering improves the sigma by about 100 µm for perpendicular tracks.

L1 chamber is very similar to the result with cosmic muons with a spatial resolution of about 600 µm for 30°. Except for perpendicular tracks which yield a spatial resolution of about 80 µm, which is almost a factor of 2 better than for cosmic muons. It is expected not to have a round curve for small reference angles, but a more straight curve towards 0°. A measurement with a duration of about one day and the same parameters as the long measurement has shown an almost straight line from 0° towards larger and smaller angles (see fig. 6.30). This means there is a variation in time of the positions of the large prototype Micromegas and the reference detector, which seems to occur due to thermal expansion and movement. The contribution of the thermal movement is about 100 µm. The hall, in which this measurement took place, is air conditioned, but only with an accuracy of about 1-2 K. Thus according to the size of the experimental setup a contribution due to thermal expansion and movement in the order of 100 µm is reasonable. In this case no cuts on multiple scattering were applied due to low statistics. The spatial resolution for the short measurement in the CRF is very similar to the result of the testbeam campaign with the large prototype Micromegas, but not as good as the result for the small test Micromegas (T4). The energy loss of 120 GeV pions is about a factor of 2 higher than for cosmic muons and thus the ionization of 120 GeV pions is much more homogeneous than the ionization of cosmic muons. Therefore it is not surprising to get better results in testbeam campaigns. This is the case for the T4 chamber, which had a very low noise level during the testbeam campaign in contrast to the L1 chamber, which was very noisy during the testbeam cam-

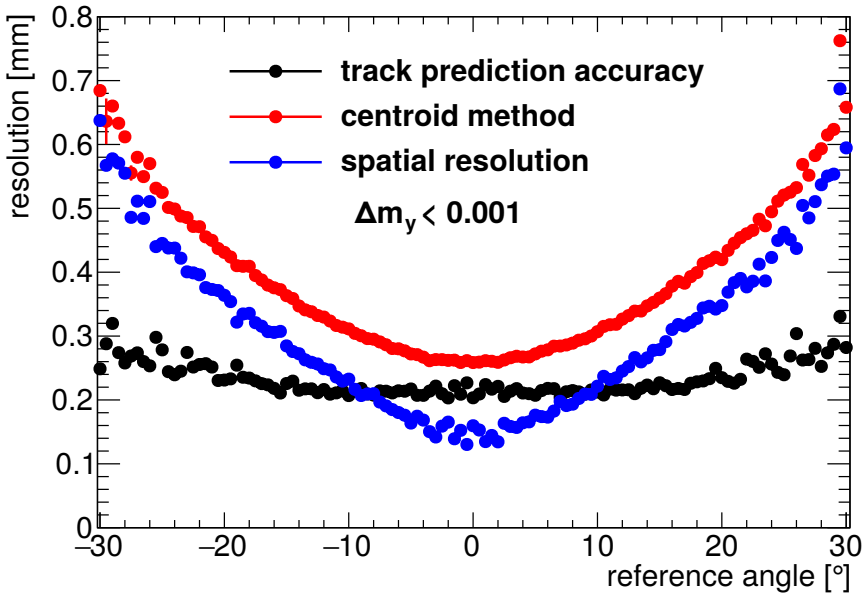

Figure 6.28: Spatial resolution of the prototype Micromegas as a function of the reference angle (blue) as well as the track prediction accuracy (black) and the curve for the sigma of the residual distribution (red), all for a cut on multiple scattering of $\Delta m_y < 0.001$. The spatial resolution has a minimum of about 150 µm for tracks perpendicular to the detector plane, rises linearly up to a reference track angle of about 25° and reaches its maximum of about 600 µm for track inclinations of 30°.

paign (see sec. 7.2.4). During the measurements in the CRF the noise level was a factor of 2 smaller. It is assumed that the effect occurring due to noise and the effect occurring due to the less homogeneous energy loss of the cosmic muons cancel each other. Hence the spatial resolution is similar in both measurements not considering the multiple scattering of the cosmic muons.

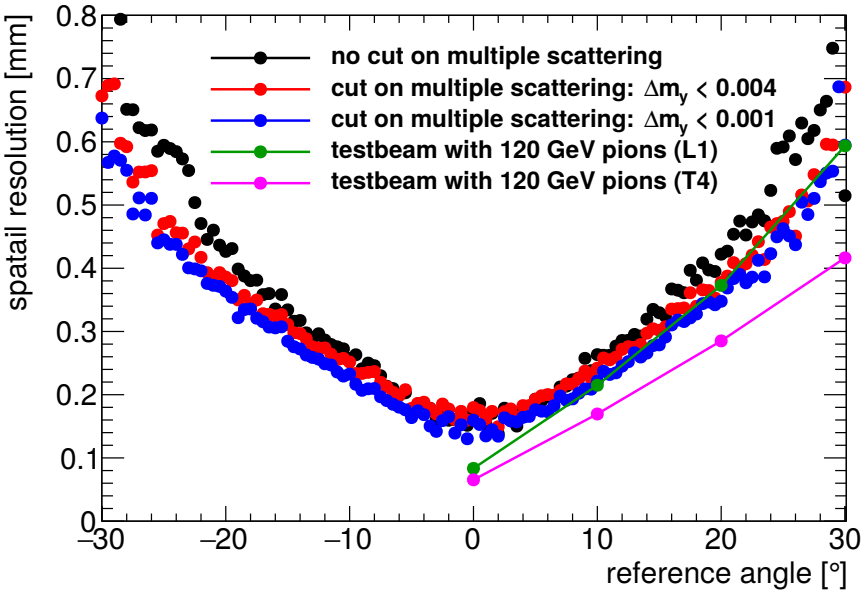

Figure 6.29: Spatial resolution of the prototype Micromegas as a function of the reference angle for various cuts on multiple scattering. The spatial resolution improves with cuts on multiple scattering for large angles, but only slightly for perpendicular tracks with a minimum of about 150 µm. Additionally the result of a testbeam campaign with 120 GeV pions is shown in green for the large prototype Micromegas (L1) and in magenta for a small test Micromegas (T4) (see sec. 7.2.4). The T4 chamber shows for all angles a better spatial resolution compared to the measurement with cosmic muons. This is probably because of the energy loss of the 120 GeV pions being a factor of 2 higher and thus the more homogeneous ionization in the active volume. But for the L1 chamber this is not observed due to a notably higher noise level during the testbeam campaign. The lines are only to guide the eye.

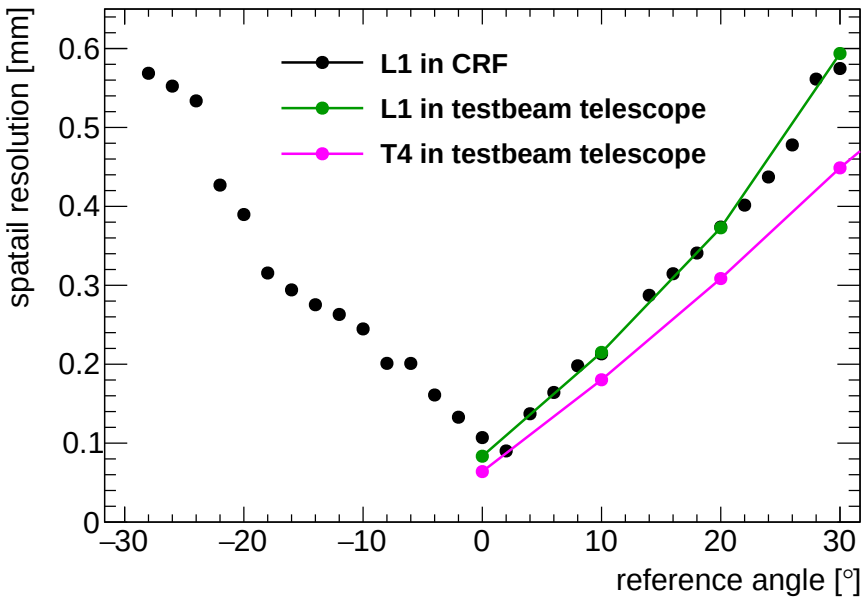

Figure 6.30: Spatial resolution of the prototype Micromegas as a function of the reference angle for a measurement of a duration of about one day in the CRF without cuts on multiple scattering (black). The spatial resolution is very similar to the spatial resolution determined for the testbeam campaign with 120 GeV pions (green). It seems there is a contribution of about 100 µm due to thermal expansion and movement of the experimental setup. Additionally the result for a small test Micromegas (magenta) is shown (see sec. 7.2.4). The lines are only to guide the eye.

6.6 Module Validation

Additionally to a successful calibration the SM2 modules have to fulfill a variety of criteria to be validated for the installation into the ATLAS detector. This is shown here at the example of the large Micromegas prototype detector. All these measurements were studied in the CRF as well. The validation criteria are still preliminary and under investigation to be optimized. These values will probably be adapted for ATLAS during the first few modules under investigation.

The first measurement is to localize noisy strips in the detector. Therefore 60000 random triggers were created to check if the detector shows peaks at an amplification voltage of 570 V. The prototype Micromegas is again read out using the Zero-Suppression (ZS) firmware of the FEC cards. Localized peaks are not allowed to contain more than 5 % of the events triggered on. Hence peaks under 3000 entries are accepted in figure 6.31. It shows the noise count as a function of the strip number. Two larger peaks around strips number 850 and 2000 can be seen, but the height of the peaks is well within the requirements.

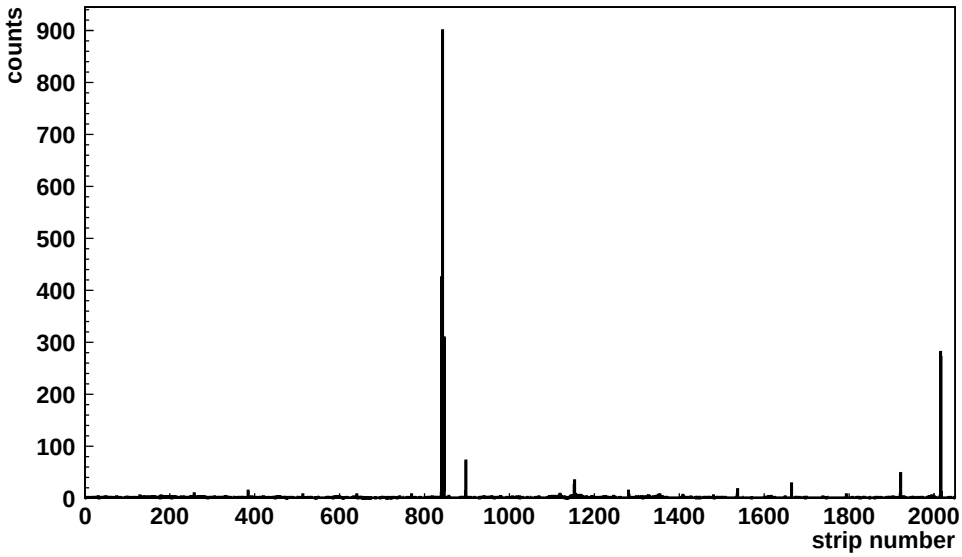

Figure 6.31: Noise count as a function of the strip number. The two peaks around strip number 850 and 2000 are well within the requirements.

Dead and noisy channels can also be determined in a high statistics measurement with cosmic muons. Therefore the counts on each strip, which exceed the ZS threshold, are plotted as a function of the strip number (see fig. 6.32) and the average number of counts is determined. Channels are declared as noisy if the count number on the channel exceeds 5 times the average. The acceptance criterion is less than 2 noisy channels per readout board. For the prototype Micromegas the first readout board has 3 noisy channels and the second has one noisy channel. This is the case due to soldering problems during the soldering of the Panasonic plugs on the test chamber. If the tin shortens two strips, they

are a lot more noisy and one of them could be dead. The level for dead channels is defined as counts on a channel below 10 % of the average. Again the acceptance criterion is less than two dead channels for each readout board. So the prototype Micromegas would pass this test with only three dead channels for the whole detector. But it seems the detector has eight more dead strips or at least not well working strips. Hence the criterion for dead channels is probably too low.

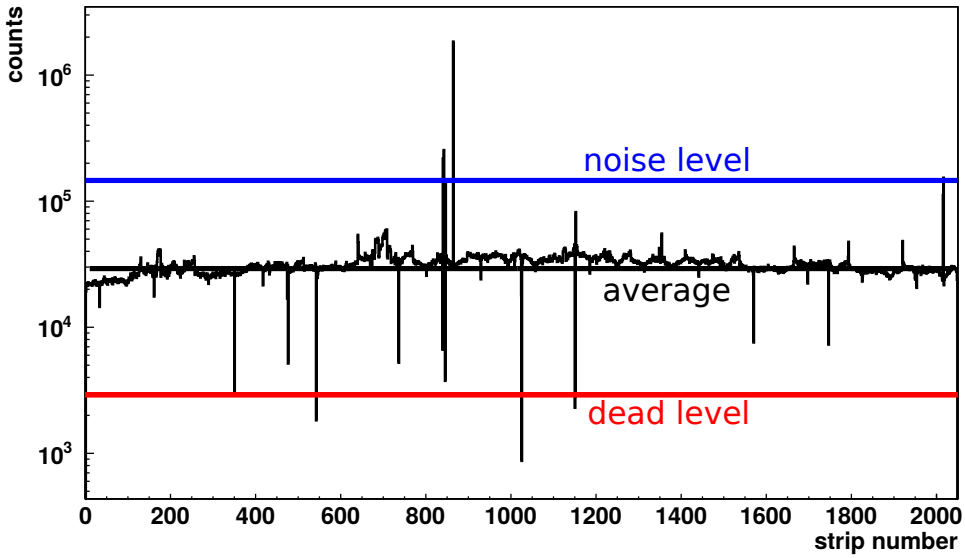

Figure 6.32: Count of the strips exceeding the ZS threshold as a function of the strip number measured with cosmic muons. The black line is the average over all strips, the red line at 10 % of the average is the level, where channels are declared as dead and the blue line at 5 times the average is the level, where channels are declared as noisy. The criterion for the dead channels is probably too low. It seems there are eight more dead strips or at least not well working strips.

Additionally the pulser test (see sec. 5.8) was performed on the prototype Micromegas. 20000 pulses were applied on the silver conduct high voltage distribution line and hence on each resistive strip and then capacitively coupled to the readout strips. The signals on each strip are averaged over the 20000 pulses and the maximum of this averaged pulse is determined as a function of time. Figure 6.33 shows the averaged pulse height as a function of the strip number. The dead or badly working readout channels in figure 6.32 can also be identified. But here even more strips do not properly respond. This has to be further investigated with the SM2 modules. The fluctuation of the pulse height occurs due to the APV25 specific pedestals for the readout channels as well as the periodic peaks.

The SM2 modules are supposed to have a homogeneous gas gain distribution over the whole active area. To assure this the pulse height distribution for each partition of the calibration is fitted with a Landau function. The most probable value for each partition is shown in figure 6.34. It seems quite homogeneous. This detector is read out by APV25 pairs, master and slave (see sec. 3.1). Figure 6.34 shows, that the pulse height of the slave

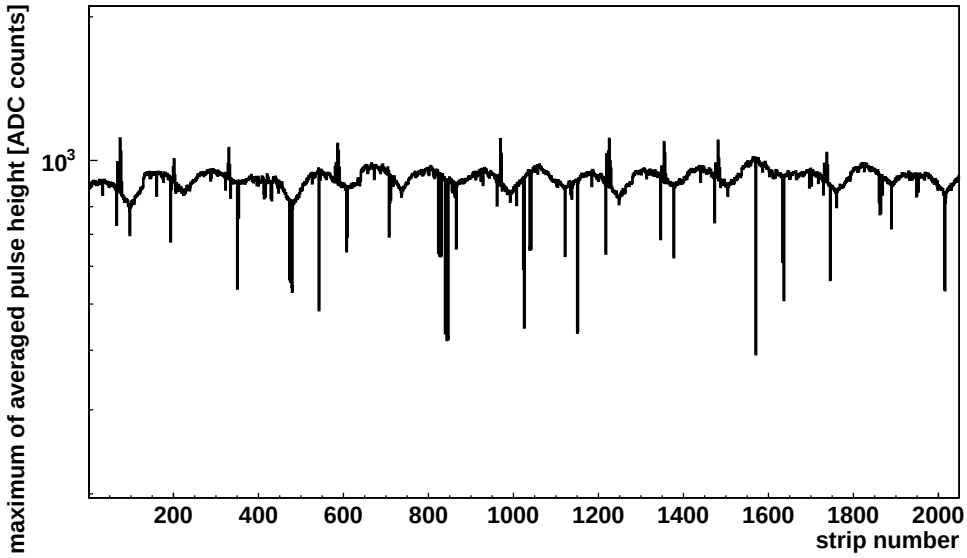

Figure 6.33: Averaged pulse height as a function of the strip number measured with the pulser test (see sec 5.8). The variation of the distribution occurs due to the systematically different pedestals of each readout channel as well as the peaks towards higher pulse height. Most of the strips with a lower pulse height correspond to dead or badly working strips in the high statistics measurement with cosmic muons (see fig. 6.32).

APV25 is systematically higher than for the master APV25. This is due to the wrongly chosen PLL phase of the APV25 (see sec. 3.1). The PLL phase has to be adjusted to the length of the HDMI cables between APV25 and FEC card. A scan of the PLL phase has shown a good value for the PLL phase is 3 for 1.5 m long HDMI cable with a 5 m extension. Figure 6.35 shows the homogeneity of the gas gain with PLL phase set to 3. It can be seen, that the gas gain of the lower readout board is slightly lower than for the upper one. Additionally a slight inhomogeneity due to the gas circulation can be seen. Due to only one gas inlet in the upper left corner and one gas outlet in the lower right corner the gas gain is homogeneous along the diagonal of the detector. The other two corners show a smaller pulse height. The pulse height towards the center of the Micromegas is higher due to the deformation of the drift region, hence the longer path of the muons in the active volume. Therefore the primary ionization increases. The SM2 validation criterion for the gas gain is a variation below 50 % with respect to the average value. This would be fulfilled for the prototype Micromegas with an RMS of 17 % for PLL phase 3.

With PLL phase 3 the efficiency for each detector partition was determined. The ATLAS requirement is to determine the 5 mm-tracking efficiency. This means the number of tracks with a residual smaller than 5 mm is divided by the number of tracks traversing the detector. The prototype Micromegas shows a homogeneous efficiency distribution with a mean value at (94.9 ± 0.9) % (see fig. 6.36). At the edges of the Micromegas the efficiency is lower due to muons only traversing partially the active volume of the detector. In this case the position is reconstructed wrongly. This effect is larger in x direction, because of the

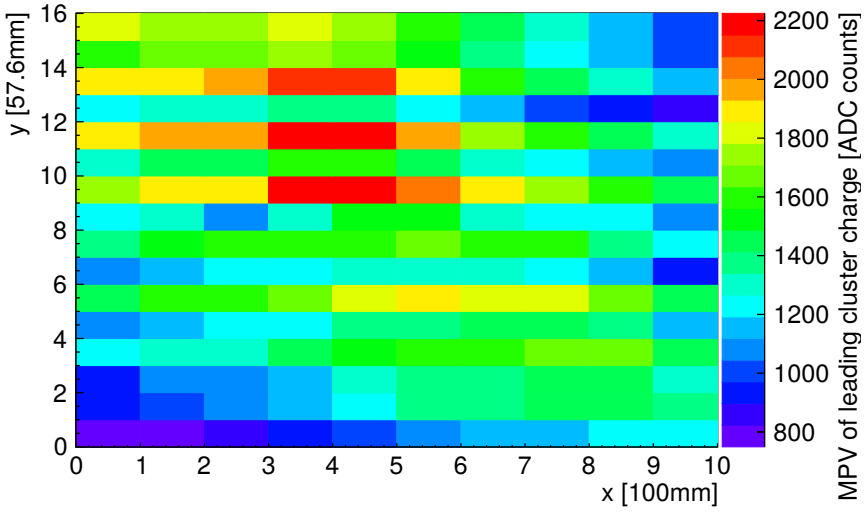

Figure 6.34: Most probable value of the pulse height distribution fitted with a Landau function for each partition of the calibration. The gas gain is rather homogeneous with a mean value of (1434 ± 309) ADC counts, but deviations between master and slave of the APV25 pairs can be seen. The pulse height of the slave APV25 is systematically higher due to the not optimal APV25 PLL phase of 0.

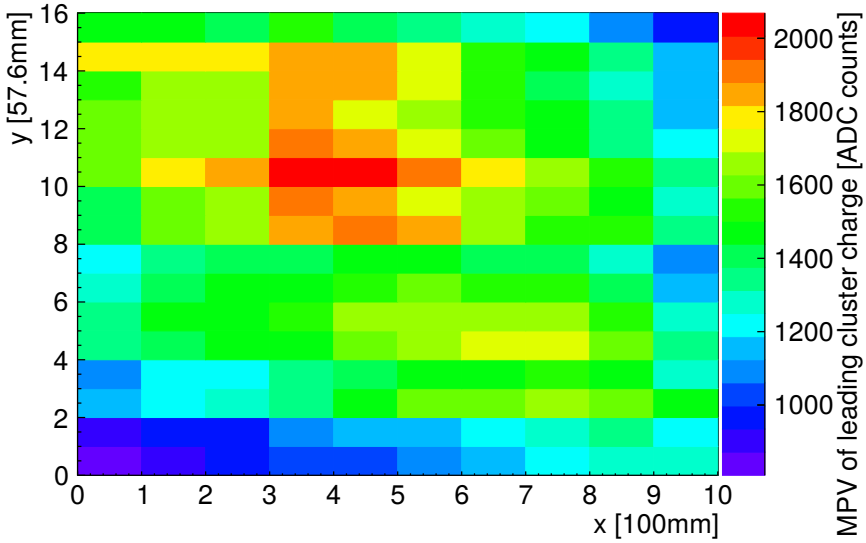

Figure 6.35: Most probable value of the pulse height distribution fitted with a Landau function for each partition of the calibration.The gas gain is rather homogeneous with a mean value of (1467 ± 247) ADC counts. This is an RMS of about 17 %. This was measured with an optimized APV25 PLL phase of 3. The lower readout board shows slightly lower gas gain than the upper. As well as the lower left and the upper right corner show lower gas gain. This is due to insufficient gas circulation. The prototype Micromegas has only one gas inlet on the upper left corner and one gas outlet on the lower right corner.

more difficult alignment in x. The criteria for the module validation is an efficiency above 95 % on more than 98 % of the active area. This would not be fulfilled for the prototype Micromegas. Due to multiple scattering the efficiency measurement is limited in the CRF. With the SM2 modules there are possibilities to determine the efficiency in other ways, for example to check if the other three layers of the quadruplet show good hits. This would increase the efficiency.

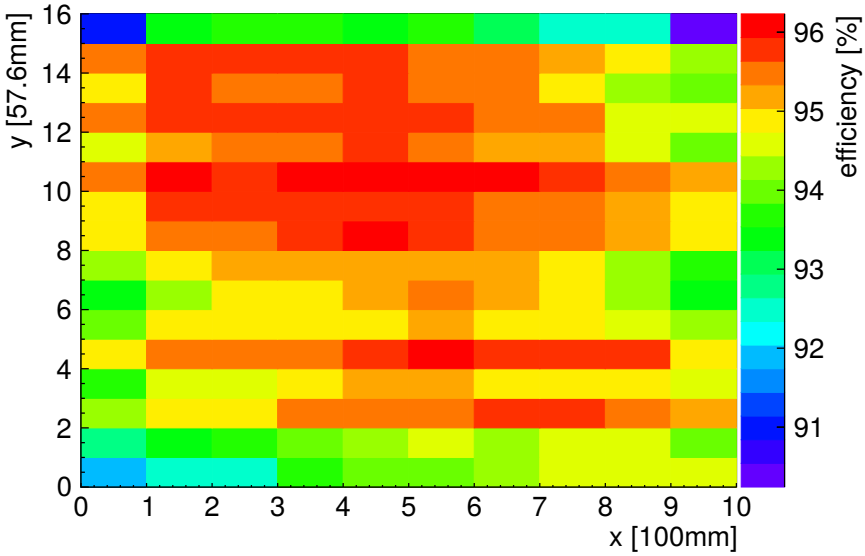

Figure 6.36: Tracking efficiency for each partition of the calibration. The tracking efficiency is determined by dividing the number of tracks with a residual below 5 mm by the number of tracks traversing the detector. This is homogeneous with an averaged efficiency of (94.9 ± 0.9) %. At the edges of the detector the efficiency is lower due to muons traversing the active volume only partially.

So far, all measurements were performed with an amplification voltage of 570 V and a drift voltage of 300 V. The last criterion for the validation of the modules is the tracking efficiency as a function of the amplification voltage for determining the working point (see fig. 6.37). The measurement for each data point took about 2 hours. The efficiency of the prototype Micromegas reaches a plateau at an amplification voltage of 560 V, hence the working point is between 560 V and 580 V with an efficiency of 95 %. The criterion for the module validation is a plateau above 98 %.

If all criteria are fulfilled the modules will be installed in the ATLAS NSW detector.

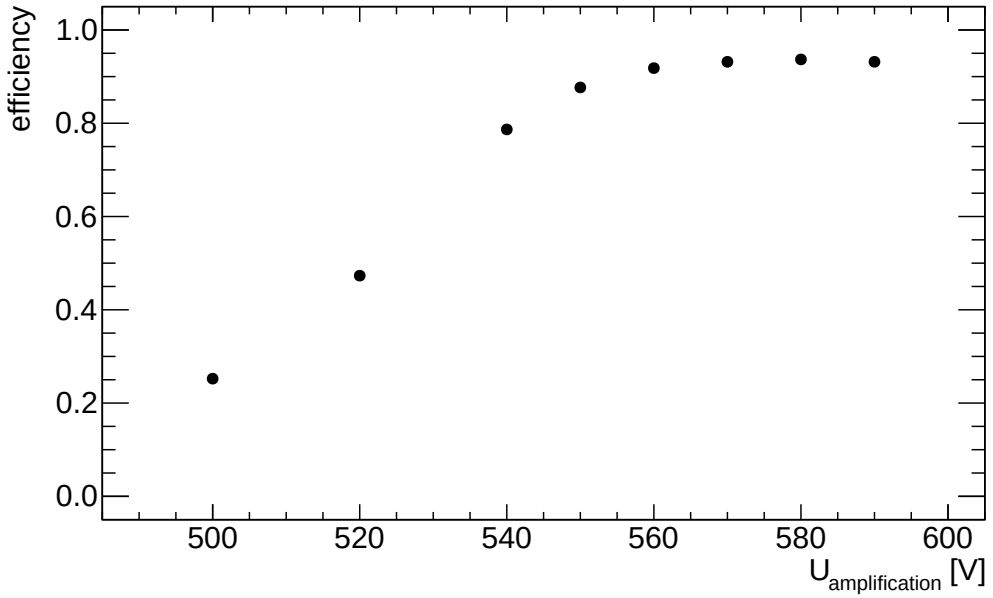

Figure 6.37: Tracking efficiency as a function of the amplification voltage. A plateau of 95 % is reached at an amplification voltage of 560 V.

Chapter 7

Comparison of Small and Large Micromegas

In this chapter the influence of the strip length on the performance of the Micromegas will be discussed. This is done based on measurements with 120 GeV pions at SPS/CERN and measurements with cosmic muons in the Cosmic Ray Facility.

7.1 Influence of the Strip Length

The most intuitive influence of the strip length is the noise behavior. But there are two other basic influences. The capacitive coupling between the strips, which shows a major impact on the reconstruction of the track angle in a single plane. And the signal propagation time on the strip lines. In literature a signal propagation time $t_{propagation}$ of 5.64 ns m^{-1} is given for strip lines similar to the readout of the Micromegas [Nührmann, 1994]. A measurement performed with the prototype Micromegas used for the calibration in chapter 6 yielded a signal propagation time $t_{propagation}$ of (6.1 ± 0.6) ns m^{-1} [Lösel, 2013], which is in good agreement with the literature value.

7.1.1 Noise behavior

Due to the readout strips acting as antennas the noise on the readout channels rises with the strip length. The noise is determined by averaging the sigmas of the pedestals for all readout channels of one APV25 front-end board (see chap. 6). Figure 7.1 shows the noise as a function of the strip length. In this case the whole strip length is considered including the routing of about 10 cm to the front-end electronics outside of the active area. The noise of a small Micromegas with an active area of (10×10) cm^2 has a total strip length of about 20 cm and shows a mean sigma of the pedestals of about 12 ADC counts. Whereas the large Micromegas with a total strip length of about 110 cm shows an about two times higher noise. The value at 0 strip length represents the noise for the readout electronics detached from the detector. This result is in good agreement with a measurement performed at

CERN, where various strip lengths of Micromegas were measured. A linear rise of the noise as a function of the strip length can be seen in both measurements with a steep drop at strip length 0.

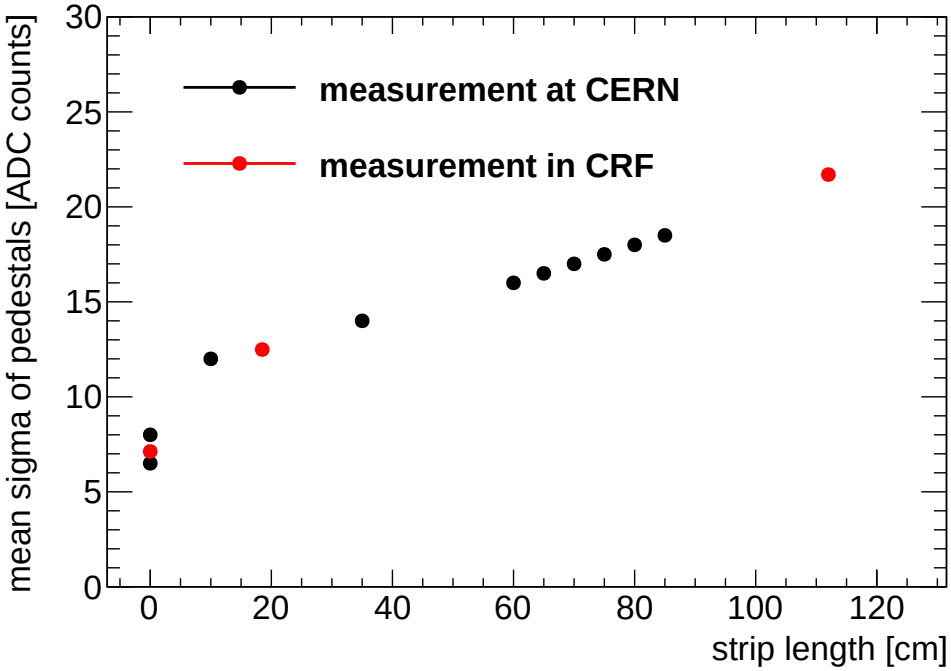

Figure 7.1: Measured noise of the Micromegas as a function of the strip length. The total strip length is considered including the routing of about 10 cm to the front-end electronics outside of the active area. The value at 0 represents the readout electronics detached from the detector. The same linear rise can be seen for the measurement at CERN (black) as well as for the measurement in the CRF (red). CERN data points taken from [Iengo, 2016].

A simplified Monte-Carlo simulation was developed to investigate the influence of the noise level on the spatial resolution of Micromegas. For this five strips were considered with a Gaussian pulse height distribution across the strips, which represents the charge distribution for a track perpendicular to the detector plane. Then randomly noise was added to the pulse heights. Therefore a Gaussian function centered around 0 with the noise-to-signal ratio $R_{N/S}$ as sigma represents the noise. On this noisy simulation input data the centroid method (see sec. 2.4.2) for the position reconstruction was applied and the resulting distribution fitted with a Gaussian function. The quadratic difference of this sigma and the width of the Gaussian pulse height distribution gives the degradation of the spatial resolution due to noise. Figure 7.2 shows the degradation of the spatial resolution as a function of the noise-to-signal ratio. The linear rise reaches at a noise-to-signal ratio of 10 % a degradation of the spatial resolution of about 20 µm in agreement with figure 6.29.

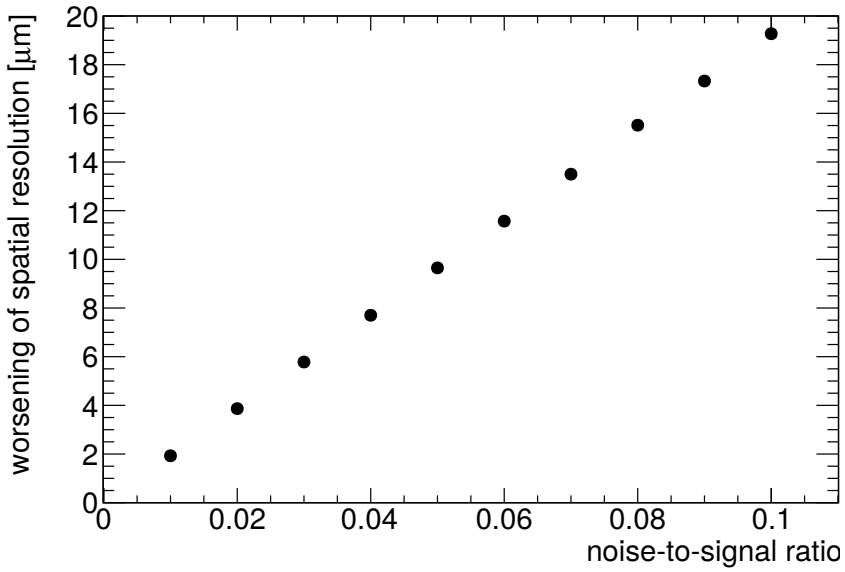

Figure 7.2: Simulated degradation of the spatial resolution as a function of the noise-to-signal ratio. Therefore charge was Gaussian-like distributed on five strips as pulse height for a perpendicular track. After adding randomly distributed noise to the pulse height the position was reconstructed using the centroid method (see sec. 2.4.2).

7.1.2 Capacitive Coupling between Strips

Capacitive coupling between the strips transfers a part of the signal on one strip to the neighboring strip and vice versa. For resistive strip Micromegas this coupling is mainly due to the coupling between the resistive strips, which have a high resistivity. Therefore the charge signal disperses slowly and drains to the terminal. In this step the charges couple to the neighboring resistive strips. Figure 7.3 shows a schematic drawing of this process with only three resistive strips, three readout strips and their preamplifiers. If charge is applied on the resistive strip in the middle it couples strongly to the neighboring strips. Now the resistive strips transfer their charge to the readout strips as it is intended to read out the Micromegas. The induced charge on the readout strips couples now again to adjacent readout strips. For the position reconstruction by the centroid method this does not matter due to the equally split charge. But when using the TPC-like method this effect has to be corrected. As example for inclined tracks some ionization electron arrive earlier on the readout strips than others. Thus theses charges are first capacitively coupled to a neighboring strip and then the ionization electrons arrive on that strip. Therefore it seems like a slower signal rise, but really it is the superposition of two signals. This leads to a systematically larger angle for the reconstruction of the track angle in a single plane.

To correct for this effect the exact percentage of capacitive coupling has to be determined. This is done with a simulation using *LTspice* [Linear Technology Corporation, 2010]. Figure 7.4 shows a screen shot of the circuit diagram drawn with *LTspice*. All couplings which were mentioned above are considered in the simulation. The ratio at the

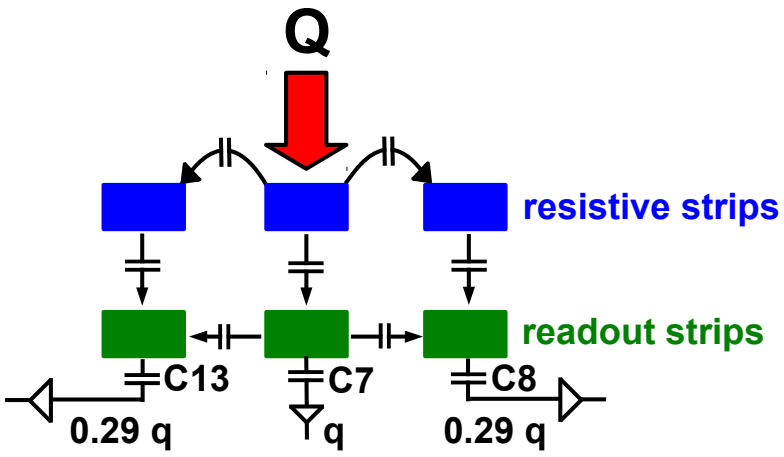

Figure 7.3: Schematic drawing of the capacitive coupling between neighboring strips. This is a simplified Micromegas network with three resistive strips, three readout strips and the preamplifier. The ionization electrons arrive on the resistive strip in the middle, which couples to the neighboring resistive strips. All resistive strips couple to the readout strips, which finally couple to the neighboring readout strips. The capacitors for which the capacitive coupling is calculated are labeled the same way as in figure 7.4.

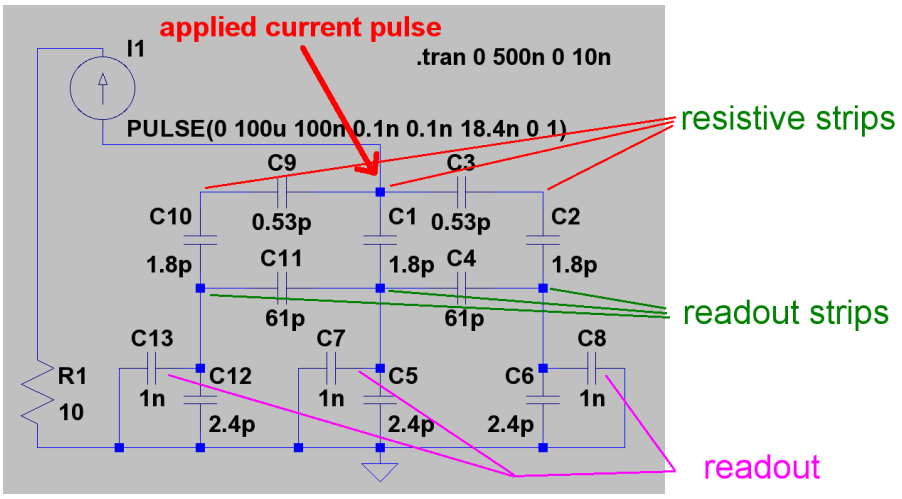

Figure 7.4: Screen shot of the *LTspice* [Linear Technology Corporation, 2010] circuit diagram for the simulation of the capacitive coupling between strips. The locations of the resistive strips, the readout strips and the readout circuits are indicated. The various capacitive couplings are simulated by different capacitances.

readout is the relevant value, which will be used for the charge correction. The result for 100 cm long readout strips is shown in figure 7.5. By dividing the two currents the charge ratio is calculated. For 100 cm long readout strips the capacitive coupling is 29.1 %, and 23.4 % for 10 cm long readout strips.

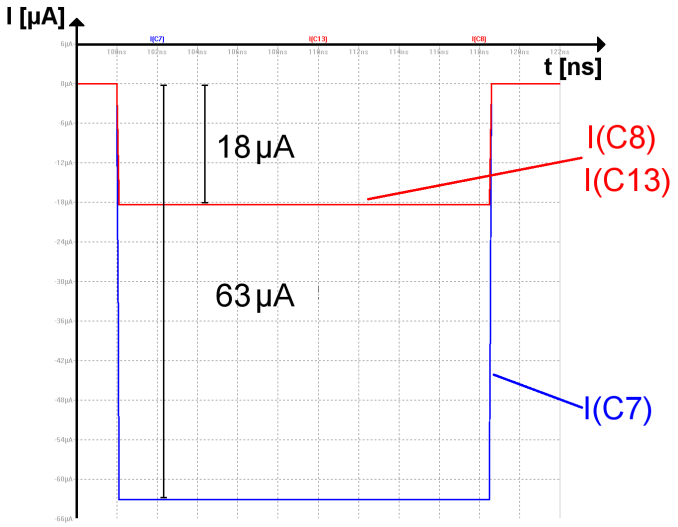

Figure 7.5: Current at the readout of two neighboring strips. The ratio gives the capacitive coupling between the strips. Simulated with *LTspice* [Linear Technology Corporation, 2010].

Figure 7.6 shows the simulated capacitive coupling as a function of the strip length. In this case only the strip length in the active area of the Micromegas is considered. Only the capacitors between the readout strips were varied to simulate the strip length due to the short range of the coupling of the resistive strips. This shows that the main coupling comes from the resistive strips and rises linearly with the length of the readout strips. The small Micromegas used in measurements for this thesis have a strip length of 10 cm, the large prototype Micromegas has a strip length of about 100 cm and the longest strips of the SM2 modules are about 150 cm long.

7.2 Investigation of Pion Testbeam Data

For the comparison of the performance of large and small Micromegas the detectors were investigated in a testbeam campaign with 120 GeV pions at the H8 beam line at the experimental area north of the Super Proton Synchrotron (SPS) located at CERN (see fig. 1.2). The SPS accelerates the protons to 450 GeV. It is not only the final injector for proton beams for the LHC, but allows also for testbeam campaigns with high energy muons and pions in the experimental area to investigate detector components.

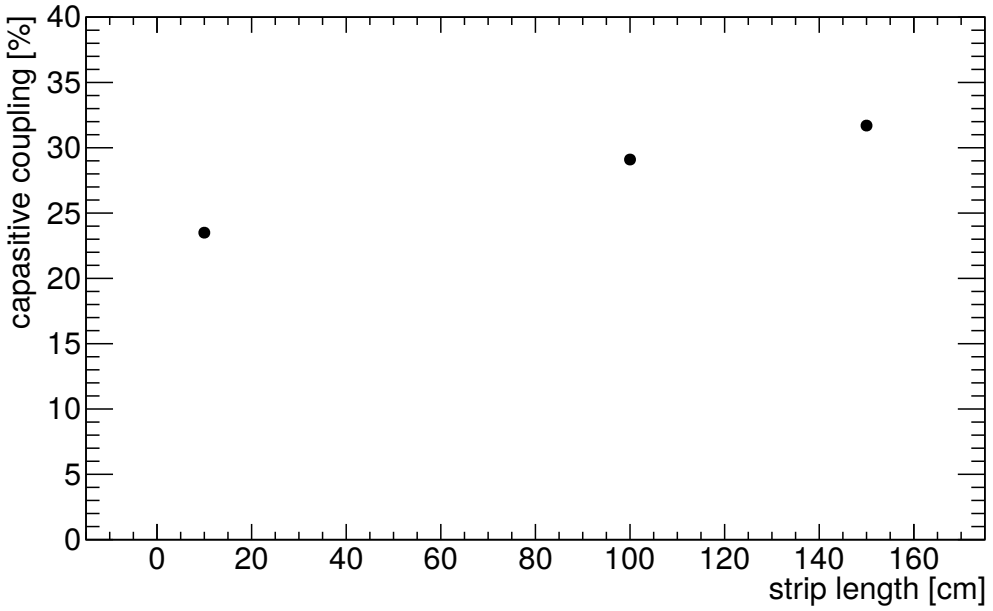

Figure 7.6: Capacitive coupling between strips as a function of the strip length. A linear behavior can be seen dominated by the short range of the coupling of the resistive strips. Simulated with *LTspice* [Linear Technology Corporation, 2010].

7.2.1 Experimental Setup

A photo of the experimental setup of the testbeam campaign with 120 GeV pions is shown in figure 7.7. Two trigger scintillators triggered on coincident signals created by pions passing through their overlapping area of about $(10 \times 3)\,\mathrm{mm}^2$. The Micromegas telescope consisted of in total thirteen detectors, the $1\,\mathrm{m}^2$ prototype Micromegas (see sec. 6.2), four $(9 \times 9)\,\mathrm{cm}^2$ reference Micromegas with two dimensional readout and a strip pitch of 250 µm, and eight $(10 \times 10)\,\mathrm{cm}^2$ test Micromegas with one dimensional readout and a strip pitch of 400 µm (see fig. 7.8). This measurement was taken to investigate the performance of the Micromegas under different track inclination. Therefore the eight test Micromegas and the large prototype Micromegas were rotatable. The four reference Micromegas were always located perpendicular to the pion beam. Due to a lack of readout electronics this measurement was split into a measurement with the large prototype Micromegas and the four reference Micromegas, and a measurement with the eight test detectors. In the measurement with the eight test Micromegas seven served as reference chambers for the eighth. All eight chambers were arranged with alternating orientation, so-called back-to-back, to minimize the distance between the pairs of two test Micromegas. Every Micromegas had a drift region of 5 mm and were operated with the same drift voltage of 300 V. The amplification voltage varied depending on the detector type, the reference Micromegas were operated with 540 V, the small test Micromegas with 500 V and the large prototype Micromegas with 550 V. For information on the alignment of the Micromegas in the telescope see [Lösel, 2013].

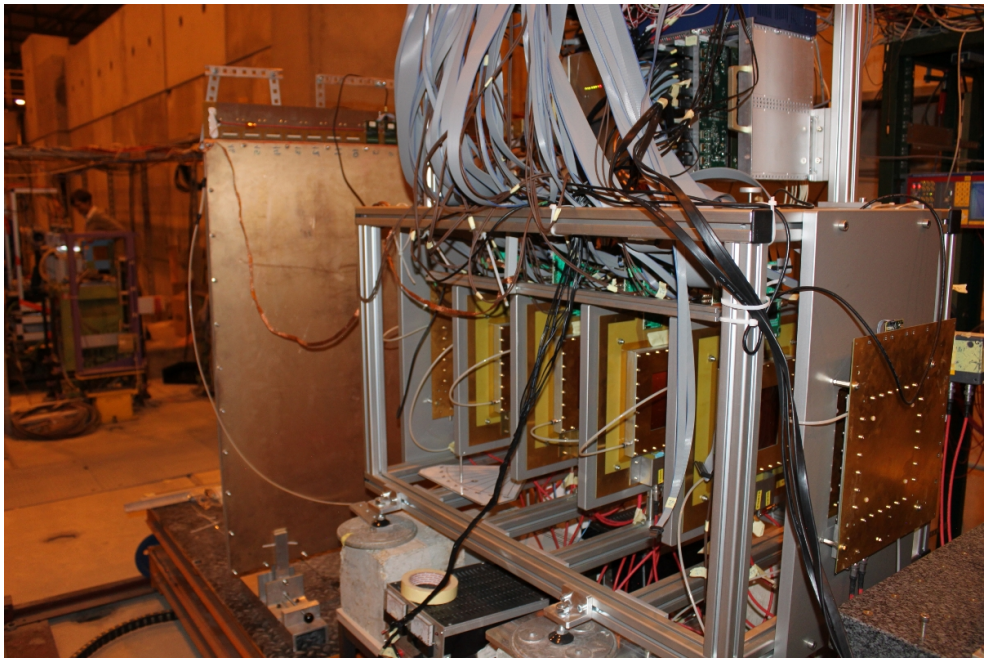

Figure 7.7: Photo of the Micromegas telescope in the 120 GeV pion beam. In the background the large prototype Micromegas can be seen. All small detectors, four two dimensional reference detectors and eight one dimensional test Micromegas, were installed in the aluminum frame to the right.

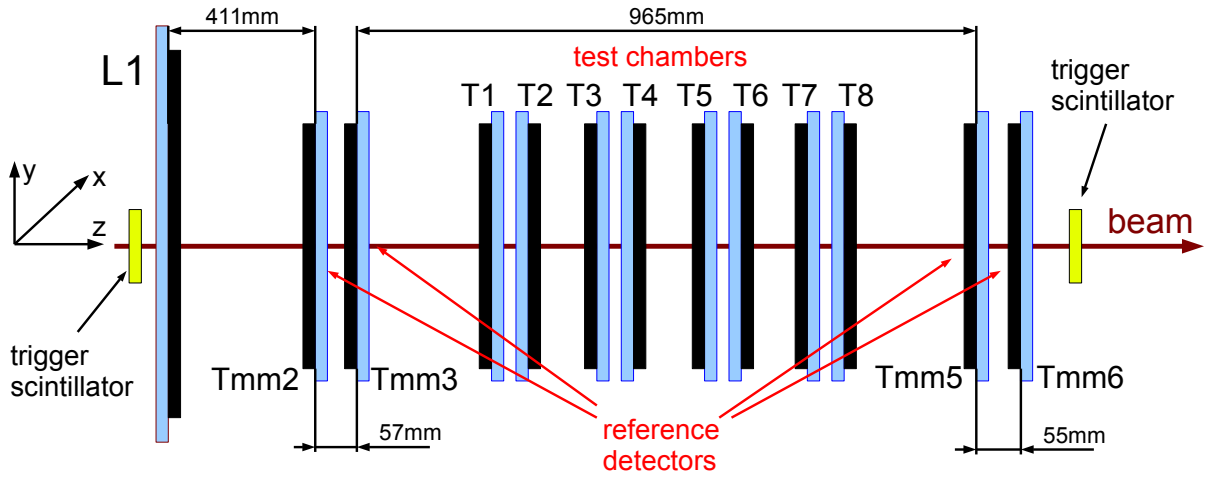

Figure 7.8: Schematic drawing of the Micromegas telescope. Additional to the thirteen Micromegas two trigger scintillators are shown and the pion beam direction. The orientation of the Micromegas is given by the black bars, which represent the drift regions. The precision direction of Micromegas is the x direction. The distances between the detectors are indicated for the measurement with the large prototype Micromegas and the four reference detectors (Tmm2, Tmm3, Tmm5 and Tmm6).

7.2.2 Reconstruction of the Track Angle

Using the TPC-like method (see sec. 2.4.3) the percentage of capacitive coupling between the strips from section 7.1.2 can be verified. To do so the measurement with the eight test Micromegas will be discussed first.

Not to be concerned with nonlinear transformations, only the slope of the linear fit of the TPC-like method is considered at first (see fig. 2.10). Table 7.1 gives the calculated slope of the TPC-like method $m_{\mu TPC,\ calc}$ for a known chamber rotation Θ for the test Micromegas (T) and an electron drift velocity of $0.047\,\mathrm{mm\,ns^{-1}}$ for an electric field of $600\,\mathrm{V\,cm^{-1}}$. Figure 7.9 shows the slope distributions for one $(10 \times 10)\,\mathrm{cm}^2$ test Micromegas under various rotations. It can be seen that the reconstruction of the track angle works quite well for a rotation of 40°, but for a rotation of 10° it does not work.

Table 7.1: Calculated slope of the TPC-like method $m_{\mu TPC,\ calc}$ for various chamber rotations Θ given for the test Micromegas (T). In the calculated slopes the signal timing is given in the 25 ns sampling steps of the readout electronics (see chap. 3).

Θ [°]	$m_{\mu TPC,\ calc}$
10	1.93
20	0.94
30	0.59
40	0.41

Now the charge correction for the capacitive coupling between the strips with the simulated percentage of 23.4 % is applied (see sec. 7.1.2). This is done as a function of time, i.e. in this case sampling steps of the signals. The percentage of the transferred charge is calculated sampling step-wise, subtracted from the neighboring strips and added to the pulse height of the originating strip. Therefore the time shift induced by the capacitive coupling between the strips is eliminated. Figure 7.10 shows the result for the angle reconstruction with charge correction. This improves the TPC-like method for all chamber rotations. For 30° and 40° the most probable value is exactly the expected value. The reconstruction of the track angle works as well for 20°, but the most probable value is slightly shifted. Whereas for 10° it still does not work very well. But this is due to too few strips hit. Therefore the signal timing for all strips hit is too similar and the angle cannot be reconstructed very well.

Figure 7.11 shows the reconstructed angle as a function of the chamber rotation. The reconstruction of the track angle works for all eight test Micromegas similarly well. Small variations between the chambers can be seen, but this is due to the not perfect mechanical rotation of the test Micromegas.

For 30° chamber rotation the signal timing of the first and last responding strip of the detector T4 is shown in figure 7.12. The dashed lines represent the borders of the drift region at the middle of the rising and falling edge, respectively, of the timing distributions with a difference of about 110 ns, which is in good agreement with the simulation for a 5 mm drift region shown in figure 6.17.

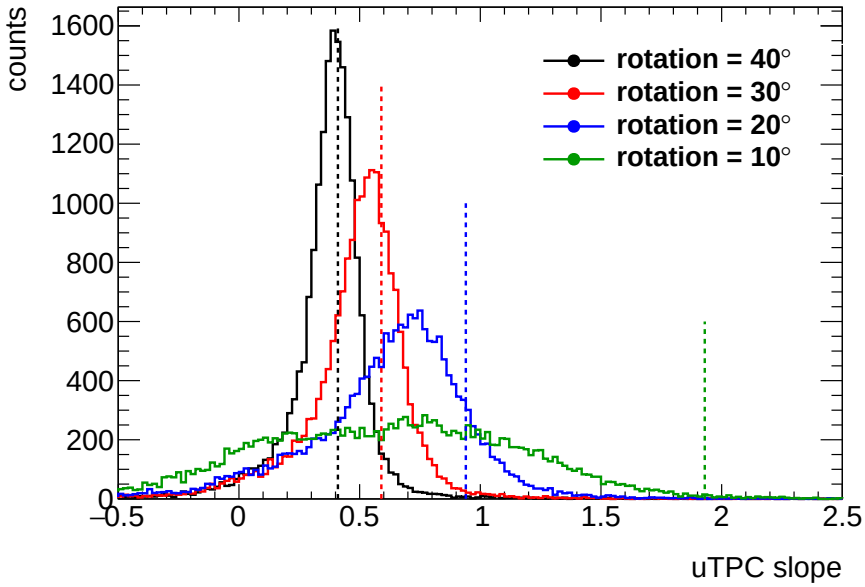

Figure 7.9: Slope of the linear TPC-like fit for various angles without correction for the capacitive coupling between strips. For 40° the reconstruction works quite well, but the smaller the rotation, the worse the reconstruction of the track angle works. The vertical dashed lines represent the expectation of the most probable values of the distributions (see tab. 7.1).

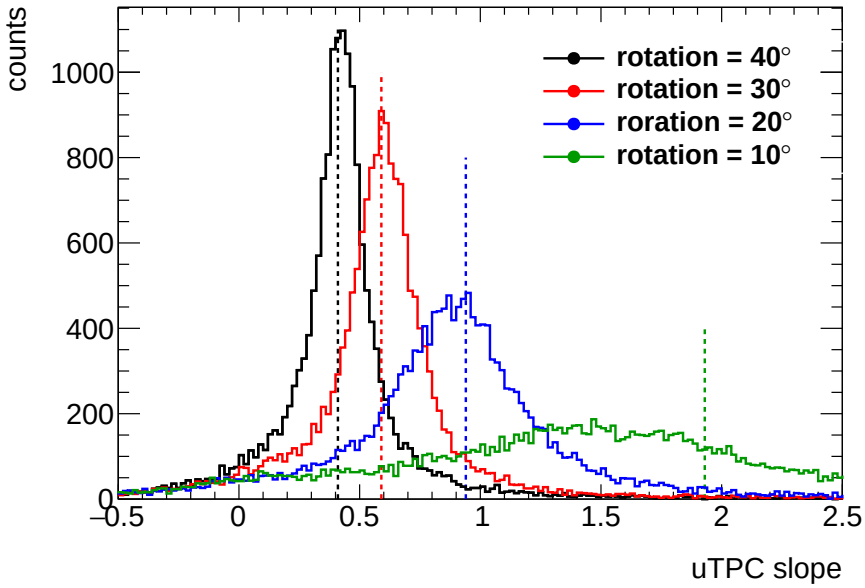

Figure 7.10: Slope of the linear TPC-like fit for various angles with correction for the capacitive coupling between strips by the simulated value of 23.4 %. The reconstruction of the track angle works now well for all rotations except for 10°. But this is pathological for very small angles. The vertical dashed lines represent the expectation of the most probable values of the distributions (see tab. 7.1).

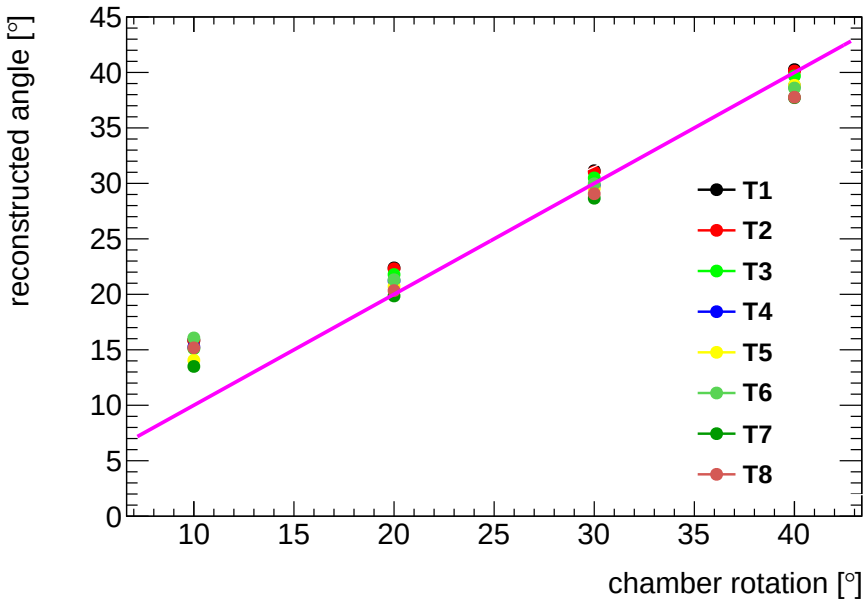

Figure 7.11: Reconstructed angle as a function of the chamber rotation for all test Micromegas. It works for all test chambers similarly well. The slight differences in the reconstructed angles are due to the rotation of the chambers by hand and therefore not by exactly the expected value. The shift at 10° is pathological and the reconstructed angle at 20° is a little bit too large. The line represents the angle bisector.

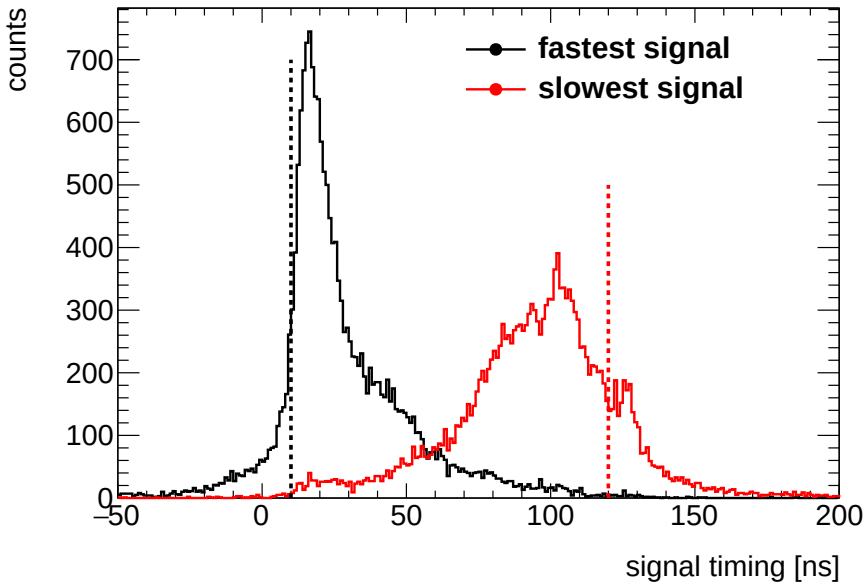

Figure 7.12: Signal timing of the fastest (black) and slowest (red) responding strips for a chamber rotation of 30° of the test Micromegas T4. The difference of about 110 ns corresponds to the height of the drift region of 5 mm. The vertical dashed lines represent the borders of the drift region.

7.2.3 Angular Reconstruction under the Influence of Increased Noise

This method is applied on the measurement with the large Micromegas. Therefore the deformation of the drift region has to be determined first. The signal timing of the first and last responding strip is shown in figure 7.13. Again the dashed lines represent the borders of the drift region with a difference of about 165 ns. This corresponds to a drift region of about 7.2 mm for the measurement in the middle of the active area of the Micromegas. Therefore the deformation of the drift region in the center of the Micromegas is about 2.2 mm, which leads to an electric field of 417 V cm^{-1} and hence to a drift velocity of about 0.0436 mm ns^{-1}. The calculated slope of the TPC-like method $m_{\mu TPC,\ calc}$ for a known chamber rotation Θ for the large prototype Micromegas (L1) is given in table 7.2.

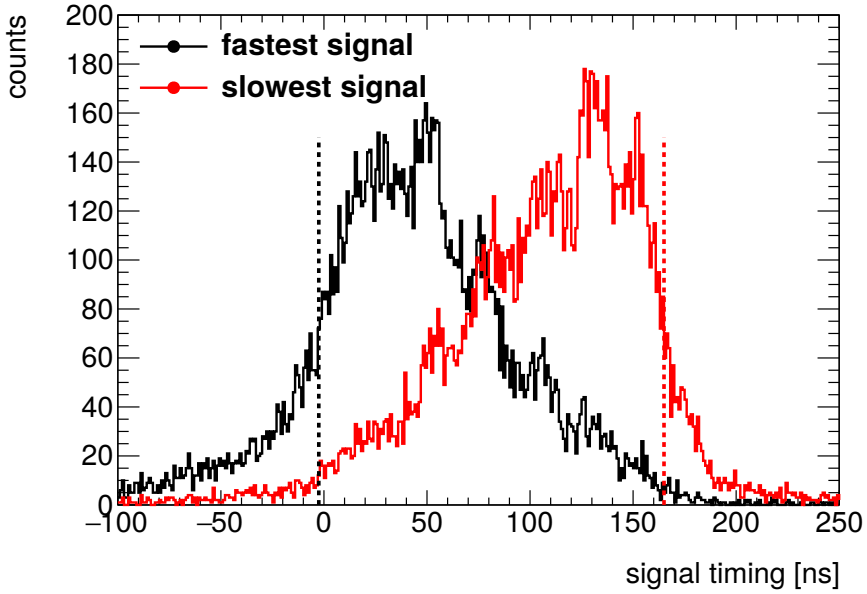

Figure 7.13: Signal timing of the fastest (black) and slowest (red) responding strips for a chamber rotation of 30° of the large prototype Micromegas L1. The difference of about 165 ns corresponds to the height of the drift region of 7.2 mm in the center of the active area. Therefore the drift region is deformed by 2.2 mm from the construction value of 5 mm. The vertical dashed lines represent the borders of the drift region.

Figure 7.14 shows the result for the reconstruction of the track angle for the large prototype Micromegas with charge correction by the simulated factor of 29.1 % (see sec. 7.1.2). In this case the reconstruction of the track inclination does not work as expected. For a chamber rotation of 30° the peak is almost at the position of the calculated slope $m_{\mu TPC,\ calc}$. But a lot of data points are shifted towards 0, thus the distribution broadens. This is probably due to an increased noise level compared to the small test Micromegas. Figure 7.15 shows the sigma of the electronic pedestals of the readout channels as example for the 128 channels of one APV25, which yields a noise-to-signal ratio of about 9 %. The

Table 7.2: Calculated slope of the TPC-like method $m_{\mu TPC,\ calc}$ for various chamber rotations Θ given for the large prototype Micromegas (L1). In the calculated slopes the signal timing is given in the 25 ns sampling steps of the readout electronics (see chap. 3).

Θ [°]	$m_{\mu TPC,\ calc}$
10	2.34
20	1.14
30	0.72

noise level of the large prototype Micromegas was about four times higher during this measurement compared to the test Micromegas T4. But during the measurement for the calibration of the large prototype detector in the LMU Cosmic Ray Facility (CRF) the noise level was about a factor of 2 smaller than during the CERN testbeam campaign. And for the CRF measurement the reconstruction of the track angle worked reasonably well (see fig. 6.23).

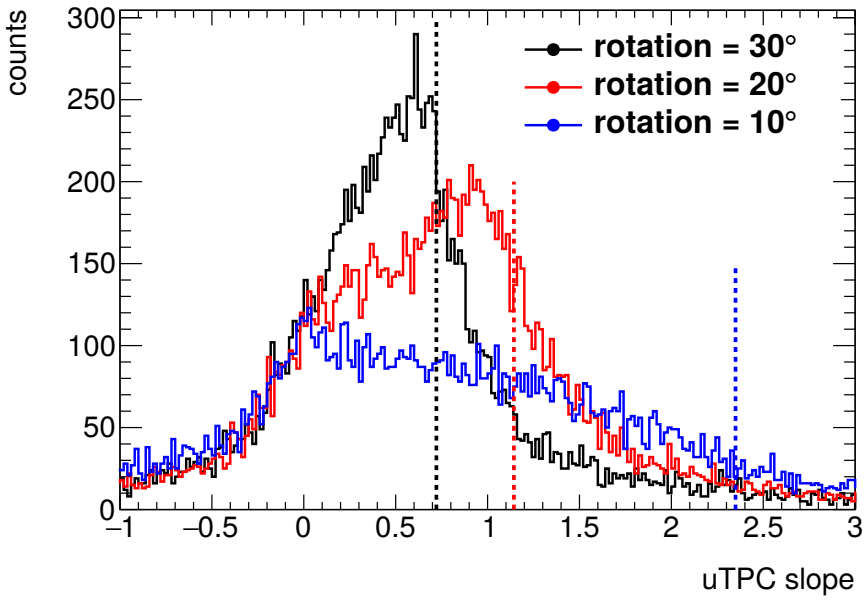

Figure 7.14: Slope of the linear TPC-like fits for various angles with correction on the capacitive coupling between strips by the simulated value of 29.1 %. The reconstruction of the track angle works not as well as for the small test Micromegas. For 10° it does not work at all, but for 30° the most probable value is almost at the expected value. The distributions are broader than for the test Micromegas as well. The vertical lines represent the expectation of the most probable value of the distributions (see tab. 7.2).

It seems to be necessary to have a noise-to-signal ratio below 5 % to achieve a reasonably good reconstruction of the track angle in a single plane using the electron drift time measurement.

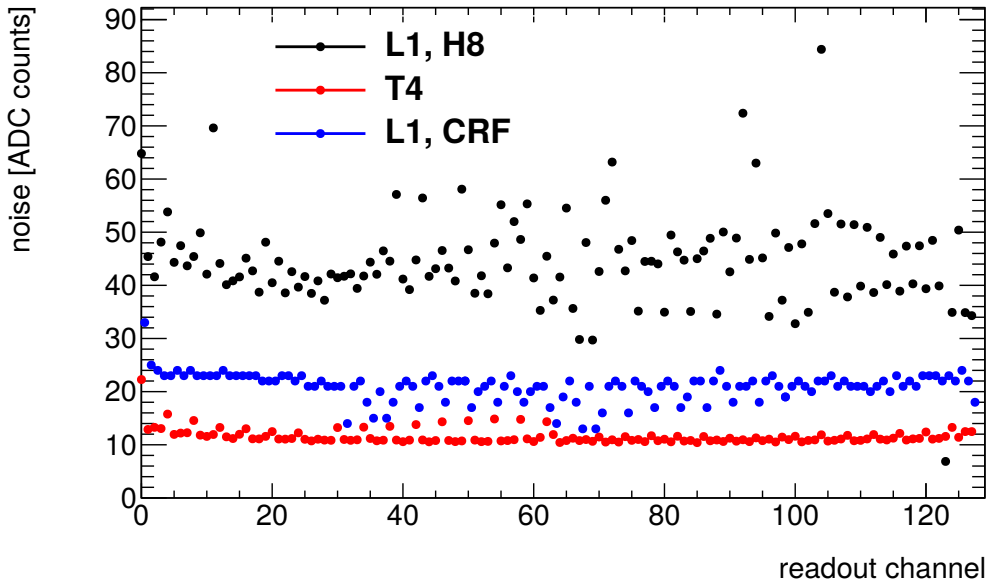

Figure 7.15: Sigma of the electronic pedestal of the readout as a function of the readout channel exemplary for one APV25. The black dots represent the data points for the large prototype Micromegas (L1) during the CERN testbeam campaign with 120 GeV pions. Compared to the small test Micromegas (T4) (red) they are about a factor of 4 higher. Whereas during the measurement for the calibration of the L1 in the CRF (blue) the noise level is only a factor of 2 higher than for the small test Micromegas. The large prototype Micromegas had a noise-to-signal ratio of about 9 % during the testbeam campaign.

7.2.4 Spatial Resolution

At first only the position reconstruction using the centroid method (see sec. 2.4.2) will be discussed. The spatial resolution of the Micromegas is again determined considering the track prediction accuracy (see eq. 6.4). For the measurement with the large prototype Micromegas the reference detectors have a fixed position and no rotation. The track prediction accuracy of the reference detectors varies according to figure 7.16 for the position of the detector under investigation. The track prediction accuracy for the position of the L1 chamber is $\sigma_{\text{track}}(z = 0) = (58 \pm 3)\,\mu\text{m}$.

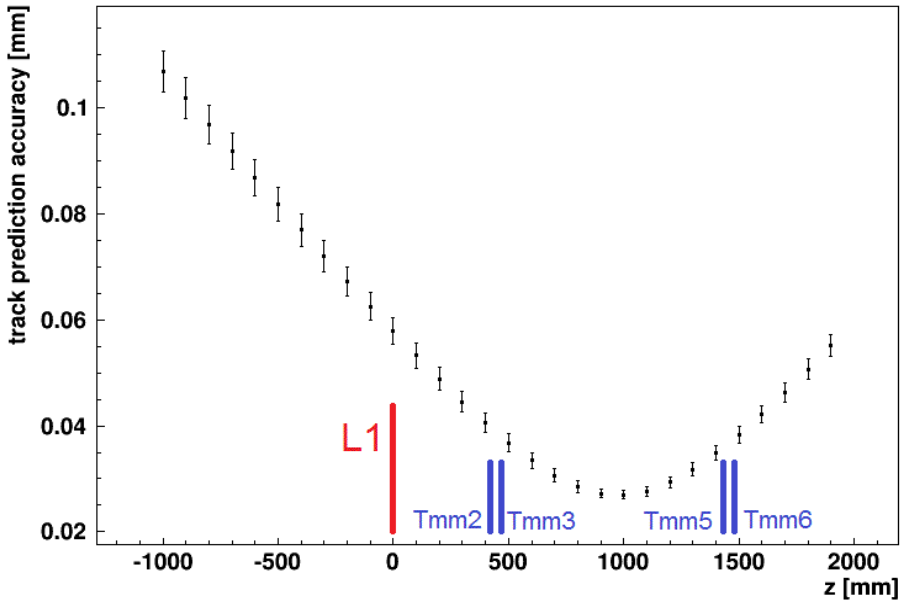

Figure 7.16: Track prediction accuracy as a function of the detector position in the telescope. Indicated are the positions of the large prototype Micromegas (L1) and the four reference detectors (Tmm2, Tmm3, Tmm5 and Tmm6). Figure taken from [Lösel, 2013].

To calculate the track prediction accuracy the spatial resolutions $\sigma_{\text{sr, ref}}$ of the reference detectors have to be known. This is estimated by fitting the track once with all reference detectors and again with one detector excluded from the fit. The respective residual distributions are fitted with Gaussian functions resulting in σ_{in} and σ_{ex}. The geometric mean of the two sigmas gives then the estimation for the spatial resolution of the reference chambers (see eq. 7.1) under the assumption of identical spatial resolution for all four reference detectors [Carnegie et al., 2005]. For these four reference Micromegas the hit position is always determined using the centroid method. The result for the track prediction accuracy will be used for all measurements with the large prototype Micromegas.

$$\sigma_{\text{sr, ref}} = \sqrt{\sigma_{\text{in}}\sigma_{\text{ex}}}\ , \tag{7.1}$$

where σ_{in} is the sigma of the residual distribution with the detector included in the fit of

the track and σ_{ex} with the detector excluded.

Figure 7.17 shows the spatial resolution of the large prototype Micromegas L1 as a function of the chamber rotation. The spatial resolution for perpendicular tracks is $(83 \pm 4)\,\mu m$ and rises almost linearly to a value of $(594 \pm 6)\,\mu m$ for a chamber rotation of 30°. For tracks perpendicular to the detector plane the center of the pulse height distribution is well defined due to the Gaussian-like charge distribution. Whereas for inclined tracks the charge distribution is not Gaussian-like anymore, but neither uniformly due to the inhomogeneous ionization of the MIPs (see sec. 2.1). Thus for inclined tracks the centroid method does not work as well as for perpendicular tracks.

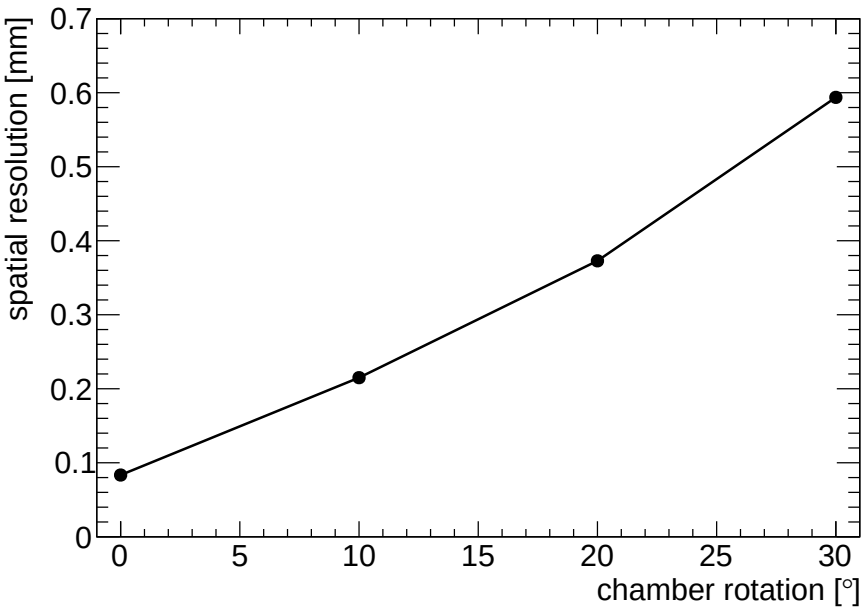

Figure 7.17: Spatial resolution as a function of the chamber rotation. An almost linear rise can be seen starting at a spatial resolution of $(83 \pm 4)\,\mu m$ for tracks perpendicular to the detector plane. The lines are only to guide the eye.

A sketch of the measurement with the eight test Micromegas is shown in figure 7.18 indicating the distances between the detectors. All eight detectors are mounted in a common frame and can be rotated only in common. The positions are relevant for the determination of the track prediction accuracy as well as the chamber rotation. The track prediction accuracy is much better for detectors in the center of the telescope. Due to the rotation dependency of the spatial resolution the track prediction accuracy degrades also with a larger chamber rotation of the detector in the telescope. The track prediction accuracy as a function of the detector position for all test Micromegas and various chamber rotations is shown in figure 7.19. For this purpose the spatial resolution for the seven detectors acting as reference is again estimated with equation 7.1.

Figure 7.20 shows the spatial resolution for all test detectors determined with equation 6.4. Here it can be seen that the determination of the spatial resolution works well, because all test chambers show a similar result despite their position in the telescope. They show

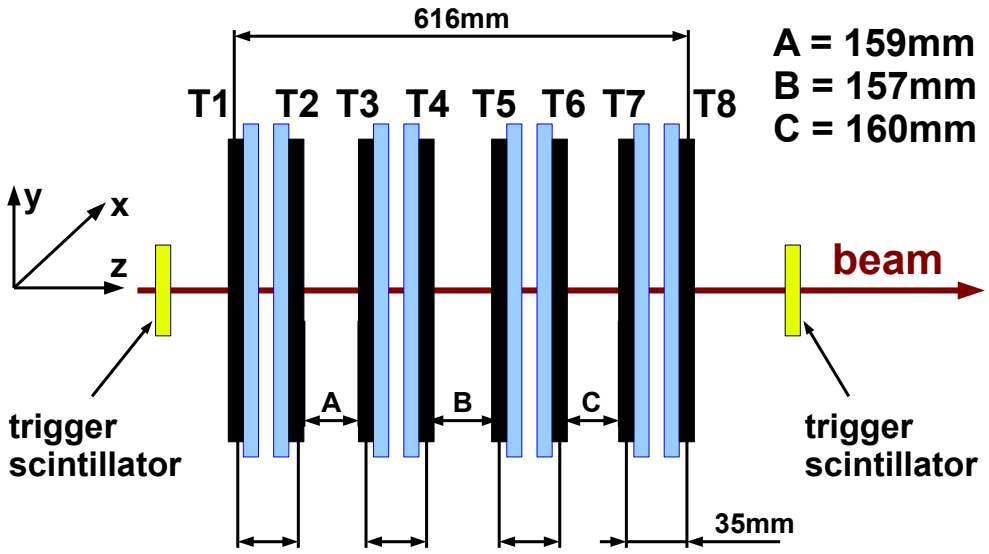

Figure 7.18: Sketch of the experimental setup of the measurement with eight test Micromegas. As well as the orientation with respect to the pion beam the distances between the detectors are indicated. The test Micromegas are arranged with alternating orientation, so-called back-to-back, to minimize the distance within a pair of detectors.

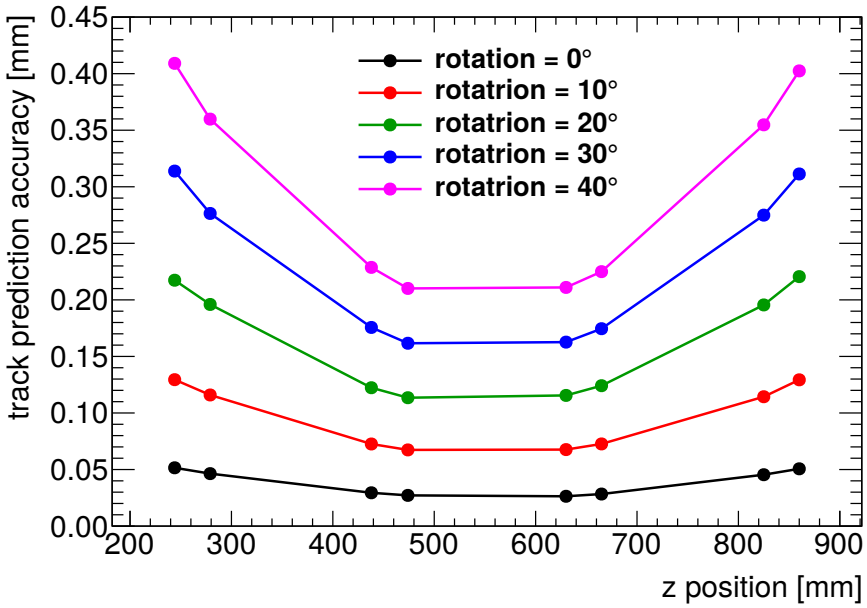

Figure 7.19: Track prediction accuracy as a function of the detector position for various chamber rotations. The track prediction accuracy is highly dependent on the chamber rotation due to the degraded spatial resolution of each of the seven rotated Micromegas acting as reference. For perpendicular tracks the track prediction accuracy is below 50 µm, but for 40° it rises up to 400 µm depending on the position in the telescope. The lines are only to guide the eye.

a spatial resolution of (63 ± 3) µm for tracks perpendicular to the detector plane. It rises linearly to a value between 500 and 550 µm for the Micromegas rotated by 40°.

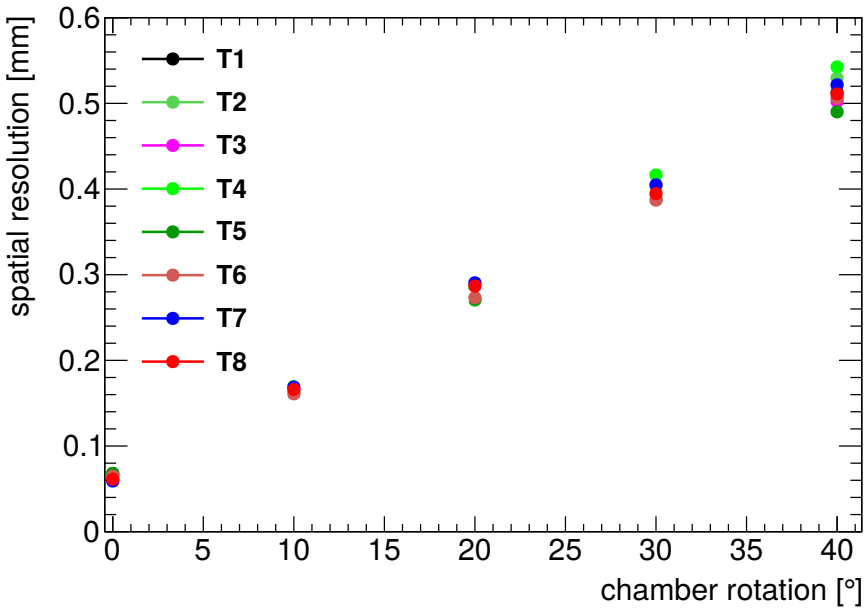

Figure 7.20: Spatial resolution for all test Micromegas as a function of the chamber rotation. All detectors show a similar spatial resolution starting around 60 µm for perpendicular tracks and rising linearly to a value between 500 and 550 µm for a chamber rotation of 40°.

For the comparison of large and small Micromegas the test chamber T4 is chosen to serve as an example, because it is located in the center of the telescope. And from now on only this chamber will be discussed. In figure 7.21 the spatial resolutions for the T4 chamber and the large prototype Micromegas (L1) are shown as a function of the chamber rotation. The spatial resolutions are comparable for tracks perpendicular to the detector plane with a difference in the spatial resolution of about 20 µm. The L1 chamber has a noise-to-signal ratio of about 9 %, whereas the test Micromegas T4 has a noise-to-signal ratio of about 2 % only. The Monte-Carlo simulation of the noise impact (see sec. 7.1.1) shows a degrading of the spatial resolution of about 14 µm (see fig. 7.2). This is in agreement with the measurement, but the rise of the curve is much steeper for the large prototype Micromegas. This is probably also due to the higher noise level in the large prototype Micromegas as shown in figure 7.15. The resolution ratio between large and small Micromegas stays almost constant at a value of about 1.4.

For the determination of the spatial resolution using the TPC-like method (see sec. 2.4.3) the time-jitter (see sec. 3.1)[1] has to be considered. In principle it is possible to determine the time-jitter by comparing the intercept $t_{\mu TPC,\ fit}$ of the TPC-like fit of two Micromegas oriented back-to-back. The time-jitter shifts the signal timing of all detectors

[1]The time-jitter is created by the difference of the timing of the cosmic muon signal and the successive 25 ns clock of the data acquisition system starting the acquisition.

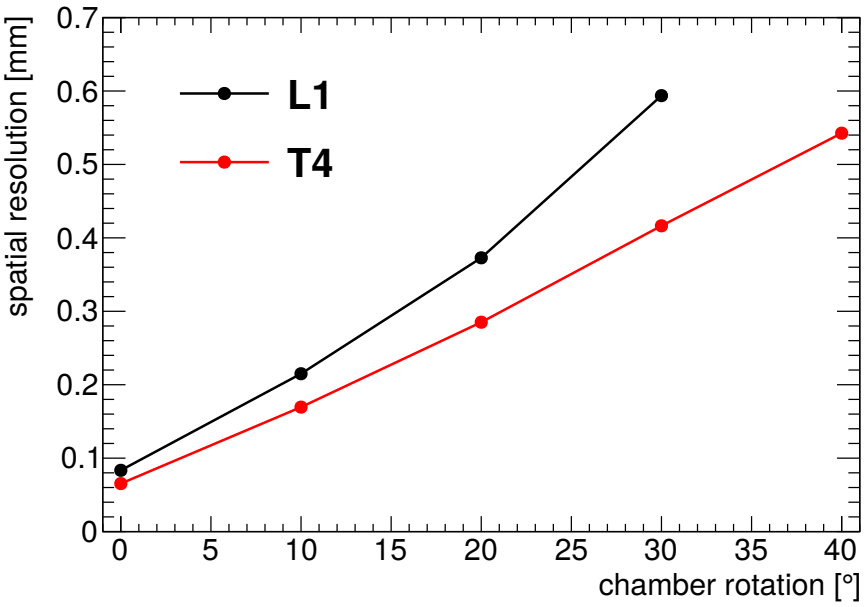

Figure 7.21: Spatial resolution as a function of the chamber rotation for the large prototype Micromegas (L1) and a small test Micromegas (T4). For perpendicular tracks the spatial resolution varies by about 20 µm similar to the noise prediction from section 7.1.1, but for larger chamber rotation the difference between large and small Micromegas gets larger. This is probably due to the higher noise level in the large prototype Micromegas. The lines are only to guide the eye.

in the same direction (see fig. 7.22). But if two Micromegas are oriented back-to-back the reconstruction of the hit position using the TPC-like method is shifted in opposite direction and thus is the intercept of the TPC-like fit. Therefore the time-jitter can be calculated as half of the intercept difference between two Micromegas with back-to-back orientation. This works quite well for 40° and 30° chamber rotation due to the well working TPC-like method. But the distributions are not as rectangular as expected (see fig. 7.23). The magenta rectangle represents the expected distribution of the time-jitter. For a chamber rotation of 40° the width of the distribution is similar to the expected value of 25 ns, but is superimposed by the finite time resolution of the Micromegas and results thus in the broad distributions like for the reconstructed angles. For smaller chamber rotation it gets more inefficient and for 10° it is not possible to determine the time-jitter reasonably well, because for a chamber rotation of 10° the expected amount of responding strips is $N_{\text{strips}} = 5\,\text{mm} \cdot \tan(10°)/0.4\,\text{mm/strip} \approx$ 2-3 strips. Whereas the measured width of a cluster is typically about 4-6 strips. Hence this method cannot be used to compare the spatial resolution under different chamber rotations using the TPC-like method for the determination of the hit position.

To get rid of the time-jitter in the following only detectors with the same orientation are used as reference, because the time-jitter shifts the hit position in the same direction. This means only three detectors act as reference for the fourth with the same reconstruction

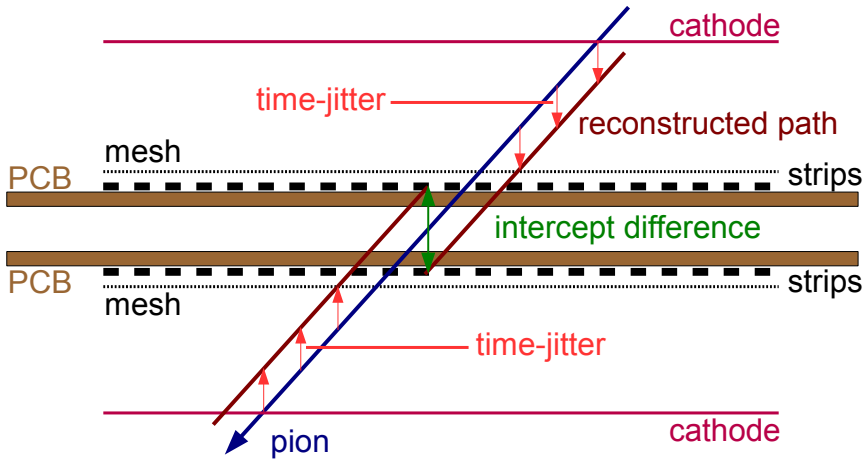

Figure 7.22: Sketch of two Micromegas oriented back-to-back with a pion traversing both active volumes under a certain angle. As example the time-jitter shifts the signal timing in both detectors to smaller timing. The reconstructed paths in both detectors are fitted linearly. Thus the time-jitter can be determined by the difference of the two intercepts of the TPC-like fits. The time-jitter effect is scaled-up to elucidate the shift.

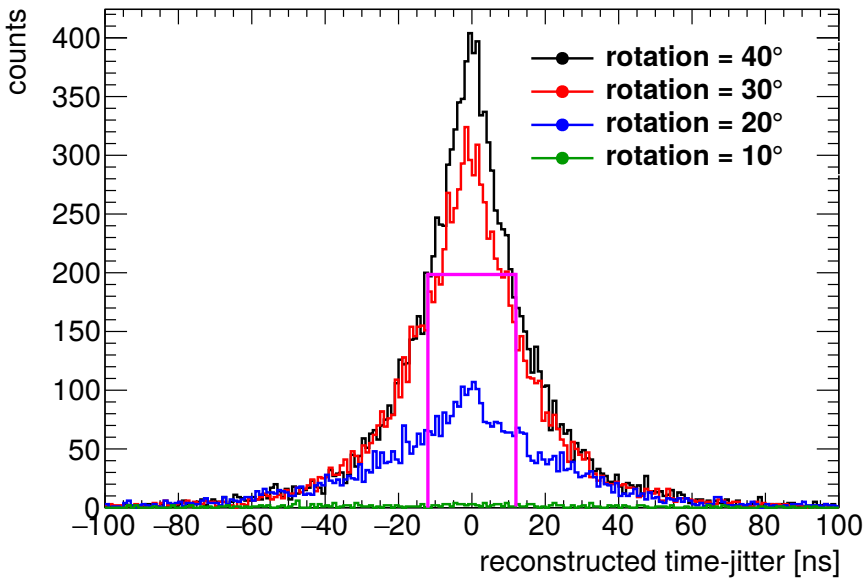

Figure 7.23: Reconstructed time-jitter using the difference of the intercept from the TPC-like fit between two back-to-back oriented Micromegas for various chamber rotations. For 40° and 30° this method can be used to determine the time-jitter although the distributions are broadened by the time resolution of the Micromegas of about 10 ns. But for smaller chamber rotations this method does not work anymore. The magenta rectangle represents the expected distribution of the time-jitter with a width of 25 ns.

method. Therefore this method is also insensitive to the effective time for a hit in the middle of the drift region t_{mid}, because, if t_{mid} is wrongly determined for the detectors, all hit positions are shifted for all detectors by the same value in the same direction. This means it acts like a global shift of the reconstructed track. And the track prediction accuracy is then not influenced by the time-jitter as well. The same procedure is applied for the determination of the spatial resolution using the combined method (see sec. 2.4.4). But by combining the centroid and the TPC-like method the measurement is not insensitive to t_{mid} and the time-jitter anymore, because the positions are combined before the comparison, where the centroid method is time-insensitive and the TPC-like method is not. Therefore the positions do not have to shift for all detectors by the same value in the same direction and it cannot be seen as a global shift of the reconstructed track. Thus the combination of these two methods is time-sensitive. Figure 7.24 shows the track prediction accuracy as a function of the chamber rotation for the three hit reconstruction methods, centroid, TPC-like and the combination of this two methods. It is in the same order of magnitude for all reconstruction methods and proportional to the spatial resolution of the detectors. Unexpectedly the track prediction accuracy for reconstruction using the TPC-like method improves with larger chamber rotation up to 20°, but degrades again for chamber rotations of 30° and 40°.

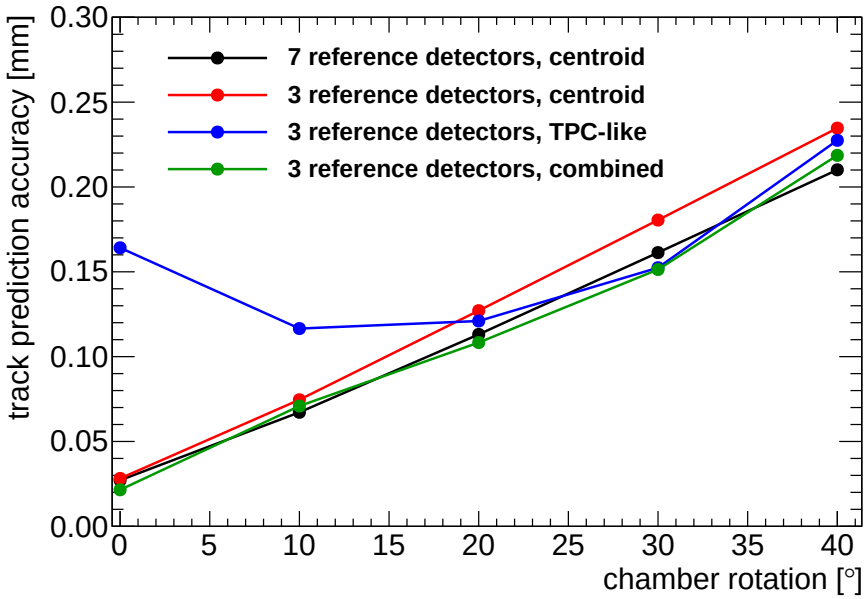

Figure 7.24: Track prediction accuracy as a function of the chamber rotation for all reconstruction methods at the position of the test Micromegas T4. The difference between the hit position reconstruction using the centroid method with seven and three reference detectors is as expected. Unexpectedly the track prediction accuracy for reconstruction using the TPC-like method degrades again for chamber rotations above 20°. The track prediction accuracy is also a measure for the detector resolution. The lines are only to guide the eye.

Figure 7.25 shows the spatial resolution of the small test Micromegas T4 for the different hit position reconstruction methods. The measured spatial resolution using seven test Micromegas as reference is slightly better than using only three reference detectors. With this method for the determination of the spatial resolution considering the track prediction accuracy the spatial resolution should be independent of the number of reference detectors, because the spatial resolution is a property of the detector and not of the reconstruction method. Therefore the track prediction accuracy is probably slightly under-estimated for chamber rotations larger than 0°. But the two versions of the spatial resolution using the centroid method for the reconstruction of the hit position are still in good agreement. The spatial resolution using the TPC-like method improves from 0° to 20°, but degrades again for chamber rotation larger than 20°. In theory, the spatial resolution using the TPC-like method should improve for larger chamber rotations. It could be due to the decreasing of the pulse height on a single strip and thus by worse defined signals.

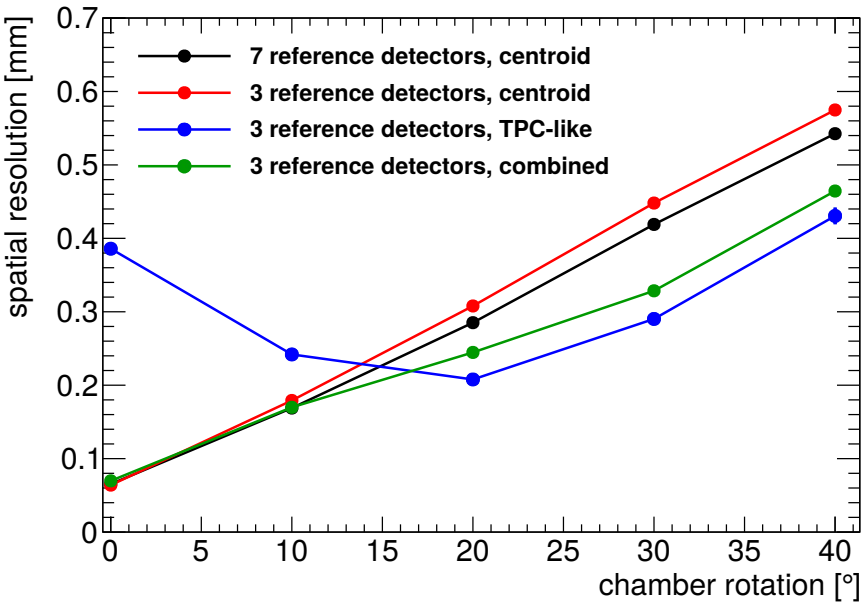

Figure 7.25: Spatial resolution as a function of the chamber rotation for all reconstruction methods for the small test Micromegas T4. The spatial resolutions determined using the centroid method with seven and three reference detectors are comparable. Whereas the spatial resolution using the TPC-like method reaches a minimum of about 200 µm for 20° chamber rotation. Using the combined method the spatial resolution is as expected, dominated by the centroid method for chamber rotations up to 10° and by the TPC-like method for larger rotations. Due to the lack of the time-jitter correction the combined method is not better than the TPC-like method starting at 20°. The lines are only to guide the eye.

Figure 7.26 shows the pulse height of the leading strip in the cluster, i.e. the strip with the highest pulse height, as a function of the chamber rotation. The pulse height decreases with the chamber rotation due the spreading of the ionization charge over more strips for

larger track inclinations. Probably the spatial resolution would be better with a higher gas amplification for 30° and 40°. The result for the spatial resolution using the combined method to determine the hit position is as expected, dominated by the centroid method for small chamber rotation and and by the TPC-like method for chamber rotations starting at 20°. For 10° and 20° this method shows the best result, but for larger angles the spatial resolution determined using the TPC-like method is better. This is probably the case due to the influence of the time-jitter on the TPC-like method, on which could not be corrected for the combined method.

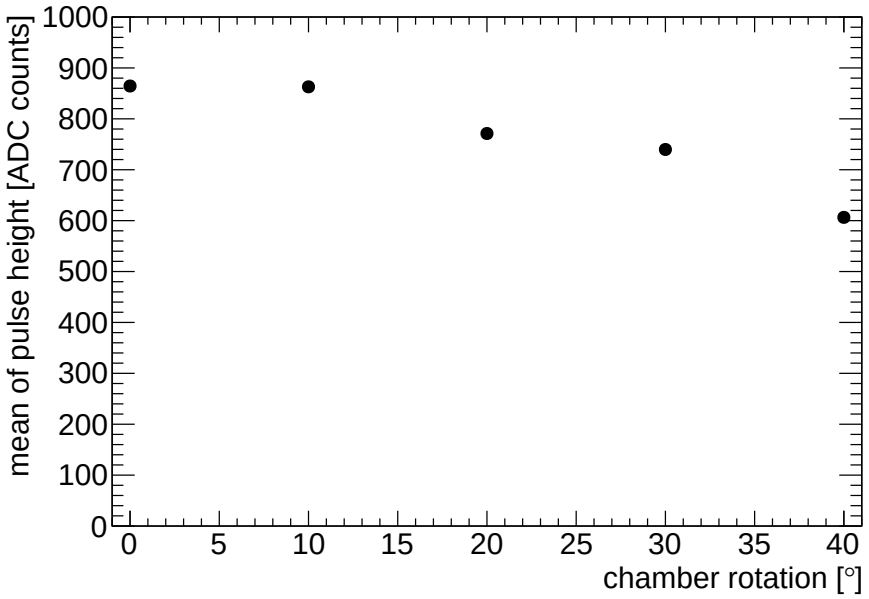

Figure 7.26: Averaged pulse height for the strip with the highest pulse height in one cluster as a function of the chamber rotation. With larger chamber rotation the pulse height decreases due to the spreading of the ionization charge over more strips. The lines are only to guide the eye.

By comparing the measured hit position in two Micromegas oriented back-to-back the spatial resolution can be determined as well. Assuming the spatial resolution of both detectors to be identical the result has to be divided by $\sqrt{2}$ due to the superposition of the two Gaussian functions. This method is insensitive to the time-jitter and t_{mid} as well, except for the combination of centroid and TPC-like method, because the effect due to the time-jitter does not have to have the same impact on the reconstructed hit position for both detectors and the same traversing pion. The results for this back-to-back method are shown in figure 7.27 for the three methods hit position reconstruction, the centroid method, the TPC-like method and the combination of these two methods. Using the combined method for the hit position reconstruction yields the best results for the back-to-back method, but it is not as good as the spatial resolution, when tracking the pions through the Micromegas telescope. Again the spatial resolution using the TPC-like method does not improve for larger chamber rotations.

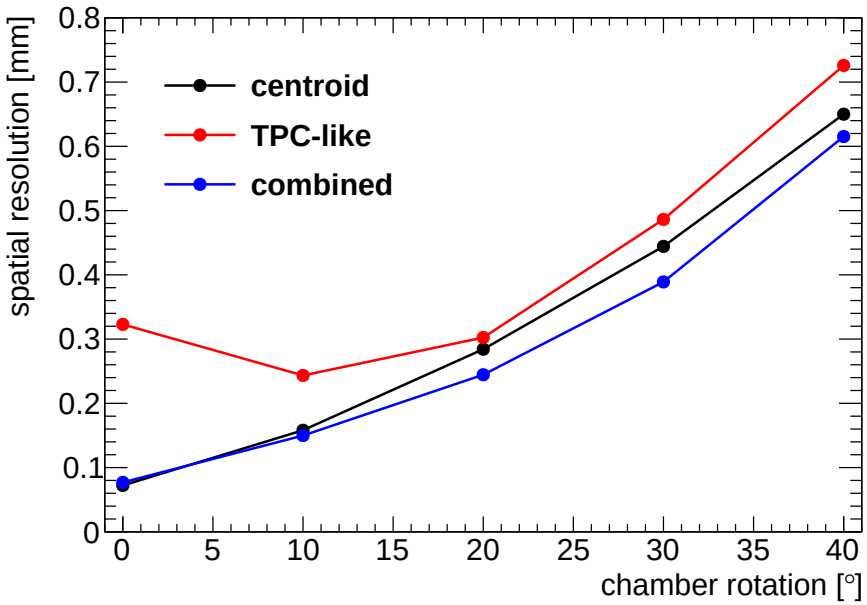

Figure 7.27: Spatial resolution as a function of the chamber rotation determined with two detectors oriented back-to-back. The result for this reconstruction method is not as good as the result for the spatial resolution for tracking the pions and comparing the predicted hit position with the measured hit position. The back-to-back reconstruction method is insensitive to the time-jitter and the effective time for a hit in the middle of the drift region, except for the combined method, which is not insensitive on the time-jitter. For the back-to-back method the spatial resolution using the combined method shows the best result for all chamber rotations. The lines are only to guide the eye.

For the determination of the spatial resolution of the large prototype Micromegas L1 it is not possible to eliminate the time-jitter, because the reference detectors were not rotated during the measurement. Thus the spatial resolution degrades with chamber rotation using the TPC-like or combined method (see fig. 7.28). Additionally the high noise level of the

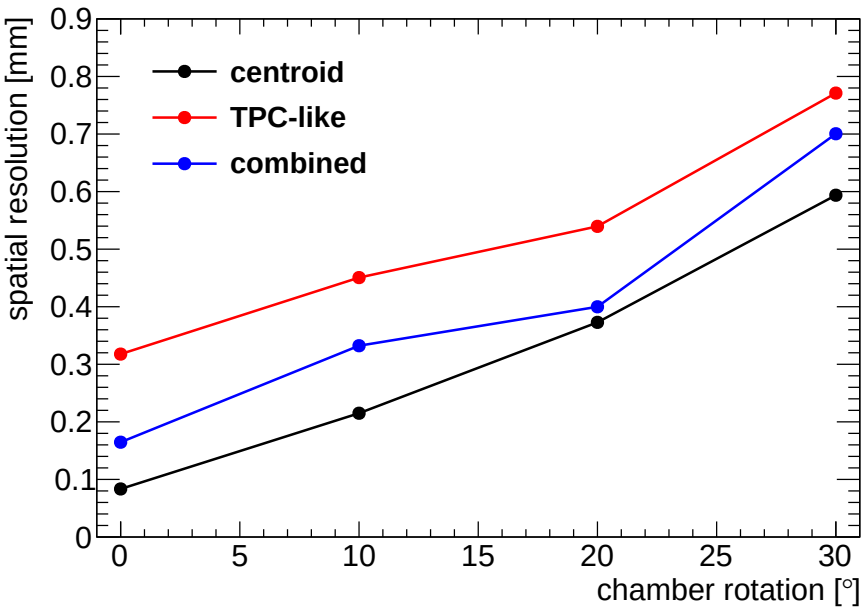

Figure 7.28: Spatial resolution as a function of the chamber rotation for all reconstruction methods for the large prototype Micromegas L1. The spatial resolution using the TPC-like hit reconstruction is for no chamber rotation better than the centroid method, because of the high noise level of this detector and thus the reconstruction of the track angle not working well. Furthermore it is not possible to correct for the time-jitter. This worsens the spatial resolution as well. Therefore the spatial resolution using the combined method to reconstruct the hit position also cannot be better than using the centroid method. The lines are only to guide the eye.

detector degrades the reconstruction of the track angle and thus the hit reconstruction using the TPC-like method. In this case the spatial resolution using the centroid method is the best for all chamber rotations. This measurement is sensitive to the timing t_{mid}, which is the effective time for a hit in the middle of the drift region. The distribution shown in figure 7.13 was used to determine $t_{mid} = 81.25\,\text{ns}$. To verify if this value is correct, it was varied in 5 ns steps in both directions and the spatial resolution using the TPC-like method was determined. Figure 7.29 shows the spatial resolution as a function of t_{mid}, which stays constant between about 65 ns and 85 ns. It seems $t_{mid} = 81.25\,\text{ns}$ is a reasonable value for the timing equivalent to the middle of the drift region.

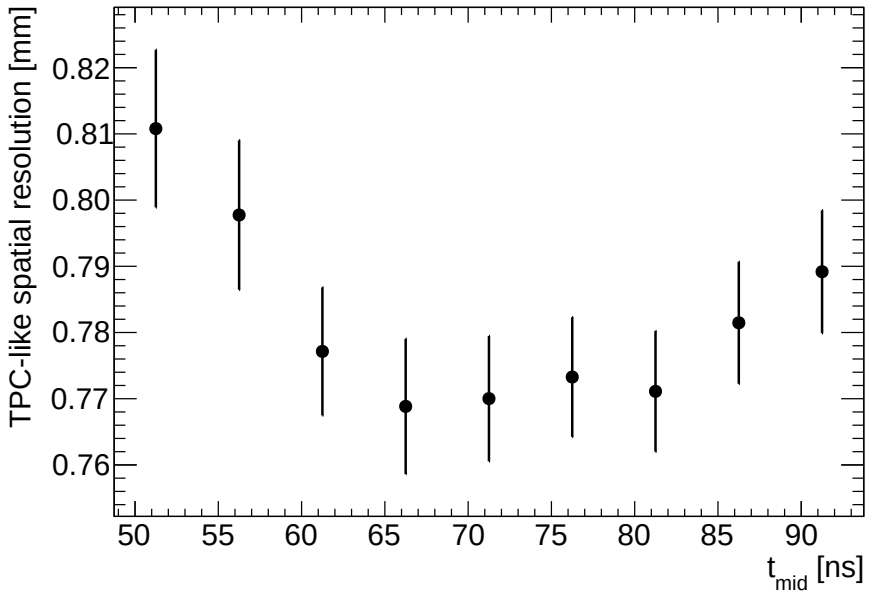

Figure 7.29: Spatial resolution as a function of the timing t_{mid}, which is the effective time for a hit in the middle of the detector volume determined with the TPC-like method. $t_{mid} = 81.25\,\text{ns}$ is the timing determined using the drift-time spectrum shown in figure 7.13. The spatial resolution does not improve using other timing due to a possible mis-reconstruction of t_{mid}. Therefore the reconstructed value of t_{mid} is appropriate.

7.3 Comparison to CRF Results

The spatial resolution as a function of the reference angle is determined for the calibration measurement in the Cosmic Ray Facility (CRF) for a one day measurement with the same parameters as during the testbeam campaign. No cut on multiple scattering was applied for determining the spatial resolution due to the low statistics. Figure 7.30 shows the result for all three hit position reconstruction methods. With a measurement of the time-jitter in the CRF by storing the trigger time the signal timing is corrected for the time-jitter. The black dots represent the spatial resolution using the centroid method (see sec. 6.5). For the determination of the spatial resolution using the TPC-like method t_{mid} as a function of the measured deformation of the drift region was used. t_{mid} was determined considering the deformation of the drift region of the large prototype Micromegas (see sec. 6.4.2). Only tracks with a measured reference angle larger than 28° were considered for the determination of t_{mid} (see fig. 6.21), which yields the best result for the spatial resolution

The progression of the spatial resolution as a function of the reference angle for the large prototype Micromegas of the measurement in the CRF is very similar to the results for the small test Micromegas of the testbeam campaign with 120 GeV pions. But the absolute values are larger. This is probably due the multiple scattering of the cosmic muons, which was not considered due to low statistics. The TPC-like position reconstruction does not work as well as for the measurement during the testbeam campaign due to a

more sophisticated method to determine t_{mid}. But a minimum of the spatial resolution between 10° and 20° can be observed, which is in agreement with the result of the testbeam campaign. Compared to the results of the testbeam campaign the position reconstruction using the combination of the centroid and TPC-like method works better for large angles due to the correction of the time-jitter.

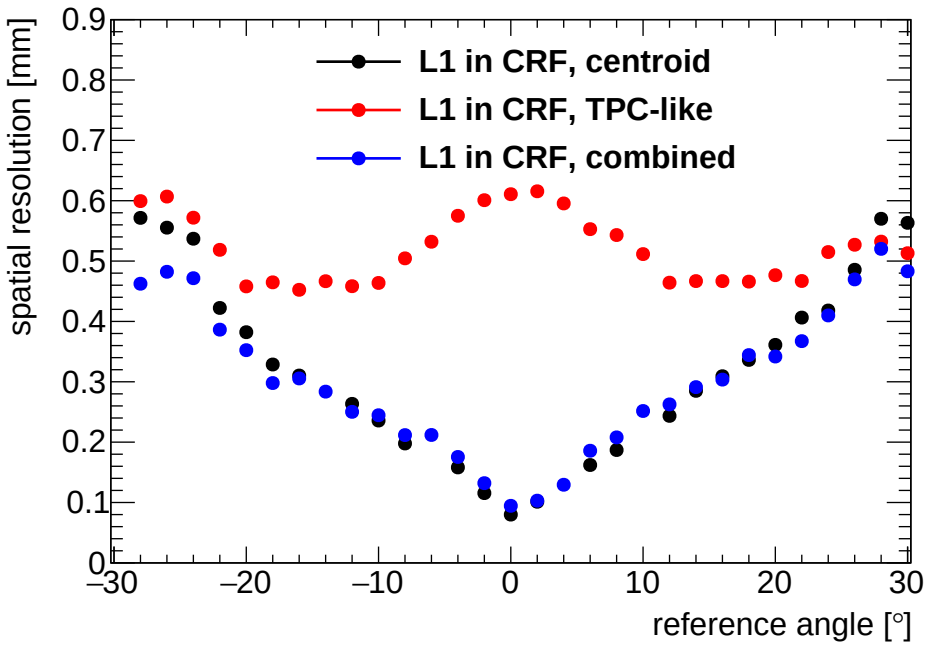

Figure 7.30: Spatial resolution for the large Micromegas prototype as a function of the reference angle measured using cosmic muons for the three hit position reconstruction methods. The spatial resolution determined using the TPC-like method has a minimum for reference angles between 10° and 20° and converges to the spatial resolution using the centroid method for 30°. The combined method yields a spatial resolution, which is as expected dominated by the centroid method for reference angles smaller than 15° and thus very similar. For reference angles larger than 15° the spatial resolution determined using the combined method shows the best result.

Chapter 8

Investigation of Argon and Neon Based Drift Gases

The drift of the electrons in the electric field is a key feature of the Micromegas. Depending on the gas mixture and the electric field in the drift region the drift velocity, the electron transparency of the mesh, and the transverse and longitudinal diffusion vary. All these gas properties have an impact on the spatial resolution. Even the high rate-capability is a function of the electron drift velocity. In the Cosmic Ray Facility (CRF) two different gas mixtures were investigated using the large prototype Micromegas L1, namely Ar:CO_2 93:7 vol% and Ne:CF_4 80:20 vol%. Measurements with a duration of about one day were taken varying the electric field in the drift region of the Micromegas. Differences in pulse height, tracking efficiency and spatial resolution of the two gas mixtures will be discussed.

8.1 Pulse Height and Efficiency

For a good comparison the pulse heights for the measurements using the two gas mixtures have to be similar. The amplification voltage of 570 V was chosen for the measurement with Ar:CO_2 93:7 vol% as it was the same for the calibration measurement. Figure 8.1 shows the pulse height as a function of the drift field. The pulse height is determined by using the most probable value of the Landau-like cluster charge distribution. For the measurement with Ne:CF_4 80:20 vol% an amplification voltage of 540 V was chosen, which yields a similar pulse height due to the larger gas amplification for Ne:CF_4 80:20 vol%. At the optimal working point of this detector of $E_{\text{drift}} = 300\,\text{V}\,\text{cm}^{-1}$ the pulse height using Ar:CO_2 93:7 vol% is almost the same as using Ne:CF_4 80:20 vol% (see fig. 8.1). The pulse height for both gas mixtures is the highest at $E_{\text{drift}} = 300\,\text{V}\,\text{cm}^{-1}$. Using Ar:$CO_2$ 93:7 vol% the rise at smaller drift fields is due to the much smaller electron drift velocity. With a low electron drift velocity not all electrons created in the drift region can be recorded during the integration time window of the readout. This effect occurs as well using Ne:CF_4 80:20 vol%, but is much smaller due to the larger drift velocity at low drift fields (see fig. 2.3). Due to the lower electron transparency of the mesh at higher drift fields the pulse

height drops again after the peak at $E_{\text{drift}} = 300\,\text{V}\,\text{cm}^{-1}$. Using Ar:$CO_2$ 93:7 vol% this effect is larger than using Ne:CF_4 80:20 vol% due to the lower electron transparency of the mesh (see sec. 4.2).

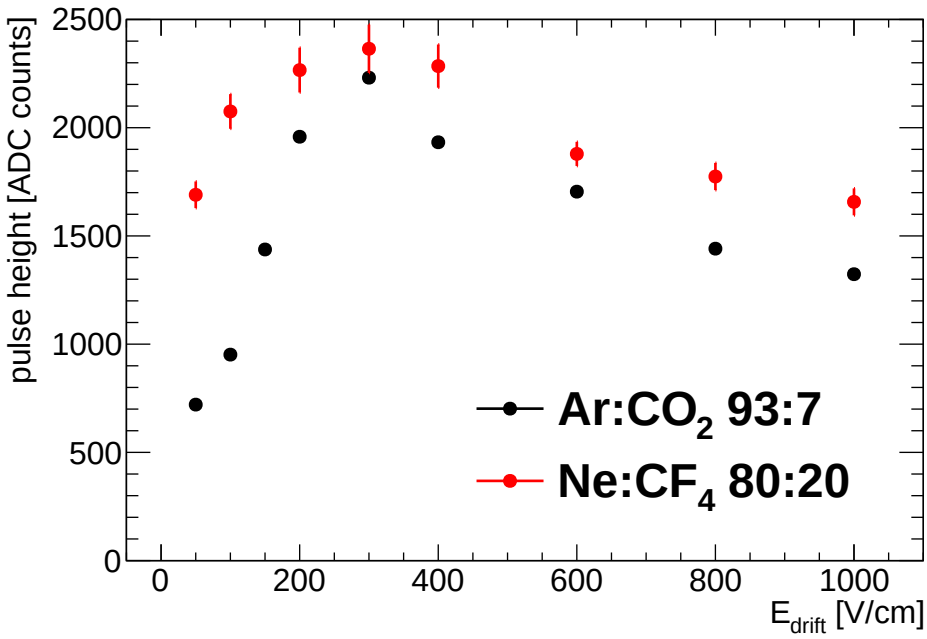

Figure 8.1: Pulse height as a function of the electric field in the drift region for Ar:CO_2 93:7 vol% (black) and Ne:CF_4 80:20 vol% (red). The rise at low electric fields is due to the small electron drift velocity such that the electrons created close to the cathode cannot be recorded during the integration time window of the readout. This effect is larger for Ar:CO_2 93:7 vol% than for Ne:CF_4 80:20 vol% due to the much faster electron drift in Ne:CF_4 80:20 vol%. The pulse height drop after the peak at $E_{\text{drift}} = 300\,\text{V}\,\text{cm}^{-1}$ follows the drop of the electron transparency of the mesh at higher drift fields, which drops faster for Ar:CO_2 93:7 vol% than for Ne:CF_4 80:20 vol%.

Figure 8.2 shows the number of strips in the leading cluster as a function of the electric field in the drift region. The curve for the strip multiplicity is similar to the curve for the pulse height, especially at low electric drift fields, where the lateral diffusion is similar for both gas mixtures. But at higher drift fields the lateral diffusion for Ar:CO_2 93:7 vol% is a factor of 2 to 3 larger than for Ne:CF_4 80:20 vol% (see fig. 2.4). This eliminates the effect of the lower electron transparency of the mesh and thus the strip multiplicities for both gas mixtures are almost equal.

The impact of the diffusion and drift velocity on the track efficiency is not as large as on the pulse height. The tracking efficiency is determined with the same criterion as in section 6.6. An event is counted as efficient, if the difference between measured hit position and predicted hit position is smaller than 5 mm. At low electric fields in the drift region a lower efficiency due to the before mentioned effect of integration time window can be seen in figure 8.3. For Ar:CO_2 93:7 vol% the efficiency plateau is almost reached at

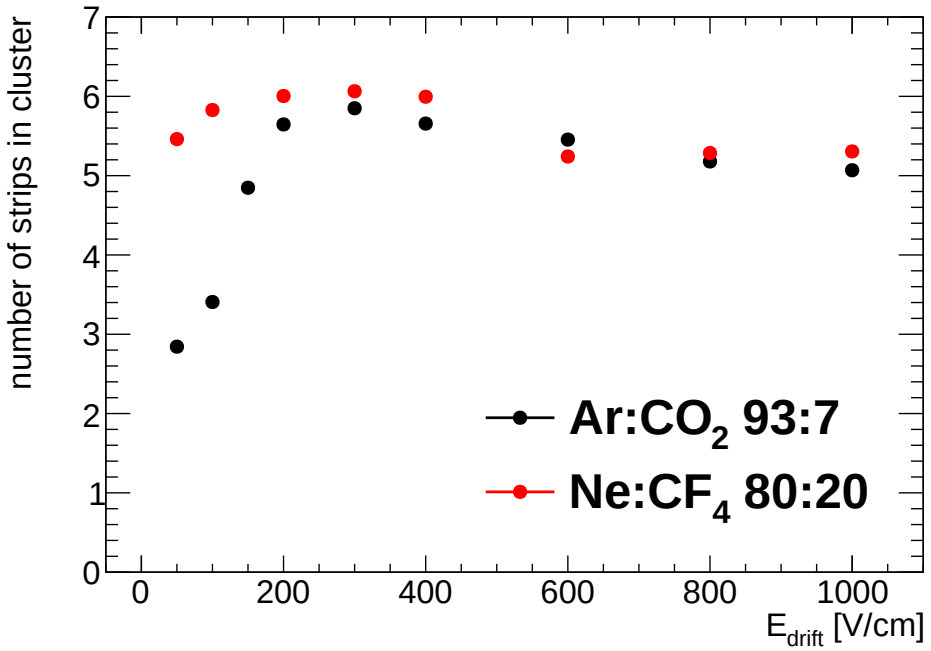

Figure 8.2: Number of strips in the leading cluster as a function of the electric field in the drift region for Ar:CO_2 93:7 vol% (black) and Ne:CF_4 80:20 vol% (red). For low drift fields the strip multiplicity is smaller due to the slower electron drift and the finite integration time of the readout. At $E_{\text{drift}} = 300\,\text{V}\,\text{cm}^{-1}$ the number of strips in the leading cluster is almost equal for Ar:CO_2 93:7 vol% and Ne:CF_4 80:20 vol%. As well as for higher drift fields, but here the two effects work in different directions. Ne:CF_4 80:20 vol% has a smaller lateral diffusion and Ar:CO_2 93:7 vol% has a lower electron transparency of the mesh. This results in almost the same strip multiplicity.

$E_{\text{drift}} = 150\,\text{V}\,\text{cm}^{-1}$, whereas for Ne:$CF_4$ 80:20 vol% the efficiency plateau starts already at $E_{\text{drift}} = 100\,\text{V}\,\text{cm}^{-1}$. For high drift fields a small influence of the electron transparency of the mesh can be seen, but the efficiency loss is not very large.

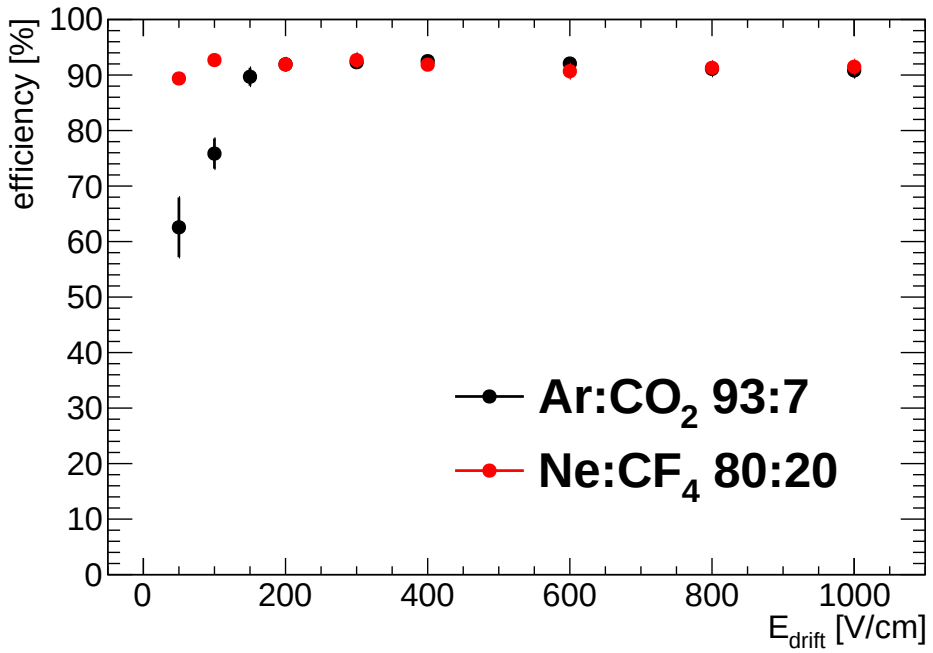

Figure 8.3: Tracking efficiency as a function of the electric field in the drift region for Ar:CO_2 93:7 vol% (black) and Ne:CF_4 80:20 vol% (red). The effect of the slower electron drift can be seen again for low drift fields, but for higher drift fields the tracking efficiency for both gas mixtures is equal and almost constant.

8.2 Spatial Resolution

The spatial resolution is determined for a point of the track on the plane in the middle of the drift region. For the discussion of the spatial resolution determined using the centroid method (see sec. 2.4.2) an ideal drift region of 5 mm is assumed for the calculation of the electric field in the drift region. This means the deformation of the drift region is not considered and the mentioned drift fields are the maximum drift fields for each configuration. Whereas the deformation of the drift region needs to be considered for the determination of the drift time measurement used for the TPC-like method (see sec. 2.4.3).

Figure 8.4 shows the spatial resolution determined using the centroid method as a function of the reference angle for Ar:CO_2 93:7 vol% and various electric fields in the drift region. For a drift field of $50\,\text{V}\,\text{cm}^{-1}$ the spatial resolution seems to be very good, but due to the integration time window of the readout only a small amount of the total ionization charge created in the detector is read out. This mimicks a very thin drift region, which is good for the position reconstruction using the centroid method. But the

efficiency is only about 60 % (see fig. 8.3). All other drift fields yield a very similar spatial resolution. It seems that the spatial resolution improves slightly from $E_{\text{drift}} = 150\,\text{V}\,\text{cm}^{-1}$ to $E_{\text{drift}} = 300\,\text{V}\,\text{cm}^{-1}$ due to an increasing transverse diffusion (see fig. 2.4). But the spatial resolution degrades again for drift fields higher than $600\,\text{V}\,\text{cm}^{-1}$ despite the further increasing transverse diffusion. This is due to the decreasing electron transparency of the mesh, which acts in the opposite direction as the transverse diffusion. The electron transparency of the mesh is only about 60 % at $1000\,\text{V}\,\text{cm}^{-1}$ (see fig. 4.7).

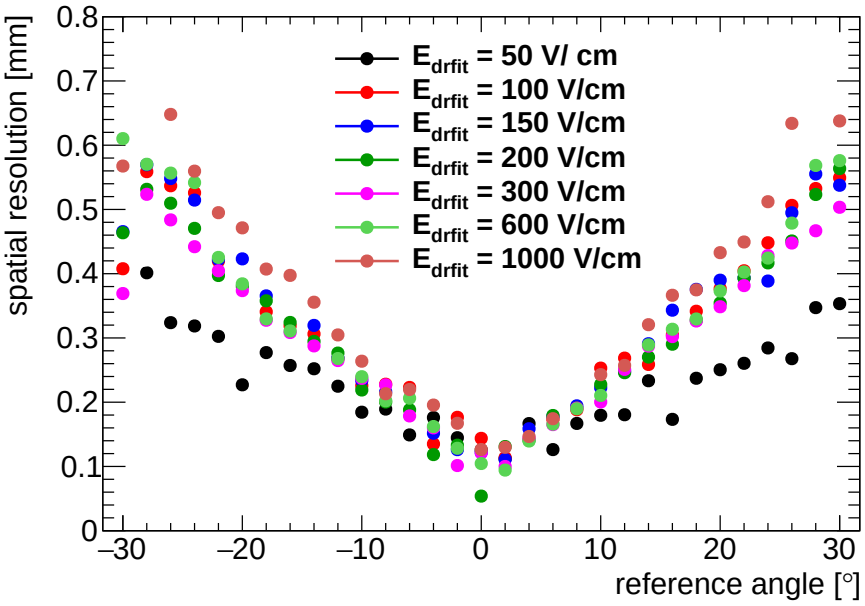

Figure 8.4: Spatial resolution as a function of the reference angle determined using the centroid method for various drift fields in Ar:CO_2 93:7 vol%. Almost all drift field yield a similar spatial resolution, except for $E_{\text{drift}} = 50\,\text{V}\,\text{cm}^{-1}$, where the spatial resolution for larger track inclinations is better, and for $E_{\text{drift}} = 1000\,\text{V}\,\text{cm}^{-1}$, where the spatial resolution degrades due to a lower electron transparency of the mesh.

The results of the spatial resolution determined with the centroid method for Ne:CF_4 80:20 vol% and various drift fields are shown in figure 8.5. For Ne:CF_4 80:20 vol% the spatial resolution for all drift fields is even more similar than for Ar:CO_2 93:7 vol%. At an electric field of $50\,\text{V}\,\text{cm}^{-1}$ the spatial resolution yields the largest values, which is probably an effect of the integration time window of the readout. But not like for Ar:CO_2 93:7 vol% at $E_{\text{drift}} = 50\,\text{V}\,\text{cm}^{-1}$, where a thinner drift region is mimicked and signals on some strips are completely lost, but probably only the peaks of the slowest signals are lost. Therefore the pulse height on individual strips is wrongly reconstructed. The efficiency at $E_{\text{drift}} = 50\,\text{V}\,\text{cm}^{-1}$ is only slightly degraded similar to the efficiency of Ar:CO_2 93:7 vol% at $E_{\text{drift}} = 150\,\text{V}\,\text{cm}^{-1}$. Therefore this effect has only a small impact on the spatial resolution. For higher electric fields the spatial resolution decreases again slightly due to the decreasing electron transparency of the mesh. This effect is not as strong as for Ar:CO_2 93:7 vol%. Even at $E_{\text{drift}} = 1000\,\text{V}\,\text{cm}^{-1}$ the electron transparency of the mesh is still at about 90 %

(see fig. 4.8). But the transverse diffusion for Ne:CF_4 80:20 vol% is smaller than for Ar:CO_2 93:7 vol%. Therefore this effect does not act against the electron loss at the mesh.

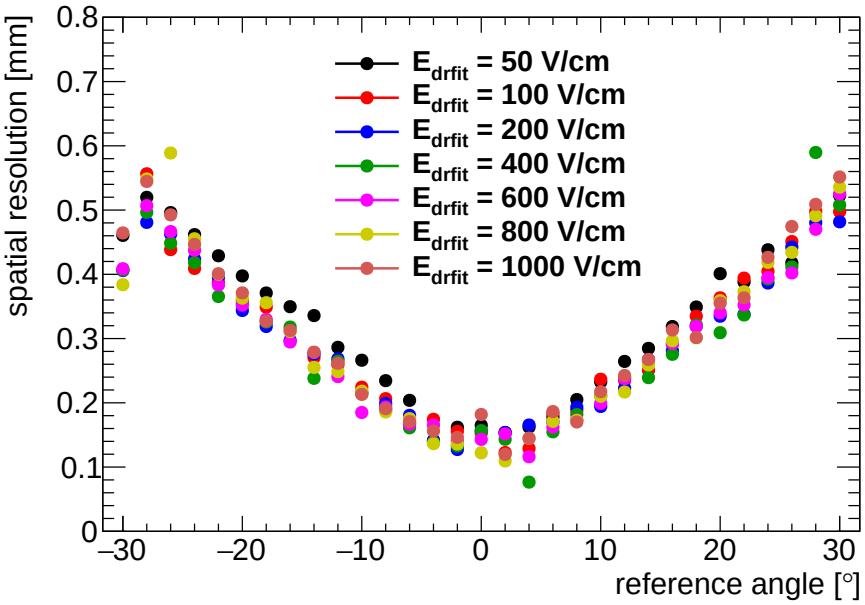

Figure 8.5: Spatial resolution as a function of the reference angle determined using the centroid method for various drift fields in Ne:CF_4 80:20 vol%. All drift fields yield a similar spatial resolution.

For the determination of the spatial resolution using the TPC-like method the effective time t_{mid} for a hit in the middle of the drift region is determined as a function of the deformation of the drift region (see sec. 6.4.2). Only muon tracks with an inclination larger than 28° were considered for the determination of t_{mid}, which yielded the best result. Figure 8.6 shows the spatial resolution determined using the TPC-like method for Ar:CO_2 93:7 vol% and various drift fields. At a drift field of 50 V cm^{-1} the TPC-like method shows the worst result due to the loss of signals, which could not be recorded due to a drift time larger than the integration time window of the readout. For drift field from $E_{\text{drift}} = 100\,\text{V}\,\text{cm}^{-1}$ to $E_{\text{drift}} = 200\,\text{V}\,\text{cm}^{-1}$ the spatial resolution improves, because the integration time effect and the transverse diffusion gets smaller. Starting around $E_{\text{drift}} = 300\,\text{V}\,\text{cm}^{-1}$ the electron transparency decreases and the transverse diffusion increases, therefore the spatial resolution degrades. It seems, that the impact of the longitudinal diffusion is negligible, which starts decreasing around $E_{\text{drift}} = 300\,\text{V}\,\text{cm}^{-1}$ (see fig. 2.5) and thus should improve the spatial resolution.

The spatial resolution determined using the TPC-like method for Ne:CF_4 80:20 vol% and various drift fields is shown in figure 8.7. At a drift field of 50 V cm^{-1} the TPC-like method yields the best result for the spatial resolution. The spatial resolution degrades as a function of the drift field despite the decreasing transverse and longitudinal diffusion, which should improve the spatial resolution. Probably the spatial resolution using the TPC-like method degrades with larger drift fields due to the very high electron drift velocity of

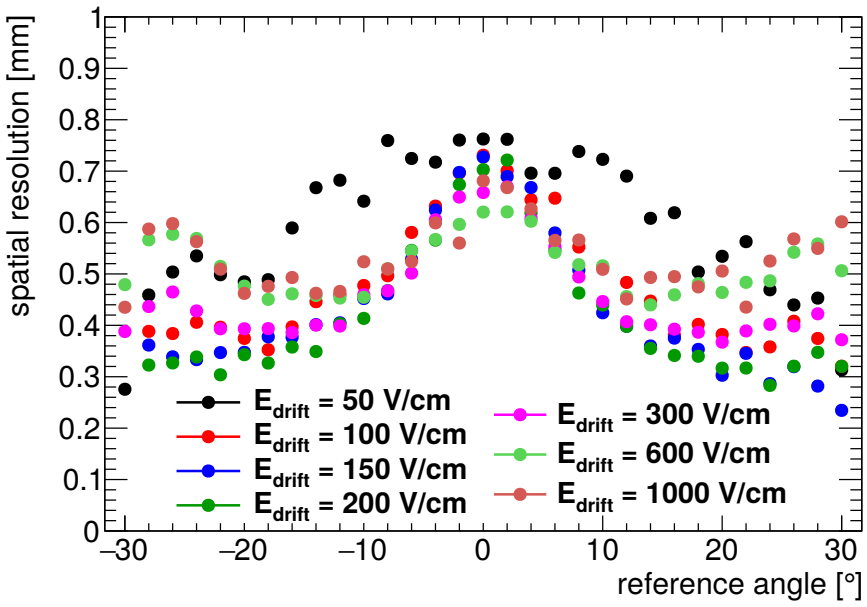

Figure 8.6: Spatial resolution as a function of the reference angle determined using the TPC-like method for various drift fields in Ar:CO_2 93:7 vol%. For $E_{\text{drift}} = 50\,\text{V}\,\text{cm}^{-1}$ this method does not work due to the loss of signals with a drift time larger than the integration time window of the readout. The spatial resolution improves from $E_{\text{drift}} = 100\,\text{V}\,\text{cm}^{-1}$ to $E_{\text{drift}} = 200\,\text{V}\,\text{cm}^{-1}$, but degrades again starting at $E_{\text{drift}} = 300\,\text{V}\,\text{cm}^{-1}$.

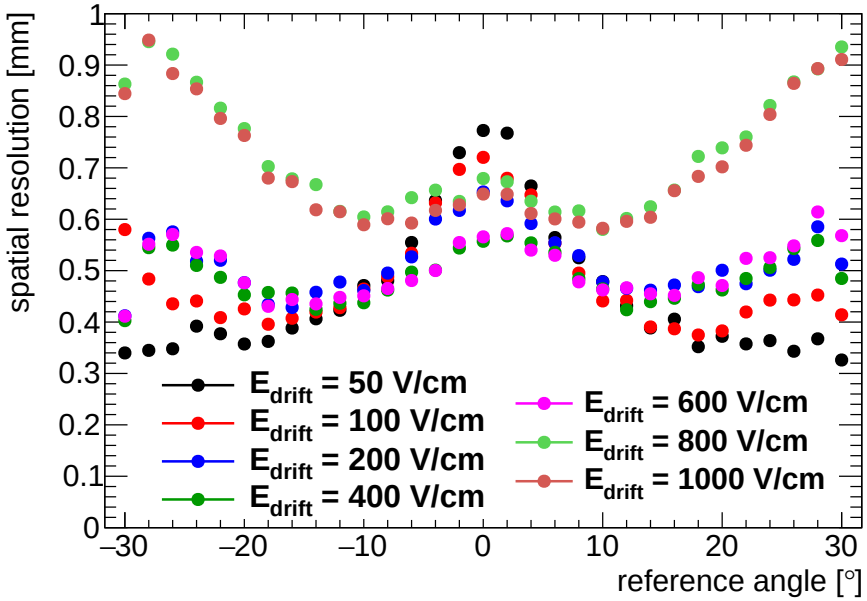

Figure 8.7: Spatial resolution as a function of the reference angle determined using the TPC-like method for various drift fields in Ne:CF_4 80:20 vol%. The spatial resolution degrades while increasing the drift field.

Ne:CF_4 80:20 vol% (see fig. 2.3). Therefore fitting the signal timing as a function of the strip number does not work very well, if the signal timing on all strips hit is very similar. For $E_{\text{drift}} = 800\,\text{V}\,\text{cm}^{-1}$ and $E_{\text{drift}} = 1000\,\text{V}\,\text{cm}^{-1}$ the determination of t_{mid} failed probably due to the mis-reconstructed signal timing.

Figure 8.8 shows the difference of the signal timing of the first and the last responding strip for a single particle track in Ne:CF_4 80:20 vol% at $E_{\text{drift}} = 1000\,\text{V}\,\text{cm}^{-1}$ (left) and for Ar:CO_2 93:7 vol% at $E_{\text{drift}} = 600\,\text{V}\,\text{cm}^{-1}$ (right). The drift velocity for Ne:CF_4 80:20 vol% at $E_{\text{drift}} = 1000\,\text{V}\,\text{cm}^{-1}$ is twice as large as for Ar:CO_2 93:7 vol% at $E_{\text{drift}} = 600\,\text{V}\,\text{cm}^{-1}$ (see fig. 2.3). Therefore the difference of the signal timing for the first and last responding strip should be a factor of 2 smaller than for Ar:CO_2 93:7 vol% at $E_{\text{drift}} = 600\,\text{V}\,\text{cm}^{-1}$. But the order of magnitude of the difference of the signal timing for both gas mixtures is similar. It seems that the reconstruction of the signal timing for Ne:CF_4 80:20 vol% at $E_{\text{drift}} = 1000\,\text{V}\,\text{cm}^{-1}$ does not work as well as for Ar:CO_2 93:7 vol% at $E_{\text{drift}} = 600\,\text{V}\,\text{cm}^{-1}$. If the difference of the signal timing of the first and last responding strip is larger, the position reconstruction using the TPC-like method yields better results for lower electron drift velocities.

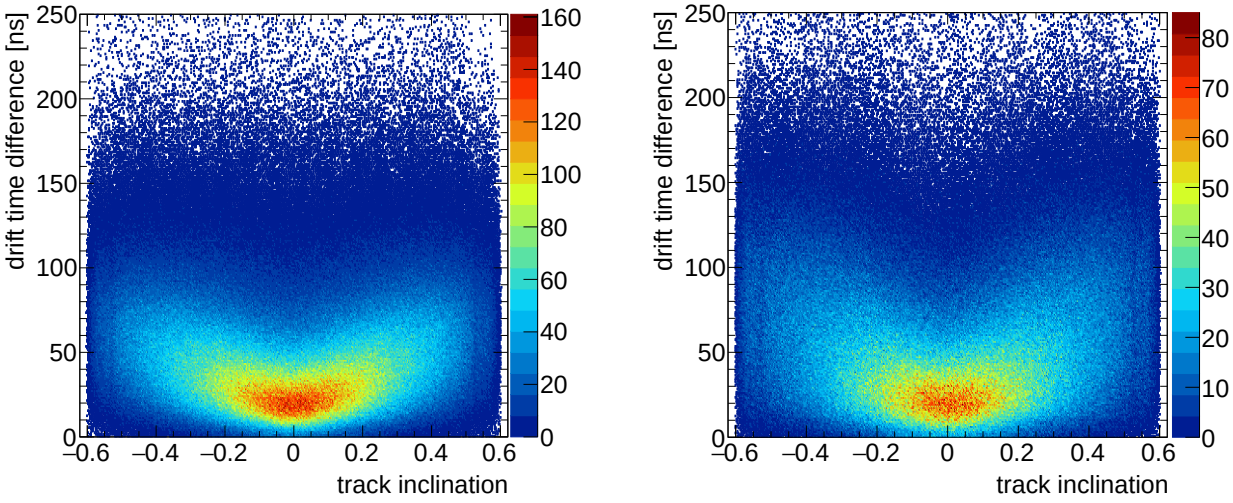

Figure 8.8: Difference of the signal timing of the first and last responding strip for a single particle track as a function of the track inclination. Left: For Ne:CF_4 80:20 vol% at $E_{\text{drift}} = 1000\,\text{V}\,\text{cm}^{-1}$. Right: For Ar:$CO_2$ 93:7 vol% at $E_{\text{drift}} = 600\,\text{V}\,\text{cm}^{-1}$. The difference of the drift time for Ne:CF_4 80:20 vol% is in the same order of magnitude as for Ar:CO_2 93:7 vol%, but it should be a factor of two smaller due to the twice as large electron drift velocity.

For Ne:CF_4 80:20 vol% all drift field have shown a similar spatial resolution using the centroid method. The hit position reconstruction using the TPC-like method works best for Ar:CO_2 93:7 vol% at $E_{\text{drift}} = 200\,\text{V}\,\text{cm}^{-1}$ for track inclination above 15°. This configuration yields also a good result for the hit position reconstruction using the centroid method and should be used as working point.

Chapter 9

Muon Tomography with the Cosmic Ray Facility

One application of cosmic muons is the muon tomography. Using the two reference tracking detectors of the Cosmic Ray Facility (CRF) in Garching (see sec. 6.1) the intersection point of the tracks reconstructed by the MDT chambers can be determined in y and z direction. This point corresponds to the scattering point of the traversing muon. And therefore the region between the two MDT chambers with the most dense material can be resolved.

Figure 9.1 shows the point of Coulomb scattering for a 10 cm wide segment along the MDT wires. A limited region in x direction was chosen to prevent the superposition of various items located in the CRF. Only scattering angles above 3° were considered due to the increased uncertainty on the intersection points for the two reconstructed tracks with a small slope difference, whereas the width of the most probable scattering angle in the large prototype Micromegas L1 is about 0.1° (see sec. 2.1). The two multilayers of both MDT chambers can be seen in the upper and lower part in the figure. And additionally the large prototype Micromegas (see sec. 6.2) installed between the two MDT chambers. It has an aluminum frame around the active area, which can be seen at $y = -500$ and $y = 500$. At $y = -750$ and $y = 750$ the holding structure can be seen on which the Micromegas is placed. It consists of $(10 \times 5)\,\mathrm{cm}^2$ hollow bars with a wall thickness of about 5 mm. Figure 9.2 shows a sketch of the setup as explanation. The increased amount of points of Coulomb scattering in the upper multilayer of the lower MDT ($-400 < z < -300$) occurs probably due to the additional energy loss of the cosmic muon in the large prototype Micromegas.

According to figure 9.1 it seems like the resolution of the muon tomography is in the order of the binning of the histogram and thus about 1 cm for the precision direction (y). But the position of the Coulomb scattering is not as well defined for the z direction due to the determination of the intersection point. The most probable track inclination is 0° for cosmic muons. If the two tracks have a similar slope the uncertainties on the slopes have a huge impact on the reconstructed z position, but only a small impact on the reconstructed y position of the intersection point. Therefore the y position of the intersection point is much better defined than the z position. It seems that the resolution is about 5 cm in z direction.

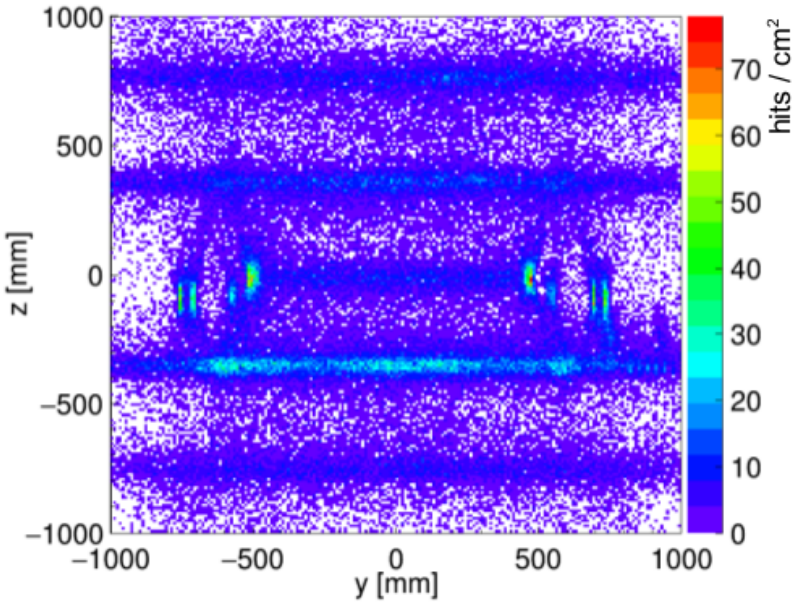

Figure 9.1: Measured intersection of the two reference tracks for a 10 cm wide segment in x direction and for scattering angle above 3°. The higher the density of the material the more probable is a Coulomb scattering of the traversing muon. The two multilayers of each MDT chamber and the large prototype Micromegas with its holding structure can be seen, especially the aluminum bars, which frame the active area of the Micromegas. Figure taken from [Herrmann, 2017].

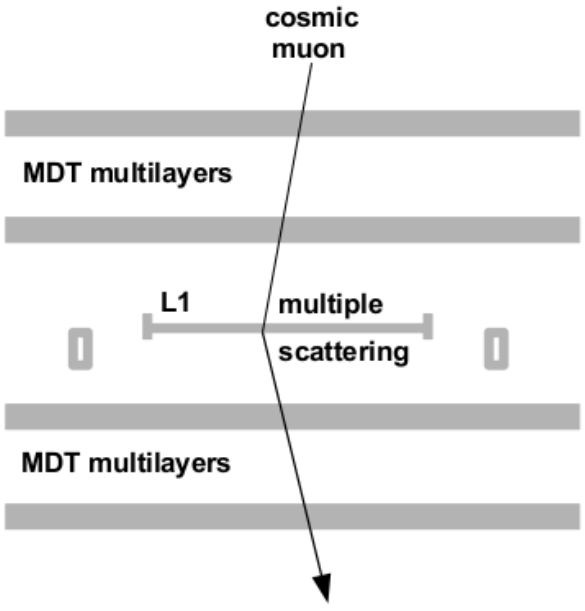

Figure 9.2: Schematic of the experimental setup in the Cosmic Ray Facility. With the muon tomography the two multilayers of each MDT chamber, the large Micromegas prototype (L1) and its holding structure can be resolved.

Chapter 10

Summary

Due to the upgrade of the Large Hadron Collider (LHC) at CERN to the High Luminosity LHC the instantaneous luminosity will increase up to $7 \times 10^{34}\,\mathrm{s^{-1}cm^{-2}}$ and maybe even up to $10 \times 10^{34}\,\mathrm{s^{-1}cm^{-2}}$. The currently used detector technologies in the inner end-cap regions of the ATLAS Muon Spectrometer, the so-called Small Wheels, cannot cope with the increasing background hit rate requiring an upgrade of the Small Wheels as well. This upgrade is called New Small Wheel upgrade project (NSW). The new detector technologies have to be high-rate and trigger capable with excellent spatial resolution of around 100 µm to maintain the current momentum resolution of 15 % at 1 TeV muons. Small strip-Thin Gap Chambers (sTGC) and MICRO-MEsh GAseous Structure detectors (Micromegas) were chosen for this purpose. Each NSW will consist of eight small and eight large sectors, each on its own consisting of two sTGC wedges sandwiching two Micromegas wedges. Thus each NSW is a fully redundant system of eight active detection layers of sTGCs and eight active detection layers of Micromegas for tracking and triggering. The main purpose of the sTGCs, which are multi-wire proportional chambers, is the triggering and the main purpose of the Micromegas, which are micro pattern gaseous detectors, is precision tracking. This thesis focuses on the outer module of the small Mircomegas sectors (SM2), which are built at German construction sites. To assure the excellent spatial resolution and thus the momentum resolution in the ATLAS experiment the detectors have to be constructed very accurately and have to be calibrated, in case a perfect construction is not possible.

Each module is assembled of five sandwich panels, three drift panels and two readout panels. The gas volumes between the panels are the four active detection volumes. Hence a module is also called quadruplet. Each panel consists of an aluminum honeycomb core framed by aluminum bars and sandwiched by printed circuit boards (PCB). The PCBs contain either the anode structures or the cathodes of the Micromegas, both photo-lithographically etched. Due to size limitation of the width of the PCBs the active detector layers of the SM2 modules have to be constructed out of three PCBs. To assure the alignment of the readout strips with an accuracy of 30 µm dedicated precision tools were developed. Additionally the stiffening panels have to have a planarity with an RMS of 37 µm. The first pre-series module has shown, that these ATLAS requirement can be fulfilled. After gluing of the sandwich panels the quadruplet is assembled using precision

spacers glued into the panel to guide the panels accurately on rails mounted on the assembly frame. With these spacers the relative alignment of the two readout panels is assured, which is conserved using precision pins and bushes glued into the panels as well. During assembly also six so-called interconnections are installed in the quadruplets to prevent a deformation of the drift region due to a slight overpressure or 2-3 mbar during operation in the ATLAS detector.

After the assembly of the quadruplets they will be installed in the LMU Cosmic Ray Facility (CRF) in Garching. The CRF consists of two Monitored Drift Tube chambers (MDT) as reference tracking detectors sandwiched by two trigger hodoscopes, which provide a coarse position information perpendicular to the precision direction and a trigger with sub-ns time-resolution. The CRF has an active area of about $(2.2 \times 4)\,\mathrm{m}^2$ with an angular acceptance between $-30°$ and $+30°$. Between the lower MDT and the lower trigger hodoscope a 34 cm thick iron absorber in installed, thus only cosmic muons with an energy above 600 MeV trigger the readout. To develop the calibration procedure a $1\,\mathrm{m}^2$ prototype Micromegas was installed in the CRF. The large prototype Micromegas was constructed out of two readout PCBs and had no stabilization against overpressure. For the alignment of the Micromegas to the reference muon tracks the detector was subdivided into 160 partitions using the 16 APV25 front-end boards and the position information along the strips provided by the trigger hodoscopes. Aligning each of the subdivisions separately a shift between the two readout PCBs of about 100 µm and a rotation of about $350\,\mu\mathrm{m\,m}^{-1}$ was determined. This calibration measurement is also very sensitive to strip pitch variation in the order of a few nanometers. Whereas the assumed strip pitch of the large prototype Micromegas is 450 µm a deviation of 60 nm for one readout PCB and 20 nm for the other was reconstructed. Additionally a deformation of the drift region of about 3 mm could be measured, which is in good agreement with an ANSYS finite element simulation and was confirmed by a drift time measurement. Considering the single track prediction accuracy of the MDT reference chambers the large prototype Micromegas yielded a spatial resolution determined with the charge weighted strip position (centroid) of about 150 µm for tracks perpendicular to the detection plane. The spatial resolution using this centroid method degrades with a higher track inclination up to a value of about 700 µm at reference angles of $\pm 30°$. With cuts on the slope difference of the muon track in both MDTs at the plane of the large prototype Micromegas the spatial resolution for perpendicular tracks stays almost constant, but for higher track inclination the spatial resolution improves by about 100 µm with the cut on the reference slope. This is probably caused by the ambiguities in the track reconstruction of the MDTs at $\pm 30°$ due to the hexagonal close packing of the tubes. Either the muons traverse close to the tube walls, where the spatial resolution is better than close to the wire, but with increased material in the muon path, or the muons traverse close to the wire with less material in the path, but a degraded spatial resolution. This calibration measurement took about one week. A shorter measurement of about one day has yielded a spatial resolution of about 80 µm for tracks perpendicular to the detection plane. It seems there is a contribution of about 100 µm as a function of time due to thermal movement of the experimental setup, which is reasonable considering the size of the experimental setup.

To investigate the influence of the strip length on the detector performance the large prototype Mircomegas was installed in a Mircomegas telescope consisting of eight $(10 \times 10)\,\mathrm{cm}^2$ test Micromegas with one dimensional readout and four $(9 \times 9)\,\mathrm{cm}^2$ reference detectors with two dimensional readout in a testbeam campaign with 120 GeV pions at CERN. During this measurement the large prototype Micromegas had a signal-to-noise ratio of only about 10 and thus the reconstruction of the track angle in a single plane using a drift time measurement did work only minorily, whereas in the CRF with a two times higher signal-to-noise ratio this method worked reasonably well. Due to the high noise level of the large prototype Micromegas during the testbeam campaign the spatial resolution determined using the centroid method for position reconstruction was not as good as for the small test Micromegas, which have also shown a degradation of the spatial resolution for larger track inclination up to 550 µm at 40°. Using the drift time measurement for the reconstruction (TPC-like) of the hit position the small test Micromegas yielded the best result for a chamber rotation of 20°. Whereas the combination of both methods is dominated by the centroid method for small track inclinations, it is dominated for larger track inclination by the TPC-like method as expected. This behavior could also be observed with the calibration measurement in the CRF.

Measurements with different drift gas mixtures, namely Ar:CO_2 93:7 vol% and Ne:CF_4 80:20 vol%, have shown, that Ne:CF_4 80:20 vol% has a higher gas amplification. The pulse height and tracking efficiency is limited at low electric field in the drift region due to slower electron drift and the finite integration time window of the readout. If the electron drift velocity for ionization close to the cathode is very small, the electrons do not reach the readout strips within the integration time window. This effect is much stronger for Ar:CO_2 93:7 vol% due to the smaller drift velocity than for Ne:CF_4 80:20 vol%. A simulation of the electron transparency of the mesh using Garfield led to the selection of the mesh for the NSW Micromegas with a higher electron transparency. Additionally it has shown that the electron transparency of the mesh drops for Ne:CF_4 80:20 vol% below 90 % at a drift field of about $1000\,\mathrm{V\,cm^{-1}}$, whereas for Ar:$CO_2$ 93:7 vol% it drops already at $500\,\mathrm{V\,cm^{-1}}$ below 90 %. Therefore Ar:CO_2 93:7 vol% shows a larger variation of the spatial resolution as a function of the drift field, which is partly compensated for by the increased lateral diffusion. The best result for the spatial resolution determined with the TPC-like method is for Ar:CO_2 93:7 vol% at $E_{\mathrm{drift}} = 200\,\mathrm{V\,cm^{-1}}$ and for Ne:CF_4 80:20 vol% at $E_{\mathrm{drift}} = 50\,\mathrm{V\,cm^{-1}}$. It seems like the impact of the longitudinal diffusion, which is smaller for Ne:CF_4 80:20 vol% and thus should improve the spatial resolution, is negligible.

One application of cosmic muons is muon tomography. Using the two reference track detectors in the CRF the scattering point of the cosmic muons can the determined and thus areas with dense material can be resolved. This demonstrates the excellent resolution of the Cosmic Ray Facility.

At the end of this thesis all requirements for a series production and calibration of the large SM2 Micromegas are settled and will be met. All tools to investigate, to analyze, and to calibrate these $2\,\mathrm{m}^2$ sized SM2 modules in either testbeam or in the CRF are ready for application. The full production of the SM2 modules will now provide precisely calibrated SM2 modules for the NSW upgrade of the ATLAS detector.

Appendix A

Simulated Electron Drift Velocities for Various Gas Mixtures

Figure A.1 to A.3 show the electron drift velocity as a function of the drift field computed with *MAGBOLTZ* [Biagi, 1999] for various gas mixtures.

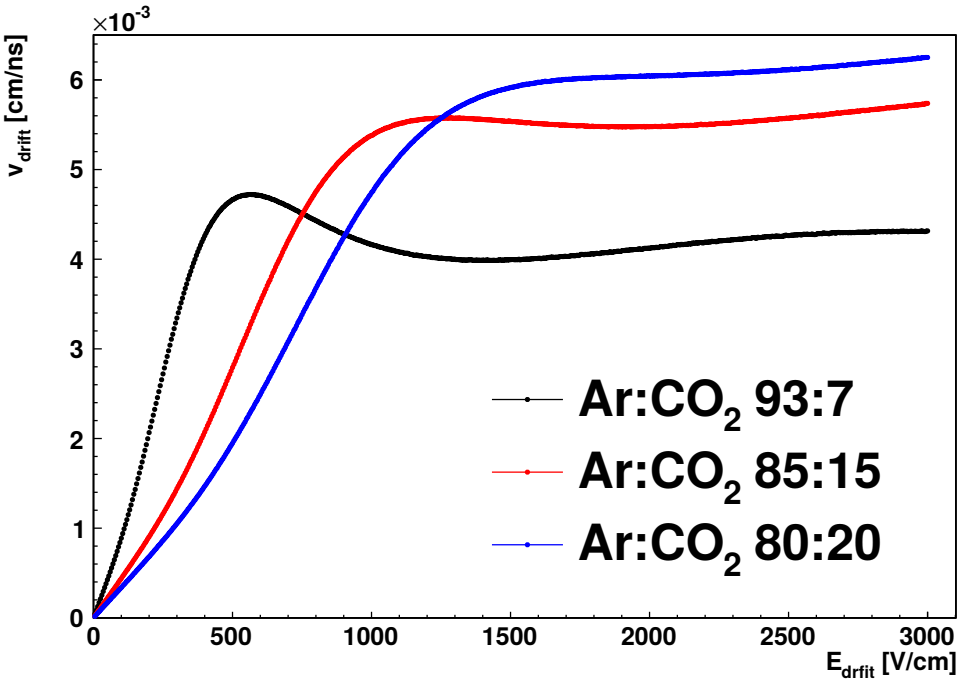

Figure A.1: Electron drift velocity as a function of the drift field for Ar:CO_2 with mixtures 93:7 vol%, 85:15:7 vol% and 80:20 vol%. Computed with *MAGBOLTZ* [Biagi, 1999].

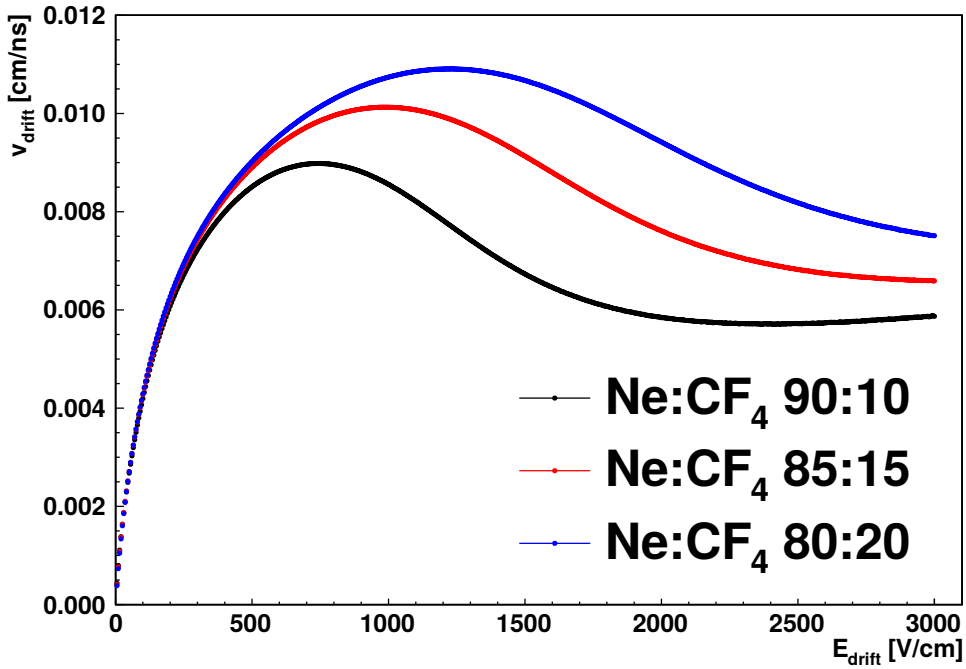

Figure A.2: Electron drift velocity as a function of the drift field for Ne:CF_4 with mixtures 90:10 vol%, 85:15:7 vol% and 80:20 vol%. Computed with *MAGBOLTZ*.

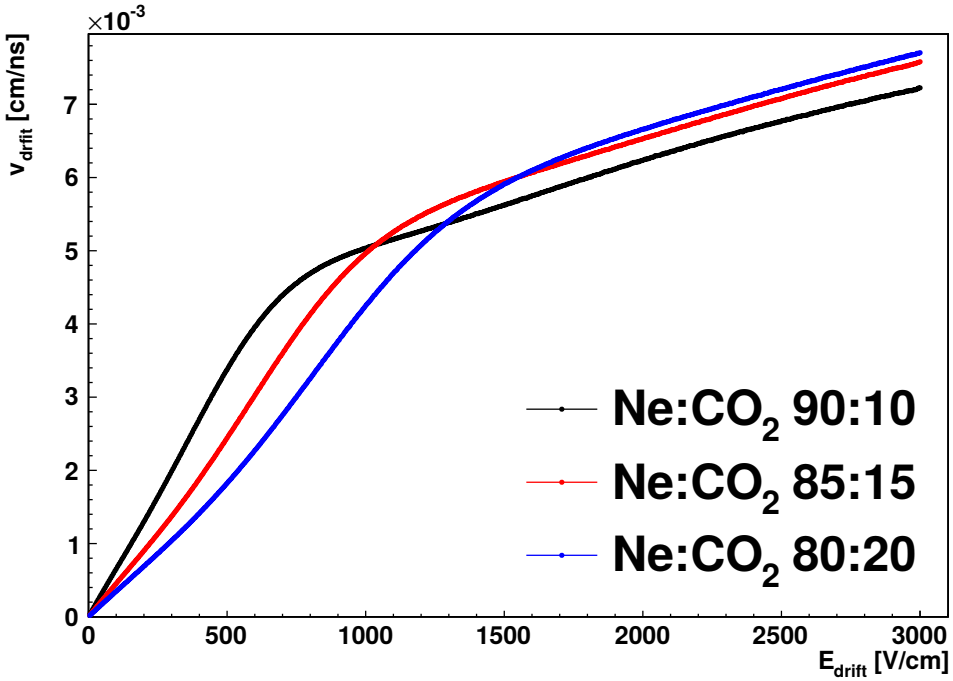

Figure A.3: Electron drift velocity as a function of the drift field for Ne:CO_2 with mixtures 90:10 vol%, 85:15:7 vol% and 80:20 vol%. Computed with *MAGBOLTZ*.

Appendix B

Drawing of the Zebra Holder

Figure B.1 shows a drawing of the Zebra holder used for the readout of the NSW Micromegas detectors constructed by CERN [EDMS CERN, 2016].

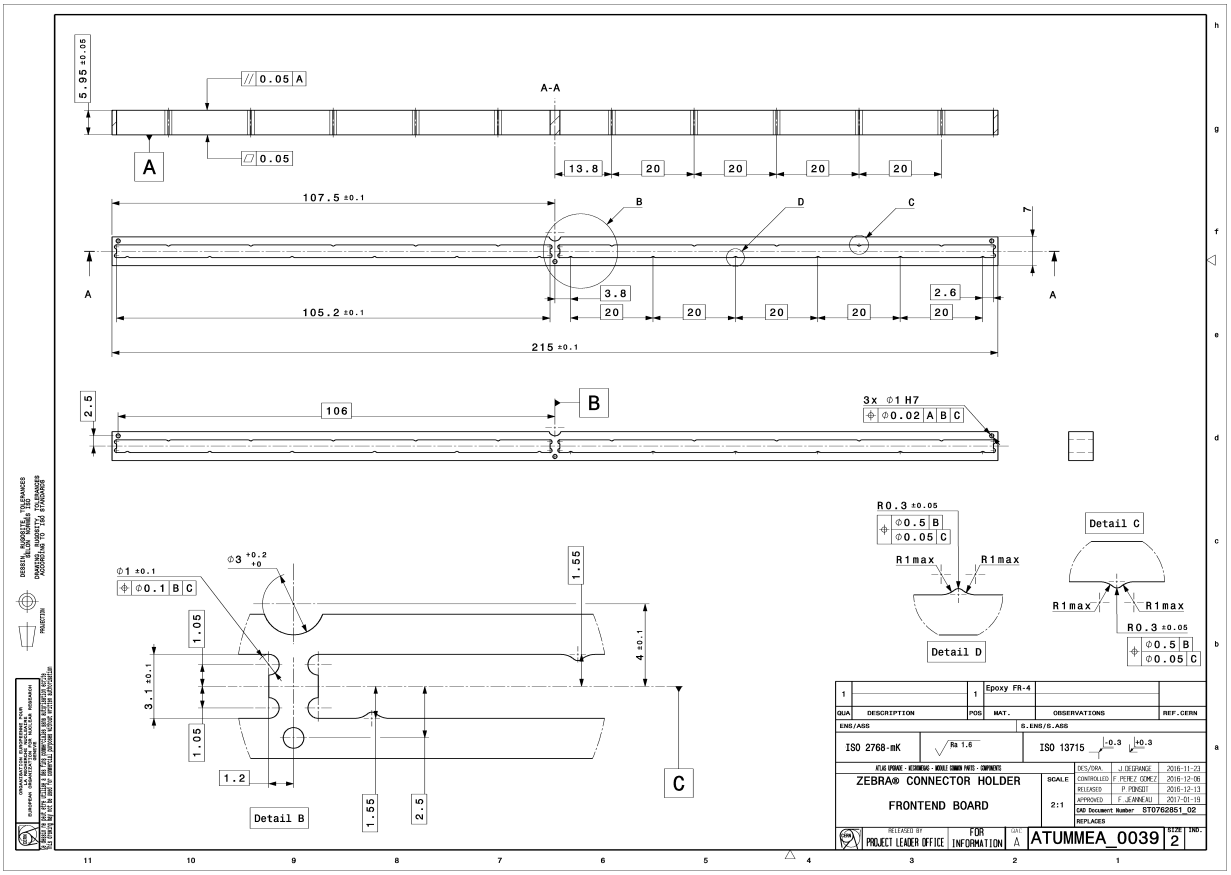

Figure B.1: Drawing of the Zebra holder used for the readout of the NSW Micromegas detectors. Eleven teeth are milled in the slots for the Zebra connector to fixate them. Figure taken from [EDMS CERN, 2016].

Appendix C

Spatial Resolution of MDT Chambers

Figure C.1 shows the spatial resolution of a single tube of Monitored Drift Tube (MDT) chambers as a function of the tube radius for various background irradiation rates. The spatial resolution of close to the tube wall is much better than close to the wire.

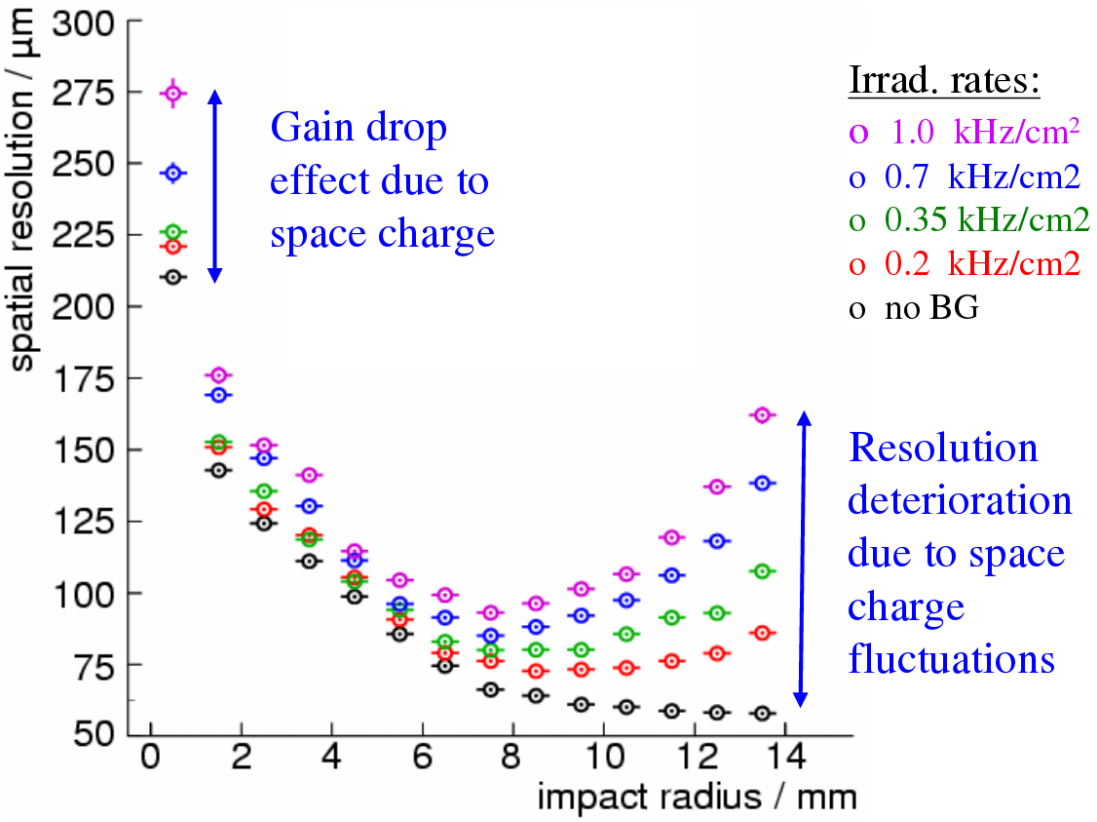

Figure C.1: Spatial resolution of a single MDT tube as a function of the impact radius for various irradiation rates. For an impact close to the wire the spatial resolution without background irradiation is about 210 µm and improves to about 60 µm close to the tube wall. Figure taken from [Richter et al., 2010].

Bibliography

[Adler, 2006] Adler, C. (2006). Radiation length of the ALICE TRD. *http://www-physics.lbl.gov/~gilg/PixelUpgradeMechanicsCooling/Material/Radiationlength.pdf*.

[Alexopoulos et al., 2011] Alexopoulos, T., Burnens, J., Oliveira, R. d., Glonti, G. Pizzirusso, O., Polychronakos, V., Sekhniaidze, G., Tsipolitis, G., and Wotschack, J. (2011). A spark-resistant bulk-micromegas chamber for high-rate applications. *Nucl.Instrum.Meth. A*, 640:110–118.

[ANSYS, Inc., 2017] ANSYS, Inc. (2017). Ansys mechanical apdl element reference. *http://www.ansys.com/*, (last visited 11.5.2017).

[ATLAS Collaboration, 2008] ATLAS Collaboration (2008). The ATLAS Experiment at the CERN Large Hadron Collider. *JINST*, 3.

[ATLAS Collaboration, 2013] ATLAS Collaboration (2013). New Small Wheel Technical Design Report. (May).

[ATLAS website, 1997] ATLAS website (1997). Homepage of the ATLAS experiment. *https://cern.ch/atlas*.

[Beringer, J. et. al. (Particle Data Group), 2012] Beringer, J. et. al. (Particle Data Group) (2012). Review of Particle Physics. *Physical Review D*, 86(1):010001.

[Biagi, 1999] Biagi, S. F. (1999). Monte Carlo simulation of electron drift and diffusion in counting gases under the influence of electric and magnetic fields. *Nucl.Instrum.Meth. A*, 421:234–240.

[Bortfeldt, 2014] Bortfeldt, J. (2014). Development of Floating Strip Micromegas Detectors. *Dissertation (LMU Munich)*.

[Carnegie et al., 2005] Carnegie, R. K., Dixit, M. S., Dubeau, J., and Karlen, D. (2005). Resolution studies of cosmic-ray tracks in a TPC with GEM readout. *Nucl.Instrum.Meth. A*, 538(February 2008):372–383.

[CERN website, 2008] CERN website (2008). Big Science. *http://bigscience.web.cern.ch*, (last visited 10.3.2017).

[CERN website, 2016] CERN website (2016). The HL-LHC Project. http://hilumilhc.web.cern.ch/about/hl-lhc-project, (last visited 10.3.2017).

[COMPELMA, 2015] COMPELMA (2015). RUBBER ELASTOMERIC CONNECTOR. http://www.compelma.com/medias/pdf/rubber_elastomeric_connector.pdf.

[DuPont Electronic Materials, 2017] DuPont Electronic Materials (2017). Pyralux. http://www.bestfpc.com/design-guide/Dupont-Photo-Image-Coverlay.pdf, (last visited 18.6.2017).

[EDMS CERN, 2016] EDMS CERN (2016). Drawing of Zebra holder. https://edms.cern.ch/ui/file/1736537/0/atummea_0039-v0.pdf.

[Elmer website, 2005] Elmer website (2005). https://www.csc.fi/web/elmer/.

[ESL ElectroScience, 2017] ESL ElectroScience (2017). Polymer Silver. http://electroscience.com/sites/default/files/datasheets/1901-S.pdf, (last visited 18.6.2017).

[Garfield website, 2010] Garfield website (2010). http://garfield.web.cern.ch/garfield/.

[Gere, 2004] Gere, J. (2004). *Mechanics of Materials*. Brooks/Cole - Thomson Learning, Belmont.

[Giomataris et al., 1996] Giomataris, Y., Rebourgeard, P., Robert, J. P., and Charpak, G. (1996). MICROMEGAS : a high-granularity position-sensitive detector for high particle-flux environments. *Nucl.Instrum.Meth. A*, 376:29–35.

[Gmsh website, 2009] Gmsh website (2009). http://geuz.org/gmsh/.

[Groom et al., 2001] Groom, D. E., Mokhov, N. V., and Striganov, S. I. (2001). Muon Stopping Power and Range Tables 10MeV - 100TeV. *Atomic Data and Nuclear Data Tables*, 78(2):183–156.

[Herrmann, 2016] Herrmann, M. (2016). Methods and Techniques for Construction of large area Micromegas. *Master thesis (LMU Munich)*.

[Herrmann, 2017] Herrmann, M. (2017). Internal communication.

[Huntsman, 2015] Huntsman (2015). Araldite 2011. https://www.freemansupply.com/datasheets/Araldite/2011.pdf.

[Iengo, 2016] Iengo, P. (2016). Collaboration communication.

[Jones, 2001] Jones, L. (2001). APV25-S1 User Guide. (September).

[König, 2015] König, V. (2015). Zusammenbau und Inbetriebnahme von dünnen Floating Strip Micromegas mit zweidimensionaler Auslesestruktur. *Bachelor thesis (LMU Munich)*.

[Krempel, 2017] Krempel (2017). Akaflex. *http://www.dralmi.it/pdf/Prosp-Basis-ENG.pdf*, (last visited 18.6.2017).

[Leo, 1994] Leo, W. R. (1994). *Techniques for Nulear and Particle Physics Experiments*. Springer, second edition.

[Linear Technology Corporation, 2010] Linear Technology Corporation (2010). LTspice user guide. *http://www.linear.com/designtools/software/*.

[LOCTIDE, 2013] LOCTIDE (2013). LOCTIDE 4305. *http://tds.loctite.com/tds5/Studio/ShowPDF/4305-EN?pid=4305&format=MTR&subformat=REAC&language=EN&plant=WERCS*.

[Lösel, 2013] Lösel, P. (2013). Performance Studies of Large Size Micromegas Detectors. *Master thesis (LMU Munich)*.

[Lösel, 2017] Lösel, P. (2017). Construction and quality assurance of large area resistive strip Micromegas for the upgrade of the ATLAS Muon Spectrometer at LHC/CERN. *JINST*, 12(06):C06005.

[Martoiu et al., 2011] Martoiu, S., Muller, H., and Toledo, J. (2011). Front-end electronics for the Scalable Readout System of RD51. *Nuclear Science Symposium and Medical Imaging Conference (NSS/MIC)*, pages 2036–2038.

[Müller, 2017] Müller, R. (2017). Quality Control of Micromegas Detectors for the ATLAS New Small Wheel Upgrade Project and Optimization of the Spatial Resolution of Possumus Detectors in two Dimensions. *Dissertation (LMU Munich)*.

[Ntekas, 2016] Ntekas, K. (2016). Performance characterization of the Micromegas detector for the New Small Wheel upgrade and Development and improvement of the Muon Spectrometer Detector Control System in the ATLAS experiment. *Dissertation (NTU Athens)*.

[Nührmann, 1994] Nührmann, D. (1994). *Das komplette Werkbuch Elektronik, Band 3&4*. Franzis'.

[Nygren and Marx, 1978] Nygren, D. R. and Marx, J. N. (1978). The Time Projection Chamber. *Physics Today*, (October):46.

[Raether, 1964] Raether, H. (1964). *Electron avalanches and breakdown in gases*. Butterworths, London.

[Richter et al., 2010] Richter et al. (2010). Development of Precision Muon Drift Tube Detectors for the High-Luminosity Upgrade of the LHC. *http://www.bo.infn.it/sminiato/sm10/presentations/s11/r-richter.pdf*.

[Smakhtin et al., 2009] Smakhtin, V., Mikenberg, G.and Klier, A., Rozen, Y., Duchovni, E., Kajamovitz, E., and Hershenhorn, A. (2009). Thin Gap Chamber upgrade for SLHC: Position resolution in a test beam. *Nucl.Instrum.Meth. A*, 598:196–200.

[Zibell, 2014] Zibell, A. (2014). High-Rate Irradiation of 15mm Muon Drift Tubes and Development of an ATLAS Compatible Readout Driver for Micromegas Detectors. *Dissertation (LMU Munich)*.

Acknowledgments

I would like to take the opportunity to thank all people, who have helped me to write this thesis.

In particular I want to name:

- my supervisor, Dr. Ralf Hertenberger, for the devoted support during my almost 5 years in this group and for always having time for discussions and help, even with the days full of meetings (especially Thursdays).
- my doctorate supervisor, Prof. Dr. Otmar Biebel, for the opportunity to write this thesis and the support in every matter.
- Priv. Doz. Dr. Peter Thirolf for writing the second evaluation of this thesis.
- Prof. Dr. Andreas Burkert and Prof. Dr. Thomas Kuhr for participating in the thesis defense.
- Prof. Dr. Dorothee Schaile for creating a very good atmosphere in the group.
- The hardware group for the fun during long nights with measurements during test-beams and late evenings in the ATLAS hall during gluing stuff (sometimes with one or two bottles of beer).
- The rest of the group for long nights during DPG and at summer or Christmas parties and the (un-)wanted distractions.
- And my family and my friends. They know why.

So long and thanks for all the glue.